DESIGN OF MULTICOMPONENT NANOSTRUCTURED SURFACES WITH TAILORED OPTICAL PROPERTIES

A Dissertation
Presented to
The Academic Faculty

by

Jeffrey A. Geldmeier

In Partial Fulfillment
of the Requirements for the Degree
Doctor of Philosophy in the
School of Materials Science and Engineering

Georgia Institute of Technology
August 2017

DESIGN OF MULTICOMPONENT NANOSTRUCTURED SURFACES WITH TAILORED OPTICAL PROPERTIES

Approved by:

Dr. Vladimir V. Tsukruk, Advisor
School of Materials Science and Engineering
Georgia Institute of Technology

Dr. Wenshan Cai
School of Electrical and Computer Engineering,
School of Materials Science and Engineering
Georgia Institute of Technology

Dr. Zhiqun Lin
School of Materials Science and Engineering
Georgia Institute of Technology

Dr. Younan Xia
Coulter Department of Biomedical Engineering
School of Chemistry and Biochemistry
Georgia Institute of Technology

Dr. Seung Soon Jang
School of Materials Science and Engineering
Georgia Institute of Technology

Date Approved: June 9th, 2017

Dedicated to my family and friends who helped me reach this point.

ACKNOWLEDGEMENTS

I would like to first and foremost thank my advisor, Prof. Vladimir V. Tsukruk, for his support and guidance these past years. From the start, he encouraged me to think critically about my experimental results, helped me develop strong technical skills, and provided helpful feedback on future plans. Prof. Tsukruk also provided a supportive lab environment that encouraged collaboration and constructive criticism and gave me the opportunity to attend several conferences which greatly helped in my professional development. I am also grateful to my committee members Prof. Zhiqun Lin, Prof. Younan Xia, Prof. Seung Soon Jang, and Prof. Wenshan Cai for taking time out of their busy schedules to provide helpful feedback and to review my dissertation.

I also want to thank our collaborators, Prof. Mostafa El-Sayed and his research scientist, Dr. Mahmoud A. Mahmoud. Dr. Mahmoud was instrumental for much of the work published here with his synthesis of plasmonic nanostructures and his expertise with Langmuir Blodgett deposition. His advice and recommendations for current and future projects were invaluable as well.

Finally, I would like to thank all SEMA lab group members that helped me during this work. In particular, special thanks go to Dr. Tobias König for his mentoring when I first joined the group. I would also like to thank Dr. Petr Ledin, Dr. Ju-Won Jeon, and Jing Zhou who have all contributed to the DOE project and helped me frequently. Final thanks go to Ren Geryak for his valuable insight and productive discussions.

TABLE OF CONTENTS

LIST OF TABLES

LIST OF FIGURES

LIST OF EQUATIONS

SUMMARY

Two promising ways of manipulating light-matter interactions at the nanoscale are through the use of noble metal plasmonic nanostructures and quantum dots. However, the majority of previous studies focus on single particle properties in solution instead of in mesoscale, organized, substrate-bound arrays and films. Understanding and guiding the assembly behavior of nanostructures in a large-scale, bottom-up, and controllable manner has important ramifications for controlling resultant unique properties for emerging optical applications. The primary goal of this research is therefore understanding, both experimentally and computationally, the principles that govern plasmonic and emissive properties of nanostructure assemblies that possess novel emergent optical properties.

This work was focused into three concrete tasks for understanding, controlling, and tuning nanoscale optical properties through the use of nanoparticle coupling interactions, polymeric components, and large-scale assemblies:

- Understanding the nanostructure assembly fundamentals that can result in broadband absorbing plasmonic nanostructure assemblies through controlled coupling and assembly behavior;
- Gaining insight into the various morphologies of conjugated polymer and plasmonic nanostructure composites and how their combination can be utilized for reversible and stimuli-responsive plasmonic resonances;
- Examining the morphology of quantum dot/polymer composite films and how their interfacial properties can be altered for the enhancement of quantum dot fluorescence using dewetting-induced far-field scattering.

Specifically, the coupling of silver nanocubes with a nanogroove-containing gold film by using a polymer spacer layer was demonstrated to provide high broadband absorption in the visible-near-infrared range over a wide range of incident light angles. The extension of broadband absorption to a total-internal-reflection framework was accomplished using a silver nanocube aggregation gradient. Silver nanodisks, gold nanocubes, and gold nanorods were combined with different conjugated polymers to achieve reversible electrically controllable resonance modulation. Novel light-sensitive compounds were also synthesized and combined with silver nanocubes to create light-driven, extinction modulating films. Finally, the dewetting behavior of quantum dot/polymer composite thin films was utilized to increase film emission. In particular, this method was able to generate large area photoluminescence intensity enhancements in a controllable and facile manner in comparison to other enhancement methods. Realistic finite-difference time-domain electromagnetic simulations that took factors such as nanoparticle edge rounding, nanoparticle coupling, and the presence of surfactants and substrates were also instrumental in clarifying the mechanisms behind observed assembly phenomena.

Overall, the integration of multiple components in nanoscale assemblies and the subsequent characterization processes presented in this work can be used to address several existing challenges in present photonic and sensor applications. The controlled combination and assembly of noble metal and semiconductor nanostructures realized during the course of this work can serve as future guides and frameworks for further control of light-matter interactions at the nanoscale.

CHAPTER 1. INTRODUCTION

Light-material interactions occur due to the interactions of light's incident oscillating electromagnetic fields with the electrons in matter. This motion may lead to several mechanisms such as the absorption, scattering, transmission, reflection, or emission of photons. The demand to find novel ways to govern these light-matter interactions has risen as more control of local energy transfer, photo-thermal effects, and energy dissipation is sought for applications such as photovoltaics,[1] waveguiding,[2, 3] and sensing.[4, 5] The manipulation of electromagnetic fields beyond the diffraction limit is also critical for emerging technologies such as optical circuitry,[6, 7] metamaterials,[8, 9] and heightened lithography capabilities.[10, 11]

Two promising ways of manipulating light-matter interactions at the nanoscale are through the use of noble metal plasmonic nanostructures and semiconductor nanoparticles (quantum dots). Plasmonic nanostructures possess size-, shape-, and environmentally-controlled optical absorption and scattering spectra that enable a wide range of tunability, and they are able to confine light below the diffraction limit into nanometer-sized regimes. Quantum dots possess size-dependent emissive properties due to the quantum confinement of excitons and can be additionally distinguished by their broadband absorption, narrow emission peak, and high stability in a multitude of environments.

1.1 Plasmonic Nanostructures

1.1.1 *Introduction to plasmonic nanostructures*

Plasmonic nanostructures refer to nanostructures typically composed of noble metals such as gold or silver that allow for the fine control and manipulation of a structure's electromagnetic fields due to interactions between incident light and free electrons in the material. For instance, light can be confined and guided using plasmonic materials into spatial regimes much smaller than the wavelength of light.[3] Depending on the size and shape of the nanostructure, incident light can produce either localized surface plasmon resonances (LSPRs) or surface plasmon polaritons (SPPs) (**Figure 1.1**).[12] Currently, a wide range of nanostructure shapes such as spheres, wires, cubes, rods, prisms, and disks with high yields can be synthesized for various applications. The shape and size of the nanoparticles largely determine their spectral shapes and locations, although most nanoparticle extinction spectra are confined to the visible-near infrared (IR) wavelength range. The size of the nanostructure also impacts the relative intensities of their extinction

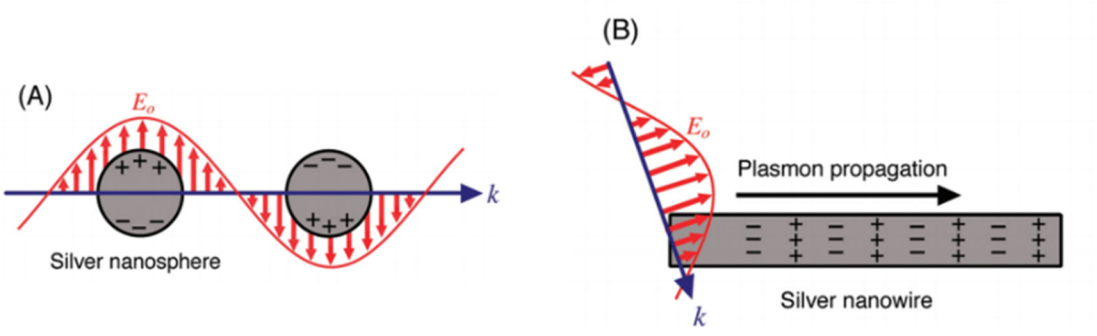

Figure 1.1: (a) Nanostructures smaller than the wavelength of incident light result in LSPRs. (b) Nanostructures with a dimension larger the wavelength of exciting light result in SPP propagation. Reproduced from ref. 12.

components, absorption and scattering, and affects whether their electric fields are local or propagating in nature. Apart from their spectral extinction spectra, plasmonic nanostructures are often employed for their regions of high electric field enhancement, which will be discussed later in further detail.

The incorporation of plasmonic active materials in devices provides a way to tune the light-matter interactions of materials. Numerous applications for such materials have already arisen, such as spectrum filters[13-16], chemical and biological sensors[17-20], superlenses[21], photonic circuitry,[7, 22] and increased absorption in solar cells,[1, 23] and there is still a continued and growing demand to develop novel plasmonic structures and metamaterials that give rise to unique properties.[24]

1.1.2 *Plasmonic nanostructure synthesis*

The precise control over nanoparticle shape and size has progressed very rapidly and been largely successful. These approaches include bottom-up colloidal synthesis and top-down lithographic techniques that have been able to offer low shape and size polydispersities.[25-27] One-pot and seed-mediated bottom-up synthesis methods are the most commonly used techniques and will be briefly discussed, followed by an examination of several available lithographic and template approaches.

One-pot synthesis

One-pot synthesis entails a single-step, single-reaction process and remains widely used due to its simplicity and reproducibility. Reducing agents are used in solution to reduce metal ion precursors into atoms and subsequent nanoparticles, which are often further

controlled by the presence of stabilizing agents. For instance, 10-20 nm diameter gold nanoparticles can be created with the popular Turkevich method, first introduced in 1951, by using $HAuCl_4$ as a precursor and sodium citrate as both a reducing and a stabilizing agent in boiling water.[28] Larger nanoparticles ranging from 20 to 120 nm were created as well by Frens in 1973 by tailoring the sodium citrate:Au ratio, although this historically led to larger polydispersity as well.[29] Recently, more monodisperse gold nanoparticles 20-40 nm in size have been created using modified Turkevich-Frens methods with different salts, reaction temperatures, and solution pHs.[30, 31]

One-pot synthesis methods can also be used for shape control over the resultant nanoparticles provided appropriate capping agents are used. In the polyol process for instance, $AgNO_3$ can be reduced by ethylene glycol, which acts as both a reducing agent and a solvent, to form sphere-like nanoparticles.[32] In the presence of a poly(vinyl pyrrolidone) (PVP) capping agent however, nanoparticles can be precipitated as wires due to the selective binding of PVP to Ag {100} facets.[33] Increasing the concentration of $AgNO_3$ while maintaining the same molar ratio of PVP:$AgNO_3$ instead can be used to produce nanocubes, demonstrating the versatility of this process.[34] By controlling reactant concentrations and introducing trace coordination ligands such a Cl^- and Br^- ions, the polyol process can also be used to form a variety of other nanostructures such as right bipyramids, beams, and triangular plates(**Figure 1.2**).[12] Lastly, asymmetric nanoparticles can also be produced using one-pot synthesis techniques with multiple reducing agents. In a recent example, $AgNO_3$ was simultaneously reduced with ascorbic acid (AA) and $NaBH_4$ in the presence of a PVP capping agent.[35] The two resultant rates of reduction created

asymmetric nanoparticle seeds with stacking faults, which further developed into silver nanodisks, although the resultant nanoparticles were up to 25% polydisperse in nature.

Despite the growing number of nanoparticles that can be synthesized using one-pot methods, there are some nanoparticle material and shape combinations, such as gold nanorods (AuNRs), that cannot be produced in this facile manner.[36-38] Another factor that

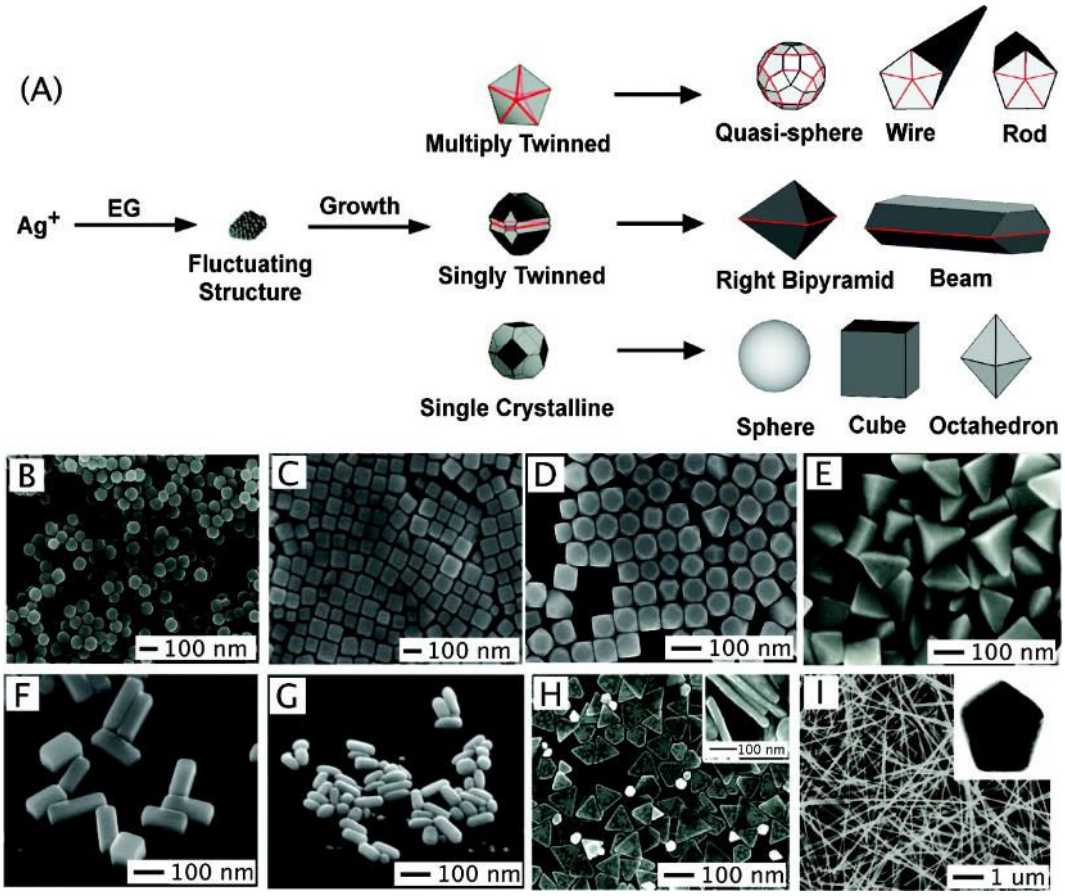

Figure 1.2: (a) The polyol process for the synthesis of Ag nanostructures. Initial reactant concentrations determine the dominant seed type which can ultimately develop into a variety of nanostructures (b)-(i) Different Ag nanostructures produced by the polyol process. Reproduced from ref. 12.

often limits one-pot methods is the inherent combination of the nucleation and growth processes, which can hinder monodispersity and shape selection.[39]

Seed-mediated synthesis

Seed-mediated synthesis methods are frequently used to overcome the inherent drawbacks of one-pot synthesis methods. In these methods, the generation of nanoparticle seeds and the subsequent growth of them are decoupled from one another, allowing finer control over each process. The seed morphology and symmetries, as mentioned previously with the formation of silver nanodisks, largely dictate what resultant nanoparticles can be produced. After seed formation, growth can be initiated in a controllable manner in growth solutions using mild reducing agents that cannot induce spontaneous nucleation of the precursor agents.[40]

One of the most familiar seed-mediated synthesized nanoparticles are AuNRs.[41, 42] For these nanoparticles, one method entails that Au seeds approximately 1-2 nm are first prepared by the reduction of $HAuCl_4$ using $NaBH_4$ in the presence of cetyltrimethylammonium bromide (CTAB).[42] Seeds can then be added to growth solutions containing AA, $AgNO_3$, $NaBH_4$, and CTAB to produce nanorods with aspect ratios up to 4.7. Rods with larger aspect ratios up to 10 can be produced using a surfactant mixture of CTAB and benzyldimethylhexadecylammonium chloride (BDAC) and by aging the nanorod solution for up to 7 days. Different nanoparticle shapes such as hexagonal prisms,

nanocubes, and triangular prisms can also be produced simply by varying the AA and seed concentrations (**Figure 1.3**).[43]

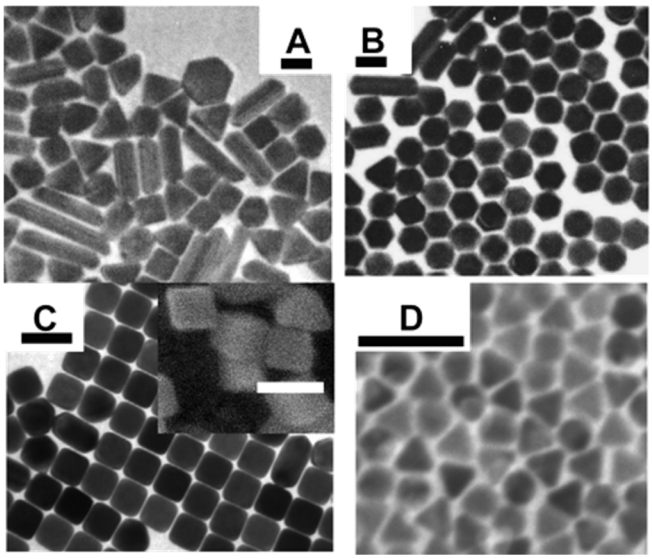

Figure 1.3: Au nanoparticles synthesized using seed-mediated techniques. AA increases from (a) to (c), and seed concentration increases from (c) to (d). Reproduced from ref. 43.

Lithographic techniques

Although remarkable progress has been achieved in synthesized a wide variety of nanostructures using colloidal techniques, the subsequent directed placement of these nanoparticles on substrates remains a challenge. For applications that require precise nanostructure placement, top-down lithographic approaches such as electron beam lithography (EBL) or focused ion beam (FIB) milling may be used instead.

In EBL, an electron beam is used to expose selected areas of a polymer resist layer. Exposed areas may be negative and resistant to subsequent development solvent, such as hydrogen silsequioxane (HSQ), or positive and decomposed with the development solvent

as in the case of poly(methyl methacrylate) (PMMA).[44, 45] After development, the polymer pattern can be used as a mask for metal deposition or etching and can be subsequently removed (**Figure 1.4a**). Such techniques have been used to create highly ordered nanoparticle arrays with sub-10 nm resolution, as Duan et al. demonstrated using HSQ (**Figure 1.4b**).[46]

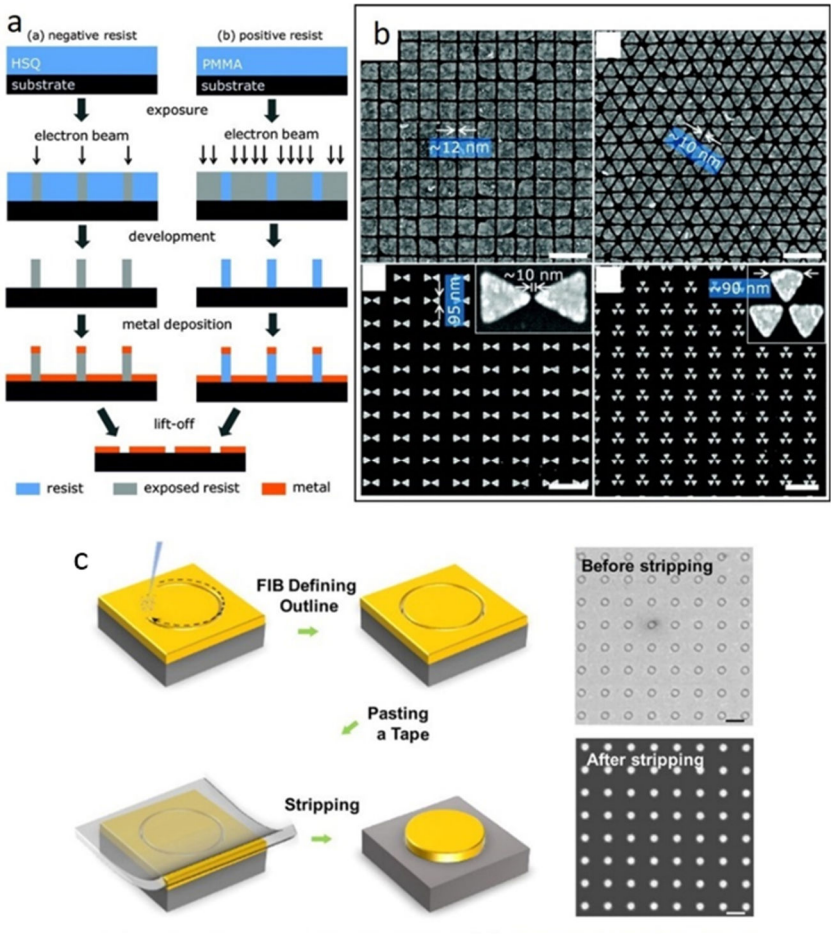

Figure 1.4: (a) The EBL process for creating nanostructures using either a positive or negative resist. (b) Different Au nanostructures fabricated with sub-10 nm gaps using an HSQ negative resist. Reproduced from ref. 46. (c) FIB "sketch and peel" process for fast nanostructure milling. Reproduced from ref. 50.

FIB can be used instead to directly mill nanostructures from metallic films using ion beams at resolutions typically down to 10-15 nm.[47-49] Such a process can be used for the creation of "negative" nanoholes with various shapes or "positive" nanostructures albeit with longer processing times due to the larger amount of material needed to be removed. Recently however, Chen et al. dramatically improved the throughput of FIB-milled positive nanostructures in a "sketch and peel" process by first tracing their outlines into the silicon substrate.[50] Sputtered Si atoms were then redeposited on the nanostructure walls and prevented their lift-off after common scotch tape was used to peel the film (**Figure 1.4c**).

1.1.3 *Assembly strategies*

Apart from the effects of the shape and size of plasmonic nanoparticles, the local assembly of them has a significant impact on their resultant optical properties. Therefore, controlling their assembly and orientation on substrates is critically important when using colloidally synthesized nanoparticles. Many methods can be used to generate 1D or 2D nanoparticle arrays or to facilitate the local assembly of nanoparticles into dimers, satellite structures, and other hierarchical assemblies, and several will be discussed here; additionally, a number of excellent reviews exist that cover this topic more comprehensively.[51-53]

Ligand-directed assembly

Functionalizing nanoparticle surfaces with assembly-directing ligands has proven largely successful at creating both large-scale, organized arrays as well as local assemblies of nanoparticles. For instance, Gao et al. assembled Ag nanocubes into oriented 1D chains by grafting nanocubes with thiol-terminated PVP or polyethylene glycol (PEG) chains.[54] Due to the hydrophilic nature of the polymer ligands, the nanocubes phase-segregate when

introduced into a hydrophobic polymer matrix. The organization of the nanoparticles within the chains could also be controlled; by tailoring the ligand length (2.0-5.7 nm), edge-to-edge or face-to-face orientations of the nanocubes within the chains are preferred (**Figure 1.5a, b**).

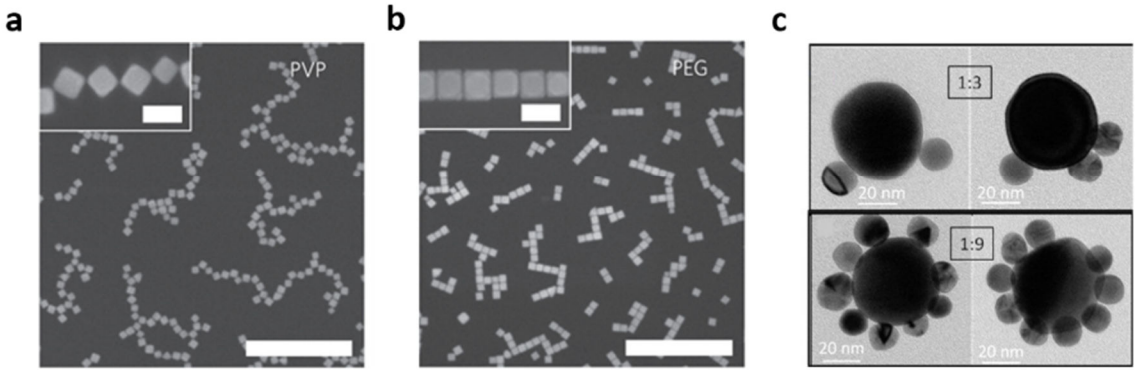

Figure 1.5: Ag nanocubes oriented (a) edge-to-edge with grafted PVP chains and (b) face-to-face with grafted PEG chains. Scale bars are 1 μm and inset scale bars are 100 nm. Reproduced from ref. 54. (c) Planet-satellite clusters composed of different size Au nanoparticles. The number of satellites is controlled by adjusting the satellite:core ratio in solution. Reproduced from ref. 61.

Nanoparticle clusters or core-satellite heterostructures composed of different types of nanoparticles can also be created using strategic ligand functionalization. In a type of functionalization useful for many sensing strategies, nanoparticles can be functionalized with single-strand DNA to form dimers or aggregates with complementary strand-functionalized nanoparticles.[55, 56] This technique has proven to be useful for even single base pair mismatch specificity.[55] This concept can be extended with "DNA origami," where DNA complementary strands are rationally chosen to form complex patterns, to form nanoparticle assemblies such as chains, chiral tubes, and planet-satellite clusters.[57-60]

Planet-satellite clusters can also be formed by linker molecules that bind different types of nanoparticles together. In one example, Gandra et al. functionalized core Au nanoparticles with p-aminothiophenol (p-ATP) that were able to use the binding affinity of the terminating amine to capture smaller satellite Au nanoparticles (**Figure 1.5c**).[61] The number of satellite nanoparticles was also controllable by varying the satellite:core ratio in solution.

Langmuir Blodgett deposition

The Langmuir Blodgett (LB) technique is commonly used to create nanoparticle monolayers on substrates in a controllable manner in comparison to common deposition techniques such as spin-coating and spray-coating that result in aggregation.[62] First, a nanoparticle solution is dispersed on a water subphase layer using a volatile solvent such as chloroform which quickly evaporates. Substrates are then raised or lowered through the nanoparticle layer and subsequently lift off a uniform monolayer of nanoparticles. By controlling the surface pressure of the nanoparticle layer on the water subphase, the density of nanoparticles on the surface can also be increased or decreased. For instance. Tao et al. demonstrated the dependence of the monolayer color before deposition and the monolayer morphology after deposition on the film's surface pressure at the trough surface (**Figure 1.6a-c**).[63] At low surface pressures, the nanoparticles adopt an ordered hexagonal lattice organization due to hard sphere-like interactions. As the surface pressure is increased, close-packed nanoparticle islands begin to nucleate, and further compression results in a close-packed film. In a combinatorial approach involving both ligand functionalization as well as LB deposition, Mahmoud synthesized large-area 2D arrays of PEG-functionalized Ag nanocubes (**Figure 1.6d, e**).[64] Ag nanocubes closely packed with one another due to

the affinity of PEG with itself, although large voids were present due to free CTAB/PEG micelles. Shorter chain PEG (2,000 M_w) promoted high nanoparticle alignment, small cube-to-cube distances of 4.1 nm, and cracking in the assembly (**Figure 1.6d**). In comparison, longer chain PEG (6,000 M_w) resulted in less alignment, larger cube-to-cube distances of 6.4 nm, and less cracking (**Figure 1.6e**).

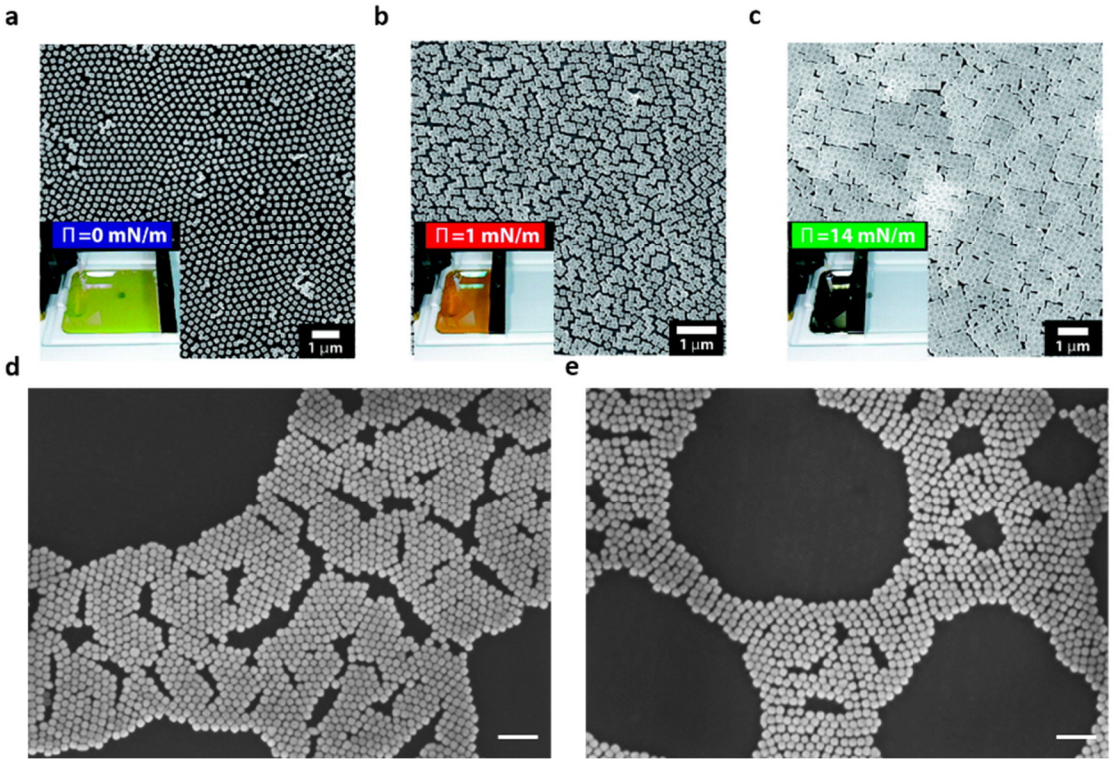

Figure 1.6: LB monolayers of Ag nanoparticles deposited at (a) 0, (b) 1, and (c) 14 mN/m. Insets depict the monolayers while on the LB subphase. Reproduced from ref. 63. Ag nanocube monolayers with grafted PEG of (d) 2,000 M_w and (e) 6,000 M_w. Scale bars are 200 nm. Reproduced from ref. 64.

Templated assembly

Lastly, nanoparticle assembly can be accomplished using different templating techniques, although such methods may involve pre-deposition lithographic steps for template fabrication. One popular method is to draw nanoparticle solutions over hard recess templates, resulting in nanoparticle clusters in the recesses.[65-67] The cluster sizes and distributions can be tailored my modifying the recess shape and size. In one example, Henzie et a. assembled Ag octahedra inside circular holes, with the cluster size being correlated with the hole size (**Figure 1.7a**). In a novel templated assembly method that did not required lithographic techniques, Hanske et al. employed wrinkled elastomer stamps that were created by simple plasma oxidation of a stretched polydimethylsiloxane (PDMS) layer (**Figure 1.7b**).[68] After plasma oxidation, the PDMS layer was relaxed and buckled into wrinkles due to the mechanical mismatch between the oxidized PDMS and the unmodified PDMS. The wrinkle width and periodicity could also be tuned by simply adjusting the preset strain and the plasma dose. Au nanoparticles then spin-cast onto the

PDMS layers naturally collected in the wrinkles and could be easily stamped onto other substrates, resulting in highly organized lines of nanoparticles (**Figure 1.7c**).

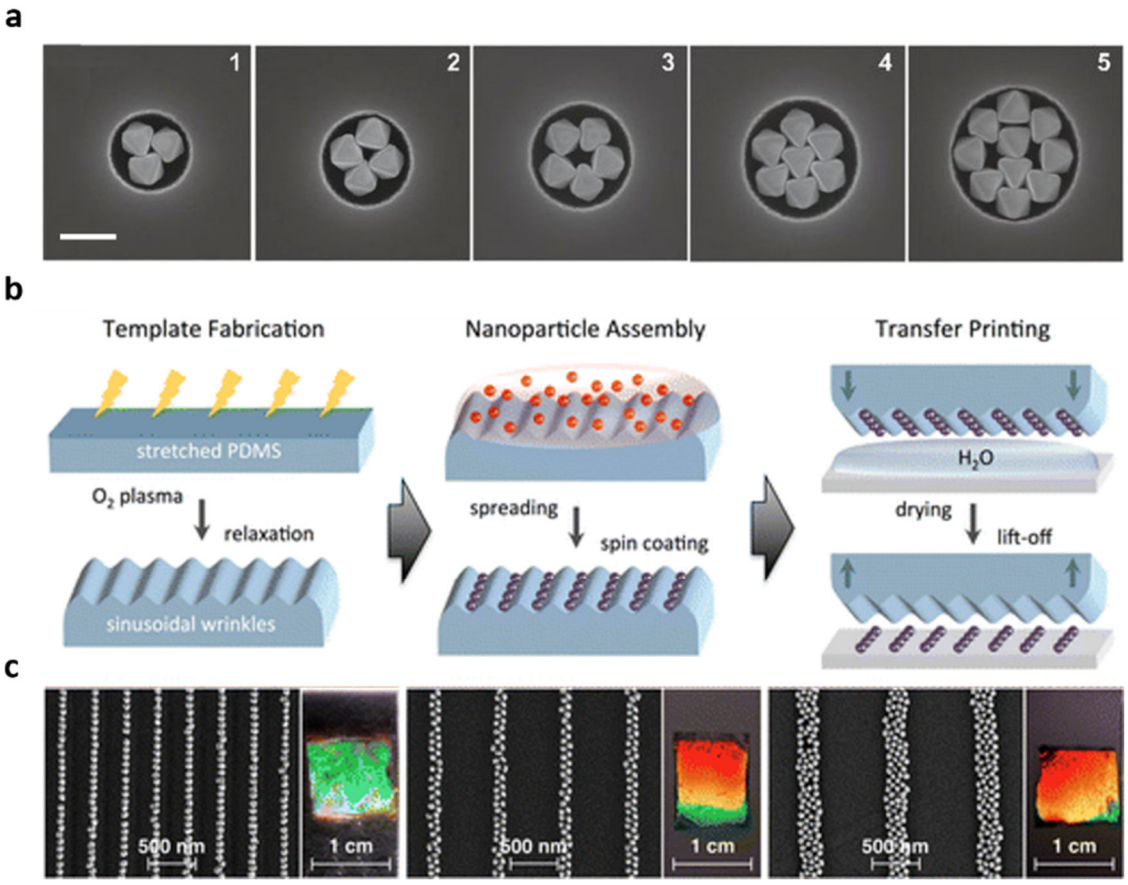

Figure 1.7: (a) Ag octahedra assembled inside templated circular holes. Scale bar is 500 nm. Reproduced from ref. 67. (b) Fabrication of wrinkled PDMS stamps and subsequent Au nanoparticle deposition. (c) Resulting nanoparticle assemblies after stamping onto quartz substrates. Reproduced from ref. 68.

1.1.4 *Localized surface plasmon resonances*

LSPRs arise when light interacts with small metallic nanoparticles with dimensions smaller than the wavelength of incident light ($R/\lambda<0.1$).[4] The light causes the coherent oscillation of the free electrons in a particle, leading to an accumulation of polarization charges on the

nanoparticle surface. For the simple case of a metallic nanosphere, Mie's solution of Maxwell's equations can be used to obtain a particle's extinction cross-section (C_{ext}):[69, 70]

$$C_{ext} = \frac{24\pi^2 R^3 {\varepsilon_d}^{3/2}}{\lambda} \frac{\varepsilon_m''}{\left(\varepsilon_m' + 2\varepsilon_d\right)^2 + \left(\varepsilon_m''\right)^2} \quad (\mathbf{1})$$

where R is the radius of the nanoparticle, ε_d is the relative dielectric constant of the medium, ε_m' is the real part of the dielectric constant of the metal, and ε_m'' is the imaginary part. This cross-section can be further classified into absorption and scattering cross-sections, where $C_{ext}=C_{abs}+C_{scat}$. Scattering scales with R^6 while absorption scales with R^3, meaning that large particles (>50 nm) predominantly scatter light while small particles (<50 nm) predominantly absorb light.[71, 72] From Equation **1**, it can be seen that large values of C_{ext} are only possible when ε_m' is close to $-2\varepsilon_d$ and ε_m'' is small. A quality factor

$$Q = \frac{\omega\left(d\varepsilon'/d\omega\right)}{2\left(\varepsilon''(\omega)\right)^2} \quad (\mathbf{2})$$

therefore exists that is dependent on wavelength and the dielectric properties of different metals (**Figure 1.8**).[12, 73] Based on the quality factor of different metals, it is apparent that silver and gold can be most readily used over the visible-NIR regime, although copper can be used above 650 nm.[74-76] Besides their nanoparticle constituent materials, LSPRs are also extremely sensitive to other factors such as their size, shape, the surrounding medium, and the proximity of other metallic surfaces or particles.[72, 77-83]

As mentioned previously, size has a significant impact on the extinction properties of a nanoparticle and whether it is predominantly absorbing or scattering. It should be noted as well that the overall extinction will increase with an increase in size due to scaling with the volume of the nanoparticle ($C_{ext} \propto R^3$).[84] The size of the nanoparticle also influences its

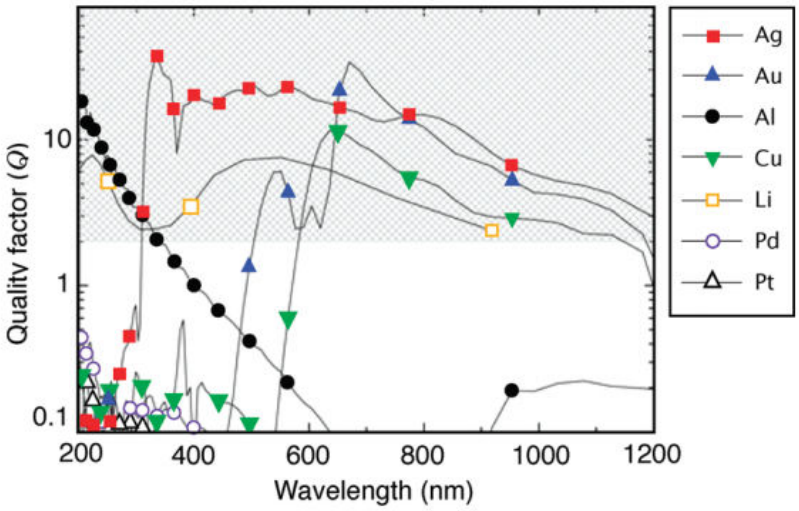

Figure 1.8: Quality factor (Q) for a metal-air interface, with higher numbers denoting stronger plasmonic resonances. Reproduced from ref. 12.

LSPR peak wavelength, with an increase in size generally corresponding with a redshift of the LSPR peak wavelength. For instance, an Au sphere increasing from 10 nm to 100 nm in diameter will approximately redshift 47 nm.[85] Similarly, silver nanodisks exhibit a 158 nm redshift with a size increase from 26 to 47 nm.[35] Larger nanoparticles also exhibit broader LSPR peaks due to radiative damping of their dipole oscillations.[86] Finally, large nanoparticles may even exhibit new peaks. For instance, Ag nanocubes typically exhibit a large dipolar peak and a smaller quadrupole one, but peak splitting can be induced in the dipole peak as the nanocube size is increased, which can be attributed to the separation of the absorption and scattering spectra from one another as the size is increased.[87, 88] Larger nanoparticles also exhibit broader LSPR peaks due to radiative damping of their dipole oscillations and higher order multimodes can arise as the particle size is increased as well due to more possible surface charge distributions.[86] With these combined effects, the Ag

nanocube peak can be seen to significantly broaden as the size is increased from 36 to 172 nm (**Figure 1.9a**).[89]

The shape of the nanoparticle has the largest influence on the nanoparticle LSPR resonances, and therefore the controlled synthesis of differently shaped nanoparticles has been of the utmost interest for the past decades. Silver nanoparticles of various shapes and sizes display plasmonic resonances that span the entire wavelength range of 320-1100 nm.[12] For instance, Ag spheres, pentagonal particles, and triangular prisms of roughly the same size are seen to display respective LSPRs in the blue, green, and red wavelength regions (**Figure 1.9b**).[90, 91] The rounding of nanoparticle edges and corners can have a drastic influence on LSPR spectra despite the relatively low change in shape. In general, rounding removes regions of high charge density that can collect on sharp facets from the so-called "lightning rod effect" and results in an LSPR blueshift and the reduction of higher order modes. For example, Ag nanocubes with no edge rounding exhibit 6 plasmon modes due to the high polarizability of the sharp edges, while a rounding of 17% results in only 3 plasmon modes.[92] In another example, the dipole peak of 100 nm triangular Ag prisms blueshifts from 770 to 670 nm by truncating the tips by 12 nm on each side.[93] Also, when a particle becomes non-symmetric in nature (i.e. nanorods), it exhibits a longitudinal mode and a transverse mode.[77, 87, 94, 95] The intensity and spectral position of these resonances depend on the aspect ratio of the particle; when a particle's aspect ratio is increased, the longitudinal mode will redshift while the transverse mode remains at the same spectral position, as seen in the case of Ag nanobars (**Figure 1.9c**).[39, 77]

Another important consideration for nanoparticle plasmonic phenomena is the effect of the surrounding environment. Generally, an increase of the refractive index of the environment

has the effect of redshifting the plasmon peak wavelength, with the shift magnitude being determined by the nanoparticle's refractive index sensitivity (RIS). For a homogeneous environment, the RIS can be determined by:

$$\Delta\lambda_{LSPR} = m\Delta n \quad (\mathbf{3})$$

where $\Delta\lambda_{LSPR}$ is the change in the LSPR peak wavelength, m is the RIS, and Δn is the change in the refractive index of the environment.

In a recent example, Shen et al. fabricated gold mushroom arrays that demonstrated a high RIS of 1,015 nm/RIU due to their high surface area contact with the environment as opposed to nanoparticles resting on a substrate. (**Figure 1.9d**).[96] If the environmental refractive index is altered in a more localized manner, such as in the case of polymer shells around nanoparticles, the LSPR peak wavelength change can instead be calculated by:[70]

$$\Delta\lambda_{LSPR} = m\Delta n\left[1 - \exp\left(\frac{-2d}{l_d}\right)\right] \quad (\mathbf{4})$$

where Δn is the refractive index change between the shell and the environment, d is the thickness of the shell, and ld is the intrinsic electric field decay length of the nanoparticle.

Nanoparticle LSPRs are also very sensitive to other structures such as substrates, metallic films, or the presence of other nanoparticles. Introducing a substrate to the nanoparticle

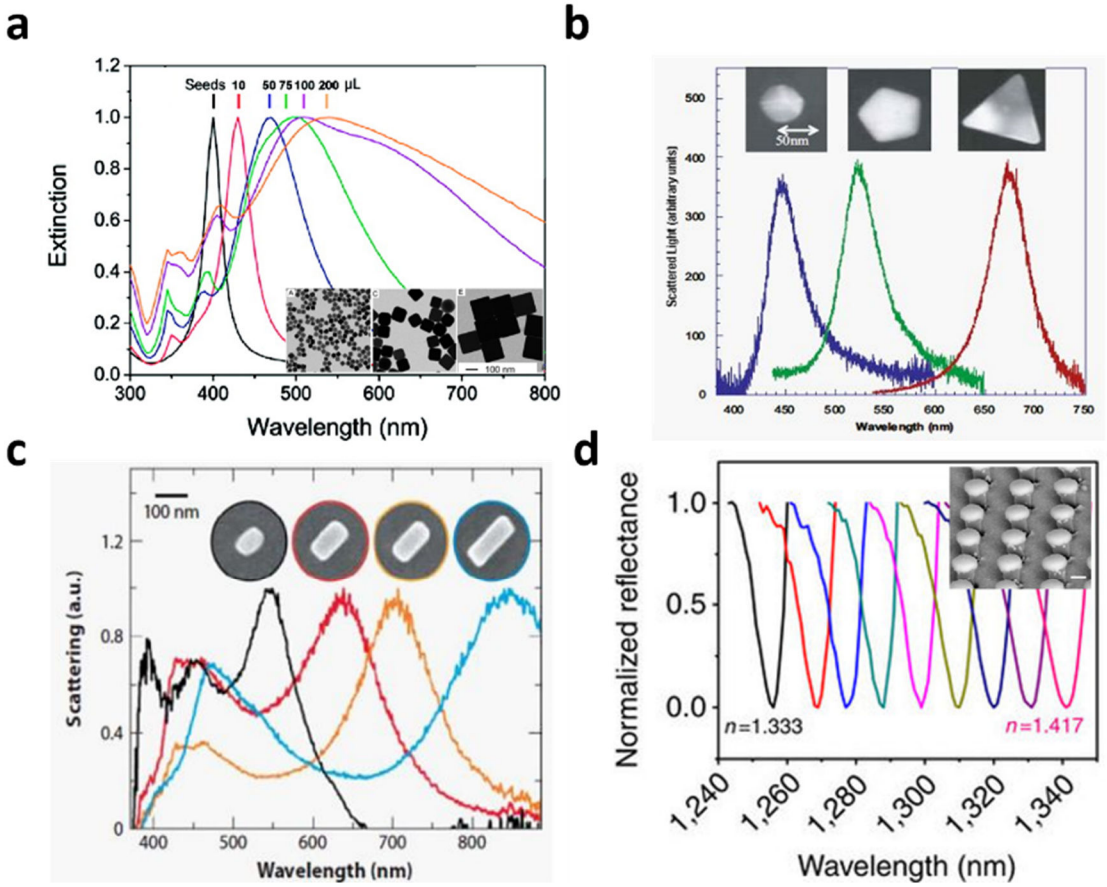

Figure 1.9: (a) The extinction spectra of Ag nanocubes as their size is increased. The insets from left to right correspond respectively with the pink, green, and orange spectra. Reproduced from ref. 89. (b) The extinction spectra of Ag nanospheres, pentagons, and triangular prisms of approximately the same size. Reproduced from ref. 90. (c) The longitudinal LSPR of Ag nanobars redshifts as their aspect ratio is increased. Reproduced from ref. 39. (d). The extinction spectra of a gold mushroom array as a function of the environment refractive index. Reproduced from ref. 96.

environment can result in various interactions. First, in a manner analogous to that of an increasing refractive index environment, substrates typically are a higher refractive index than the medium and will redshift the nanoparticle dipolar LSPR.[97] In a constant dielectric environment, small particles interact with light primarily through their dipole modes. The introduction of a substrate causes a coupling between the bright dipolar and the dark

quadrupolar modes of a particle due to the charge "images" in the substrate, potentially leading to a significant peak splitting effect (**Figure 1.10a**).[98] These peaks can be classified as bonding modes that display symmetric field intensities and anti-bonding modes that are asymmetric in nature. Fano resonances may also occur when dark quadrupolar and bright dipolar mode significantly overlap. In these cases, the hybridized peak is asymmetric and displays a narrower bandwidth that has a high figure of merit for applications such as colormetric chemical sensing.[98]

If the substrate is dielectric in nature as discussed previously, the particle's image charges are screened by a factor of $(\varepsilon - 1)/(\varepsilon + 1)$ and the degeneracy between different plasmon modes is lifted.[99, 100] When the substrate is instead metallic and exhibits plasmon modes, the image charges are much stronger, and hybridization also occurs with the surface plasmons of the substrate which will be discussed later in further detail.[101] The image charge coupling will always result in a redshifted peak, while SP hybridization can result in either a redshift or blueshift depending on the respective energy levels of the LSPR and the surface plasmon.[101] This shift is also highly dependent on the distance between the nanoparticle and the metallic film. For instance a silver nanosphere separated from a gold film by a dielectric spacer displays an LSPR that blueshifts with an increasing spacer layer thickness (**Figure 1.10b**).[102]

Lastly, the presence of other plasmonic nanostructures has a significant impact on the resultant LSPR and the local electric field distribution. When one or more nanoparticles are close to one another, their plasmonic resonances will hybridize in a manner similar to that of a nanoparticle and a metallic film. This coupling interaction causes a redshift of the LSPR of a single particle, although the exact peak position is highly dependent on the

interparticle gap between particles.[103] For example, Au nanodisks dimers with interparticle spacings between 2 and 212 nm demonstrate pronounced redshifts as the gap distance is decreased (**Figure 1.10c**).[104] In fact, the LSPR shift can be universally fitted using the plasmon ruler equation:

$$\frac{\Delta\lambda}{\lambda_0} = A\exp\left(\frac{-(s/D)}{B}\right) \quad (\mathbf{5})$$

where $\Delta\lambda/\lambda_0$ is the fractional plasmon shift, s is the interparticle edge-to-edge separation distance, D is the nanoparticle diameter, and A and B are constants.[104] It should be noted that this equation specifically applies for nanoparticle dimers. In practice, nanoparticle coupling is often seen for nanoparticle aggregates instead, which display much broader and redshifted LSPRS due to the existence of multiple coupling modes; additionally, such coupling is usually unpredictable. LSPR coupling can extend to distances as large as ~2.5 times the particle diameter.[105] However, small gaps are often more desirable for the formation of "hot spots" between the particles. While nanoparticles possess regions of localized enhanced electromagnetic fields at their tips or edges, hot spots contain field intensities that are orders of magnitude stronger than those of single particles.[106-108] Highest enhancements are found for LSPRs confined to extremely small spatial regions, such as a gap between two Au nanospheres. (**Figure 1.10d**).[70, 109]

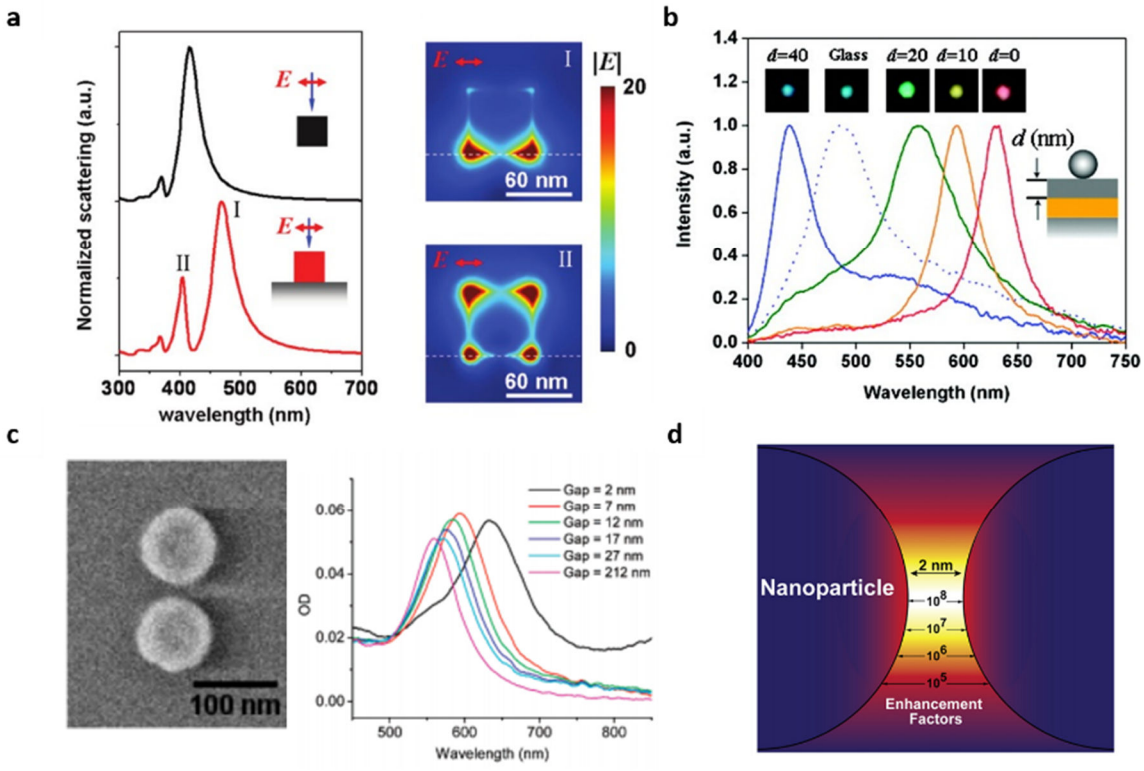

Figure 1.10: (a) Peak splitting of an Ag nanocube LSPR into bonding (I) and anti-bonding (II) modes due to the introduction of a substrate. Electric field distributions of the I and II modes are also shown. Reproduced from ref. 98. (b) Optical scattering spectra for silver nanoparticles separated from a gold film by a silica spacer layer of varying thickness. Reproduced from ref. 102. (c) An Au nanodisk dimer displays a varied LSPR peak position depending on the interparticle gap distance. Reproduced from ref. 104. (d) The enhancement factor distribution in an Au nanosphere dimer hot spot with a 2 nm gap. Reproduced from ref. 70.

1.1.5 *Surface plasmon polaritons*

Surface plasmons (SPs) are coherent free electron oscillations that exist at any interface where the real part of the dielectric function changes signs, such as a metal-dielectric interface. These charge oscillations also create electromagnetic fields in the vicinity of the surface; the combination of these two effects, the charge motion and the associated electromagnetic fields, is what has been termed a SPP. SPs were first predicted by Ritchie in 1957 when he noticed energy losses in very thin gold foils upon bombardment with fast

electrons.[110] Since then, researchers have discovered and manipulated the coupling of incident photons with SPs. By solving Maxwell's equations with the appropriate boundary conditions, one can find this SP dispersion relationship to be:[111]

$$k_{SP} = k_0\sqrt{\frac{\varepsilon_d\varepsilon_m}{\varepsilon_d+\varepsilon_m}} \quad (6)$$

The SP wavenumber, k_{SP}, is dependent on the free-space wavenumber ($k_0=\omega/c$) and the permittivities of the metal, ε_m, and the dielectric, ε_d. Based on the equation above, the momentum of the SP mode is greater than that of a photon's with the same frequency in air, meaning that light cannot ordinarily excite or couple to the SP. One way to resolve this mismatch is to employ a prism (**Figure 1.11a**).[112, 113] The wave number of incident light passing through a prism increases to a wavenumber of kn for $n>1$. If this light wave undergoes total internal reflection (TIR) on the inner surface of the prism, it will produce an evanescent wave outside of the prism with a momentum greater than k_o which can couple to SPs (**Figure 1.11b**).[114] Another way to resolve the mismatch in momentum is to provide local defects, such as holes or bumps.[115, 116] Lastly, a grating may be used to excite SPPS as they provide a momentum increase of $2\pi/\Lambda$ to the horizontal component of the wave vector (**Figure 1.11c**).[117] This leads to a resonance wavelength at:

$$\lambda_{sp} = \frac{a_0}{m}\left(\frac{\varepsilon_1\varepsilon_2}{\varepsilon_1+\varepsilon_2}\right)^{1/2} \quad (7)$$

where a_o is the period of the grating, ε_1 is the dielectric constant of the medium, ε_2 is that of the metal, and m is a constant.[118, 119]

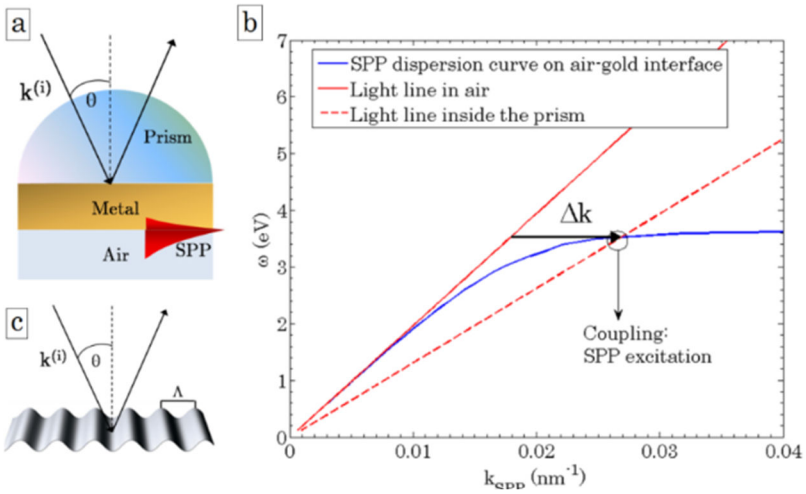

Figure 1.11: (a) The coupling of incident light to surface plasmons via the Kretschmann prism configuration. (b) The SPP dispersion line (blue) compared to the light lines in air (solid red) and using a prism (dotted red). (c) The coupling of light to surface plasmons via a grating with a period of Λ. Reproduced from ref. 114.

Once light couples to SPPs, several interesting properties arise. Perpendicular to the surface, the field decays exponentially and is near-field in character due to the bound nature of the free electrons in the metal. Instead, SPPs will propagate along the surface until absorbed by the metal. This propagation length, δ_{SP}, can be on the order of hundreds of microns and is governed by the equation:[120]

$$\delta_{SP} = \frac{1}{2k''_{SP}} = \frac{c}{\omega}\left(\frac{\varepsilon'_m+\varepsilon_d}{\varepsilon'_m\varepsilon_d}\right)^{\frac{3}{2}}\frac{(\varepsilon'_m)^2}{\varepsilon''_m} \quad (8)$$

where the imaginary component of the wavenumber, k''_{SP}, is a function of the real and imaginary parts of the dielectric function of the metal ($\varepsilon_m = \varepsilon'_m + i\varepsilon''_m$). While analytical solutions to simple geometries such as spheres or films do exist, the light-matter interactions of more complex devices or assemblies can best be ascertained by numerical simulation techniques.

1.1.6 *Finite-difference time-domain modeling*

Surface plasmons are well described by macroscopic electromagnetic theories, such as Maxwell's equations, if the electron mean free path in the metal is shorter than the plasmon wavelength.[121] This condition is usually met at optical frequencies, meaning plasmonic resonances of metals can be readily identified and modeled by several simulation techniques. Of these different methods, finite-difference time-domain (FDTD) modeling has proven to be one of the more robust and accurate methods for the modeling of SPs.[122] FDTD can be used to design, optimize, and characterize a wide array of interactions relevant to numerous light-matter applications. Simulations can provide insights into LSPR peak locations, electric field distributions as seen in **Figure 1.10**, separation of absorption and scattering spectra, and surface charge maps for the assignment of dipolar or higher order modes. For instance, Kodiyath et al. determined the surface charge modes of a rounded nanocube in this fashion (**Figure 1.12a**).[123]

As known, FDTD modeling works off of the principle of solving Maxwell's differential equations stepwise through time.[122] Specifically for the TM case, Maxwell's equations reduce to:

$$\frac{\partial D_z}{\partial t} = \frac{\partial H_y}{\partial x} - \frac{\partial H_x}{\partial y} \quad \textbf{(9)}$$

$$D_z(\omega) = \varepsilon_0 \varepsilon_r(\omega) E_z(\omega) \quad \textbf{(10)}$$

$$\frac{\partial H_x}{\partial t} = -\frac{1}{\mu_0}\frac{\partial E_z}{\partial y} \quad \textbf{(11)}$$

$$\frac{\partial H_y}{\partial t} = \frac{1}{\mu_0}\frac{\partial E_z}{\partial x} \quad \textbf{(12)}$$

where H, E, and D refer to the magnetic, electric, and displacement fields and $\varepsilon_r(\omega)$ is the complex dielectric constant.[124] Any time-dependent change in a local electric field is dependent upon the derivative of the magnetic field with respect to space (the magnetic curl). Conversely, the time derivative of the magnetic field is dependent upon the curl of the electric fields. By repeatedly alternating these two calculations for a meshed area, one can calculate the stepwise progression of electromagnetic waves. Because calculating the curl in multiple dimensions becomes difficult when simultaneously solving for the H- and E-fields, Yee proposed a cell with staggered H- and E-field vector components; this "Yee" cell eliminates the need for solving simultaneous equations but does require an upper bound on the number of time-steps (**Figure 1.12b**).[125, 126]

Materials in FDTD simulations are modeled by assigning complex permittivy values to the cells specified. Tradiontal models such as Drude, Debye, or Lorentz materials can be used to simulate dispersive materials that display differences in permittivity over a wavelength range.[124, 127] More recently, multi-coefficient models (MCMs) have been proposed as an

alternative to the traditional ideal models.[124] MCMs rely on a set of basic functions to describe any dispersive material; this characteristic allows better fits for materials that do not fall under a traditional model category as well as the ability to adapt to "real" materials that contain defects or impurities as well as nonlinear and gain materials.

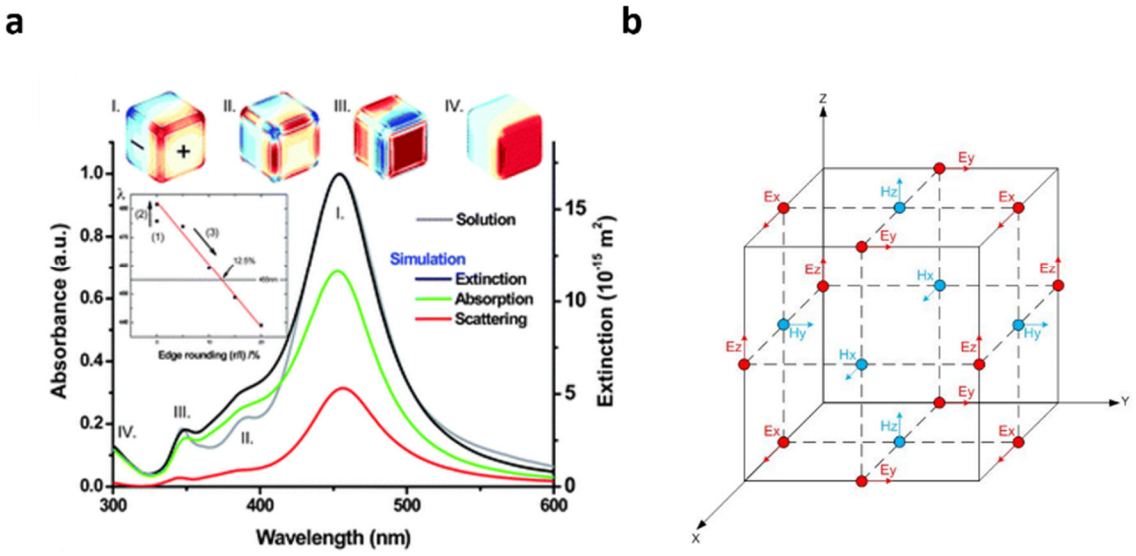

Figure 1.12: (a) The surface charge modes and extinction spectra of a rounded Ag nanocube. Reproduced from ref. 123. (b) A standard Yee cell, with electric field vectors on the cell edges and magnetic field vectors on the cell faces. Materials are mapped into Yee cell spaces by assigning permittivity values to each electric field vector and permeability values to each magnetic field vector. Reproduced from ref. 126.

FDTD has the advantages of being a versatile modeling technique for several types of materials including gain[128], nonlinear[128, 129], and dispersive[130] materials as well as being able to use broadband pulses for individual simulations. However, very large computational domains are needed for small mesh sizes (less than a few nanometers). The necessary finite domain of the modeled area also necessitates artificial boundaries at the

edges that absorb incoming light. These perfectly matched layers (PMLs) do not reflect light for normal incidence but may cause errors for larger angles of incidence.[131]

1.1.7 *Plasmonic nanostructure applications*

Biosensors

As mentioned previously, plasmonic nanoparticles possess unique optical properties that are extremely responsive to their local environment. Plasmonic nanostructures exhibit changes in their peak wavelength with a change in the refractive index or with coupling to nearby nanostructures. These properties can be exploited with rationally designed systems for the optical detection of analytes and biomolecules at very low concentrations.

Surface plasmon resonance (SPR) biosensing, having been first established in the 1990s, has already proven to be a versatile and useful technique for biosensing approaches.[132] Typically, an SPP is formed between a gold film and the sensing medium at a specific incident angle by employing a prism in the Kretschmann configuration.[133] A change in refractive index of the sensing medium leads to a change in the incident light angle in order to excite the plasmon with the same wavelength. By adsorbing biomolecules directly on the gold surface, or more commonly, by functionalizing the gold surface with biomolecule recognition units, one can detect the capture of biomolecules solely by the refractive index change the adsorption causes (**Figure 1.13a**). Using this principle, an SPR sensor may achieve refractive index sensitivities (RIUs) as high as $2*10^{-6}$.[134]

While SPR biosensing has been successfully commercialized and is a relatively mature field, LSPR biosensing remains less investigated and has few commercial products.

Although SPR has roughly a $2*10^6$ nm/RIU sensitivity while LSPR sensing has one of $2*10^2$ nm/RIU, the two techniques result in roughly the same detection limit after their sensing volumes are taken into account.[135] The SPP evanescent field used in SPR can have a sensing volume that extends hundreds of nanometers from the surface while an LSPR's field extends only tens of nanometers. Recently, pathogenic bacterial DNA was also detected at a very low concentration of 2.45 fM by using RNA-functionalized AuNPs.[136] Upon exposure to the target DNA and exposure to NaCl, the RNA was cleaved and allowed the AuNPs to aggregate together (**Figure 1.13b**).

Plasmonic nanoparticles are also highly sensitive to the local refractive index, which can be exploited for biosensing applications. One of the main advantages to this method as opposed to using coupling interactions is that biomolecules can be detected label free. For instance, the binding of label free streptavidin to biotin-functionalized silver nanotriangles resulted in a 27 nm LSPR peak shift, leading to a limit of detection in the low-picomolar regime.[137]

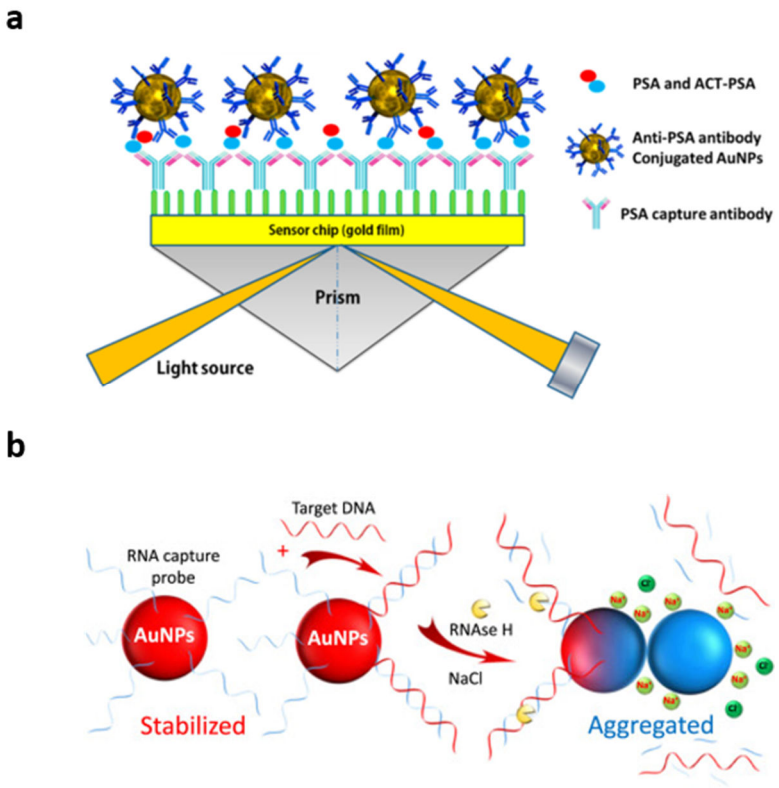

Figure 1.13: (a) A conventional Kretschmann SPR configuration with a functionalized gold film for detecting analytes. Reproduced from ref. 133. (b) The aggregation of DNA-functionalized gold nanoparticles for target DNA detection. Reproduced from ref. 136.

Surface-enhanced Raman scattering detection

Surface-enhanced Raman scattering (SERS) makes use of the localized enhanced electromagnetic fields around plasmonic nanoparticles and surfaces to improve the Raman scattering signature of molecules excited under laser illumination. The near field intensity, $|E|^2$, of the light determines the strength of a molecule's induced dipole. However, the near field intensity can also enhance the emission of a molecule's dipole, meaning that for small

Stokes shifts, the enhancement factor approximately scales with $|E|^4$.[138] The strong, localized electromagnetic fields around plasmonic nanoparticles are therefore ideal for improving the Raman signature of molecules. This concept was first observed in 1974 on a roughened silver film but since then, SERS has been achieved primarily using closely-packed plasmonic nanoparticles with interparticle hot spots that display large enhancement factors.[139, 140] For example, Kodiyath et al. deposited a high density of silver nanocubes (AgNCs) into porous alumina membranes (PAMs) using polyelectrolyte-mediated infiltration as a means to achieve highly efficient and reusable SERS substrates (**Figure 1.14a**,**b**).[123] The high 3-dimensional hotspot cross-sections for the aggregated AgNCs also enabled a detection limit of 3 ppb for explosive binder n-methyl-4-nitroaniline (MNA).

Another recent development in SERS platforms has been the incorporation of a slippery liquid-infused porous surface coined as SLIPSERS.[141] This technique entails placing a liquid droplet concentrated with analyte and gold nanoparticles on the SLIP surface, which then forms a concentrated analyte/nanoparticle aggregate as the droplet evaporates. This is in contrast to other surfaces, which pin the receding water lines and lead to the coffee ring effect. Using this technique, S. Yang et al. were able to achieve Rhodamine 6G detection down to ~75 fM, and when combined with a SERS mapping technique, down to ~75 aM.

Absorbers

While less mature than the applications in sensor and SERS fields, plasmonic nanostructures are being progressively more used for the increased absorption of light in applications such as solar cells,[142] hot-electron generation,[143] thermal emitters,[144] and thermophotovoltaic cells.[145] Such absorbers are able to concentrate electromagnetic energy

to specific regions or films and more easily generate hot electrons that can be harvested. For instance, Zhou et al. recently reported on a broadband (200 nm to 10 μm) plasmonic absorber composed of gold nanoporous templates and gold nanospheres for steam generation (**Figure 1.14c**,**d**).[146] The device was able to absorb approximately 99% of incident light, resulting in approximately a 90% conversion efficiency when covered with water and exposed to solar irradiation. The design also enabled the easy flow and collection of steam for subsequent use.

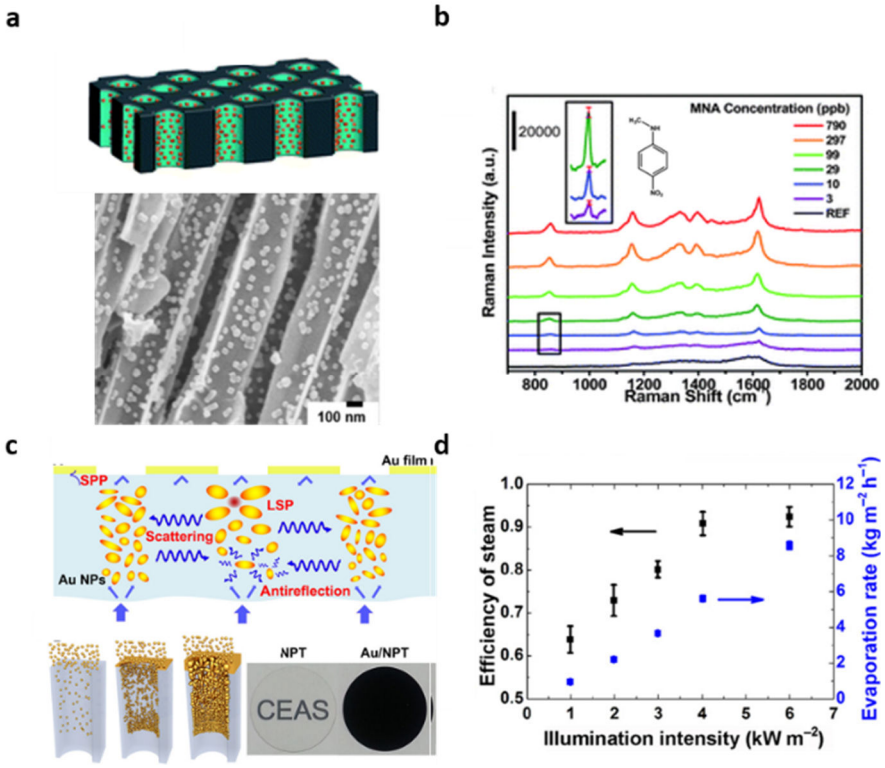

Figure 1.14: (a) An AgNC-infiltrated PAM for SERS detection. (b) The SERS signal of MNA for the AgNC-infiltrated PAMs at various concentrations. Reproduced from ref. 123. (c) An absorber material composed of Au nanoparticles deposited into nanoporous templates. (d) The steam efficiency and evaporation rate of the absorber material. Reproduced from ref. 146.

1.2 Quantum dots

1.2.1 *Introduction to quantum dots*

In contrast to plasmonic nanoparticles, quantum dots (QDs) are fluorescent particles 2-10 nanometers in diameter that are typically composed of an inorganic semiconductor core and potentially a second semiconductor shell as well as passivating ligands.[147-151] Their photoluminescent properties derive from the quantum confinement of their energy levels as the size shrinks below the exciton Bohr radius, resulting in discrete energy bandgaps of their electron-hole pairs when compared to bulk semiconductor materials that exhibit a continuous density of states.[152] Similar to plasmonic nanostructures however, the energy of the QD's bandgap is directly related to its size, meaning that the bandgap energy level can be adjusted by altering the size of a QD even while retaining the same material composition. Their strong absorption, tunable and narrow emission, and their stability have made them attractive components for many optical applications such as biological labels,[153] LEDs,[154, 155] and solar cells,[156] and they remain an active area of research.

1.2.2 *QD synthesis*

In contrast to the many synthesis routes available for plasmonic nanostructures, QDs are prepared almost exclusively in a colloidal one-pot manner. Typically, organometallic liquid precursors are combined with trioctylphosphine (TOP) and tricotylphosphine oxide (TOPO) in high temperature (290-350 °C) solutions.[157] Along with promoting uniform growth in solution, the TOP/TOPO liganize the QD surface and prevent aggregation after synthesis.[158] Under these conditions, nucleation occurs rapidly followed by epitaxial growth until the reaction is quenched once the desired size is reached.[159] Because the

uniformity and average QD size can be affected by a variety of parameters including temperature differences of less than 1 °C, size exclusion processes such as precipitation in butanol can be performed afterwards to promote monodispersity.[160] Although the QD size directly affects its emission wavelength, the tunability is limited to dimensions below the core material's excition Bohr radius. To cover the visible-NIR spectrum, a wide variety of QD core materials such as CdS, CdTe, ZnO, and InP among others have been successfully employed (**Figure 1.15**).[161-166]

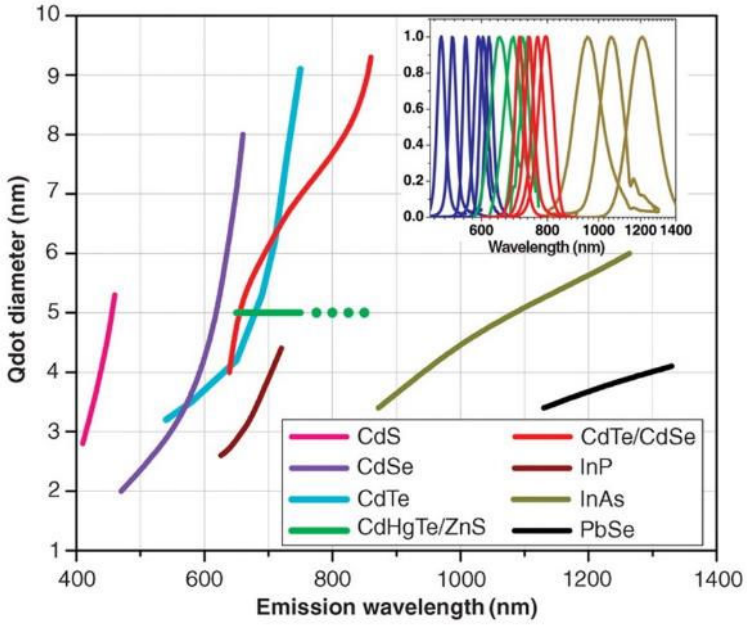

Figure 1.15: QD emission wavelength as a function of QD diameter and core material. The inset depicts representative emission spectra for some QD types. Reproduced from ref. 161.

QDs were first created as simple core nanostructures composed entirely of a single semiconductor material.[167] However, such nanostructures have lower quantum yields and are inherently unstable due to surface oxidative defects gradually accumulating in what are

known as “traps.” More commonly now, a second semiconductor material possessing a larger bandgap is grown as a passivating shell around the initial core, resulting in improved stability and the reduction of trap sites.[157, 159, 168] The most common and commercially available QD of this type have a CdSe core and a ZnS shell, as ZnS has a larger bandgap and a very similar lattice parameter to that of CdSe, resulting in lower interfacial strains.[157] Other improvements to QD synthesis involve the creation of multishells, “giant” shells, or graded shells for suppressed Auger recombination and suppressed re-absorption.[169-173]

QD shells are typically passivated with organic TOP/TOPO ligands natively from synthesis. These ligands are not soluble in aqueous solutions, and other ligands may be preferential depending on the application. For instance, Malak et al. demonstrated how the ligand length can impact the QD packing behavior in films and consequently alter their optical gain from between 61 and 518 cm^{-1} despite the otherwise identical QD morphology.[174] Ligand exchange procedures are therefore normally done to exchange the native TOP/TOPO for hydrophilic or alternate organic ligands. Commonly, bifunctional ligands with anchoring moieties such as thiols or amines can be directly exchanged with the more weakly bound TOP/TOPO.[150, 175, 176] Other strategies involve the formation of silica shells around the QDs for further functionalization or the interdigitation of new ligands between the TOP/TOPO.[177-179]

Lastly, one of the main drawbacks to QDs is their toxicity due to their heavy metal components such as Cd, Pb, or Hg. These materials restrict usage for in-vivo applications and consumer electronics, severely limiting their use in applications to date. In the past several years, increasing focus has been put on heavy metal-free QDs that circumvent this issue. For instance, non-toxic ZnCuInS core QDs have been fabricated in several studies

for LED applications with high quantum yields of ~50%.[180, 181] Additionally, Cd-free CuInS2/ZnS QDs have been demonstrated to have a 10-fold lower toxicity than a CdTeSe/CdZnS analogue *in vivo*.[182]

1.2.3 *QD optical properties*

A QD's emission is also, as mentioned, dictated by its size. Below the Bohr exciton radius, semiconductors exhibit discrete energy bands instead of a continuous wavefunction. Higher confinement (smaller QDs) leads to an increase in the band gap and consequently a blueshifted emission (**Figure 1.16a**).[147, 151, 183, 184] The exciton radius is dependent on the QD material but is generally limited to 2-10 nm, leading to the wide range of QD materials needed to cover the visible spectrum as seen in **Figure 1.15**.[185, 186] Along with the narrow emission band, the semiconductor quantum confinement results in a broad absorption band that gradually increases towards the UV and consequently large effective Stokes shifts greater than 100 nm (**Figure 1.16b**).[152]

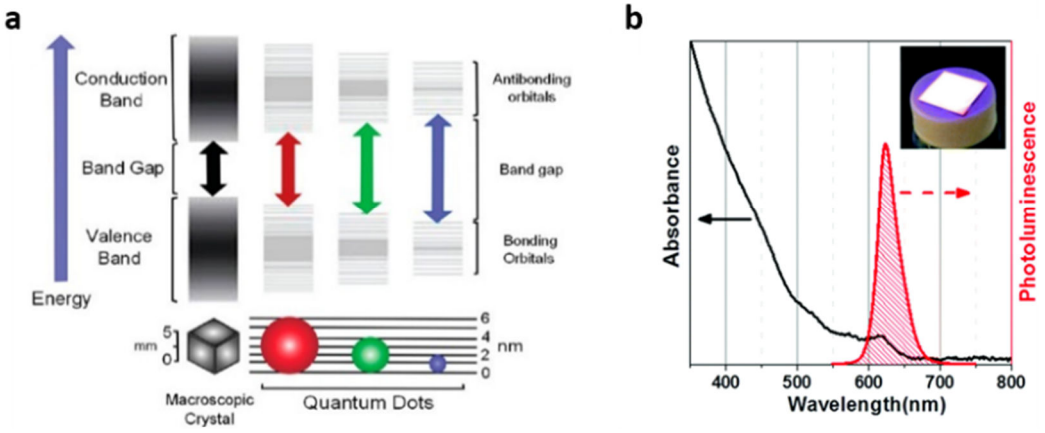

Figure 1.16: (a) The bandgap structure of QDs as a function of size. Reproduced from ref. 184. (b) Typical absorption and PL spectra for a QD film. Reproduced from ref. 174.

As mentioned previously, the optical properties of QDs are also highly on their constituent materials as well as their size. Apart from partially determining emission and absorption characteristics, the QD materials can be used to classify them into three different types depending on where the exciton is confined: type-I, type-II, and quasi type-II.[187] Type-I QDs possess electron and hole energy levels that results in the exciton being confined to the QD core. These type of QDs, such as the prevalent CdSe/ZnS core/shell QDs) are often used in optical emission applications, as the shell can serve to both confine the exciton and to prevent environmental degradation of the core.

Type-II QDs confine the excited electrons and holes in different regions of the QD; for instance, excited electrons may be confined to the shell while excited holes are present in the core. Type-II QDs allow access to emission wavelengths not achievable with a single material by tuning of both the QD core diameter and the shell thickness, and the inherent separation of charges makes these QDs more desirable for photovoltaics or photoconductive applications.[188] Lastly, quasi type-II QDs have either a hole or electron wavefunction delocalized over the entire QD. Quasi type-II QDs are ideal for delivering multiple electrons to catalysts or redox mediators due to their long multiexciton lifetimes and their slow recombination rates.[189]

Apart from radiative emission, QD excitons can decay through a number of intrinsic non-radiative pathways such as Auger recombination and trap states. Auger recombination occurs when an exciton transfers its energy to a third carrier (electron or hole), thereby quenching the radiative recombination.[190] Auger recombination has been shown to be more prevalent in smaller QDS due to an increase in electron-electron coupling over electron-phonon coupling and is also largely influenced by the QD core/shell interface potential.[191]

Typical routes used to reduce Auger recombination include the alloying of the core/shell interface to reduce the interface potential, the use of larger QDs, and the utilization of type-II or quasi type-II QDs that have a reduced overlap between the electron-hole wavefunctions.[170, 192, 193] Trap states can refer to vacancies, lattice mismatches, dangling bonds, or adsorbates on the QD surface.[151] These sites can trap excited holes or electrons in local energy minima states, thereby preventing their radiative recombination. While QD shells and ligands can help suppress trap formation and passivate the surface, lattice mismatch between the QD core and shell can cause stresses that result in defect sites after photorelaxation.[194, 195]

Additionally, QD emission can also be heavily impacted, both negatively and positively, by the surrounding environment. In a well-known example, fluorescence resonance energy transfer (FRET) can occur between QDs and other fluorophores or dipoles.[196, 197] FRET may lead to quenching if an excited QD serves as a donor to an acceptor fluorophore and transfers its energy through non-radiative dipole-dipole coupling. However, FRET enhancement of QD emission can also occur if a fluorophore's emission is quenched by a QD's absorption. Since FRET is inversely proportional to the sixth power of the distance between the donor and acceptor, FRET interactions are typically limited to distances below 10 nm.[152, 198]

In the past decade, metal nanoparticles have also been shown to have a profound influence on QD emission. Small nanoparticles that primarily absorb light and exhibit strong localized electromagnetic fields can undergo FRET interactions with nearby QDs due to their own dipole interactions.[198, 199] In this case, the LSPR peak of the metal nanoparticle must overlap with the QD absorption for FRET enhancement to occur (**Figure 1.17a**).

Nanoparticles may also affect QD fluorescence over larger distances of 10-50 nm if the plasmon peak overlaps the QD emission peak in what is known as the Purcell effect (**Figure 1.17b**).[200] The Purcell effect occurs due to a resonant cavity interaction that modifies the local density of states (LDOS) of the fluorophore and can lead to either quenching if the nanoparticle is absorbing in nature or enhancement if the nanoparticle primarily scatters. Both FRET and Purcell interactions are highly dependent on optimizing interparticle distances and LSPR peak locations, as metal surfaces are generally known to quench fluorescence through electron-electron coupling.[201, 202]

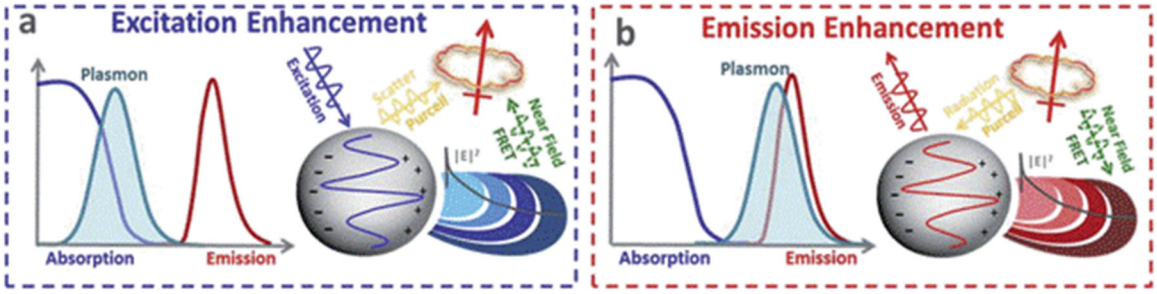

Figure 1.17: (a) The FRET enhancement of fluorophores with an overlap of the LSPR and the fluorophore absorption peak. (b) The Purcell enhancement of fluorophores with an overlap of the LSPR and the fluorophore emission peak. Reproduced from ref. 198.

Lastly, QDs are prone to aggregation and uneven deposition depending on the relative strengths of the QD-QD and QD-substrate interactions.[203] One way of circumventing this issue and promoting the formation of planar QD films is through the use of compatible polymer matrices.[204-207] Additionally, such composite films promote further QD stability, tunable QD loading, and integration into many commercial deposition processes. Such film- or fiber-QD composites can also act as emissive waveguides while being pumped

from any direction due to high internal waveguiding of the generated light by the large effective refractive indices of such composites.[208, 209]

1.2.4 *QD applications*

Biolabels and sensors

As mentioned previously, QDs' stability, easy functionalization, and small FWHM make them excellent candidates as photoluminescent tags. Many biosensing applications outside of *in vitro* and *in vivo* imaging involve FRET between QDs and attached biomolecules that impact their photoluminescence. In one early example of photoluminescence enhancement detection, Medintz et al. used QDs functionalized with a β-cyclodextrin dark quencher (**Figure 1.18a**).[196] By adding maltose, the β-cyclodextrin was displaced, enabling the QDs to fluoresce and provide an easy detection scheme for the maltose biomolecule. FRET has also been accomplished using gold nanoparticles and graphene oxide as acceptors for detection of various biomolecules.[210, 211] Lastly, organic fluorophores have been used as acceptors for QD donors to achieve FRET-based fluorescence. Algar and Krull demonstrated multiplexed detection of fluorophore labeled oligonucleotides using complementary QD-conjugated oligonucleotides in this manner.[212]

LEDs

The tunability, narrow emission peak, and stability of QDs are of great interest for lighting applications. Currently, QDs have already demonstrated commercial viability in television displays as back-light units to improve color contrast and increase power efficiency.[213] Additionally, QDs are compatible with many of the same low-cost processes used for

OLEDs today.[214] While the emission of QD-LEDs can be accomplished using photoexcitation as described previously, QD layers are more commonly sandwiched between electron-transporting and hole-transporting layers.[215-217] With an applied electric current, excitons are created in the QD layer and recombine for subsequent light emission (**Figure 1.18b**).

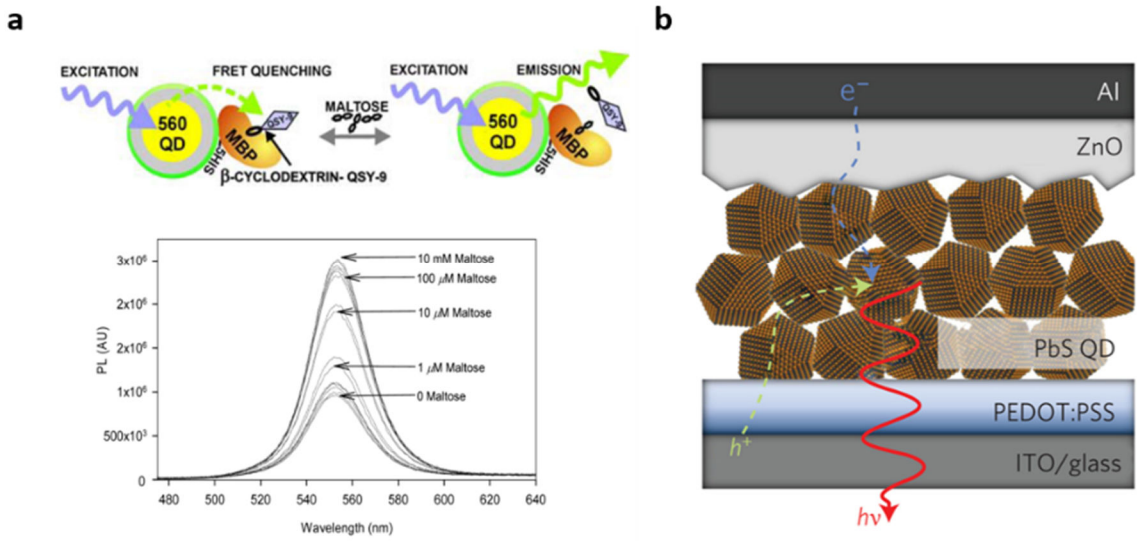

Figure 1.18: (a) A FRET-based QD biosensor for the detection of maltose. Reproduced from ref. 196. (b) A QD-LED with electron- and hole-transporting layers. Reproduced from ref. 217.

1.3 Summary of critical issues and motivation

As discussed above, much research has gone into synthesizing plasmonic noble metal nanoparticles and semiconducting QDs as well as deducing and analyzing their optical phenomena. However, many studies focus on single particles in solution instead of the mesoscale, substrate-bound arrays that are more suitable for certain applications. Understanding and guiding the assembly behavior of nanostructures in a large-scale,

bottom-up, and controllable manner has important ramifications for controlling resultant unique properties for emerging optical applications.

For instance, work remains to be done on the assembly behavior of plasmonic nanostructures, especially when two or more nanostructures with different sizes or shapes are involved. Uncontrolled interactions between nanostructures can lead to random aggregation or destructive interference between plasmon modes while regulated plasmonic interactions can result in collective property enhancement. In particular, the large-scale assembly of anisotropic nanoparticles has not been fully developed or optimized. Furthermore, the effects of nanoparticle coupling on emergent optical properties often remain fundamental in nature and are not practically explored for application development.

In addition, the use of polymeric components such as spacer layers or shells can enhance the optical properties of or introduce new functionalities to nanoparticle assemblies. However, plasmonic phenomena for hybrid organic-inorganic assemblies with polymer matrices and components are less understood when compared with the simple cases of isolated nanoparticles on substrates or in media. Additionally, selecting "complementary" functional polymer materials that can not only passively support nanostructures but can also be actively involved in enhancing and mediating the nanostructure properties remains a challenging task. The influence of polymeric shells, the coupling of nanoparticles across polymeric media, and the effects of anisotropic environments for resultant light-matter interactions such as extinction and emission also all need to be theoretically understood for the construction of real devices and components.

Finally, the assembly of QDs on substrates and with mediating polymeric components for controlled fluorescence enhancement is an understudied area and has important ramifications for emissive applications. Controlling the placement of QDs with respect to plasmonic nanoparticles, photonic crystals, or light scattering centers can result in fluorescence enhancement but is often limited to single particle studies or involves time-intensive and costly experimental steps. In contrast, exploiting the interfacial dynamic relationship between QD-polymer composites and substrates could be explored for introducing enhancement in a controllable and facile manner as well as for tuning the emissive properties for certain applications.

CHAPTER 2. RESEARCH GOALS, OBJECTIVES, AND OVERVIEW

2.1 Research goals

The primary goal of this research is understanding the principles that govern **noble metal and QD nanostructure substrate-bound assemblies with novel emergent optical properties such as broadband absorption, reversible LSPR peak modulation, and fluorescence enhancement**. Importantly, bottom-up assembly methods are used to govern assembly parameters such as nanoparticle density to control the coupling behavior between nanoparticles as well as their interactions with other plasmonic components. Polymeric components such as shells and spacer layers are additionally used for the mediation of these coupling interactions, for the control of large scale assembly behavior, and as stimuli-responsive complements to plasmonic nanostructures. Furthermore, FDTD simulation techniques are used to predict, confirm, and understand optical phenomena. In this manner, the understand of coupling between nanostructures and other nearby nanostructures and the effects of polymeric matrices on light-matter interactions is furthered as well.

Much effort remains on elucidating how nanoparticle assembly properties, such as interparticle distances and cluster sizes, can result in improved optical properties beyond their single nanoparticle behavior. Broadband absorption, reversible LSPR peak modulation, and fluorescence enhancement are all targeted in this case as properties that can be controlled and tuned using coupling interactions, polymeric components, and large scale assemblies. The ultimate goal of this work, summarized in **Figure 2.1**, is therefore

split into these three concrete tasks that share the same design principles and are discussed below.

Task 1: Understanding the fundamentals behind the suppression of reflection through the use of complementary plasmonic modes and the subsequent rational configuration of nanostructures for broadband light absorption. Different nanostructure assembly designs, constituent nanostructures, and absorber configurations are considered for this task. Rational nanostructure coupling strategies that suppress reflection and allow control over LSPR peak positions are central to this task and are emphasized with the aid of FDTD simulations.

Task 2: Gaining insight into the assembly behavior of conjugated polymers and plasmonic nanoparticles and ascertaining how polymeric media can influence plasmonic extinction spectra of nanoparticles in a changing refractive environment. This knowledge is then used in the creation of hybrid light- and electrically-active noble metal/plasmonic nanomaterials with reversible resonance modulation. Specific designs such as nanostructure/polymer composites and core/shell nanoparticles are assessed for different polymeric and plasmonic constituent materials. An emphasis is also placed on how the coupling behavior of plasmonic nanostructures affects the resultant optical properties of the hybrid nanostructures.

Task 3: Studying the emissive behavior of composite QD/polymer films and how the film morphology can consequently be altered to improve the farfield outcoupling of fluorescence and reduce internal waveguiding to enhance their emissive properties. In particular, the influence of poor solvents on film/substrate interactions and consequent

dewetting behavior is investigated to increase scattering interactions of the films with light. Additionally, this knowledge is used in conjunction with photopattern light exposure for further investigation into the modification of film/substrate interactions and the development of novel photoluminescence patterning methods.

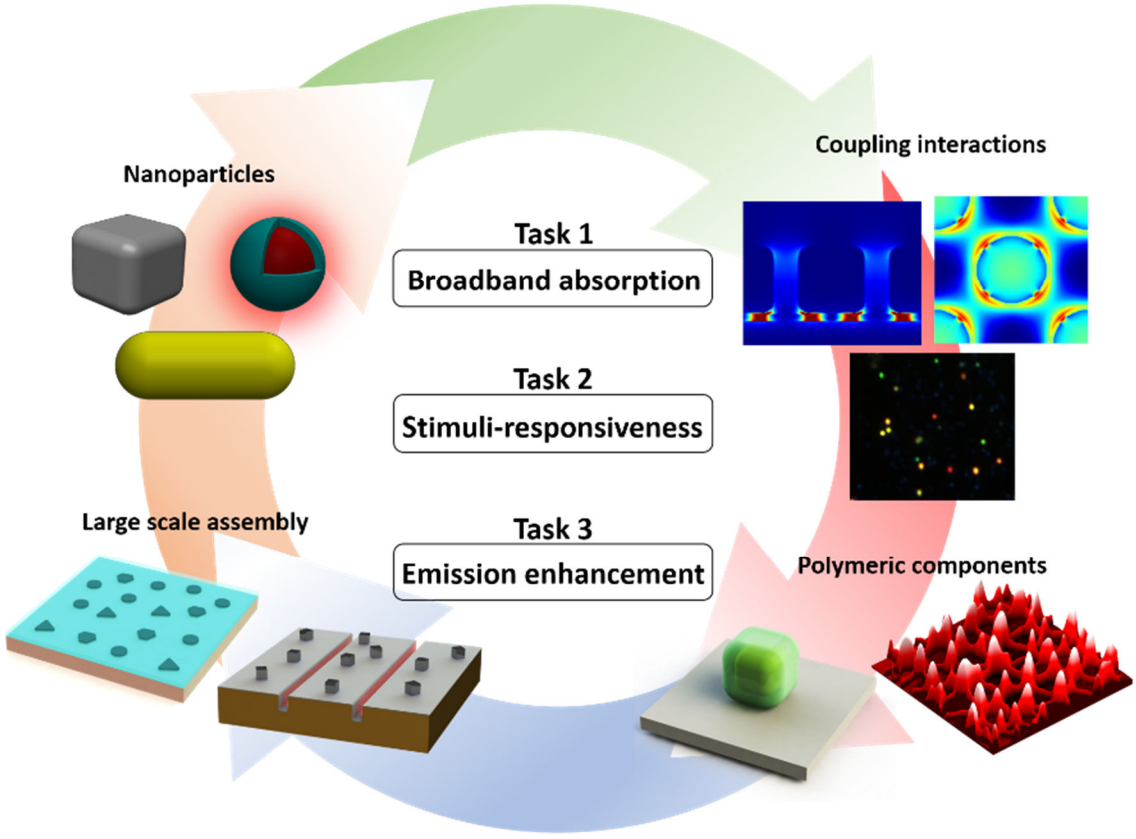

Figure 2.1: The design and fabrication of large scale, nanostructured assemblies with novel optical properties using rationally chosen nanoparticles, coupling interactions, and polymeric components for the three distinct tasks of broadband absorption, stimuli-responsiveness, and emission enhancement.

2.2 Technical objectives

As discussed above and presented in **Figure 2.1**, the overarching focus of this work is on achieving a better understanding of emergent light-matter properties arising from local and large scale nanostructure assemblies and their combination with polymeric components to achieve optical properties that cannot be realized by single nanostructures alone. The use nanostructure coupling behavior and nanostructure-polymer interactions to control light-matter interactions in a way that enhances their absorption, stimuli-responsiveness, or emission as described above will be broken down into specific objectives here.

Objective 1: Broadband light absorption behavior

- Characterize the plasmonic modes of individual nanostructures in order to understand the effects of size, shape, edge rounding, and organic surfactants on their resonances;
- Fabricate novel plasmonic nanostructure assemblies that can result in broadband light absorption, such as the rational combination of film-coupled nanocubes and nanogrooves or the gradiental assembly of nanocubes, while avoiding destructive interference between their coupled modes;
- Experimentally control coupling between nanostructures using EBL, polymer spacer layers, and LB assembly;
- Determine the influence that nanoparticle coupling and density have on the nanocube LSPR position, the reduction in reflection, and the overall light absorption when combined with nanogrooves;

- Corroborate experimental findings with FDTD electromagnetic simulations that model realistic nanoparticle shapes, interparticle distances, and environmental conditions (substrates and surfactant layers) to clarify the mechanisms behind broadband absorption in the nanostructure assemblies.

Objective 2: Stimuli-responsive LSPR modulation

- Determine suitable nanoparticles, such as nanocubes, nanorods, and nanodisks, for use with both commercial and newly developed conjugated polymers for the creation of light- and electrically-responsive nanostructure assemblies;
- Investigate different nanostructure/polymer morphologies such as composite films and core/shell particles to achieve large and reversible LSPR modulation;
- Experimentally characterize optical and electrical properties of novel conjugated polymers to ascertain their effects on final LSPR shifts and stability;
- Employ electromagnetic simulations to determine the influence of nanoparticle geometry and coupling interactions on their plasmon mode field distributions, sensitivity, and electric field decay.

Objective 3: QD fluorescence enhancement

- Determine complementary QD and polymer materials and suitable assembly methods for composite film fabrication that do not result in large-scale phase separation or emission decay;
- Determine routes for the intentional dewetting of films to promote emissive far-field outcoupling via increased light scattering without detrimentally affecting the intrinsic QD quantum yield or stability;

- Examine effects of composite film properties such as thickness, morphology, and QD loading on final outcoupling behavior;
- Ascertain and verify controllable dewetting mechanisms of polymer/QD composite films that lead to improved emissive properties;
- Establish facile methods for the patterning of such films that do not detrimentally affect intrinsic QD properties or require additional lithographic steps.

2.3 Organization and composition of dissertation

Chapter 1 provides a detailed review of literature involving plasmonic nanostructures and QDs. Synthesis routes and assembly methods are discussed for both types of nanostructures as well as the fundamental principles such as size, composition, and coupling interactions that govern their optical phenomena. Current applications for these nanostructures are also detailed. Lastly, a summary of critical issues facing the field and the motivation for this research are presented.

Chapter 2 outlines the research goals and technical objectives of this dissertation. The organization and a brief description of this dissertation's body of work are also presented.

Chapter 3 outlines the materials, synthesis techniques, assembly methods, and characterization methods used during this research. In some cases, described methods were conducted by collaborators, the details of which can be found in the pertinent chapters. Detailed descriptions for specific techniques can also be found in the relevant sections.

Chapter 4 focuses on the fabrication of a metal-dielectric-metal assembly for enhanced broadband absorption in the visible spectral range by combining the plasmonic resonances

of different plasmonic nanostructures. Silver nanocubes (AgNCs) and gold nanogrooves are coupled to one another through a dielectric polymer spacer layer of controllable thickness, resulting in a large multiplicative enhancement of the absorption across a broad spectral range. The individual plasmon resonances of these nanostructures are located at significantly different optical frequencies, and the constructive combination of their resonances allow a significant increase of light absorbance to an average value of 84% across the 450-850 nm wavelength range.

Chapter 5 examines the fabrication of an AgNC aggregation gradient monolayer for broadband light absorption. The varying amount of randomly distributed nanocube aggregates with difference surface coverages allows for continuous control of the polarization-sensitive absorption of the incoming light over a broad spectrum. Optical characterization under total internal reflection (TIR) conditions combined with electromagnetic simulations reveal that the broadband light absorption depends on the relative orientation of the nanoparticles to the polarization of the incoming light. The s-polarization shows dramatic changes of the plasmonic resonances at different angles of incidence. With a low surface nanocube coverage, we observed a polarization-selective high absorption of 80% (with an average 75%) of the incoming light over a broad optical range in the visible region from 400-700 nm.

Chapter 6 reports on the optical properties of silver nanodisk (AgND) monolayers when combined with an electroactive conjugated polymer layer and varying amounts of nanoparticle coupling. AgND monolayers were deposited using the LB technique, and monolayers in the liquid expanded–gaseous (Le–G) phase demonstrated individual plasmon resonance behavior while monolayers deposited in the liquid condensed–liquid

expanded (Lc–Le) and solid–liquid condensed (S–Lc) phases exhibited plasmon coupling between closely packed adjacent nanoparticles. AgND monolayers were then used in conjunction with a conjugated poly(3-hexylthiophene-2,5-diyl) (P3HT) medium to reversibly modulate the LSPR by changing the local refractive index around the nanoparticles. Ultimately, a high reversible LSPR shift of 27 nm was observed with an applied electropotential of ±500 mV to the P3HT-coated AgND monolayer. A high RIS of 141 nm per RIU was found for monolayers deposited in the Lc–Le phase due to an increase in hot spot formation.

Chapter 7 presents the synthesis of novel branched organic–inorganic azo-polyhedral oligomeric silsesquioxane (POSS) conjugates (Azo-POSS) and their use as a stable active medium to induce reversible plasmonic modulation of embedded nanostructures using light. A dense monolayer of AgNCs was deposited on a quartz substrate using the Langmuir–Blodgett technique and subsequently coated with an ultrathin Azo-POSS layer. The reversible light-induced photoisomerization between the trans and cis states of the azobenzene-terminated branched POSS material results in significant changes in the refractive index, up to 0.17, at a wavelength of 380 nm. We observed that the pronounced and reversible change in the surrounding refractive index results in a corresponding hypsochromic plasmonic shift of 6 nm in the plasmonic band of the embedded AgNCs. The reversible tuning of the plasmonic modes of noble-metal nanostructures using a variable-refractive-index medium raises the possibility of fabricating photoactive, hybrid, ultrathin coatings with robust, real-time, photoinitiated responses for prospective applications in photoactive materials that can be reversibly tuned by light illumination.

Chapter 8 reports on the electrically controlled and reversible changes of the plasmonic signatures of hybrid polymer–metal nanostructures composed of core/shell nanostructures: gold nanocubes (AuNCs) coated with electrochromic polyaniline (PANI) shells. A reversible tuning of the LSPR peak of the AuNC core was obtained by applying an electrical potential that caused a reversible oxidation state change in the electroactive PANI nanoshell. A significant shift of the main LSPR peak was achieved with high reversibility and electrochemical stability due to the interplay of the local decay of the electromagnetic field and the controlled thickness of the surrounding polymer shell. Here, the PANI shell acts as an electroactive medium as well as a physical spacer to prevent uncontrollable plasmonic coupling.

Chapter 9 presents a rational approach for fabricating another plasmonically active hybrid polymer–metal nanomaterial with electrochemical tunability of the LSPR. The key requirement for being able to significantly modulate the LSPR band position is a close overlap between the refractive index change of a stimuli-responsive polymeric matrix and the intrinsic LSPR bands. For this purpose, gold nanorods (AuNRs) with a controlled aspect ratio, synthesized to provide high refractive index sensitivity while maintaining good oxidative stability, were combined with a solution-processable electroactive and electrochromic polymer (ECP): alkoxy-substituted poly(3,4-propylenedioxythiophene) [PProDOT($CH_2OEtHx)_2$]. Spectral characteristics of the ECP, in particular the refractive index variation, were evaluated as the material was switched between oxidized and reduced states. We fabricated ultrathin plasmonic electrochromic hybrid films consisting of AuNRs and ECP that exhibited a large, stable, and reversible LSPR modulation of up to 25–30 nm with an applied electrical potential. FDTD simulations confirm a good match between the

experimentally measured refractive index change in the ECP and the plasmonic response during electrochemical modulations.

Chapter 10 highlights a new method for enhancing photoluminescence from QD/polymer composite films. Poly(lauryl methacrylate) (PLMA) thin films containing embedded QDs are intentionally dewetted from substrates with exposure to an incompatible solvent vapor. After dewetting, films exhibited increased amounts of scattering that served to outcouple photoluminescence and reduce internal waveguiding within the film. Up to a 5-fold enhancement of the film emission was achieved depending on factors such as film thickness and QD concentration within the film. An increase in film thickness was shown to increase the dewetted maximum feature size and characteristic length until a critical thickness was reached where dewetting became inhibited. A unique light exposure-based photopatterning method is also presented for the creation of emissive patterns.

Chapter 11 summarizes the general results and conclusions that can be drawn from the preceding chapters and discusses their overall significance within their broader scientific field. An analysis of future directions for polymer/nanostructure composites with controllable light interactions and potential applications is also provided.

CHAPTER 3. EXPERIMENTAL TECHNIQUES AND MATERIALS

3.1 Collaborative efforts

Much of the work presented in this thesis was done in collaboration with other research groups at the Georgia Institute of Technology. Professor El-Sayed's research group provided the plasmonic nanoparticles used in this work and frequently performed LB deposition of nanoparticles on substrates. QDs were obtained from Professor Lin's research group. Professor Reynold's group provided several different electrochromic polymers for use. An outside collaborator, Professor Shevchenko from the National Academy of Sciences of Ukraine, provided light-sensitive compounds.

3.2 Chemicals and materials

Aniline (99.5%), ammonium persulfate (98%), polyethylenimine (PEI, M_w ~25000), (3-aminopropyl)-triethoxysilane (APTES, 99%), polyallylamine hydrochloride (PAH, M_w=60 kDA), and polystyrene sulphonate (PSS, M_w=70 kDA) were purchased from Sigma-Aldrich. Toluene (99.5%) and acetone (99.5%) were purchased from BDH. Ethanol was obtained from Calbiochem. Dichloromethane (99.96%) was purchased from EMD Millipore Chemicals. Lithium bis(trifluoromethylsulfonyl)imide (LiBTI) was used as received from Acros Organics. Propylene carbonate (PC) was purchased from Acros Organics and purified using a solvent purification system from Vacuum Atmospheres. Ultrapure water was obtained using a Nanopure system (Barnstead, resistivity ≥18.2 MΩ cm).

3.3 Gold and silver nanostructures

3.3.1 *Synthesis of silver nanocubes*

Silver nanocubes (AgNCs) with edge lengths between 50-70 nm were synthesized using the polyol method as described previously.[218, 219] In a 100 mL round bottom glass flask, 70 mL of ethylene glycol (EG) was heated to 150 °C for 1 hour. Then a solution of 0.85 g PVP was dissolved in 10 mL EG and added to the hot EG. 0.4 mL of sodium sulfide (Na_2S) (3 mM) dissolved in EG and 6 mL of 282 mM $AgNO_3$ dissolved in EG were injected into the reaction mixture. The reaction mixture was stirred at 200 rpm and refluxed at 150 °C for 10 minutes until the solution became opaque. In order to purify the AgNCs for LB deposition, 5 mL of the prepared AgNC solution was diluted with 10 mL of water and centrifuged at 10,000 rpm for 10 minutes. The precipitated AgNCs were then re-dispersed in water. AgNCs were statistically evaluated using TEM images to evaluate size distributions and shapes. The AgNCs were typically covered by a surfactant PVP layer with a thickness of approximately 1.5 nm.

3.3.2 *Synthesis of silver nanodisks*

Silver nanodisks (AgNDs) were prepared by the simultaneous asymmetric multiple reduction technique (SMART).[35] In a 1 L glass bottle, 4 mL of 78.35 mM L-ascorbic acid was added to 400 mL of 0.145 mM aqueous solution of PVP (molecular weight of 55 kDa). Then, 0.60 mL of 60 mM $AgNO_3$ aqueous solution was added to the resulting mixture. While stirring, 0.12 mL of sodium borohydride (5 mM) was added and the solution was gently shaken for 10 seconds. The resulting AgNDs were cleaned by centrifugation at 12,000 rpm for 35 minutes, and the precipitated nanoparticles were dispersed in deionized

water. The cleaned AgND solution was then centrifuged again at 10,000 rpm for 20 minutes; the precipitated AgNDs were finally dispersed in 4 mL ethanol and mixed with 4 mL chloroform for deposition.

3.3.3 *Synthesis of gold nanocubes*

Gold nanocubes (AuNCs) were synthesized using a traditional seed-mediated technique in which small Au seeds were grown to AuNCs in the presence of a structure-directing agent, CTAB.[220] Briefly, the seed solution was first prepared by adding 600 μL of ice-cold $NaBH_4$ with a concentration of 0.01 M to a 7.75 mL aqueous solution containing 0.1 M CTAB and 3.23×10^{-4} M $HAuCl_4 \cdot 3H_2O$ under stirring. The stirring was continued for 2 minutes. One hour after initial seed synthesis, 0.35 mL of 10-fold diluted seed solution was allowed to grow in the growth solution, which was prepared by mixing CTAB solution (2.916 g dissolved in 400 mL of ultrapure water) with $HAuCl_4 \cdot 3H_2O$ solution (0.0394 g dissolved in 143 mL DI water) followed by adding 7 mL (1M) ascorbic acid (Sigma-Aldrich). The growth process was completed after 4 hours.

3.3.4 *Synthesis of gold nanorods*

The seed-mediated growth technique was used to prepare AuNRs.[36] The seeds were prepared as follows: in a 30 mL vial, 2.5 mL of 1.0 mM aqueous solution of $HAuCl_4$ was mixed with 5 mL of 0.2 M aqueous solution of CTAB. Then, under stirring, 0.6 mL of 10 mM ice-cold sodium borohydride solution was added. The gold seed particles were formed after 5 minutes of stirring. The growth solution was prepared by mixing 200 mL of 1.0 mM $HAuCl_4$ aqueous solution with 200 mL of 0.2 M CTAB in a 500 mL flask. Then 6 mL of 4.0 mM $AgNO_3$ solution was added, followed by 2.8 mL of 78.8 mM ascorbic acid. AuNRs

were obtained by adding 320 μL of seed solution to the growth solution and leaving the mixture to react overnight.

3.4 QDs

3.4.1 *Synthesis of CdSe/Cd1-xSe1-ySy core/graded shell quantum dots*

Red core/graded shell CdSe/Cd1-xZnxSe1-ySy QDs were synthesized by modifying a reported method.[221] Briefly, 1 mmol of CdO, 2 mmol of Zn(acetate)2, 5 ml of oleic acid, and 15 ml of 1-octadecene were inserted into a three-neck flask. The mixture was then degassed at 150 °C for 1 h. The reaction was heated to 300 °C under Ar. At the elevated temperature (300 °C), 0.2 ml of 1M Se/TOP solution was rapidly injected. After 5 min, 0.3 ml dodecanethiol was added drop-wise. The solution was kept at 300oC for 20 min followed by injection of 1ml 2M S/TOP solution. The reaction was allowed to proceed at 300°C for 10 min and then the reaction was stopped by removing the heating mantle. 10 ml of hexane was added to the solution once the temperature reached 70 °C.

3.5 Conjugated compounds and polymers

3.5.1 *Azo-POSS*

Compounds **1** and **2** were prepared using a hydrosilylation approach with POSS-H as a scaffold for the attachment of azo dyes bearing reactive allyloxy groups. Compounds **AB** and **2** were reported previously;[222] synthesis of compound **1** is described in Chapter 7 Supporting Information (**Figure D.1**).

3.5.2 *Poly(3-hexylthiophene-2,5-diyl)*

Regioregular poly(3-hexylthiophene-2,5-diyl) (P3HT) with a regioregularity ≥ 90% and a MW of ~87 kDa was purchased from Sigma-Aldrich.

3.5.3 *ECP-Magenta*

ECP-Magenta (ECP-M) electrochromic polymer was synthesized as described previously from the corresponding alkoxy-substituted 3,4-propylenedioxythiophene by oxidative polymerization with iron(III)chloride.[223] The molecular mass of the polymer is 12.4 kDa with a polydispersity index (PDI) of 1.8 as determined by gel-permeation chromatography (GPC) in tetrahydrofuran (THF) versus polystyrene (PS) standard.

3.5.4 *Aniline polymerization on AuNCs*

AuNC/polyaniline (PANI) core/shell nanostructures were synthesized according to established procedure with some modifications.[224, 225] As-synthesized CTAB-wrapped AuNCs (3.5 mL) were centrifuged at a speed of 6,000 rpm for 15 minutes, and the concentrated AuNCs were then redispersed in a mixture of aniline (2 mM, 1.5 mL) and SDS (40 mM, 0.25 mL). The solution was subjected to vortexing for 1 min to ensure complete mixing. Ammonium persulfate (2 mM, 1.5 mL) in 10 mM HCl aqueous solution was added to the mixture of AuNCs, aniline, and sodium dodecyl sulfate (SDS). The solution was vortexed for 10 seconds and subjected to polymerization for 24 hours. In this procedure, polymerization of aniline takes place on the AuNC surface as well as in the bulk solution, which gives rise to a mixture of AuNC/PANI core/shell nanostructures and PANI suspension. Afterwards, the AuNC/PANI core/shell nanostructures can be easily isolated from PANI via centrifugation owing to their density difference. The resultant solution was concentrated through centrifugation at 6,000 rpm for 15 minutes and redispersed in 1.5 mL

of 3.6 mM SDS solution. The same centrifugation process was repeated a couple of times more for further purification. For thicker PANI shells, the same polymerization process was carried out with the AuNC/PANI core/shell dispersion instead of bare AuNCs.

3.6 Film deposition

3.6.1 *Spin casting*

Spin-coating was performed by dropcasting polymer solutions (typically 1-2 wt%) onto silicon or quartz substrates and spinning the samples for 30 seconds at 3,000 rpm on a spin-coater (Laurell). For layer-by-layer (LbL) deposition, 0.2 wt% solutions of PAH and PSS were prepared by dissolving the polymers in Nanopure water. Each layer was spun cast at 3,000 rpm for 30 seconds followed by 2 rinse steps with Nanopure water.

3.6.2 *Spray casting*

Nanoparticle dispersions were sprayed with a spray gun (Iwata HP-CS) at 20 psi onto pretreated indium tin oxide (ITO) slides placed horizontally. The amount of sprayed solution was such as to completely wet the area of the slide to be covered with nanoparticles. After 5 seconds, nanoparticle solution was blown off the slide by a spray gun. The spraying sequence was repeated 10−20 times to achieve the desired nanoparticle density. After deposition, the slides were immersed in water to remove excessive CTAB for 1 minute, dried under a stream of air, and plasma-treated for 10 seconds with 100 mTorr air to remove excess ligand.

3.6.3 *LB assembly*

A Nima 611D trough with a water sub-layer was used for LB monolayer preparation. The surface pressure was measured with a paper Wilhelmy plate attached to a D1L-75 model pressure sensor. Solutions of nanoparticles dispersed in chloroform or a chloroform/ethanol mixture were sprayed over the water surface, and the monolayers were allowed to dry for 10 minutes. Monolayers were then transferred to quartz or silicon substrates by the vertical dipping method at desired surface pressures.

3.6.4 *Electron beam evaporation*

A CVC electron beam evaporator was used prior to and after EBL. First, a 20 nm thick Ti adhesion layer was evaporated onto the substrate followed by 100 nm of Au in order to create a non-transparent, optically thick mirror. After lithography, 90 nm of Au was deposited using the CVC E-beam Evaporator. The pressure inside the chamber was $8*10^{-6}$ or lower for all evaporation steps. Ti was deposited at a rate of 1 Å/s while Au was deposited at a rate of 5 Å/s.

3.7 Patterning methods

3.7.1 *EBL*

Substrates were first cleaned with Piranha solution (H_2SO_4:H_2O_2 = 3:1) for 1 hour and then rinsed thoroughly with Nanopure water (18.2 MΩ cm). For the EBL resist, PMMA 950 A4 was spun at 1,800 rpm to give an approximate 200 nm height and baked at 180 °C for 90 seconds. EBL was done using a JEOL JBX-9300FS System. Lift-off was subsequently performed using 1165 Remover for a period of 4 hours, followed by a 30 second sonication

step. The substrate was sequentially rinsed with acetone, methanol, and isopropanol and UV cleaned for 30 minutes to remove any residual resist.

3.7.2 *Photopatterning*

Polymer/QD composite films were placed under a photolithography mask and exposed to a 120 W mercury arc lamp (Lumen Dynamics, X-cite series, 120Q) for 30 minutes.

3.8 UV-Vis spectroscopy

UV–Vis spectra were recorded on a Shimadzu UV-2450 spectrophotometer with a spectral resolution of 0.5 nm for UV/vis cycling experiments and 1 nm for other measurements.

3.9 Hyperspectral imaging

Hyperspectral images were collected using a CytoViva Hyperspectral imaging system utilizing a diffraction grating spectrophotometer with a spectral range of 400-1000 nm and a spectral resolution of 2.8 nm. A tungsten halogen lamp with an aluminum reflector providing a wavelength range of 450-850 nm and a peak power of 150 Watts was used as a light source.

3.10 Ellipsometry

Spectroscopic ellipsometry was performed on a Woollam M-2000U ellipsometer with a spectral range of 245–1000 nm (D2 and QTH lamps). Ellipsometry data for all samples were acquired at 65°, 70°, and 75° angles of incidence over the spectral range and modeled with V.A.SE software (WVASE32, Version 3.7868). The thickness and refractive indices of dielectric polymer films were determined by using a Cauchy layer for the polymer. A

general oscillator layer was used for complex electroactive polymers by using 4-7 Gaussian functions and fitting point-by-point over the entire spectral range.

3.11 Atomic force microscopy

Typical atomic force microscopy (AFM) scans were conducted with a Dimension 3000 instrument (Digital Instruments) in tapping mode. Scans were performed at a rate of 0.5–1.0 Hz for 526 lines and 526 pixels/line. Silicon nitride AFM tips (MikroMasch) with a spring constant of 7 N/m and a resonant frequency of ca. 150 kHz were used. A Dimension Icon (Bruker) equipped with a Nanoscope V controller was used in conjunction with ultra-sharp silicon tips (MikroMasch) with a resonance frequency of 280 kHZ for high resolution images. Scans were performed at a rate of 1 Hz for 1024 lines and 1024 pixels/line for surface areas of 500x500 nm^2. Image processing was performed using Gwyddion 2.36 software.[226]

3.12 Scanning electron microscopy/transmission electron microscopy

Scanning electron microscopy (SEM) images were obtained using a Hitachi SU 8010 with a resolution of 1.0 nm at an operating voltage of 5 kV. Transmission electron microscopy (TEM) images were obtained on JEOL 100CX and Hitachi HT770 microscopes operated at 100 kV with samples drop-cast on carbon–Formvar-coated copper grids (Ted Pella, Inc.). The grids were allowed to dry at room temperature before TEM imaging.

3.13 Electrochemical potential measurements

Electrochemistry measurements were performed on an EG&G Princeton Applied Research model 273 using a three-electrode cell with Corrware software. Several different aqueous

and nonaqueous electrolytes were used for electrochemical investigations including 0.5 M of lithium bis(trifluoromethyl)sulfonylimide (LiBTI) in propylene carbonate (PC) and acetonitrile, 0.5 M HCl, 0.5 M NaCl in 0.1 M HCl, 0.5 M NaCl in 0.01 M HCl, 0.5 M, and 0.5 M tetrabutylammonium hexafluorophosphate ($TBAPF_6$) in propylene carbonate (PC). Nanostructures on ITO and Pt wire were used as working and counter electrodes, respectively. As reference electrodes, an Ag/AgCl electrode and an Ag/Ag^+ (68 mV vs ferrocene) electrode were used for aqueous and nonaqueous electrolyte systems, respectively. During the measurement, the potential was gradually changed to a target value using a cyclic voltammetry technique at a speed of 50 mV/s to prevent abrupt current surge. UV–vis spectra at certain potentials were recorded on a Varian Cary 5000 Scan UV–vis/NIR spectrophotometer at a resolution of 1 nm. The UV–vis spectra were recorded 15 s after applying the potential.

3.14 FDTD modeling

Simulations were performed using FDTD commercial software from Lumerical Solutions, Inc. (FDTD Solutions 8.0.2-8.12.631).[227] A light source with a broadband wavelength range of 300-1000 nm was used for all simulations; a plane wave light source was used to obtain reflection spectra while a total-field scattered-field source was used to determine absorption and scattering spectra. A 1 nm mesh was used across the total monitor region, and perfectly matched layer (PML) boundaries were used for most simulations to prevent internal reflection. Silver and gold nanoparticles were modeled with a 1-2 nm PVP or CTAB surfactant layer respectively. Silver permittivity values were taken from Palik and fit with 6 coefficients, giving an RMS error of 0.150.[228] Gold permittivity values were obtained from the CRC handbook.[229]

CHAPTER 4. TAILORING THE PLASMONIC MODES OF A GRATING-NANOCUBE ASSEMBLY TO ACHIEVE BROADBAND ABSORPTION IN THE VISIBLE SPECTRUM

4.1 Introduction

The governing of light-matter interactions below the diffraction limit can be accomplished using nanofabrication methods such as electron-beam lithography (EBL)[230, 231] or self-assembly[232, 233] to incorporate plasmonic nanostructures into engineered matrices and structures. In this field, much interest has focused on obtaining light absorption at optical frequencies using plasmonic nanostructures or electromagnetic metamaterials.[234-239] These materials have a variety of applications in fields such as sensing,[240] surface enhanced Raman scattering,[241, 242] light absorbing nanowires,[243] thermal emitters,[244] thin film photovoltaics,[142] or thermophotovoltaics[23] for which efficient broadband absorption in the visible wavelength range is necessary.

However, plasmonic nanostructures are rarely able to independently achieve a broadband response due to their spectrally narrow bands that arise from their wavelength specific resonances.[12] For instance, Moreau et al. used AgNCs separated from a gold film by an insulating spacer to design a controlled reflectance surface that was able to achieve a maximum absorption of approximately 90% but only over a very narrow region with an approximate width of 25 nm.[235] Although impedance-matching metamaterials have been demonstrated that achieve near-perfect absorption, this absorption is not always broadband in nature and is often confined to the infrared or microwave regimes instead of the visible

spectrum, although recent theoretical modeling results predict different designs with high light absorption in a controllable wavelength range.[245-249]

To achieve a very high broadband absorption in the visible spectrum, it is possible to combine multiple plasmonic resonances from different nanostructure elements in a fashion that ultimately enhances the total light absorption. For instance, Aydin et al. employed the hybridized modes of fabricated trapezoidal metallic stripes (stripes with different cross-sections) in a metal-dielectric-metal stack to achieve a broadband absorption of 71% over the 400-700 nm wavelength range.[234] Yan et al. were able to fabricate a broadband absorber in the visible spectrum with an average absorption of 95% through the use of randomly-shaped and sized gold nanoislands in another metal-dielectric-metal design.[250] Most designs focus on incorporation of plasmonic resonances in particles[99, 103, 123] and nanoslits or nanogratings[251-254] which been studied extensively for their unique absorption properties. Nanoparticles support LSPRs that in addition to being angle insensitive can achieve electric field enhancements an order of magnitude larger than those of SPPs found in thin films or gratings.[77, 103]

Furthermore, the near-field enhancement between two coupled nanoparticles can be several additional higher orders of magnitude compared to single particles, which is relevant for many sensing and spectroscopy techniques.[103, 255] This effect is also applicable to nanoparticles separated from a plasmonic substrate by a thin dielectric layer; in this case, the nanoparticles generate mirror charge images in the substrate and the LSPRs also hybridize with SP modes, resulting in an enhanced, red-shifted resonance mode.[99] This resonance, known as the bonding mode, is symmetric in nature and oriented towards the substrate.[256] Anti-bonding modes are asymmetric in nature and oriented towards the

medium but only interact with light under particular circumstances.[98, 257] Small thicknesses of the spacer layer in the range of 5-20 nm have provided the strongest coupling effects and have given the best results in previous studies because resonances cannot excite well for extremely thin layers while larger layers result in poor coupling.[235, 240, 258]

Narrow grooves in a gold film and AgNCs have difference resonances that may be combined in this manner (**Figure 4.1**). The two different plasmonic nanostructures excite strong resonances with different spectral band positions that overlap with one another and allow a broadband absorption to be obtained. It has been demonstrated that narrow slits or grooves in noble metals can support localized standing plasmon modes.[253, 259] These differ from conventional gratings which excite SPPs when the conditions for Equation **7** are met.[118] Other types of nano-gratings adiabatically focus light to achieve a broadband, non-

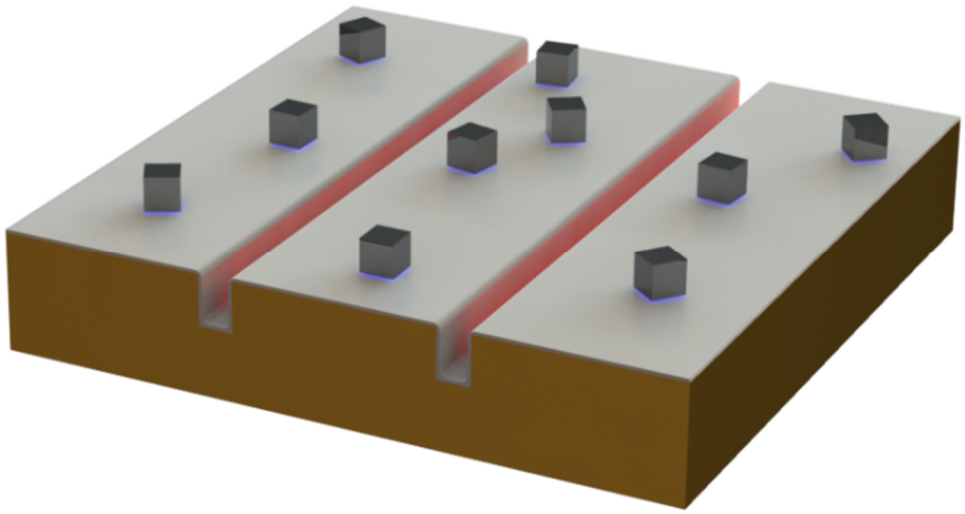

Figure 4.1: AgNCs separated from an underlying gold nano-grating by an insulating polymer spacer can be used in designing structures with broadband absorption properties.

resonant absorption but are limited to low-angle incident light as well as large structure thicknesses.[260, 261]

These nano-grating modes are in sharp contrast to the LSPR modes generated in small slits or grooves; in comparison to SPPs excited by conventional gratings, grooves can be considered as zero-order gratings and have relatively flat dispersion curves, leading to high absorption over a wide range of incident light angles.[254] Enhancement within these grooves scales with p/w, where p is the periodicity of the nano-grating and w is the width of the grooves.[252] Nano-gratings with small groove widths are attractive components for use in plasmonic absorption applications due to the ability to precisely design their structure and resulting resonances using techniques such as electron-beam lithography (EBL). However, to date little effort has been made to experimentally demonstrate how these narrow groove nano-gratings and their resonances can interact with or enhance the resonances of other plasmonic nanostructures, especially in the context of mesoscale nanostructure assemblies used for broadband absorption applications.[240]

Therefore, in this study we demonstrate the use of well-defined plasmonic resonances of noble metal nano-gratings and nanocubes in a constructive manner that ultimately enables the efficient, broadband absorption of light in the visible range at significantly higher levels than that possible for the individual elements. Our assembled nanostructure, presented in **Figure 4.2**, utilizes AgNCs with an edge length of 70 nm coupled to a thin gold substrate by a polymer dielectric spacer layer with a thickness of 8 nm. EBL fabrication of an underlying gold nano-grating of varying widths (w) and periodicities (p) is implemented in order to achieve this high broadband absorption. Using this nanostructure design enables the plasmonic resonances of the different components at two different wavelengths to

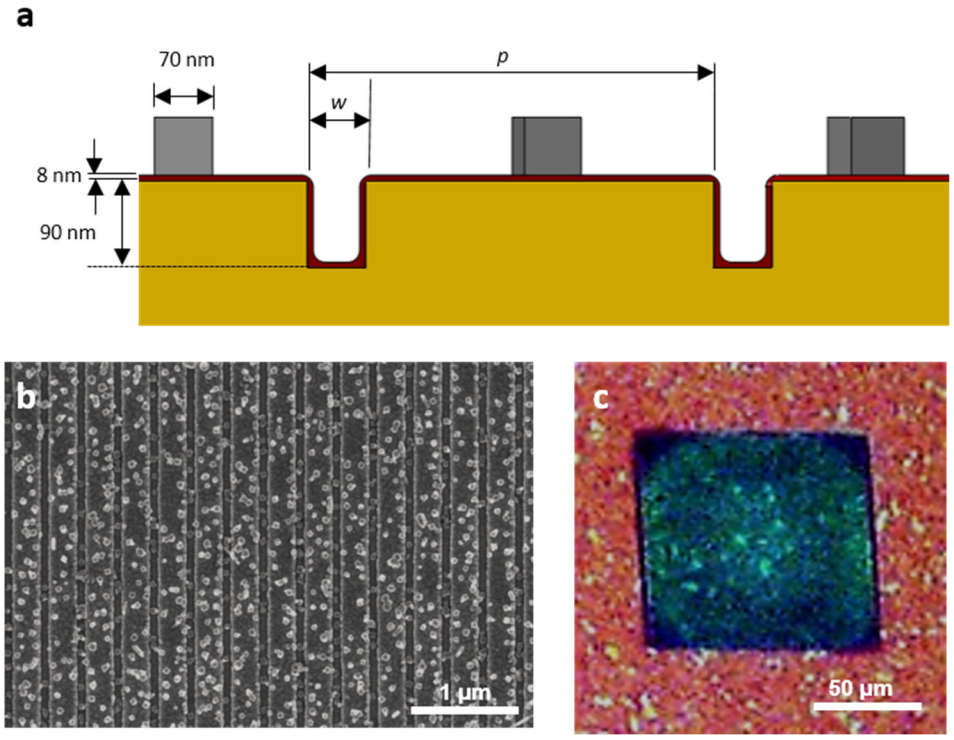

Figure 4.2: (a) Schematic of fabricated absorber with different grating widths and periodicities. (b) Scanning electron microscopy image of a fabricated grating-nanocube array with 100 nm groove widths and a 350 nm periodicity. Scale bar is 1 µm. (c) Bright field microscopy image of the same array. Scale bar is 50 µm.

multiplicatively enhance one another, as shown in this study. A high average light absorption of 84% was achieved over the broad wavelength of 450-850 nm for p-polarized (TM) light based on the different resonances of the gold nano-grating substrates and the dielectric spacer-coupled AgNCs.

4.2 Experimental Details

Polymer Spacer Nanolayers: Prior to bi-layer deposition, gratings were ozone etched for 1 minute in order to remove hydrocarbons and to make the surface hydrophilic. The thickness

of each bilayer was determined to be approximately 4 nm using a spectroscopic ellipsometer (Woollam M-2000U).

LB Deposition of Silver Nanocubes: Langmuir monolayers were transferred to substrates by the vertical dipping method at surface pressures of 1, 2, and 4 mN/m. Nanocube surface densities were analyzed using *ImageJ* binary thresholding of high contrast SEM images (**Figure A.5**).

Optical Characterization: A 10x bright field objective (NA: 0.30) in reflectance mode was used to scan the surface. P-polarized light was used to excite the nanostructures. Hyperspectral maps of the samples were normalized by a dielectric mirror with a reflectivity >99% from 350-1100 nm (Newport Corporation, 10Q20BB.HR). Approximately 3,000 pixel spectra were averaged per scan to obtain each individual spectrum (**Figure A.6**). Spectra were smoothed with adjacent averaging over a 20 nm window in order to eliminate instrumentation etalon effects while still preserving all spectra features (**Figure A.7**).

Finite-Difference Time-Domain Simulations: Two-dimensional simulations of three slit periods with periodic x-boundaries and perfectly matched layer (PML) y-boundaries were used for modeling the slits. Three-dimensional simulations of 2 cube periods with periodic x- and y-boundaries and PML z-boundaries were used for modeling the AgNCs. Nanocubes were modeled as both chains (periodic in x-direction) and square arrays (periodic in both x- and y-directions). Face-to-face, face-to-edge, and edge-to-edge orientations were considered as well. Nanocubes were modeled with a 15% edge rounding, defined as the edge radius normalized by the length of the nanocube, and a 2 nm PVP

coating as determined in previous studies.[262] Experimental values for gold's complex permittivity were found using ellipsometry and imported as a simulation material with a 6-coefficient fit, resulting in an RMS error of 0.153.

4.3 Results and Discussion

4.3.1 *Nanogroove modes*

Gold nano-gratings with groove widths of 50, 75, and 100 nm and periodicities of 350, 400, and 450 nm were fabricated with EBL in order to examine the effects of these parameters on the primary slit resonance (see Experimental). A height of 90 nm was chosen to maximize this resonance while avoiding the possibility of multilayers of AgNCs if they deposited into the grooves.

It was observed that for a constant periodicity, the primary resonance degraded and blue-shifted as the groove width was increased (**Figure 4.3a**). The absorption peak occurred at 770 nm for a 100 nm groove width and 709 nm for a 50 nm groove width which corresponds to a 1.2 nm blue-shift of the resonance peak wavelength per nm decrease of w (1.2 Δnm/nm). The reflectance minimum decreased from 17% to 9% as the groove width was decreased due to an increase of surface charges on the edges of the slits. The reflectance maximum at approximately 560 nm also experienced a slight decrease as the groove width was increased due to an increasing overlap with the main resonance. Keeping the groove width fixed and increasing the periodicity of the nano-grating had the effect of red-shifting the resonance at a rate of 1 Δnm/nm (**Figure 4.3b**). This shift may be attributed to the individual groove modes coupling to a lesser extent with one other as the periodicity was increased. A slight decrease in the resonance was also expected due to the

increase in the ratio *p*/*w* but was not experimentally observed. In all cases, the deposition of the polymer bi-layers was found to red-shift the resonance mode approximately 20 nm due to the change in the local refractive index around the nano-gratings (Error! Reference source not found.).

FDTD simulations supported the observed general trends in reflectance behavior (see Experimental). Reflectance minimum peak positions for simulated groove nanostructures are within 10 nm of experimental values (**Figure 4.3**). Experimental reflectance spectra were broader and had lower reflectance values than those of the simulated nano-gratings, but this is could potentially be due to the imperfect periodicities and geometries as well as

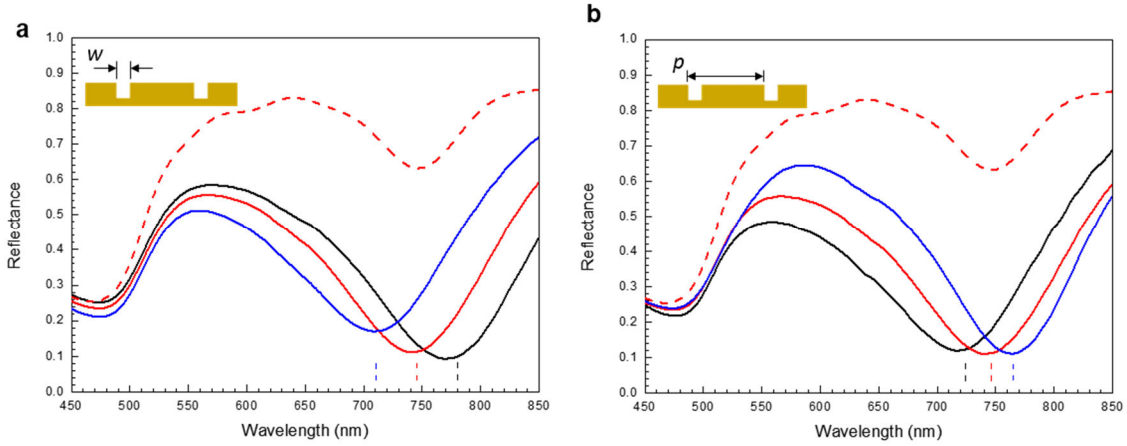

Figure 4.3: (a) Reflectance spectra for nano-gratings of a fixed *p* of 400 nm and a varying *w* of 50 nm (black), 75 nm (red) and 100 nm (blue). (b) Reflectance spectra for nano-gratings of a fixed *w* of 75 nm and a varying *p* of 350 nm (black), 400 nm (red), and 450 nm (blue). The dashed lines are the simulated spectra for the corresponding experimental spectra while the dashed markers indicate simulation peak positions for the respective experimental slit parameters.

the finite sizes of the fabricated gratings (Error! Reference source not found.).

The local electric field enhancement, $|E|^2/|E_0|^2$, was plotted for the reflection minimum of two periods for each nano-grating in order to visualize the plasmonic modes of the grooves (**Figure 4.4**). As is clear from the electric field enhancement distribution, strong

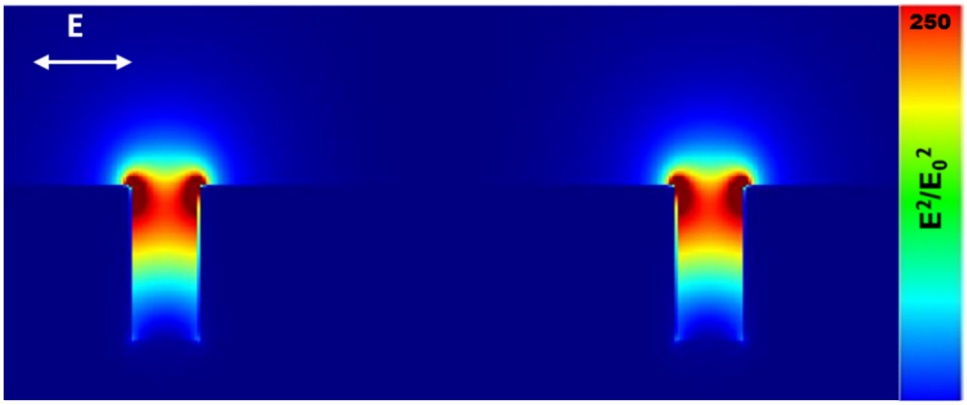

Figure 4.4: The electric field enhancement for a nano-grating with groove widths of 50 nm and a 350 nm periodicity. A maximum enhancement of 1250 occurs at the top corners of the grooves and the enhancement has been normalized to 250 for clarity.

coupling exists at the top corners of the grooves where the charge accumulation is the highest. On the other hand, little to no enhancement occurs along the outmost surface, confirming that the observed mode is local and non-propagating in nature. Such modes are also important for the angle independence absorption they exhibit.[252] This is advantageous for the broadband application being considered since SPP modes would most likely be disrupted by the sequential random deposition of nanocubes on the surface.[119]

4.3.2 *Silver nanocubes on a uniform substrate*

To study the individual resonance behavior of AgNCs separated from a bare gold substrate, the dielectric layer thickness and the cube surface concentration were varied. A polymer

dielectric thickness of 8 nm (2 bilayers) was determined to be the optimum spacer thickness for the cube surface coverages examined and resulted in the lowest reflection peak minimum values compared to the spacer thicknesses of 4 nm (1 bilayer) and 12 nm (3 bilayers) also investigated in this study.

The effects of nanocube surface coverage on the resulting reflectance properties were determined by adjusting the surface pressure during Langmuir Blodgett (LB) deposition to 1, 2, and 4 mN/m that corresponded to different gas or liquid states on a Langmuir isotherm (**Figure 4.5**). The variation of surface pressure resulted in respective nanocube surface densities of 12, 15, and 22% as determined by *ImageJ* analysis of high contrast SEM images (see Experimental).

Average interparticle distances (defined as the average distance between a cube's centroid and the centroid of its nearest neighbor) were obtained using the Image Metrology SPIP™

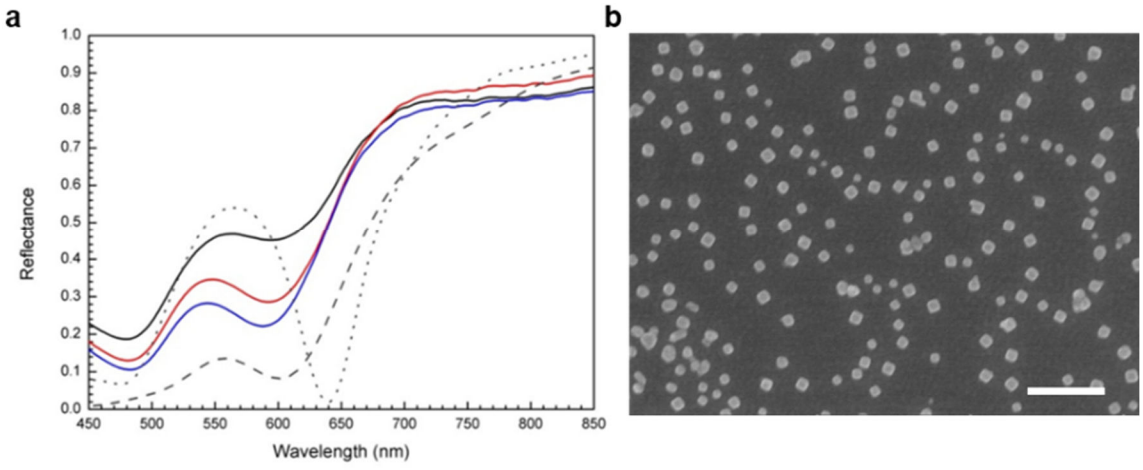

Figure 4.5: (a) Reflectance spectra for gold substrate-coupled AgNCs with surface densities of 12% (black), 15% (red), and 22% (blue). The broken curves show the simulated spectra for a 1-D interparticle spacing of 120 nm (dashed) and 300 nm (dotted). (b) SEM image of a 15% surface coverage sample. Scale bar is 500 nm.

software. For the surface densities of 12, 15, and 22%, average interparticle distances were respectively determined to be 134±40 nm, 111±42 nm, and 88±34 nm. The highest surface density investigated in this study of 22% resulted in the strongest resonance and also resulted in a slight blue-shift from the spectra of lower surface densities due to increased coupling interactions between nanocubes (**Figure 4.5**).

The spacing of nanocubes in periodic FDTD simulations of both nanocube chains (1D) and nanocube square arrays (2D) was varied within the broad range to reflect a high variability in experimental surface distribution in order to analyze the experimental results. It is important to note that because the deposited nanocubes are not strictly periodic in nature, the collective response can be approximated as such provided there are multi-cube aggregates with short-range ordering that influence the spectrum. In contrast to conventional simulations of individual aggregates which cannot be practically conducted for very large surface areas with complex topography, periodic boundaries model also allows the simulation of an infinite number of nanocubes, which is more realistic for modeling a large number of particles than the modeling of isolated clusters or chains of cubes.[54, 235, 263]

These simulations reveal that the resonance for a 1-D spacing of 300 nm between each nanocube is at 640 nm while the resonance for a 1-D spacing of 120 nm is at 600 nm and is weaker, implying that the AgNC interparticle distance plays an important role in the observed spectral characteristics (Figure 5a). For a 2-D array, an interparticle spacing of 150 nm results in the same resonance position at 600 nm (**Figure A.3**). Finally, the orientation of the cubes with respect to each other was procedurally examined to determine if it significantly altered the simulated cube resonance. Interestingly, face-to-face, face-to-

edge, and edge-to-edge orientations resulted in almost identical spectra in contrast to the differences reported previously in literature for close-packed nanocube chains, which will be discussed later (Error! Reference source not found.).[54] It is important to note that neither the 1-D or 2-D simulations exactly replicate the LB deposition, but they do serve as a model for elucidating the effect of changing the interparticle distance. The determined peak positions are also red-shifted significantly from that of AgNCs in a dilute solution due to the hybridization of the nanocube LSPR modes with the image charges and surface plasmons of the gold substrate, as has been documented in literature.[99]

Although coupled nanocubes display a higher reflectance minimum than that of isolated nanocubes, the associated blue-shift away from the slit modes and the resonance broadening are both beneficial for broadband absorption. The lower reflectance seen for the simulated coupled nanocubes compared to the experimental results can be attributed to the simulated nanocubes' perfect monodispersity and shape as well as their exact periodicity compared to experimentally broader distributions.

Electric field monitors for the reflectance minima peak wavelength of both 1-D interparticle spacings reveal the associated plasmonic modes (**Figure 4.6**). As evident from these simulations, nanocubes with a 300 nm interparticle spacing are essentially isolated from their nearest neighbors and the spectrum is dominated by the nanocube-substrate bonding modes. On the other hand, both a 1-D 120 nm spacing and a slightly larger 2-D 150 nm spacing still exhibit a strong bonding mode but also permit weak coupling between neighboring nanocubes (**Figure 4.6b**). In both the 1-D and 2-D cases, changing the orientation of the cubes with respect to each other does not significantly alter the spectrum or observed modes due to the nature of the weak, long-distance coupling

mode and the unaffected dominant bonding modes. In contrast, at much shorter interparticle distances, changing the orientation of the cubes would radically change the coupling mode and alter the spectrum as observed previously.[54] As a result, lower maximum field enhancements and higher reflectance peaks are ultimately present in the coupled nanocubes due to the delocalization of the electric field and the destructive interference between the nanocube bonding and coupling modes.

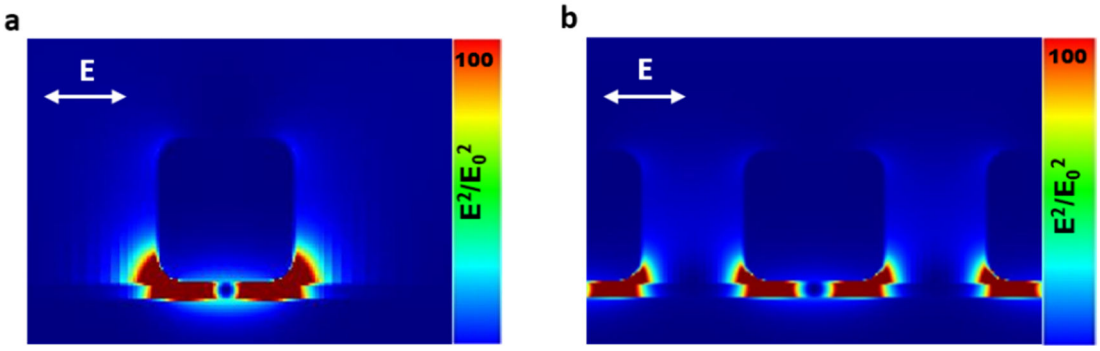

Figure 4.6: Electric field enhancements for (a) nanocubes with an interparticle spacing of 300 nm and (b) an interparticle spacing of 120 nm. Maximum theoretical enhancements of 1600 and 600 exist at the bottom corners of the cubes for the respective interparticle spacings of 300 and 120 nm, although the enhancements have been normalized to 100 for comparison.

4.3.3 *Nanogroove-nanocube assemblies*

After having separately analyzed and characterized the expected individual nanocube and nano-grating modes, AgNCs were deposited on polymer-coated nano-grating substrates (**Figure 4.2**). Because the grooves were designed to be narrow, nanocubes were expected to predominantly deposit along the top surface of the gratings. SEM images indeed confirm a high density of cubes on the top surface for all substrates, although nanocubes are also

present inside grooves with larger widths (**Figure 4.7a**). For smaller widths, nanocubes are able to deposit on top of the grooves, resulting in an approximate 20% reduction in the grooves' visible surface area (**Figure 4.7b**).

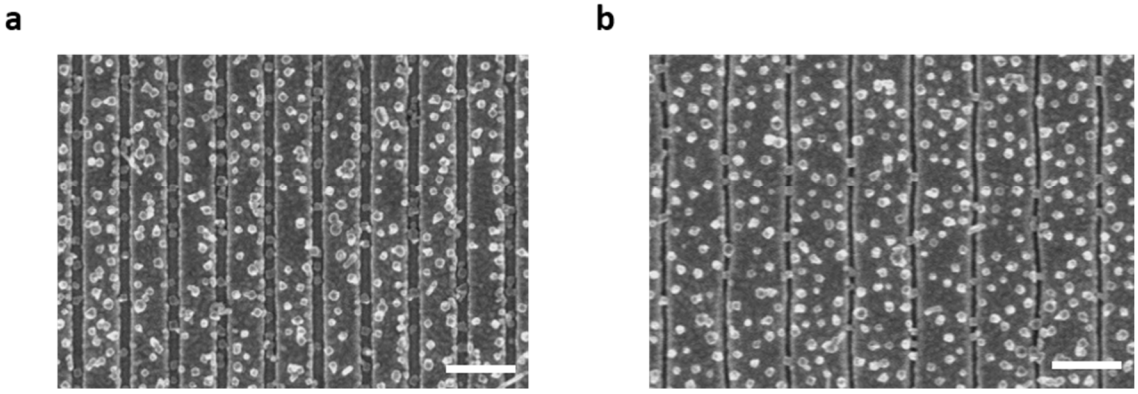

Figure 4.7: SEM images for 350 nm periodicity assemblies with groove widths of (a) 100 nm and (b) 50 nm. Scale bars are 500 nm.

In contrast to the trend seen for the individual nano-gratings where a decrease in groove width led to a slight decrease in reflectance, the grating-nanocube assembly reflectance significantly increases as the width decreases (**Figure 4.8a**). This is thought to be due to obscuration of the grooves and the alteration of their plasmonic modes by the nanocubes when they are deposited on top of nano-gratings with small grooves. Even though nanocubes can deposit into grooves of larger widths, this does not appear to adversely impact the grating mode due to the localization of the resonance around the top edges of the grooves (**Figure 4.4**). The relationship between the periodicity and the nanocube-grating assembly reflectance spectra also deviated from that of the individual nano-grating spectra. A clear increase in reflectance occurs with an increase of periodicity in contrast

to the constant reflectance seen for the nano-gratings independently, implying that the deposition of nanocubes impacts the resonance of the nano-gratings which will be discussed subsequently (**Figure 4.8b**).

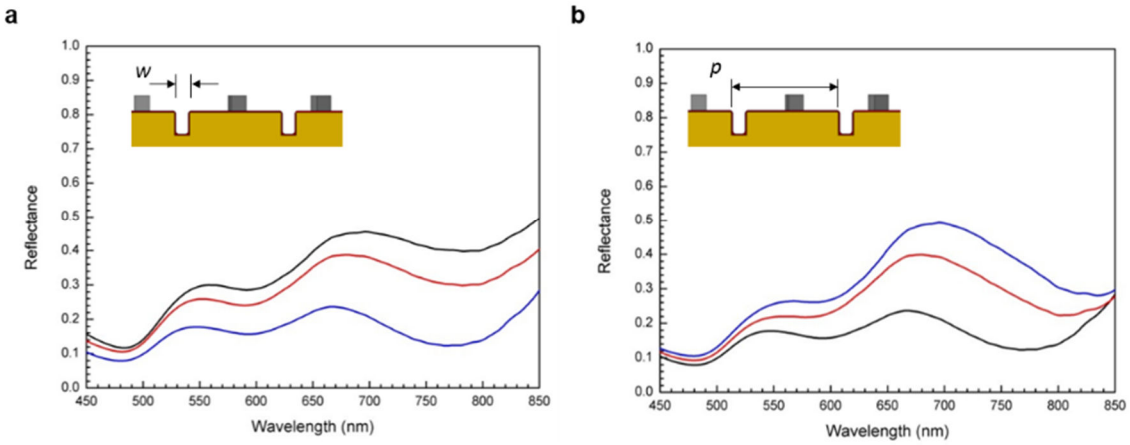

Figure 4.8: (a) Reflectance spectra for cube-nanoslit assemblies of a fixed *p* of 350 nm and a varying *w* of 50 nm (black), 75 nm (red) and 100 nm (blue). (b) Reflectance spectra for grating-nanocube assemblies of a fixed *w* of 100 nm and a varying *p* of 350 nm (black), 400 nm (red), and 450 nm (blue).

The overall shape of the spectrum can be generally reproduced by multiplying the individual reflectance spectra together in accordance with Beer's Law.[264] The total absorption (A) in the assembly is a product of a scalar coupling efficiency α and the individual component resonances:

$$A_{tot} = \alpha(A_{grooves} + A_{cubes} - A_{grooves}A_{cubes}) \quad \textbf{(13)}$$

Simulation of FDTD far-field power integrals of both the nano-grating and the nanocube reflectance monitors reveal that <5% of reflected light is scattered outside of the far-field

collection region when a numerical aperture of 0.3 is used (**Figure A.4**). This finding is in accordance with the large angle-independent absorption expected for these structures that would rarely lead to large angle scattering. This finding is also supported by previous literature results, which suggest that the absorption occurring within the structures is the dominant factor for the observed reflectance spectra.[234] If large angle scattering is therefore treated as negligible, the total reflection (R) can be expressed as:

$$R_{tot} = (1 - \alpha) + \alpha R_{grooves} R_{cubes} \quad \textbf{(14)}$$

For perfect coupling between the nanocubes and the nano-grating, the total reflection simply reduces to the multiplication of the individual resonances. The wavelength range of 450-650 nm was used to calculate the coupling efficiency as approximately 0.93 based on Equation **14** (**Figure 4.9**). These results suggest that less than one tenth of the total ideal resonance was eliminated through destructive interference between the separate modes, as seen by the only slight increase in reflectance when comparing the experimental and expected reflectance values below 650 nm to one another.

Above 650 nm, the calculated spectrum deviates from that of the experimental spectrum due to a drastic red-shift and broadening of the nano-grating resonance after nanocube deposition. Further studies are needed to exactly determine what this shift is due to, as it occurs for both nanocubes deposited only along the top surface as well as for nanocubes deposited along the top surface and into the grooves. The absorption peak red-shifts even further for larger periodicities and causes the two resonance modes to effectively split, explaining the increase in reflectance associated with an increase in periodicity (**Figure 4.8b**). While this effect is not desirable for the assembly investigated in this study, it is

worth noting that such splitting could be used to assist in the design of other broadband absorber assemblies or plasmonic multi-bandpass filters.

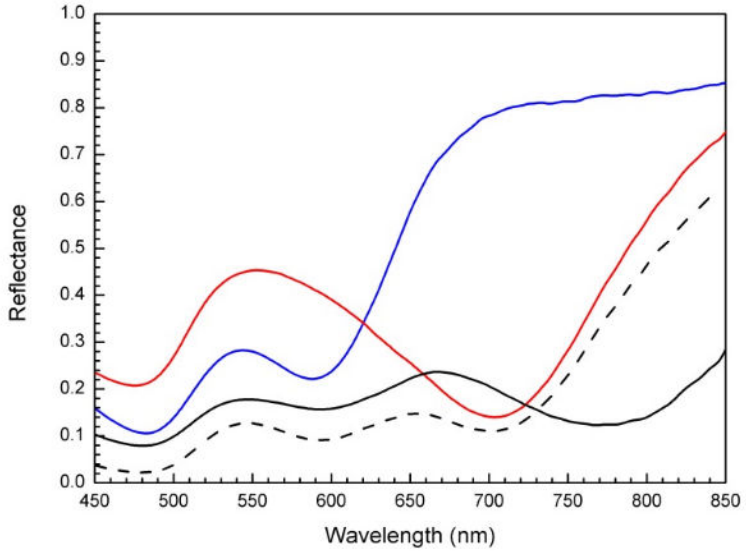

Figure 4.9: Reflectance spectra for the grating-nanocube assembly with 100 nm groove widths and a 350 nm periodicity (black), the individual slit resonance (red), and the individual cube resonance (blue). The dashed curve shows the expected calculated spectrum for the cube-slit assembly with ideal coupling (α=1).

With a decreased periodicity and increased groove width leading to lower reflectance values, the largest broadband absorption of an average 84% from 450-850 nm (approximately 92% at 450 nm to 76% at 850 nm) was ultimately found for a grating-nanocube assembly with 100 nm groove widths and a 350 nm periodicity (**Figure 4.8**). Over the same wavelength range, the individual components of the nano-gratings and the substrate-coupled nanocubes utilized in this study have much lower respective broadband absorptions of 65% and 49%, demonstrating a synergistic enhancement between the two

when they are combined in organized hybrid material structure with optimized match of their dimensions and coupling.

This materials design achieves a higher or similar broadband absorption value compared to many existing ultrathin plasmonic absorber designs and is not limited by the constraints governing impedance-matching metamaterials that make them difficult to design for broadband absorption in the visible wavelength range.[234, 236, 245, 249, 250, 261] The structure fabricated in this study also contains high electromagnetic field enhancements in the polymer dielectric layer, which may potentially be substituted for an active layer for photovoltaic or other energy conversion applications.[23] Moreover, our materials design relies on a facile ambient conditions combination of patterned substrate with simple deposition on nanocubes from water surface and does not require complex shape profiling, combining multicomponent incompatible materials, or additional high temperature post-treatment. Lastly, it is worth noting that most broadband absorber designs to date use a plasmonic film or mirror to eliminate transmission and to introduce coupling effects. In contrast, the narrow slit arrays discussed in this study can be possibly integrated into many existing designs for increased absorption properties.

4.4 Conclusions

In conclusion, this study proves the feasibility of engineering a broadband absorber by selectively combining multiple plasmonic resonances that spectrally and spatially complement one another. We demonstrated a high level of broadband absorption in the visible range for a metal-dielectric-metal nanostructure based on the principle of constructive plasmonic resonances. In particular, this design is aided by the non-

destructive overlap of two LSPRs compared to the case of combining LSPRs and periodicity-dependent SPPs which may lead to the disruption of the individual modes.[119]

In this case, AgNCs were separated by a gold nanoslit substrate by a thin polymer dielectric layer. The multiplicative enhancement created from these two resonances achieved a high average absorption of 84% from 450-850 nm for p-polarized light. Although this structure relies on p-polarized light to achieve high absorption, unpolarized light may be utilized instead by fabricating 2-D grid structures instead of 1-D grooves. Nanostructure assemblies such as this one may be useful for many optical applications in fields such as photovoltaics and thermophotovoltaics where broadband absorbance is necessary. Further enhancements to this design may be possible with the guided assembly of cubes at particular locations or the intelligent use of other overlapping, high quality resonances.

CHAPTER 5. SILVER NANOCUBE AGGREGATION GRADIENT MATERIALS IN SEARCH FOR TOTAL INTERNAL REFLECTION WITH HIGH PHASE SENSITIVITY

5.1 Introduction

AgNCs as active plasmonic components of materials and coatings have gained much attention recently because of their complex plasmonic properties and coupling phenomena in comparison with spherical nanoparticles.[256] The flat facets of a nanocube in close contact with a dielectric substrate allow hybridized plasmonic modes to appear due to the interference of dark and bright modes.[98] Chemical and biological sensors based on this effect could result in outstanding sensitivity in aggregated systems.[262, 265] Further potential advantages such as fluorescence enhancement,[266, 267] waveguide modes,[268] electrically tunable plasmonics,[269] and ideal absorbance[235] have been observed in complex materials systems with strong coupling between the nanocubes and a supporting metallic film or grating separated by an ultrathin spacer layer.[270, 271] To form an ideal light absorber in a broad range, the reflection and transmission must be controlled, which could result in improved efficiency, for instance, in thin film solar cells.[23] A general concept of topological darkness has been established which is based on local plasmonic field enhancements and the phase change of the interacting light.[272] In other words, a zero reflectance (ideal absorber) material yields sharp phase changes,[273] which allow the film-coupled nanocubes (on a dielectric or on a metallic film) to be used in two important fields: super absorption and phase-sensitive sensing.

Theoretical studies predict the super absorption of a single layer of well-spaced, periodically arranged noble metal nanoparticles.[274] Experimental studies from the Fery group show a substrate-supported technique, which enables the fabrication of periodic, well-spaced, and large-area nanoparticle systems at low costs.[275] Recently, the Käll group has realized complete light annihilation for a narrow bandwidth and for a specific polarization with gold nanodisks fabricated by hole-mask colloidal lithography.[276] In order to achieve a broadband and polarization independent super absorption[234] it is necessary to use self-oriented nanocubes[54] with a bottom-up fabrication technique. Consequently, the challenge is to build an active coating with well-spaced nanoparticles and with control over the aggregation type, which enables light trapping on the length scale below the diffraction limit for large areas.

Few investigations have been done for low surface coverage of metallic nanoparticles randomly distributed on a transparent substrate (<25%). This ultra-thin coverage with metallic nanoparticles shows manifold critical-coupling conditions compared to a solid metallic film. So far, the critical optical properties of aggregations and their relative orientation in respect to the plane of incidence have not been investigated. Therefore, we used a bottom-up, lithography and template-free, and easily scalable LB deposition to design AgNC aggregation gradients on a large centimeter scale area of solid substrates. The nanocubes were deposited on a quartz slide in the form of optical strip with controllable (step-wise) surface coverage to obtain multiple plasmonic resonances which originate from the different nanocube aggregation types. Relatively uniformly spaced AgNCs with different types of aggregation allows to obtain active hybrid coatings with absorption of virtually all incoming light, which occurs with a high phase shift.

5.2 Experimental Details

Step-wise assembly of AgNCs on quartz substrate via the LB method: A KSV2000 LB minitrough filled with Nanopure water (18.2 MΩ cm) at room temperature was used for LB deposition. The surface pressure was measured with a platinum Wilhelmy plate attached to a pressure sensor. The quartz slides (CGQ-0640-01, 75 × 25 mm) were purchased from Chemglass Life Sciences. The quartz slide (cleaned with acetone and by O_2 plasma etching for 1 min at 100 μTorr (0.13 mbar)) was submerged into a water phase prior to the formation of a monolayer. The stock solution of PVP-coated AgNC in water (1 mL) was diluted to 10 mL using deionized water (18.2 MΩ cm) in a conical-bottom glass centrifuge tube. The AgNCs were separated by centrifugation for 30 min at 4000 rpm and subsequently washed in a similar manner with EtOH–H_2O (10 ml, 1/1, v/v) and EtOH (10 mL). Finally, the residue was suspended in $CHCl_3$ (2 mL) and used within 1 h for LB deposition.

The Langmuir monolayer of AgNCs was then compressed at a rate of 5 mm min^{-1} to reach a surface pressure of 1 mN m^{-1}. The monolayer was transferred onto quartz slide at the air-water interface by pulling the substrate up vertically at a rate of 1 mm min^{-1}. After a vertical distance of 15 mm of deposition, the AgNC monolayer was compressed further at a rate of 5 mm min^{-1} to reach the surface pressure of 4 mN m^{-1} and was transferred onto next 15 mm of the quartz slide by pulling the substrate up vertically at a rate of 1 mm min^{-1}. The same procedure was repeated at the surface pressures 8 and 12 mN m^{-1} in order to create step-wise gradient in vertical direction (**Figure 5.1**). Since both sides of the quartz slide were coated with a monolayer, one side and the edges were carefully cleaned with acetone

to remove the AgNCs on that side. All samples were stored in a vacuum desiccator before characterization.

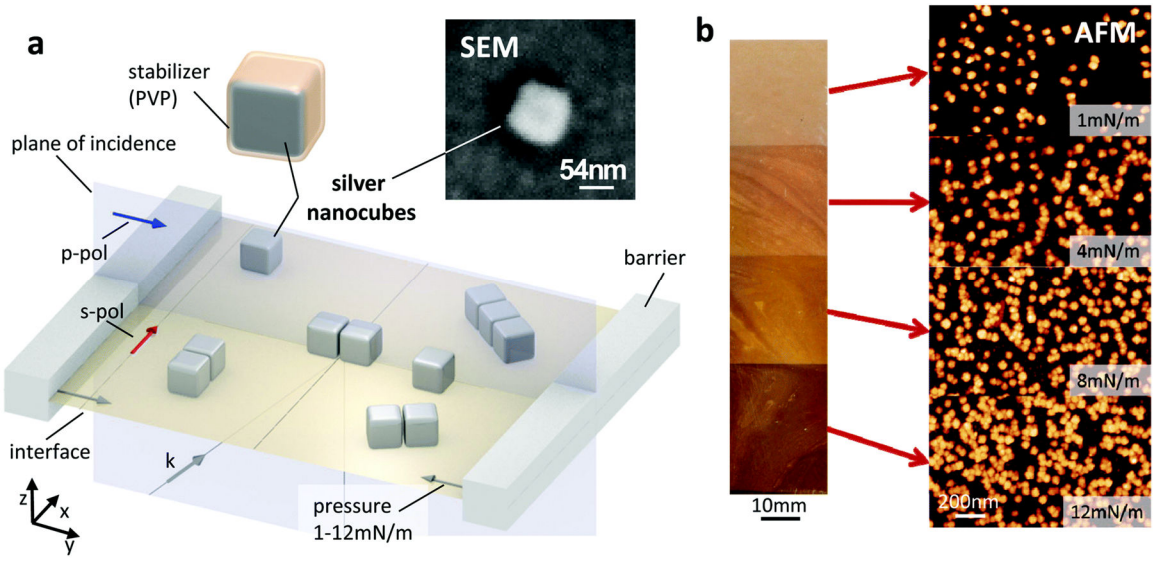

Figure 5.1: AgNC aggregation gradient fabricated with step-wise LB deposition on a macroscopic quartz glass slide. Experimental setup (a) and optical image of the aggregation gradient (b: left) and corresponding representative AFM images from different regions (b: right). Optical characterization in TIR was conducted from the backside. Arrows are defined in respect to the plane of incidence: wave vector (k), electric field vector for p-polarized (blue) and s-polarized light (red).

Spectral ellipsometry and TIR measurements: We employed a CaF_2 prism (25 mm base, right angle, uncoated) purchased from Thorlabs for TIR ellipsometry measurements. A single drop of diethylene glycol was applied to the bottom of the prism as immersion oil where the opposite (uncoated) side of the AgNC covered quartz slide made contact. Care was taken with proper coverage of immersion oil to ensure no air gaps occurred at the prism-slide interface. The prism-oil-slide setup was mounted on the ellipsometer stage with the AgNC coating facing down, making no contact with the stage (Chapter 5 Supporting

Information). As a control, an uncoated quartz slide was measured for every incident angle and polarization measurement.

Statistical analysis of AgNC aggregates: The surface coverage and aggregate fraction of samples were calculated from AFM images using ImageJ particle size analysis. A color threshold filter was used to produce a binary image that considered any cluster of nanocubes touching as a single particle with a corresponding measured area. Only the pixels highlighted by the color threshold filter were included in area measurements to account for any holes from large nanocube aggregations. From the binary image, both nanoparticles entirely within the image frame and those on the edge were considered for surface coverage calculations. To correct for artificially larger particle sizes introduced by the AFM tip convolution and image processing (*e.g.* color threshold filter), the average area for a single nanocube for a given image was calculated and divided by the average area for a single nanocube of 3025 nm^2 (as measured by TEM). Thus, adjusted values for surface coverage and number of AgNCs per square micron were computed. In order to calculate the fraction of particle aggregation type, the same binary images of particles previously mentioned were utilized. However, nanoparticles along the edges that were only partially visible in the AFM image frame were excluded from particle size analysis since the aggregation type could not be known. The resulting data were binned into X-mers by area in nm^2. Any counted nanoparticle under 3000 nm^2 was disregarded as an image artifact. Any particles in the range of 3000–9000 nm^2, 9000–15 000 nm^2, 15 000–21 000 nm^2, 21 000–30 000 nm^2, 30 000–39 000 nm^2, 39 000–48 000 nm^2, and larger than 48 000 nm^2, were defined as a monomer, dimer, trimer, tetramer, pentamer, hexamer, and *n*-mer, respectively.

Hyperspectral measurements: In order to directly compare simulation results for AgNC aggregates to experimental ones, AgNCs were spin-cast in a dilute solution to more easily identify specific aggregates and single cubes. The solution from previous steps was diluted by a factor of 10 in chloroform and spin-cast on a quartz substrate at 2000 rpm. We used these samples for analysis of individual spectral signatures because the concentration of AgNCs from LB deposition is too high to clearly separate individual nanoparticles and aggregates. AFM was used to spatially characterize the AgNCs and identify individual nanoparticles and types of aggregates while hyperspectral microscopy enabled the collection of spectra from single nanoparticles and aggregates.

About 20 pixel spectra were collected from individual aggregates and averaged to obtain aggregate spectra. Roughly, 25 000 pixel spectra were collected for an averaged monomer spectrum. All experimental spectra were smoothed with an adjacent averaging window of 15 points (17 nm wavelength span) in order to eliminate instrumentation effects.

FDTD simulations: For the modeling, the edge-rounding factor was estimated to be 25%. The refractive index of the quartz glass substrate purchased from Chemglass was measured with a spectroscopic ellipsometer (**Figure B.1a**). We included the glass substrate below the nanocubes and the stabilizing layer (PVP coating) as shown in **Figure B.1b**.

For silver permittivity, we used material data from Hagemann et al. (CRC approximation).[229] We found a much better agreement with our experimentally measured extinction spectra by using the permittivity from the CRC approximation instead of the more commonly used source from Johnson and Christy (JC).[277] The significant difference between JC and CRC is the lower imaginary component of the permittivity for the JC data,

which can be attributed to geometrical effects as Shalaev et al. have reported.[278] Reflection simulations were conducted with Bloch boundaries in the lateral directions at TIR angles instead of PML boundaries.

5.3 Results and Discussion

5.3.1 *Silver nanocube aggregation gradients*

We fabricated AgNC aggregation gradients in the form of optical strips with step-wise changes in surface coverage with the help of a conventional LB technique as described above (**Figure 5.1**). After spreading the nanocubes on the water-air-interface and applying minimum pressure, the nanocubes were mostly separated as monomers (individual nanocubes). As seen from optical images and AFM images, the surface coverage increased in a step-wise fashion with an increase in the applied surface pressure from top to bottom (**Figure 5.1b**). Increasing the pressure, the cubes begin to aggregate, preferentially face-to-face, as has been shown in solution by Klinkova *et al*.[279] We found no evidence for a preferred orientation of the aggregations on the LB trough or on the quartz slide, which would result in grating effects or polarization dependence at normal incidence (**Figure B.2**). Consequently, we consider the AgNC aggregations as randomly distributed on the quartz slide.

We quantified the apparent increase of nanocube aggregations and the increase in surface coverage up to 20% with an increasing surface pressure in **Figure 5.2a**. The fraction of aggregation type as evaluated from image analysis shows a decrease of monomer content and a corresponding increase of dimers, trimers, tetramers, pentamers, and hexamers, and *n*-mers when the surface pressure is increased up to 12 mN m^{-1} with multiple aggregate

types dominating at higher surface pressures (**Figure 5.2b**). Statistical errors are included in **Figure 5.2** with more details provided in the experimental part.

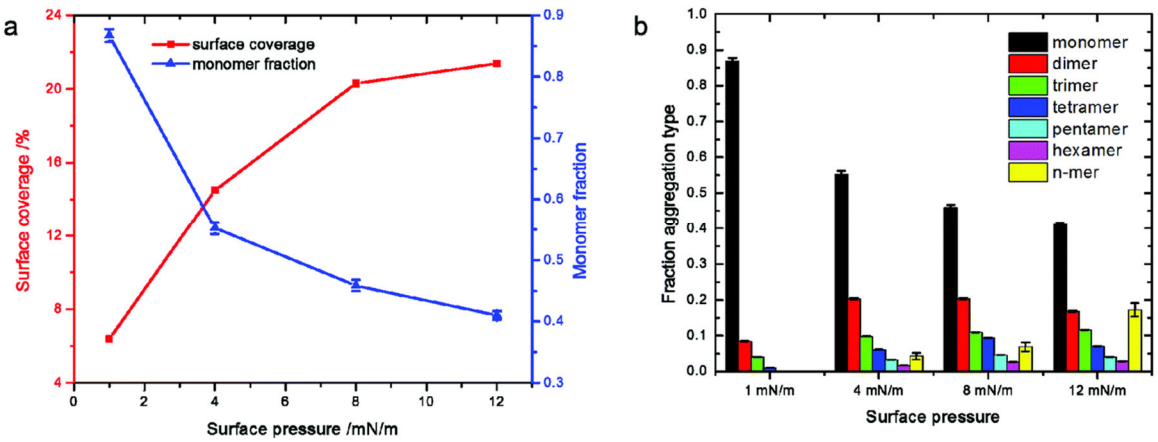

Figure 5.2: (a) Surface coverage and the fraction of monomers *vs.* LB surface pressure. (b) The fraction of each aggregate type in different regions with variable surface pressure.

5.3.2 *The role of materials parameters in total light annihilation*

The TIR regime occurs at an angle of incidence beyond the critical angle of incidence of a quartz glass-air-interface (>43°). The definition of p-polarized light (electric field vector in the plane of incidence) and s-polarized light (electric field vector perpendicular to the plane of incidence) is included in **Figure 5.1a**. More details about the optical setup can be found in the Experimental section and **Figure B.3**. The elliptical spot size of the instrument is 5 mm in diameter to ensure the scalability and the large-scale usability of the AgNC aggregation gradient. Optical light annihilation, which includes minimum reflection and

transmission, occurs at a specific frequency, polarization, and angle of incidence, and a significant challenge is to make it independent of these parameters.[23, 276] Before we go into details of the normalized reflection coefficients R_p and R_s, the measurement of the ellipsometric parameters ψ (amplitude component) and Δ (phase difference) summarize the optical response of the fabricated coatings (**Figure 5.3**).

The ellipsometric parameters are defined through the complex reflectance ratio $r_p/r_s = \tan \psi e^{i\Delta}$ where $r_p = E_p/E_i$ and $r_s = E_s/E_i$ are the amplitude reflection coefficients for parallel (p) and perpendicular (s) polarized light relative to the plane of incidence. Index i indicates the electric field of the incident light. The normalized reflection R is defined as reflected

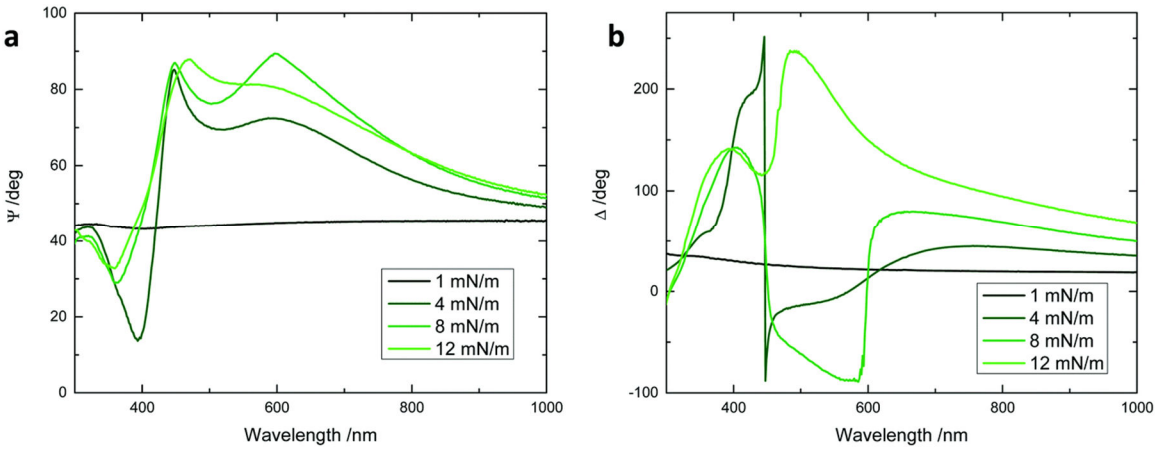

Figure 5.3: Spectral ellipsometric measurements in TIR for ψ (a) and Δ (b) observed at surface pressures between 1 mN m^{-1} and 12 mN m^{-1}.

intensity scaled by incident intensity. From the complex reflectance ratio, it follows that ψ goes to zero any time r_p goes to zero and ψ goes to 90° any time r_s goes to zero. Based on these definitions, we observe in **Figure 5.3a** that the reflected p-polarized light goes to a minimum at ~400 nm and the reflected s-polarized light goes to zero at ~420 nm

and 600 nm. These wavelengths are related to specific plasmonic modes of the higher dipolar plasmonic mode (300 nm),[123] the anti-bonding mode (~400 nm), the bonding mode (~420 nm)[98, 262] and the aggregation mode (600 nm).[269] Each LSPR occurs with a change in the phase, which can be seen from the significant slope change of the phase difference as presented in **Figure 5.3b**. A significant phase shift is of particular interest for a phase-sensitive plasmonic detection and is the highest here for a deposition surface pressure of 8 mN m^{-1}.[280] The ellipsometry spectra can be deconvoluted into specific plasmonic modes to discuss the nature of their origin.

5.3.3 *Optical response at normal incidence of the silver nanocube aggregation gradient*

To understand the optical response of AgNC aggregates and their role in light annihilation, a detailed discussion of their measured and modelled extinction spectra is necessary (**Figure 5.4**). All extinction spectra of the AgNCs on a quartz glass substrate show a typical signature of the optical interband transition at 312 nm.[281] An AgNC with a 54 nm edge length, rounded edges/corners, and suspended in a homogenous medium shows four dominant dipolar plasmonic modes (**Figure 5.4b**). Between the energetically lowest mode (dipolar mode) and energetically highest mode, which is located above the interband gap of silver (300 nm), the missing two modes appear as a left shoulder of the dipolar mode.[123] If the nanocube is in close contact with a dielectric substrate, the dipolar mode is hybridized into a bonding mode (405–410 nm) and an anti-bonding mode (380 nm).[98, 262]

The coupling of two AgNCs in close contact (2 nm) might result in a so-called peak splitting.[92, 282] Such splitting was not clearly observed in conventional absorption spectra but can be detected with spectra from individual aggregation types (**Figure 5.4a**). The

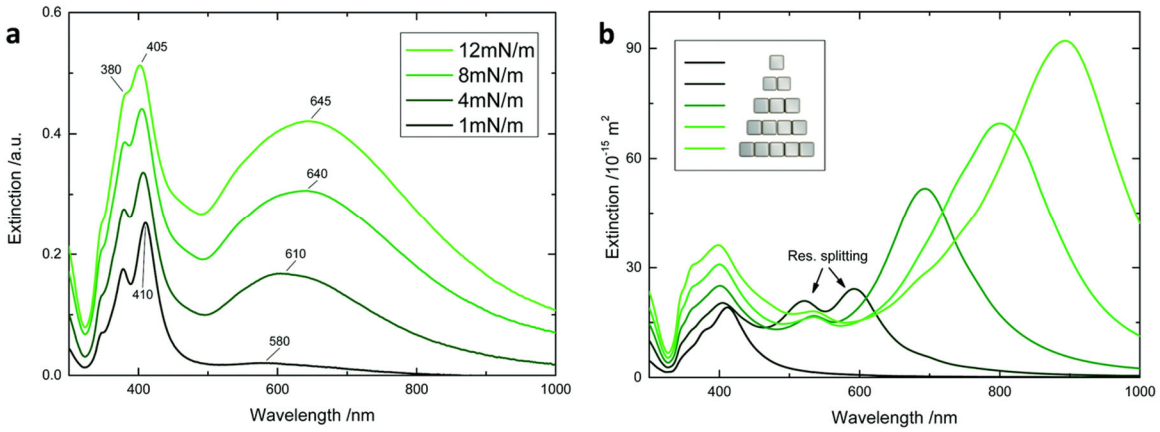

Figure 5.4: Experimental extinction cross-sections for LB monolayers deposited under different surface pressures (a) and simulations of different aggregation types at an inter-particle spacing of 2 nm (b).

additional broad peak within 580-645 nm appears for aggregated nanocubes (**Figure 5.4b**). The position and the width depend upon aggregation conditions and it can be represented as a weighted superposition of plasmonic modes resulting from self-assembled cubes with different chain lengths.[262] Theoretical simulations of specific plasmonic contributions from nanocubes aggregations at an inter-particle spacing of 2 nm with different chain lengths allows the deconvolution of the experimental aggregation peak into contributions from dimers, trimers, tetramers, pentamers, and decamers and thus analysis of the extinction properties of different individual chain-like aggregates (**Figure 5.4b**). For particle aggregates from chains longer than two particles, the energetically lowest mode is called a super-radiant mode, whereas all energetically higher modes are called sub-radiant modes (**Figure 5.4b**).[283, 284] The shift of the super-radiant mode converges with an increasing particle chain length to a specific wavelength in the far infrared, which is typically reached for aggregates from 10 particles.[285, 286]

Experimental evidence for the peak splitting and shifting can be found in hyperspectral imaging (dark field) in combination with AFM imaging of the same surface area, which allows for precise identification of specific aggregates and their spectral signatures (**Figure 5.5a**). To compare the dark field measurements (Rayleigh scattering) with the simulated results of different types of AgNC aggregations, we included all scattering cross-sections in **Figure B.4**. For example, for a selected dimer aggregate which is identified by spectral mapping and an AFM image from the same area, the local spectrum clearly shows the splitting phenomenon which is predicted by the simulated scattering cross-section (**Figure 5.5b**). Other combinations of nanoparticles into different types of aggregates result in significant shifts in plasmonic peak positions that contribute to the appearance of a broadband cross-section for nanocube coatings. Overall, as seen from the experimental spectra, AFM images, and statistical analysis, nanocube coatings with specific inter-particle spacings, the number of nanocubes present in individual aggregates, and aggregates with different chain lengths can all be adjusted by varying the surface pressure and transitioning from a gas- to liquid and then to ordered state within the LB monolayer.

5.3.4 *Separation of p-polarized and s-polarized reflected light components*

An exposure of the AgNC gradient coatings to polarized light under TIR conditions allows the study of different optical responses which are dependent on the electric field polarization vector (**Figure 5.6**). For instance, in a thin metallic film, SPPs can be excited under specific mode matching conditions, such as using the proper wavelength or angle of incidence.[287] The electric field component in the plane of incidence (p-polarized) has to match with the collective electron oscillation in the metal to excite the plasmonic resonance. At the same time, the s-polarized component remains unaffected. In the setup

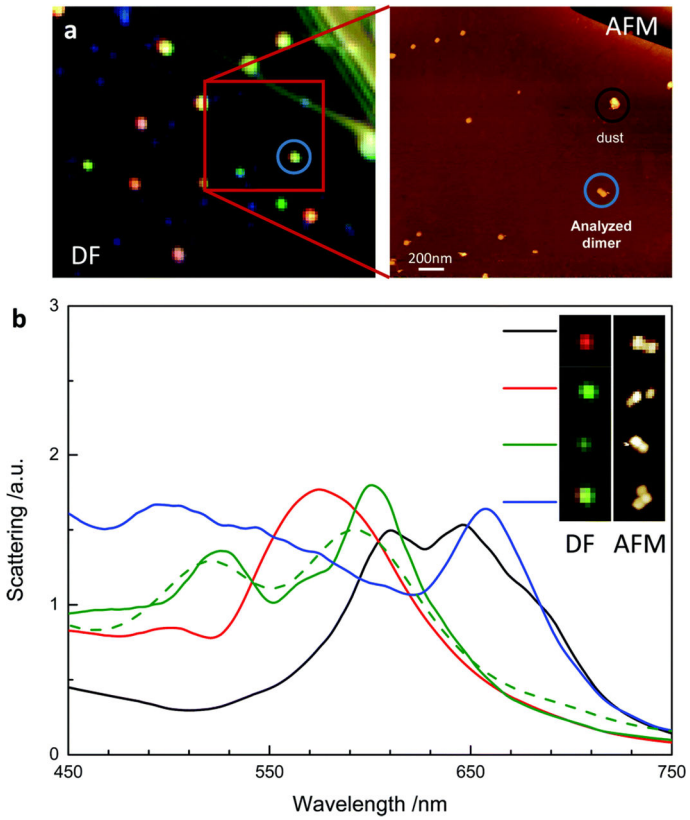

Figure 5.5: (a) Optical image of area selected for hyperspectral measurements (dark field, DF) of an AgNC dimer with AFM image overlay detailing exact composition of particle aggregates analyzed and (b) hyperspectral data for a selection of different types of aggregations that demonstrates resonant peak splitting as predicted by simulation for nanocube dimer (dashed line).

discussed here, the AgNC aggregations are sensitive to both polarization states. Reflection measurements in p-polarized TIR (**Figure 5.6a**) show a clear signature of higher plasmonic mode (300 nm), hybridized modes (~400 nm) and a slight response from nanocube aggregations (550 nm). On the other hand, the s-polarized TIR shows a similar response with a very pronounced absorption for the aggregation mode ~650 nm (**Figure 5.6b**). This absorption behavior correlates with the surface coverage controlled by the surface pressure and reached its optimal absorption at a surface pressure of 8 mN m^{-1} (about 20% surface coverage). The dependence of the TIR optical response on the surface pressure and

consequently the fraction of cube aggregates suggests that the orientation of the aggregates relative to the plane of incidence is of particular importance.

We have to point out that the nanocube aggregates on the substrate are randomly distributed at different surface pressures. However, electromagnetic simulations allow the distinction between two local orientation states, which are shown in **Figure 5.7**. We define the two orientation states as horizontal and vertical in respect to the plane of incidence. The optical response is fully described with these two orientation states. Both reflection spectra for a

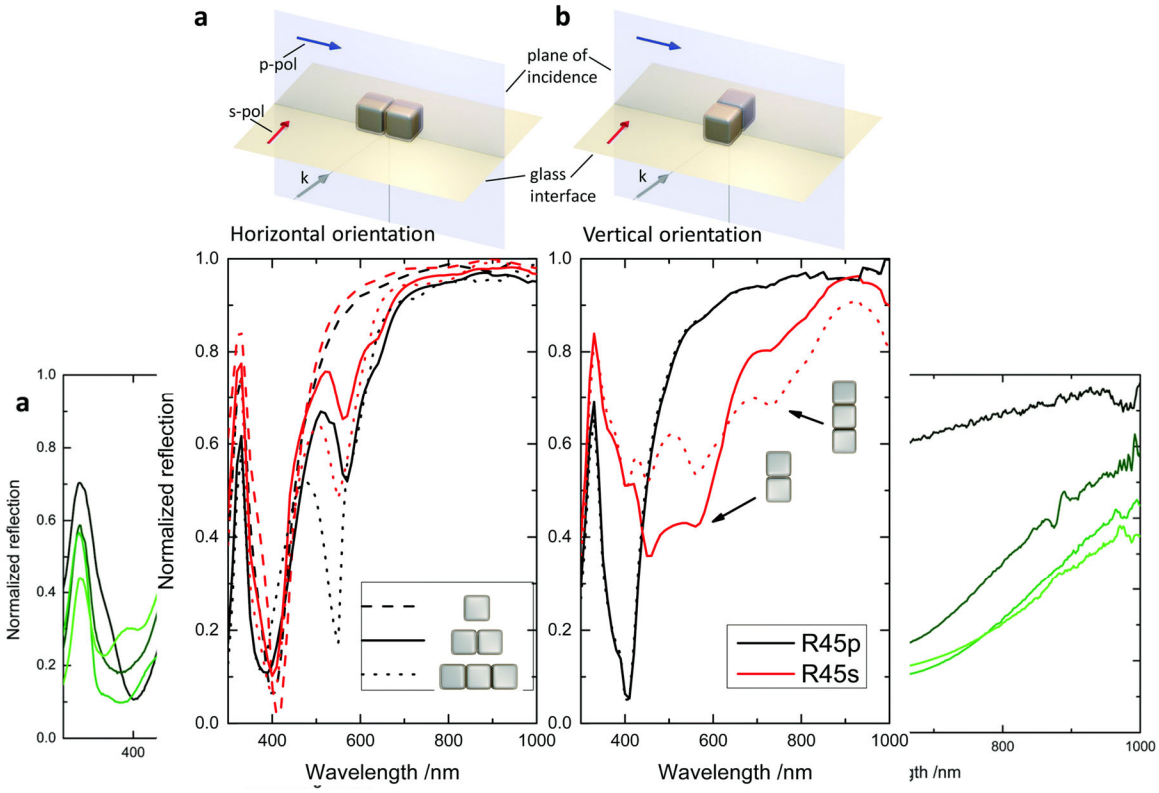

Figure 5.7: Optical setup of two aggregation orientations and simulated reflection for monomer, dimer, and trimer assembly. (a) Geometric axis of the cube assembly parallel to the plane of incidence (horizontal orientation) and (b) perpendicular to the plane of incidence (vertical orientation). The angle of incidence is constant at 45°. The arrows indicate the wave vector (k) and the electric field vectors for p-polarized (blue) and s-polarized light (red).

monomer reveal the same plasmonic response where for s-polarized light the minimum is achieved more readily (**Figure 5.7a**). The reflectance minimum value for p- and s-polarized light (both at 410 nm wavelength) is 0.07 and 0.02, respectively. As expected, simulations of dimers and trimers with s-polarized light confirm the experimentally measured broadband absorption of the aggregation peak. Furthermore, both the dimer aggregation and square aggregated tetramers contribute to the spectra. In previous work, we deconvoluted the extinction spectra of AgNC aggregates, which are located on a glass substrate in detail.[262] It is worth noting that a square aggregated tetramer shows the same longitudinal signature as a dimer but differences could be found in the cross-section intensity, which are doubled for a square aggregated tetramer compared to a dimer. The simulated reflection dip of the aggregation peak is not as smooth as observed experimentally, which can be explained by the selective simulation of two aggregates and a fixed inter-particle spacing. Our simulations suggest that the s-polarized component is sensitive to the type of aggregations (mode matching). However, under real experimental conditions, a combination of factors, such as the aggregation type varying from dimers to pentamers (and even higher), different observed inter-particle spacings, and averaging over large surface areas smooth out the individual plasmonic responses but still show major differences in polarization-dependent absorption of different nanocube coatings (**Figure 5.7**).

The mode matching with s-polarized light and the vertical orientation of the aggregates can be explained by the nature of the electric field vector of s-polarized light (E_s). The absolute value of the s-polarized vector is always constant, whereas the parallel component of the p-polarized vector changes with the angle of incidence. For instance, in SPPs, the parallel

component at the interface (p-polarized) is responsible for the excitation of the plasmonic resonance. Consequently, the plasmonic resonance can be tuned by the angle of incidence at a fixed wavelength.[288] Here, we have a match of the s-polarized component with the AgNC aggregation, when the electric field component is parallel to the geometric axis of the aggregate. In other words, the plasmonic resonance of the s-polarized light in TIR is tuned by the type of aggregations. As shown in **Figure 5.3**, we observe plasmonic resonances that are excited either by p-polarized or s-polarized light which are triggered by the AgNC aggregations. These results could lead to new phase-sensitive detectors, which are sensitive for both polarization states (enable a higher lateral resolution) as discussed in the following section.

5.3.5 *Silver nanocube aggregation gradient for tunable broadband light absorption*

Figure 5.8a shows the reflectance of an assembled AgNC aggregation gradient for broadband light absorption at different angles of incidence. We chose the best broadband absorption sample transferred to the quartz substrate at 8 mN m^{-1} surface pressure, which corresponded to a 20% surface coverage. The signatures of the various plasmonic resonance modes are clearly visible, whereas the plasmonic modes around 400 nm slightly increase in reflectivity and the aggregation peak red-shifts with an increasing angle of incidence (45, 50 and 60°). The same trend was also observed in the electromagnetic simulations for a dimer in horizontal and vertical orientations (**Figure 5.8b**). Furthermore, with simulations we can clearly distinguish between the absorption originated from the horizontal and vertical orientation of a nanocube dimer. Consequently, we found that the absorption of the aggregate mode at s-polarization can be tuned by 64 nm per 10° angle of incidence. These properties could be selectively used with anisotropically oriented

nanoparticles, which could be fabricated with template-assisted self-assembly methods.[289] The absorption at a high angle of incidence is interesting for solar cell applications, particularly for capturing the sunlight in the evening and during cloudy days.[290]

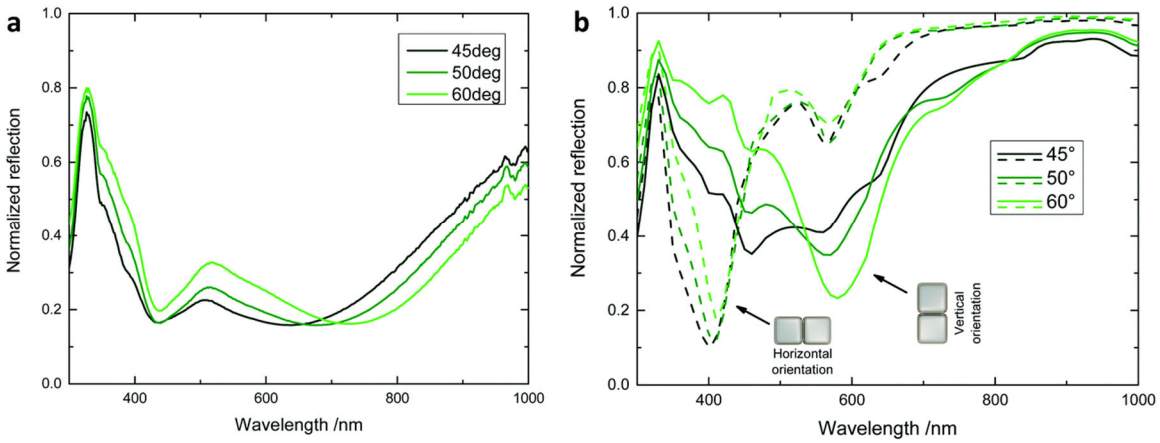

Figure 5.8: Experiment and simulation of a broadband total light annihilation shown at different angles of incidence and fixed s-polarization. (a) Experimental measured reflection for the optimal sample with 20% surface coverage (8 mN m^{-1}). (b) Simulations are constrained to dimers in horizontal and vertical orientations only.

5.4 Conclusions

In conclusion, we fabricated gradient-like monolayer coatings of AgNCs with varying amounts of aggregates (surface coverage from 5 to 20%) and studied their variable light reflection properties. The plasmonic modes of monomers and aggregates were analyzed experimentally using hyperspectral imaging and were confirmed with FDTD simulations to be an assortment of hybridized, higher dipolar, and aggregate modes. TIR measurements as well as FDTD simulations established that an increase in aggregates along with a

gradually changing surface coverage of AgNCs allows for the control of the absorption of the incoming light over a broad optical spectrum. Moreover, AgNC aggregates were found to be polarization sensitive and excited different plasmonic resonances based on their relative orientation to either incident s- or p-polarized light. In particular, the s-polarization showed a high sensitivity of the aggregate plasmonic resonance to the angle of incident light (64 nm shift per 10° increase of the angle of incidence) and also contributed to a broadband high absorption of 80% of the incoming light over a broad optical range from 400 nm to 700 nm. These large-area variable optical coatings may be of particular interest for broadband light absorption and phase-sensitive sensing for large-area (centimeter scale) coatings with position-dependent light absorption.

CHAPTER 6. THE EFFECT OF PLASMON RESONANCE COUPLING IN P3HT-COATED SILVER NANODISK MONOLAYERS ON THEIR OPTICAL SENSITIVITIES

6.1 Introduction

Single nanoparticles are often used in order to facilitate controllable and reproducible systems because plasmon coupling between adjacent nanoparticles can lead to undesired resonance shifts.[256, 291-295] However, mesoscale arrays of nanoparticles have previously been shown to possess unique optical properties not present in monomers or individual aggregates such as dimers.[231, 296, 297] While electron-beam lithography has been used to generate finely controlled, coupled nanoparticle arrays, this fabrication method is time-consuming compared to bottom-up assembly methods.[298, 299] LB has successfully been used to create large-area, well-ordered monolayers of nanoparticles and tightly controlled interparticle interactions.[63, 219, 300] By varying the surface pressure, the interparticle spacing of nanoparticles within an LB monolayer deposited on a substrate can ultimately be controlled on a large scale, thus providing a means for control of its plasmonic properties. Coupled modes between nanoparticles while used profusely in the demanding applications such as SERS for their hotspot-controlled properties, remain relatively understudied in other applications due to the difficulty in fabricating organized nanoparticle arrays in a bottom-up manner with predictable and controllable optical properties.

Several studies to date have focused on the use of nanoparticles as optical switches when used in conjunction with media that respond to applied external stimuli such as a pH

change, UV illumination, or an electric potential.[301-306] For instance, photochromic azo-benzene molecules undergo a cis-trans conformation change when exposed to UV illumination, which ultimately causes a change in the refractive index of films containing these molecules and a resultant peak wavelength shift of the LSPR of any embedded plasmonic nanoparticles.[307] Of the different types of stimuli-responsive mediums, those sensitive to applied electric potentials offer several advantages. For instance, electrochromic polymers (ECPs) react to a change in electrical potential very quickly as opposed to photochromic materials that may take longer to physically change their conformations upon UV illumination or, more commonly, thermal relaxation to the initial state.[308-310]

Electroactive materials may also be more easily integrated into existing applications and devices compared to materials that require pH or illumination changes. Several different types of electrochromic polymer and nanoparticle combinations have been considered to date for plasmonic electroactive devices.[298, 299, 311-313] Conjugated polymers such as PANI or polythiophenes (PTs) exhibit a refractive index change in the visible wavelength regime that can overlap with the LSPRs of gold or silver nanocubes or nanorods for instance.[314] Ideally, the LSPR of a single nanoparticle is at the wavelength that sees the largest shift in the refractive index of the polymer as the two are directly related by Equation **4**.[315, 316] Assuming that d is significantly larger than l_d, it can be seen that $\Delta\lambda_{max}$ is directly proportional to Δn by m, meaning the RIS can be directly evaluated if the LSPR peak shift and change in refractive index are both measured independently.

This study therefore aims to investigate the coupling of AgNDs in LB monolayers after being deposited on substrates at various surface pressures and deposition scenarios.

AgNDs were chosen for their relatively narrow LSPR bands, which arise due to their single dipole modes in the visible spectrum, and for their plasmon tunability over the entire visible spectrum.[317] Additionally, their nanoscale thickness of about 10 nm enables thinner responsive polymer layers to be used that are able to switch faster and do not dominate extinction spectra with their absorption. In contrast, nanoparticles such as nanocubes can exhibit multiple modes, significant broadening and peak splitting at longer LSPR wavelengths. A previous study reported full-width half-maximum (FWHM) values of 194 nm for gold nanoprisms and 119 nm for gold nanodisks on substrates while the AgNDs used in this study had a FWHM value of 147 nm when deposited on substrates.[318]

The readily available electroactive conjugated polymer poly(3-hexylthiophene-2,5-diyl) (P3HT) was utilized as a variable refractive index medium for AgND monolayers due to its large electrically modulated and reversible refractive index change above the 600 nm

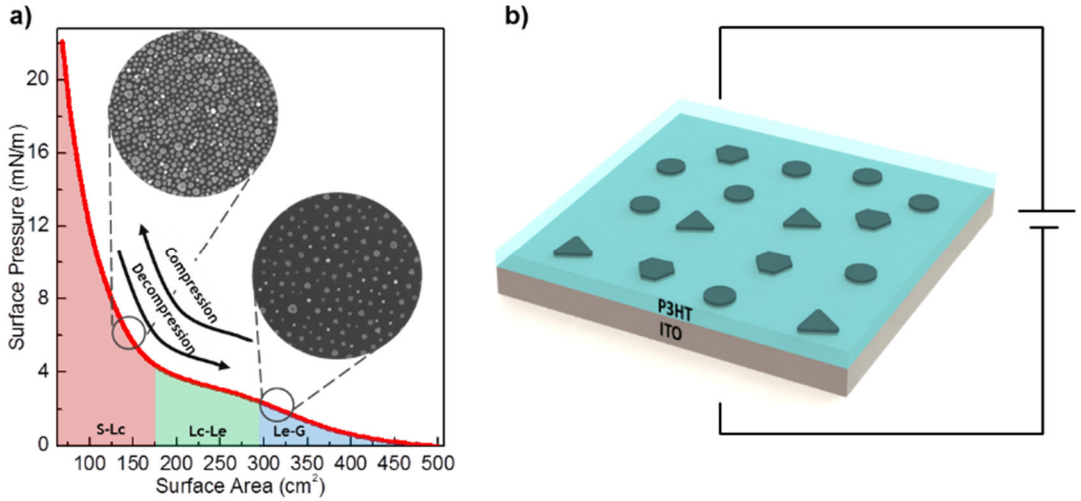

Figure 6.1: (a) LB isotherm of AgNDs with estimated Le-G, Lc-Le, and S-Lc regions. Insets show SEM images of samples deposited at surface pressures of 6 mN/m and 2 mN/m. (b) Schematic of a P3HT-coated AgND monolayer on an ITO substrate with an applied voltage for electrical optical control.

wavelength during the transition between its reduced and oxidized states. AgND monolayers were deposited on ITO electrodes in the liquid expanded-gaseous (Le-G), liquid condensed-liquid expanded (Lc-Le), and solid-liquid condensed (S-Lc) phases during both compression and decompression with and without an applied electrical potential (**Figure 6.1a**). Then, a 25 nm-thick P3HT layer was spin-cast on top of the AgND monolayers to form an electroactive assembly in order to test the ability for electrically-controlled coupling phenomena (**Figure 6.1b**).

Using this platform, we first showed that the LSRP peak position of bare AgND monolayers is correlated to the LB monolayer state and the method they are deposited in. Moreover, a large and reversible, 26 nm, electrochemically-controlled LSPR shift was demonstrated for P3HT-coated AgND monolayers deposited in the Lc-Le phase, which is on a similar scale to previous LSPR modulators utilizing different ND arrays.[302, 319] Lastly, we showed a strong correlation of the reversible, electropotential-controlled LSPR shift and RIS of P3HT-coated AgND monolayers with the LB phase they are deposited in.

6.2 Experimental Details

Sample preparation: AgND monolayers were deposited on ITO and silicon substrates at relative surface pressures of 0, 2, 4, 6, and 16 mN/m from low-to-high surface pressures (compression) and high-to-low surface pressures (decompression). P3HT was dispersed in a chloroform solvent at a concentration of 0.25 wt% and then spin cast on top of the AgND monolayers on ITO substrates at 800 rpm for 50 seconds. Finally, P3HT-coated AgND monolayers were annealed at 60 °C for 10 minutes before measurements to remove residual solvent.

Optoelectronic switching: Electrochemical switching experiments were carried out using a two-electrode electrochemical oxidation system. Two ITO substrates (0.5x 5 cm) were immersed in an electrolyte solution of 0.1 M $LiClO_4$ (Sigma-Aldrich) inside a 1 cm x 4 cm quartz cuvette. One served as the counter electrode while the other was coated with mixed P3HT-coated AgND monolayers. A power supply was used to apply a total cell electrical potential of 500 mV. The P3HT thin film on the surface of the ITO electrode was oxidized by connecting it with the positive pole of the power supply and subsequently, the oxidized P3HT film was reduced by switching the polarity of the power supply (**Figure 6.1b**). For multiple electrochemical oxidations and reduction cycles, the P3HT electrode was switched between the positive and negative poles of the power supply with an applied cell potential of 500 mV.

Characterization: UV-Vis spectra of AgNDs and P3HT-coated AgND monolayers on ITO substrates were measured using the Ocean Optics HR4000Cg-UV-NIR from the electrochemical switching experiments. UV-Vis spectra were smoothed with a 50% percentile filter and a 30-point adjacent averaging window to eliminate instrumentation artifacts. For spectroscopic ellipsometry measurements of reduced P3HT's complex refractive index, 50 nm-thick P3HT films were spin cast on silicon wafers. Oxidized P3HT's complex refractive index was obtained by first exposing the film to iodine vapor for 5 minutes.

Finite-difference time-domain simulations: Simulations were conducted with periodic boundaries, and AgNDs were modeled with a 40 nm diameter and a 10 nm height based on SEM and AFM measurements, with a PVP shell thickness of 2 nm on the sides of the AgNDs and 0 nm on the top based on previous results.[35] To model the varying surface

coverages, the AgND configuration was approximated as a 2D centered rectangular lattice structure.

6.3 Results and Discussion

6.3.1 *AgND monolayers*

AgND monolayers were first deposited on ITO electrodes while being compressed from low to high surface pressures. After zeroing the initial surface pressure of the nanoparticle solution (~1 mN/m), samples deposited at 0, 2, 4, 6, and 16 mN/m had corresponding surface coverages of 11.1, 11.9, 19.5, 33.3, and 57.6% based on ImageJ analysis of SEM images (**Figure 6.2**). The average AgND diameter for all surface pressures was approximately 40 nm and respective average nearest neighbor (centroid-to-centroid) distances were 94, 89, 74, 56, and 42 nm for the relative surface pressures of 0, 2, 4, 6, and 16 mN/m. The surface pressures of 0 and 2 mN/m lie in the Le-G phase of the LB isotherm while 4 mN/m is in the Lc-Le phase and 6, 10 (not shown), and 16 mN/m are in the S-Lc phase (**Figure 6.1a**). On these isotherms, there is no clear transition between the solid and

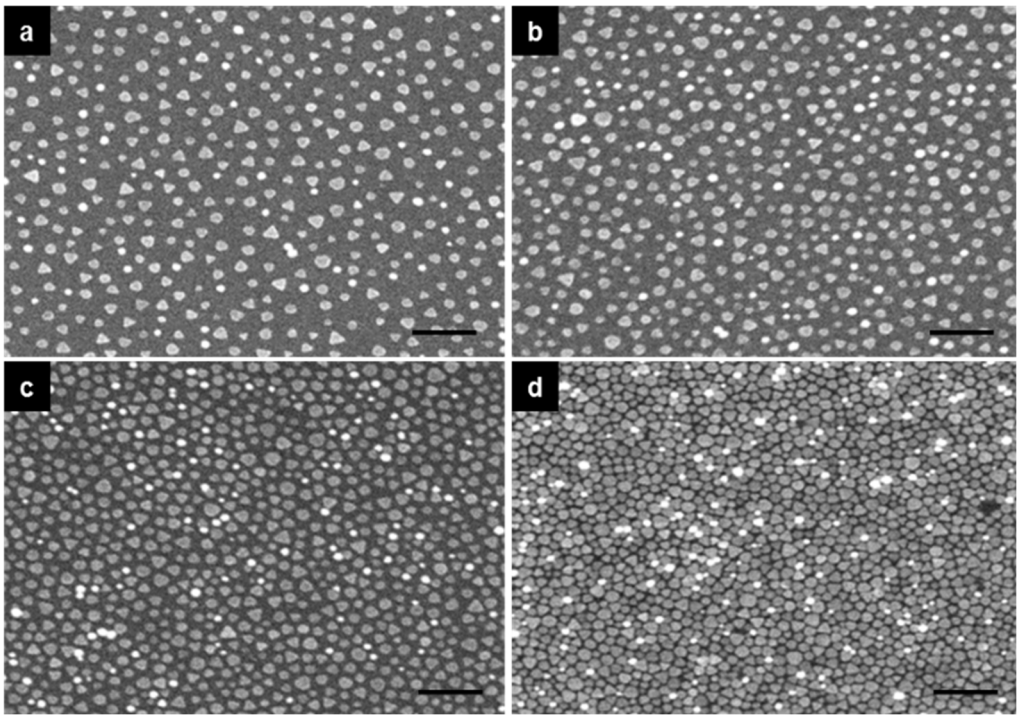

Figure 6.2: SEM images of AgND monolayers deposited at surface pressures of (a) 2, (b) 4, (c) 6, and (d) 16 mN/m. Scale bars are 250 nm.

liquid condensed phases or between the liquid expanded and gaseous phases.[320] Therefore, aggregate S-Lc and Le-G phases were defined for the purposes of this study.

The corresponding UV-Vis spectra show that between 0 and 6 mN/m, the LSPR peak position incrementally shifts 22 nm from 644 nm to 666 nm (**Figure 6.3**). From 6 to 16 mN/m, the LSPR peak shifts an additional 104 nm, from 666 nm to 770 nm. This behavior is well understood and can be attributed to the increased plasmonic coupling interactions that result in red shifted bonding modes in the AgND monolayer as the surface pressure is increased and as the distance between the AgNDs is decreased significantly.[63, 99] In the S-Lc phase, the LSPR peak rapidly changes with the surface pressure as AgND coupling interactions begin to dominate. This rapid transition in the S-Lc phase occurs with the

correlated interparticle gap spacing further decreasing from 16 nm to 2 nm as determined from the SEM measurements mentioned previously (**Figure 6.2**).

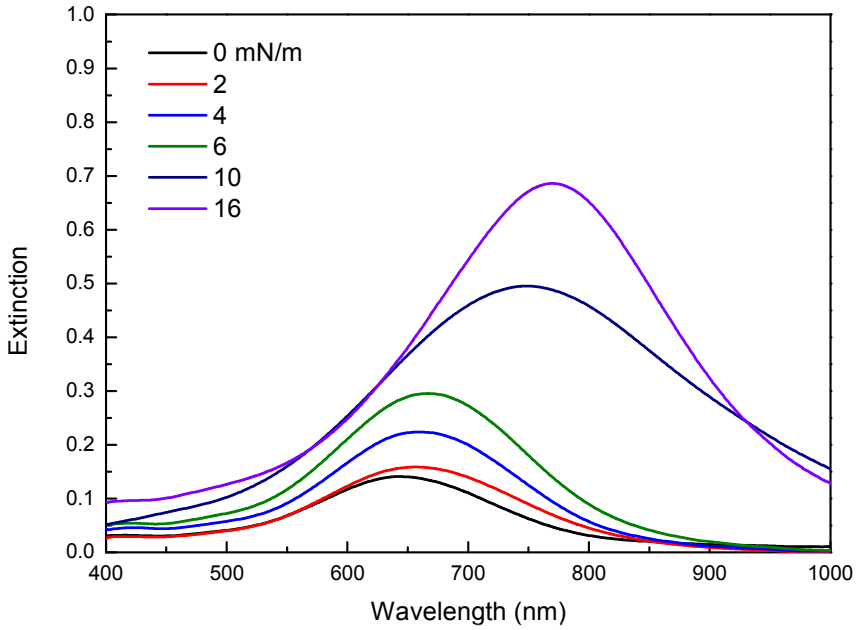

Figure 6.3: UV-Vis spectra of AgND monolayers deposited in a compressed manner on ITO substrates.

In order to confirm experimental observations and view approximate electromagnetic field distributions, FDTD simulations were conducted by approximating the packing of the AgND monolayers as a periodic 2D centered rectangular lattice comprised solely of circular disks (**Figure 6.4a**). Furthermore, for each surface pressure, the corresponding surface coverage of the AgNDs was measured and used to calculate the average interparticle distances, which were used to construct the lattice. Finally, the extinction curves of the periodic lattices were scaled by a normalization factor to account for their different lattice areas. The simulated peak positions agree well with the experimental

spectra, despite a slight blue shift of approximately 10 nm in all spectra; this observation can most likely be attributed to the unrealistic periodic lattice structure and homogeneous shape of the simulated AgNDs, as experimental nanoparticle packings are random in nature and the shape of the nanoparticle can vary. For instance, the simulated monolayer fabricated at 0 mN/m has a centroid-to-centroid distance of about 100 nm compared to the experimentally lower 94 nm. Electromagnetic field monitors at the peak wavelengths of the simulated 2, 6, and 16 mN/m samples confirm that the LSPR red shift can indeed be attributed to the increased coupling between adjacent AgNDs (**Figure 6.4b, c, d**). Indeed, no coupling is seen for the simulated 2 mN/m monolayer with an interparticle spacing of 100 nm, as seen by the monomer-like electric field intensity distributions that are confined around the individual AgNDs.

Interestingly, the simulated 6 mN/m monolayer's peak electromagnetic field intensity is actually lower than that of the 2 mN/m despite an apparent increase in coupling and an associated decrease in the interparticle spacing. This decrease in electric field intensity may possibly be due to a diffuse and delocalized coupling behavior that may act to spatially distend the resonance, leading to weaker peak electric fields when compared with uncoupled AgNDs.[63] At 16 mN/m, the coupling between AgNDs is very prominent once again and leads to higher localized electric field intensities than those seen for the 6 mN/m case. However, it should be noted that this particular lattice facilitates hot spot formation between the center AgND and its surrounding neighbors. In reality, highly packed, random

AgND monolayers will have delocalized plasmons as well due to the collective increase in nearest neighbors, although the number of hot spots may certainly increase.[321]

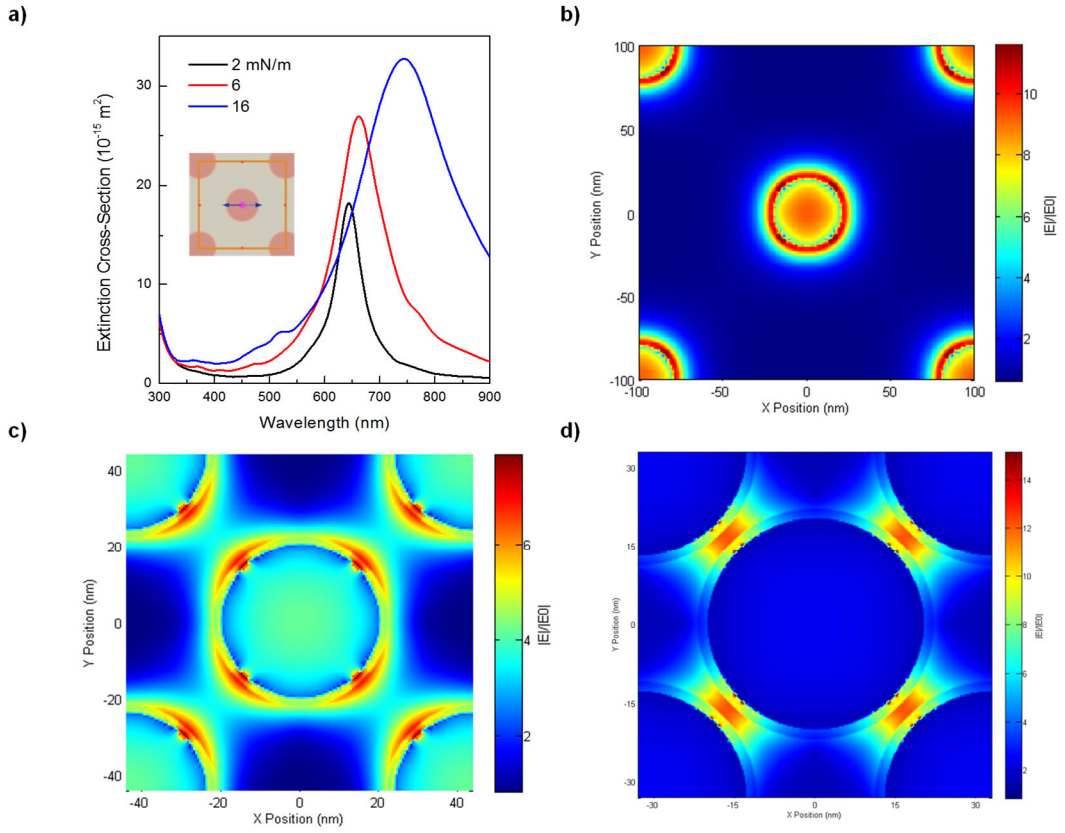

Figure 6.4: (a) FDTD-modeled UV-vis spectra of several surface coverages correlated with surface pressures. The inset depicts the simulated approximation of the disordered AgND packing with ordered cubic cells. LSPR peak E-field distributions are shown for surface pressures of (b) 2 mN/m, (c) 6 mN/m, and (d) 16 mN/m.

AgND monolayers were also deposited in a decompressed manner by reducing surface pressures from high (16 mN/m) to low (0 mN/m) in order to investigate potential AgND monolayer morphology differences after prior compression (**Figure 6.5**). To accomplish

this, AgND solution was dispersed on the water subphase and allowed to equilibrate for 10 min before the monolayer was then compressed to the high pressure of 16 mN/m. AgND monolayers were then deposited in the reverse order from 16 mN/m (S-LC phase) down to 0 mN/m (Le-G phase). Interestingly, although the UV-Vis spectra are similar to the previous compression spectra in linewidth and shape there are some notable differences (**Figure C.1**). The LSPR peak position is dramatically different for the two samples at different surface pressures in the Lc-Le and Le-G phases (**Figure 6.5**). At the lowest surface pressure of 0 mN/m, the difference in peak position is as high as 60 nm, while the 2 mN/m and 4 mN/m display respective LSPR differences of 25 and 18 nm. Samples in the S-Lc phase of the LB isotherm (6 mN/m, 10 mN/m, and 16 mN/m) display little change in peak position in contrast. A slight hysteresis effect can also be seen from the isotherm and surface coverage differences between the two types of LB deposition (**Figure C.2**).

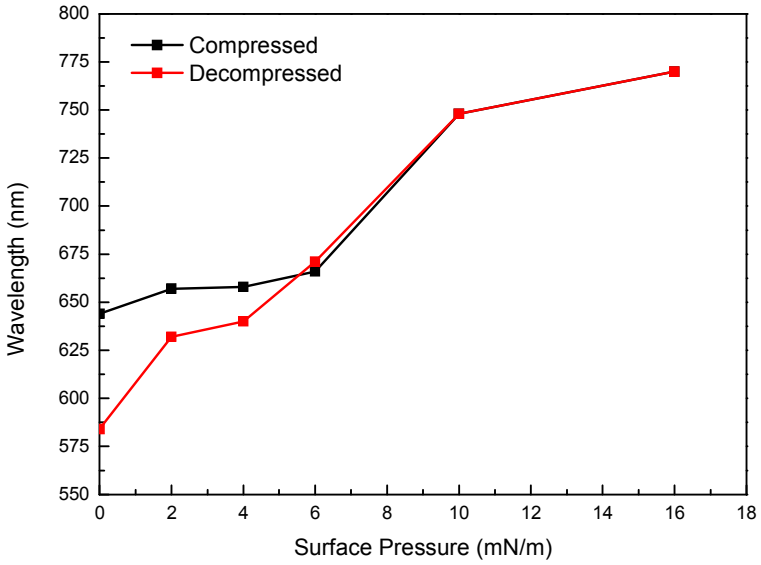

Figure 6.5: LB surface pressure versus LSPR peak wavelength for compressed and decompressed LB deposition of AgNDs.

SEM analysis of AgND monolayers fabricated at the same surface pressure reveal that the AgND size and shape is unaffected by the change in deposition method. Similarly, interparticle distances are also unaffected. Therefore, the excess PVP surfactant used in the nanoparticle synthesis that is also present in the monolayers must undergo a nonreversible morphological change upon reaching a high surface pressure during compression. It was also noted that the LSPR peak position of monolayer samples deposited in compression and decompression deposition modes remained unchanged even at low surface pressures if the surface pressure was not held constant at a high pressure for more than a few seconds, lending further support to the theory of a dynamic reconfiguration of a polymer.

Indeed, high-resolution AFM images reveal a significant change in the AgND-PVP monolayer topography between compressed and decompressed cycles (**Figure 6.6**). However, the bound capping layer around the nanoparticles appears unaffected itself by the method of the monolayer fabrication. The decompressed sample appears relatively pristine while the compressed sample is uniformly coated with excess PVP surfactant micelles, despite the solution being centrifuged and washed beforehand, which can be seen from both height and phase images. As known, PVP at a water interface above its critical molecular concentration may form disk micelles due to its hydrophilic pyrrolidone side

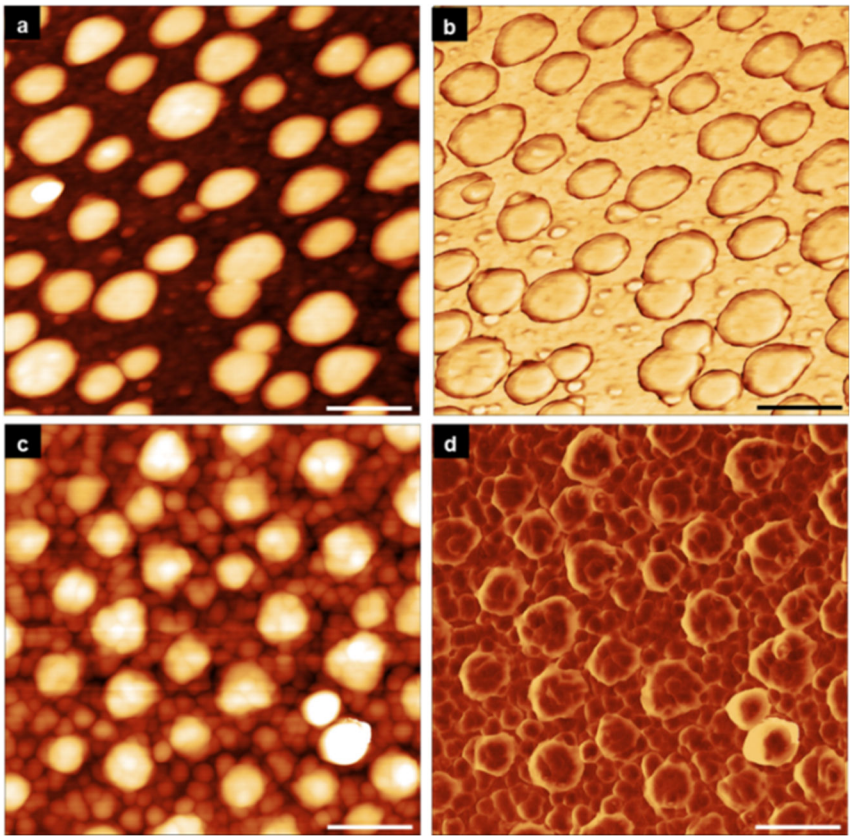

Figure 6.6: (a) The height and (b) phase of LB-decompressed AgNDs deposited at 2 mN/m. (c) The height and (d) the phase of LB-compressed AgNDs deposited at 2 mN/m. Scale bars are 100 nm and the Z-scale is 15 nm for (a) and (c).

group and its hydrophobic backbone.[322] Micelles are expected to be mostly uniform in size, as they are in **Figure 6.6**, which also confirms that the PVP is forming micelles and not aggregates. The clean AgNDs have an average height of 10.8 nm while the micelle-coated NDs have an average height of 13.4 nm (**Figure 6.7**). Thus, the micelles themselves have an average height of 3.8 nm, leading to the conclusion that micelles are only present on the top surfaces of the NDs. Approximating the micelles as cylinders with a height of 3.8 nm and a width between 10 and 20 nm based off AFM images suggests a small aggregation number of 5-15 PVP macromolecules per micelle. A cross-section of the

compressed monolayer sample was also conducted to eliminate the possibility of an underlying PVP layer as well (**Figure C.3**).

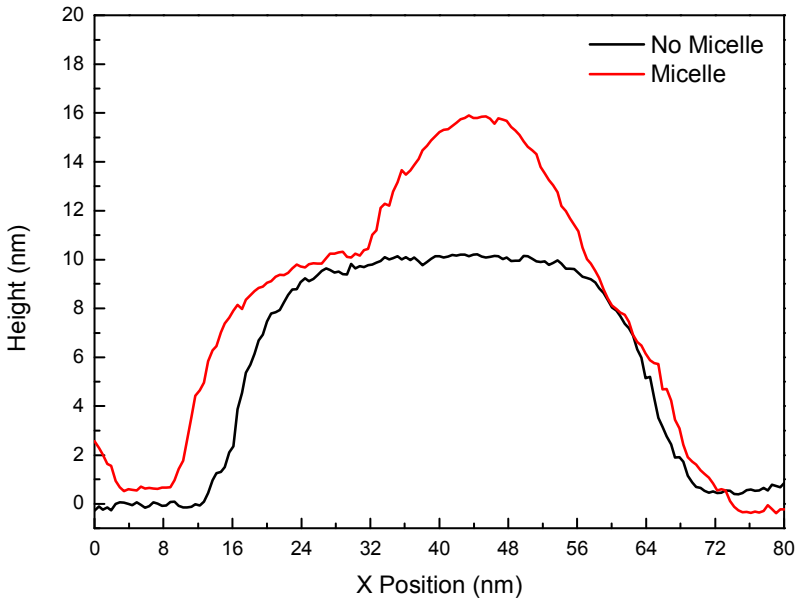

Figure 6.7: Cross-sections of individual AgNDs with and without micelles on the top surface (obtained from AFM images in Fig. S4).

We surmise that the free PVP micelles that are initially present using compressed deposition disappear as the surface pressure is increased to ~6 mN/m. This transformation can be explained by PVP depletion into the water subphase from the air-water interface as the surface pressure is increased as they have smaller surface areas and greater hydrophilicity than the AgNDs and consequently, a lower effective collapse pressure.[323] Monolayers deposited using decompression correspondingly contain fewer PVP micelles at both low and high surface pressures, as the micelles have already depleted into the subphase and are unrecoverable.

This depletion into the sub-phase most likely occurs in the start of the S-Lc regime, with little LSPR peak change evident for the 6, 10, and 16 mN/m samples between compressed and decompressed deposition methods. AFM images of samples at these surface pressures also reveal little difference in micelle morphology (**Figure C.4**). These micelles may ultimately act to screen nanoparticles from one another, as seen from the smaller wavelength shift of the LSPR at low surface pressures, and may adversely impact the sensing and switching properties of the AgNDs as well. Ultimately, micelles depleting into the sub-phase causes the composite medium's refractive index within the mixed monolayer to decrease. Indeed, PVP has a refractive index of ~1.42 while water's refractive index of 1.33 is lower. Thus, partial replacement of PVP with water might result in a decrease in the refractive index by 0.05-0.08. Such a change should cause a blue shift in the spectra accordingly.[324]

6.3.2 *P3HT films*

As the next step, a conjugated polymer, P3HT, was used as an electroactive component to modify the local refractive index around the AgND monolayers and the subsequent LSPR shifts in a reversible manner. As known, P3HT can be either reduced or oxidized by an applied electrical potential and thus, its absorption properties can be widely varied in a controlled manner. First, a P3HT film was spin-cast on ITO glass to visualize the change in extinction upon applying an oxidation-causing electric potential. Upon oxidation, the extinction can be seen to decrease below and increase above the isobestic point of approximately 635 nm (**Figure 6.8a**).

This change in extinction is indicative of a change in the complex refractive indices of the thin film, and changes in the real component, *n*, can be correlated with an LSPR shift of embedded plasmonic nanoparticles as seen by Equation **4**. Besides using an applied electric potential, chemical doping can also be used to oxidize electroactive polymers in a similar manner without the need for an electrochemical cell.[325] Although chemical doping is not practical for many applications, this technique can be used to more easily characterize electroactive polymer films using spectroscopic ellipsometry.

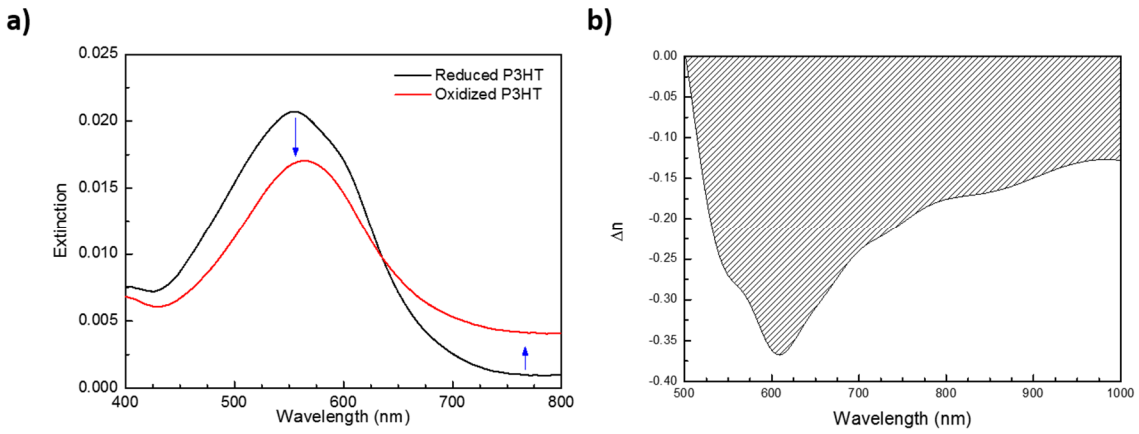

Figure 6.8: (a) Experimental extinction spectra for reduced and oxidized P3HT films. (b) *Δn* as a function of wavelength between the undoped and iodine-doped states of P3HT.

FDTD simulations of undoped and iodine-doped P3HT films using refractive index values from literature agree with the general trend of the experimental extinction spectra, although the change in extinction at higher wavelengths is significantly larger (**Figure C.5**).[326] This difference may indicate that the P3HT films in this study do not oxidize completely with

the voltage range being used to avoid damage (-500 mV to +500 mV) and under these fabrication conditions. Future studies may focus on nanoparticle-film systems that can use a wider range of voltages, as the AgNDs in this study oxidize at potentials above this range.

Because of the disagreement between literature and experimental extinction spectra, ellipsometry was used to determine refractive indices for undoped and partially iodine-doped P3HT thin films as well as Δn between them under our fabrication conditions (**Figure 6.8b**). The isobestic point for the partially iodine-doped P3HT films is at 605 nm while the electrochemically-switched films exhibit an isobestic point at 635 nm. This small variation is to be expected as iodine doping can only be used as an estimate for electrochemical switching behavior. Despite this difference, the absorption profiles are otherwise quite similar and give more accurate refractive indices than using fully-doped literature ones (**Figure C.6**). Observed change in Δn is negative for all LSPR wavelengths above 500 nm upon oxidation of the P3HT, meaning that the AgND monolayer LSPR should always blue shift with an applied potential after first being coated with P3HT. The largest Δn of -0.37 is located at approximately 610 nm and steadily decreases as the wavelength increases. Because Δn is not constant, the RIS of P3HT-coated AgND monolayers must be determined by normalizing the LSPR shifts to Δn at their respective LSPR peak wavelengths as seen by Equation **4**.

6.3.3 *Electrochemical switching of P3HT-coated silver nanodisk monolayers*

At the next stage, P3HT was spin-cast on top of the compressed AgND monolayers with an approximate 25 nm film thickness in order to ascertain the effects of plasmon coupling on the AgND monolayer LSPR modulation and RIS. P3HT without AgNDs was used as a background for the resulting UV-Vis spectra in order to eliminate the polymer absorption (**Figure 6.9**). Due to the different refractive index of P3HT from that of air for the uncoated monolayer, the LSPR peak red shifted 124, 116, 124, 122, and 82 nm for samples fabricated at 0, 2, 4, 6, and 16 mN/m. The significantly lower 82 nm shift of the 16 mN/m AgND monolayer cannot be solely attributed to the lower refractive index of the polymer at higher wavelengths, and this discrepancy will be discussed further in the following section. The presence of electrolyte solution is also seen to affect the LSPR wavelength of AgND monolayers. Bare AgND monolayers exhibit an LSPR red shift between air and electrolyte media due to the difference in refractive index. P3HT-coated AgND monolayer LSPRs,

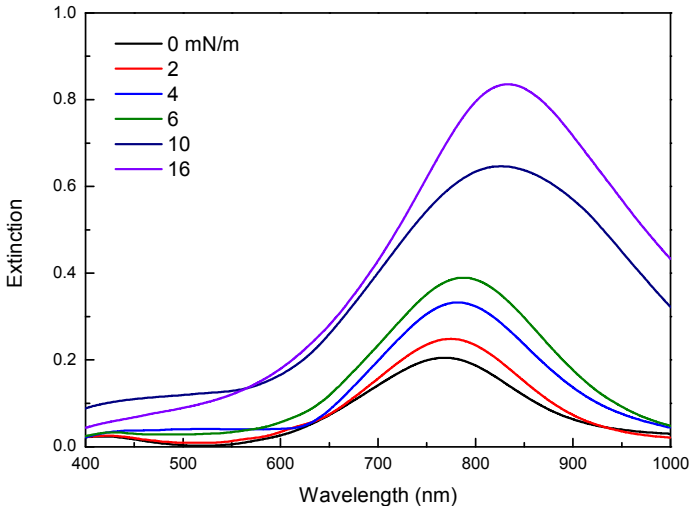

Figure 6.9: UV-Vis spectra of P3HT-coated AgND monolayers deposited in LB compression.

however, demonstrate a blue shift as the medium is switched from air to electrolyte; this observation is due to the P3HT swelling in solution and the resulting lower refractive index contribution of the electrolyte (**Figure C.7**).

P3HT was also deposited on the decompressed samples that displayed low polymer micelle concentrations (**Figure C.8**). As expected, the decompressed monolayers displayed larger shifts (approximately 15 nm) of the resonance peak after polymer deposition for surface pressures between 0 mN/m and 4 mN/m due to the free polymer micelles being removed (**Figure C.9**). At surface pressures of 6 mN/m and 16 mN/m, the LSPR shift is essentially the same for both the compressed and decompressed monolayers, lending further support to the suggestion that forced migration of the micelles into the water subphase occurs around the LB S-Lc phase transition during compression.

After P3HT deposition on AGND monolayer, a 500 mV electric potential was then applied to the mixed P3HT-coated AgND monolayers in order to oxidize the P3HT component and consequently change the effective medium refractive index. We suggest that the surfactant micelles seen in the compressed monolayer samples would result in a lower effective change Δn experienced by the mixed AgND monolayers as well as greater separation distances of the P3HT from the AgNDs, which would result in greater electric field decay and less optical sensitivity. These combined factors would cause a smaller LSPR shift for the compressed samples than for the uncompressed samples. Indeed, a decompressed monolayer sample fabricated at 4 mN/m demonstrated an initial 26 nm shift compared to a compressed sample's initial LSPR shift of 13 nm (**Figure C.10**). As a result, further LSPR switching experiments were focused solely on the decompressed samples.

In order to test the long-time electrochemical stability of the AgND monolayers, five electropotential cycles with an amplitude of ±500 mV were conducted for a decompressed AgND monolayer fabricated at 4 mN/m (**Figure 6.10**). As is apparent from the data, the changes are reversible, with the magnitude of the LSPR shift remaining approximately the same from 26 nm in the first cycle to 29 nm in the last cycle. However, the LSPR wavelength blue shifted overall roughly by 10 nm during the course of the cycling. This

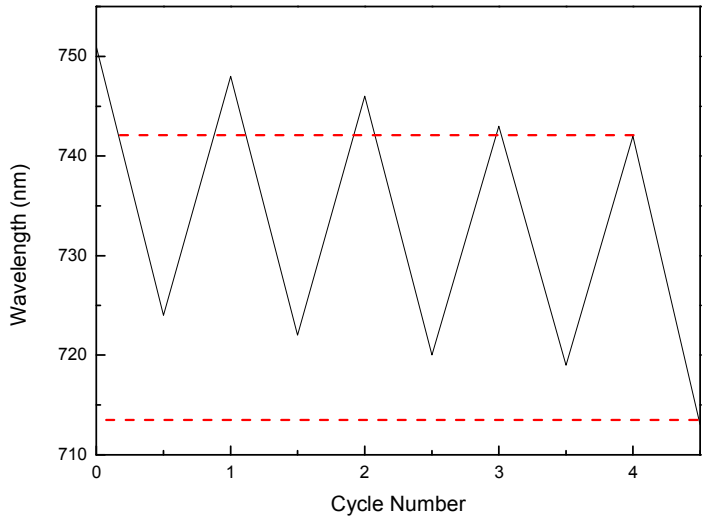

Figure 6.10: LSPR position changes of P3HT-coated AgNDs upon applying ±500 mV electric potential cycles. Dashed lines indicate final LSPR peak positions of the reduced and oxidized states.

shift can be attributed to an instability of the AgNDs, as higher voltages caused the AgND monolayer to dissolve. Since oxidation by itself of silver nanoparticles results in an LSPR red shift, the blue shift shown in **Figure 6.10** must be attributed to a change in the actual shape of the NDs.[327, 328] We suggest that the side walls of the AgNDs are prone to oxidative etching that results in the AgNDs becoming smaller and changing shape as an electropotential is maintained and cycles are repeated.[329] Indeed, ±500 mV

electrochemical cycles of just an AgND monolayer without a P3HT coating caused an even larger blue shift of 34 nm and a significant increase in the transverse LSPR peak intensity, thereby confirming our hypothesis (**Figure C.11**).

The average LSPR shift of P3HT-coated AgND monolayers fabricated at different LB surface pressures, with an additional monolayer deposited at 5 mN/m, can be seen in Fig. 11. The absolute LSPR shift increases with deposition surface pressure from 0 mN/m to 4 mN/m but drops from 4 mN/m to 6 mN/m before increasing slightly again at higher surface pressures. The highest LSPR shift was observed for the monolayer fabricated at 4 mN/m with a 27 nm LSPR shift. However, as Equation **4** shows, the AgND monolayer LSPR shift is directly proportional to Δn of the P3HT at the corresponding LSPR wavelengths. Normalizing the average LSPR peak shift of the P3HT-coated AgND monolayers to Δn of the P3HT between its reduced and oxidized states at the respective LSPR wavelengths reveals a similar trend of the RIS (**Figure 6.11**). The highest RIS of 141 nm/refractive index unit (RIU) was achieved at 4 mN/m while the lower of 90 nm/RIU was seen for the monolayer deposited at 6 mN/m. Similar to the LSPR shift, the RIS shows a sharp decrease between 4 mN/m and 6 mN/m.

Considering that individual AgNDs in the Le-G phase of the LB isotherm (0 mN/m and 2 mN/m) are very distant from one another (approximately 2-3 times the diameter of a single AgND), the coupling interactions are negligible. As the surface coverage of the AgNDs is increased, hot spots appear more frequently due to nanoparticle proximity that cause a corresponding increase in the RIS and LSPR shift in the Lc-Le phase (4 mN/m). The onset of the S-Lc phase of the isotherm (5, 6, 10, and 16 mN/m) was shown to result in a drastic decrease in the LSPR shift and RIS of the AgND monolayers; this phenomenon can be

attributed to the onset of delocalized plasmon formation.[63, 330, 331] The occurrence of delocalized plasmons in the AgND monolayer causes a broader continuum of plasmon modes to exist, meaning less energy is concentrated at the LSPR peak (larger full-width half-maximum).

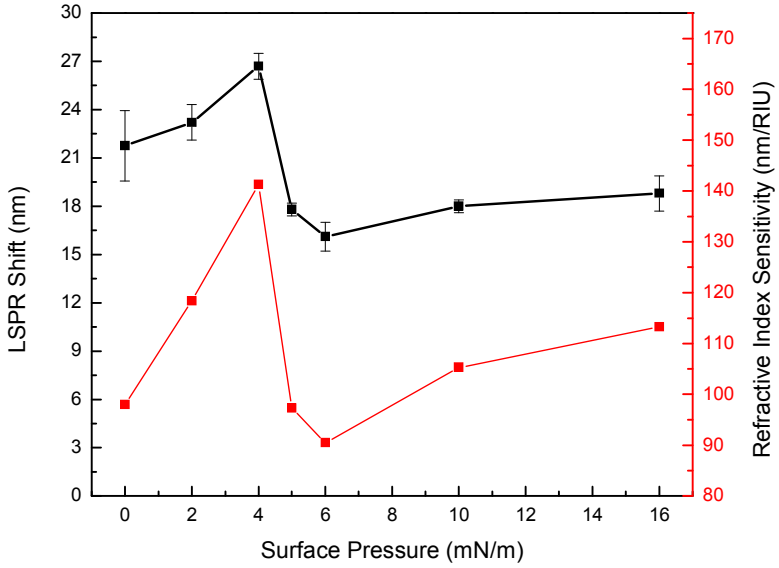

Figure 6.11: The electrochemically modulated LSPR shift (black) and RIS (red) of P3HT-coated AgND monolayers fabricated at various surface pressures.

Second, as illustrated in **Figure 6.4c**, a specific wavelength mode is less spatially confined and more film-like in nature, which correlates with a decrease in sensitivity. This behavior also accounts for the previously observed lower LSPR shift of the AgND monolayer deposited at 16 mN/m after being coated with P3HT layer. It should once again be noted that while **Figure 6.4d** exhibits well-defined hot spots for the 16 mN/m approximated surface coverage, this feature can almost certainly be attributed to the perfect periodic lattice structure of the simulation. In reality, the close-packed AgNDs are non-periodic in

nature and exhibit more diffusive plasmon behavior than what is shown in simulations. The higher LSPR shift at 16 mN/ compared to that at 6 mN/m however can be attributed to an increased number of hot spots, although the delocalized plasmon interactions still dominate when compared to monolayers deposited at lower surface pressures. Ultimately, it is shown that for an AgND monolayer, the best RIS can be obtained in the densely packed Lc-Le region of the isotherm due to an increased number of hot spots while simultaneously avoiding the occurrence of delocalized plasmons.

6.4 Conclusions

In summary, the optical properties of LB AgND monolayers were correlated with the LB isotherm phase and monolayer deposition method. The LSPR peak red shifted significantly as the LB surface pressure was increased due to an increase in plasmon coupling interactions as suggested by FDTD simulations. Differences in LSPR peak wavelengths were seen for AgND monolayers fabricated in the Le-G and Lc-Le phases depending on if they were deposited in decompression or compression. The LSPR shift of the monolayer was shown to have a strong dependence on how the monolayers were deposited. It was revealed that coupling between nanoparticles leads to higher refractive index sensitivity at intermediate nanodisk densities due to an increased number of hot spots and lower sensitivity at high nanodisk densities due to plasmon delocalization.

Ultimately, we demonstrated ultrathin and electroactive plasmonic nanoparticle-conjugated polymer monolayers for reversible LSPR modulation by both variation in surface pressure and by applying the electrical potential. Based upon these results, we suggest that the fabrication of mixed noble metal nanostructures monolayers with an

increased number of hot spots while avoiding delocalized plasmon formation may be accomplished through a polymer-nanoparticle morphology mediated by polymer micelles formation and the level of doping of the polymer component.

CHAPTER 7. LIGHT-RESPONSIVE PLASMONIC ARRAYS CONSISTING OF SILVER NANOCUBES AND A PHOTOISOMERIZABLE MATRIX

7.1 Introduction

By changing the refractive index of the dielectric environment surrounding the nanoparticle, it is possible to modulate the plasmonic characteristics, which opens up the possibility of fabricating active plasmonic devices with real-time responses.[269, 332] The most promising approach for creating a variable-refractive-index environment is the use of stimuli-responsive polymeric materials.[333] For instance, the transition between the hydrophilic swollen state and hydrophobic collapsed state of polymers such as poly(*N*-isopropylacrylamide) (PNIPAM) upon heating and cooling across the lower critical solution temperature (LCST) results in a change in the local refractive index of the polymer matrix.[304, 334-338] Furthermore, refractive index changes can be observed in pH-responsive polymers such as poly(acrylic acid) (PAA), poly(2-vinylpyridine) (P2VP), and poly(methacrylic acid) (PMAA).[301, 339] With pH-responsive polymers, the LSPR shift and damping can be controlled by both the alteration of interparticle distance, and hence coupling, and the change in the refractive index as the polymer matrix swells in response to protonation or deprotonation.[306, 340] Electrochromism of organic molecules and polymers induced by both chemical and electrochemical redox stimuli can also change the refractive index environment.[269, 295, 305]

A combination of responsive materials with plasmonically active nanostructures can be used to control light conversion.[341-345] For instance, liquid crystal matrices allow for the tuning of the dielectric environment around noble-metal nanostructures as the light-induced isotropic-to-nematic phase transition occurs.[302, 346] Azobenzene-based materials can also be used as an active medium with a changeable refractive index for noble-metal nanostructures.[347-349] The photoswitching of the LSPR of gold and silver nanostructures was recently demonstrated using self-assembled monolayers (SAMs) deposited on gold nanostructures.[350, 351] In particular, an extremely small LSPR shift of 0.04 nm was observed upon the trans–cis photoisomerization of simple azobenzenes with a propylene spacer.[352] Another report showed that an azobenzene SAM on gold nanoprisms induced up to a 21 nm LSPR shift upon trans–cis isomerization of the SAM.[353] It should be noted that both reports utilized gold nanostructures with an LSPR far from the π–π^* and n–π^* absorption bands of azobenzenes. Furthermore, SAM-based systems are often unpredictable and can depend strongly on monolayer packing and preparation conditions.[354] In photochromic materials, the change in refractive index stems from the change in electronic distribution and, hence, the molecular polarizability.[355]

Some reports have clearly demonstrated that the refractive index variation during photoisomerization is highest near the absorption wavelength of a photochromic material. For instance, Nishi et al. employed photochromic diarylethene polymer coatings on gold nanoparticles to induce changes in LSPR peak position and magnitude.[356] Baudrion et al. used a spiropyran molecule in its monomeric form to create a variable-refractive-index medium.[357] By varying the diameter of the nanoparticles, they were able to achieve strong coupling between the surface plasmon and the excited state of an organic molecule,

resulting in a large plasmonic response. Finally, our group recently established reversible LSPR switching using electrochromic polymers driven by a substantial refractive index change that accompanied a colored-to-transmissive transition.[269] Despite significant progress, issues in achieving stable and reproducible plasmonic modulation remain. For instance, the use of electrochromic active matrixes requires metal structures with high oxidative stability, and many photochromic systems lack chemical and thermal stability.[358, 359]

Here, we report on the fabrication of light-responsive AgNC arrays embedded in a photoactive medium based on newly synthesized branched azobenzene-modified polyhedral oligomeric silsesquioxanes (POSS), Azo-POSS, that are able to form uniform, stable, ultrathin films and have an absorption peak overlapping with the LSPR of AgNCs (**Figure 7.1**). This design induces LSPR modulation through the high refractive change of azobenzene in its trans and cis states in the wavelength range of 350–500 nm that is easily measurable with conventional spectrophotometers.

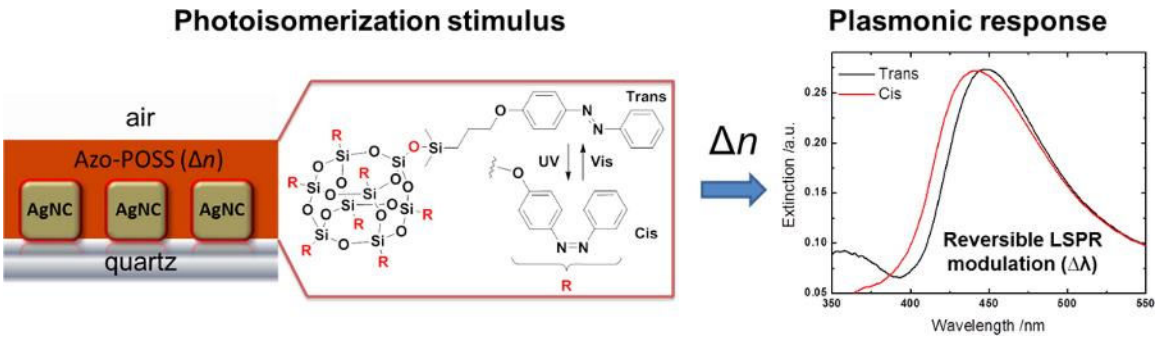

Figure 7.1: Branched Azo-POSS conjugates as a variable-refractive-index matrix for plasmonic nanoparticles.

Furthermore, we investigated the properties of these hybrid materials in search of an optimal molecular structure with the highest photoinitiated changes. We found that the Azo-POSS branched conjugate with a short spacer between the core and the dye branches has a larger refractive index variation than azobenzene dye embedded in a PMMA matrix. Most importantly, we observed a stable and reversible LSPR switching upon alternating irradiation of the coating with UV and visible light. The experimental results are supported by FDTD simulations. Finally, the observation of reflectance in TIR experiments under polarized light revealed the polarization-dependent LSPR modulation of embedded AgNCs. We suggest that the design of an active plasmonic array reported here can be further extended to include azobenzene analogues covering the entire visible spectrum for applications in stable, tunable optical materials.

7.2 Experimental Details

UV-Vis optical spectroscopy: Peak picking was performed using the OriginLab Origin 8.5 built-in peak analyzer tool (20-point local maximum). Photoisomerization experiments were performed by irradiating the samples at a 10-cm distance with 365-nm unpolarized UV light from a Blak-Ray model B-100A UV lamp (100 W) and then recording the absorbance spectra. Visible light irradiation for the reverse isomerization was conducted with unpolarized light from a 26-W compact fluorescent lamp. For kinetics measurements, the quartz cuvette containing the sample was irradiated with 365-nm UV light, and the absorption spectrum was recorded every 10 seconds. The experiment was performed in triplicate.

Film preparation: Compounds **1** and **2** in toluene (2 wt %) were filtered through a filter with a mesh size of 200 nm before spin-coating, and the films were dried in ambient conditions before measurements. The AB-PMMA thin films where the dye was not tethered to a POSS core were prepared by spin-coating from an 8 wt % solution of AB-PMMA (3:5, w/w) in anisole under the same conditions. The resulting film had a thickness of 210 nm as determined by spectroscopic ellipsometry.

Ellipsometry: The Azo-POSS layers were fit with a three-layer model consisting of a silicon substrate, a silicon oxide layer (2-nm layer thickness), and a Cauchy layer [mean squared error (MSE) < 4] in the range from 550 to 1000 nm. The complex refractive index was then determined by point-by-point fitting over the entire spectral range.

Total internal reflection: TIR measurements for the AgNC films were conducted with the spectroscopic ellipsometer in reflection mode over a wavelength range of 300–1000 nm using both s- and p-polarized light at an incident angle of 50° with a spectral resolution of 1.59 nm. The spectra were smoothed using a seven-point fast Fourier transform (FFT) filter (OriginLab Origin 8.5). For TIR, we employed a CaF_2 prism (25 mm base, right angle, uncoated, from Thorlabs). A single drop of diethylene glycol was applied to the bottom of the prism as immersion oil where the opposite (uncoated) side of the nanocube and Azo-POSS-covered quartz slide made contact. Care was taken with proper coverage of immersion oil to ensure that no air gaps occurred at the prism–slide interface. The prism–oil–slide setup was mounted on the ellipsometer stage with the AgNC coating facing down, making no contact with the stage. As a control, an uncoated quartz slide was measured for every polarization measurement.

FDTD simulations: Nine nanocubes were modeled in a "square" configuration with a 50-nm edge length, 25% edge rounding, and a 127-nm interparticle distance based on TEM and SEM analysis of a typical sample. The average nanocube edge length and edge rounding were determined using ImageJ software (**Figure D.2**). The interparticle distance was calculated using commercial SPIP image processing software. Multiple nanocubes were modeled to account for interparticle coupling between nanocubes and the resulting changes in their optical behavior. An 80-nm POSS layer was added using refractive index values imported from ellipsometry measurements for both the trans and cis isomers.

7.3 Results and Discussion

7.3.1 *Azobenzene-based hybrid materials*

Conjugation of azobenzenes to POSS results in hybrid materials with high thermal and photostability that are compatible with organic solvents for solution processing.[360-362] Indeed, it has been found that it is possible to obtain stable ultrathin films from Azo-POSS conjugates.[222, 363] Importantly, the reversible photoisomerization of azobenzene still occurs in such stable Azo-POSS films, enabling their applications in photoresponsive systems. The azobenzene conjugates, such as 4-phenylazophenol derivatives, have a relatively high energy barrier for cis-to-trans thermal relaxation, with cis isomer lifetimes on the order of days. This behavior can facilitate the examination of the material in different states. The rate of trans-to-cis photoisomerization of azobenzene in solution was found to depend only slightly on grafting to the POSS core.[360, 361] To elucidate the role of azobenzene conjugation, we utilized two AZO-POSS compounds, **1** and **2**, with different spacer lengths between the inorganic core and the azobenzene moiety (Figure 7.2). As is

known, the linker length (4 versus 10 methylene units) has a pronounced effect on thermal cis-to-trans relaxation.[362] Therefore, we synthesized two compounds: compound **1** with a

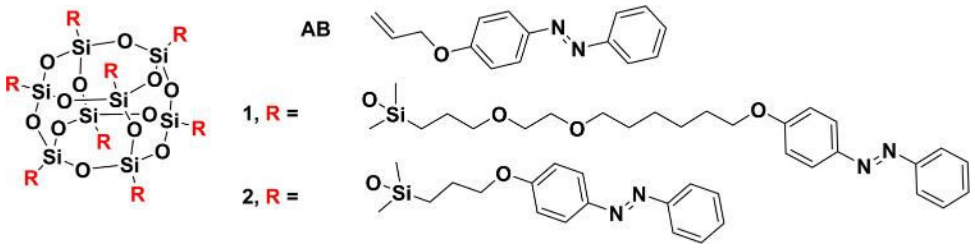

Figure 7.2: The Azo-POSS conjugates used in this study.

linker length between a Si atom of the POSS moiety and a benzene ring of 1.87 nm when fully extended and compound **2** with a linker length of 0.7 nm (estimated from Chem3D modeling). Furthermore, we employed a precursor azobenzene compound **AB** for comparison with Azo-POSS conjugates (Figure 7.2).

7.3.2 *Ultrathin films from Azo-POSS compounds*

Ultrathin films of compounds **1** and **2** can be spin-cast onto flat substrates from solutions in toluene or chloroform. A 2 wt % solution of compound **1** or **2** in toluene formed uniform films of 68 or 60 nm, respectively, when spin-cast at 3000 rpm (**Figure 7.3**).

Surface analysis using AFM revealed that compound **1** yielded a smooth film with a root-mean-square (RMS) roughness (Rq) of 1.3 nm (in a 10 μm × 10 μm selected surface area). Compound **2** under the same conditions gave a somewhat less uniform film with an increased microroughness of 5.5 nm (**Figure 7.3b**).

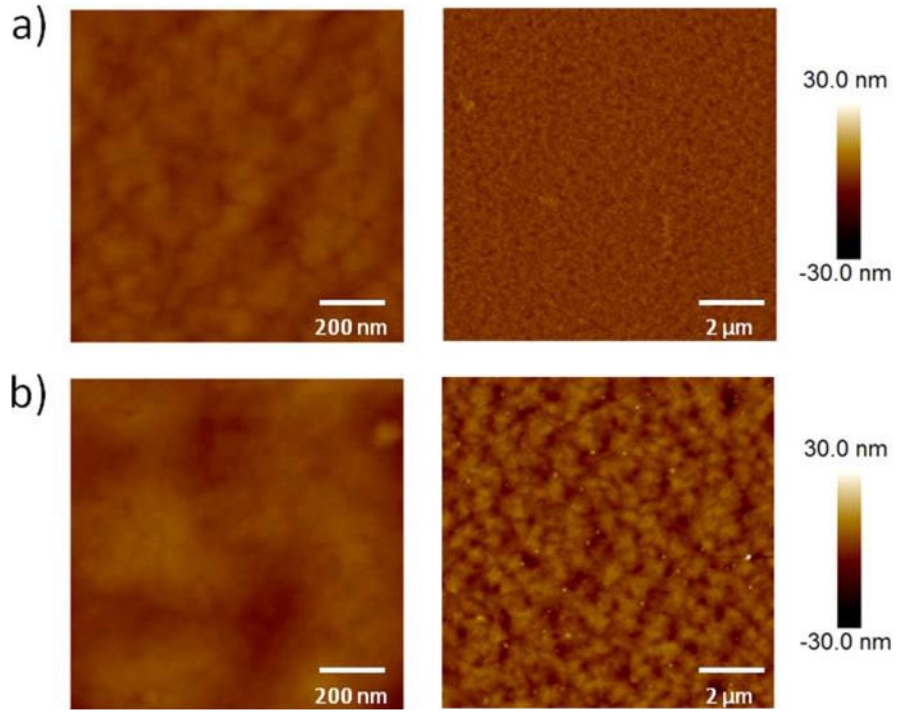

Figure 7.3: AFM topographical images of ultrathin films prepared by spin-casting (a) compound 1 and (b) compound 2 onto silicon substrates at different magnifications.

Although the UV–vis spectra of compounds **AB**, **1**, and **2** in chloroform solutions are very similar, thin-film absorption spectra reveal a striking difference between compounds **1** and **2** (**Figure 7.4**). The absorbance of compound **1** is weaker and blue-shifted (320 nm) compared to that of compound **2** despite the similar film thicknesses. Because of the sensitivity of the π–π* transition of azo dyes to aggregation, the hypsochromic shift might indicate the face-to-face stacking of planar *trans*-azobenzene moieties and formation of H-aggregates.[364] We suggest that the longer spacer between the POSS core and azobenzenes of compound **1** allows for more rotational freedom and, consequently, leads to favorable packing of the azobenzene moieties. The ability of POSS-containing compounds **1** and **2** to form ultrathin films makes it possible to accurately

determine the refractive indexes of the trans and cis isomers of these compounds for use as a photoactive layer.

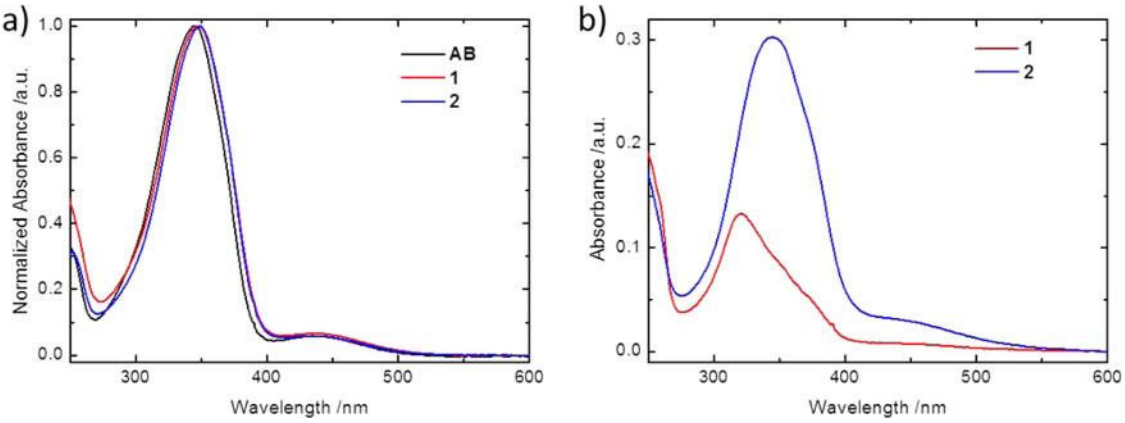

Figure 7.4: UV–vis absorbance spectra of (a) compounds AB, 1, and 2 in $CHCl_3$ (0.01 mg/mL) and (b) compounds 1 and 2 in thin films (thicknesses of 68 and 60 nm, respectively).

7.3.3 *Refractive index variation*

We first investigated the photoswitching behavior of compounds **1** and **2** in 0.01 mg/mL chloroform solutions by monitoring the decay of the π–π* transition of *trans*-azobenzene at 350 nm. The first-order rate constant of photoisomerization can be determined from the slope of a plot of $\ln[(A_0 - A_\infty)/(A_t - A_\infty)]$ versus time, where A_0, A_∞, and A_t are the absorbances before irradiation, after reaching a photostationary state, and at a given time t, respectively.[365] The photoisomerization experiment was performed in triplicate for each sample, and the averaged data points and linear fits are presented in **Figure D.3c**. We found that compounds **1** and **2** had similar photoisomerization rates in chloroform solution: 0.192 ± 0.054 and 0.186 ± 0.029 s^{-1}, respectively (**Figure D.3**).[222]

This difference indicates that the spacer length between the POSS core and the azobenzene moiety of compound **2** is already sufficient for unrestricted photoisomerization of the azobenzene arms in solution. A further increase in linker length in compound **1**, therefore, has only a small effect on the rate of photoisomerization in solution. In contrast, when the film of compound **1** was irradiated with an unpolarized 365-nm UV light, virtually no change in absorbance was observed. The thin film of compound **2**, however, exhibited a pronounced change in intensity of the π–π* transition at 350 nm, indicating efficient trans-to-cis isomerization (**Figure D.3e**).[222] We therefore focused on compound **2** as a variable-refractive-index medium for subsequent studies.

A study of film morphology during photoisomerization showed that the as-spun film of compound **2** had a roughened surface with crystalline domains clearly visible in an AFM phase image (**Figure D.4a**). However, after UV irradiation, the film surface became extremely smooth without any visible phase contrast (**Figure D.4b**). This observation can be explained by the tendency of linear-shaped *trans*-azobenzene to crystallize and the nonplanar cis isomer to have less favorable packing, resulting in a smooth thin film. The thin film of **2** returned to its initial roughened state after cis-to-trans thermal relaxation in the dark for several days. However, the cis–trans photoisomerization upon alternating UV/vis irradiation did not affect the thin-film morphology (**Figure D.4c**). To exclude the effect of film morphology, all subsequent experiments were conducted after the ultrathin film of compound **2** was subjected to one UV/Vis irradiation cycle. Also, the overall thickness of azobenzene-containing thin films was reported to change on the order of 1–2% in some cases.[366] In our experiments, we observed that the thickness of films of **2** determined by spectroscopic ellipsometry did not change upon photoisomerization.

To compare the performance of the Azo-POSS material to azobenzene-doped polymer films, we considered films in which a PMMA matrix was mixed with the precursor compound **AB** in the highest possible ratio of 3:5 (henceforth AB-PMMA). We used thin films of compound **2** and AB-PMMA to obtain the real part of the complex refractive index. In a typical experiment, the sample was irradiated for 5 min at 365 nm to achieve trans-to-cis photoisomerization and then for 5 min with white light for reverse isomerization. The refractive indices of the composites were obtained by fitting the reference data for the imaginary part of the refractive index with five (cis form) or six (trans form) Gaussian oscillators followed by a Kramers–Kronig transformation (**Figure 7.5**).

Analysis of the dispersion curves revealed that a notable change in refractive index occurred in the spectral window from 250 to 500 nm for compound **2** and AB-PMMA films. The refractive index difference (Δn) between the trans and cis forms of azobenzene-containing materials is defined as $\Delta n(\lambda) = n_{cis}(\lambda) - n_{trans}(\lambda)$. The largest change was found to occur at 380 nm and equaled −0.17 refractive index units (RIU) for compound **2** and −0.13 RIU for the AB-PMMA film upon trans-to-cis isomerization. These values compare favorably with the literature data for other chromic compounds.[295, 357, 367] The photochromic spiropyran has the highest refractive index variation at approximately 500 nm (−0.06 RIU) and 610 nm (from +0.16 to +0.19 RIU depending on the dye doping level).

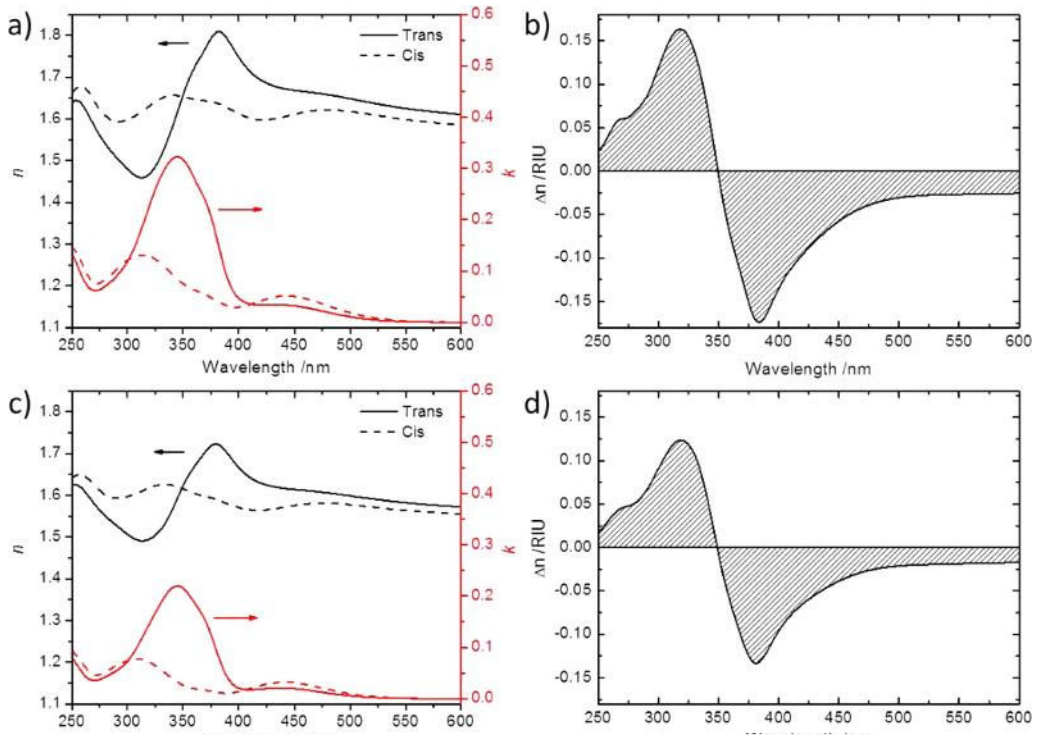

Figure 7.5: (a) Dispersion curves for thin films of compound 2 in trans and cis forms. (b) Refractive index difference between the trans and cis forms in a thin film of compound 2. (c) Dispersion curves for thin films of AB-PMMA in trans and cis forms. (d) Refractive index difference between the trans and cis forms in a thin film of AB-PMMA.

The electrochromic bistable rotaxane system provides a change of +0.011 RIU at 690 nm and −0.017 RIU at 970 nm.

Therefore, the Azo-POSS photochromes investigated in this study complement the existing active matrixes in the 350–500 nm spectral window where the plasmon resonances of individual AgNCs are located. The larger refractive index variation for compound **2** compared to AB-PMMA can be explained by a higher functional group density. Indeed, compound **2** has a POSS core-to-azo dye ratio of 1:1.7, whereas AB-PMMA has a ratio of 1:0.6 (as determined by solution concentration). The extinction coefficients measured in thin films, however, are similar: 0.32 for compound **2** compared

to 0.22 for AB-PMMA film. It should be noted that an azobenzene-to-polymer weight ratio higher than 3:5 resulted in phase separation in AB-PMMA films. Because of the higher photoinduced refractive index variation of Azo-POSS compound **2** compared to the AB-PMMA, the Azo-POSS compound is promising as an active medium to induce the variation in plasmon resonances of noble-metal nanoparticles in response to UV irradiation of a photoswitchable matrix.

7.3.4 *AgNC-(Azo-POSS) ultrathin coatings*

AgNCs with a 50-nm edge length were transferred onto pre-cleaned quartz and silicon substrates using the Langmuir–Blodgett (LB) technique and formed densely packed monolayers (**Figure 7.6a, b**).[219, 321] The relatively low surface pressure during monolayer transfer resulted in well-separated AgNCs with minimal aggregation. The average interparticle distance was estimated to be 127±30 nm based on SEM image analysis.

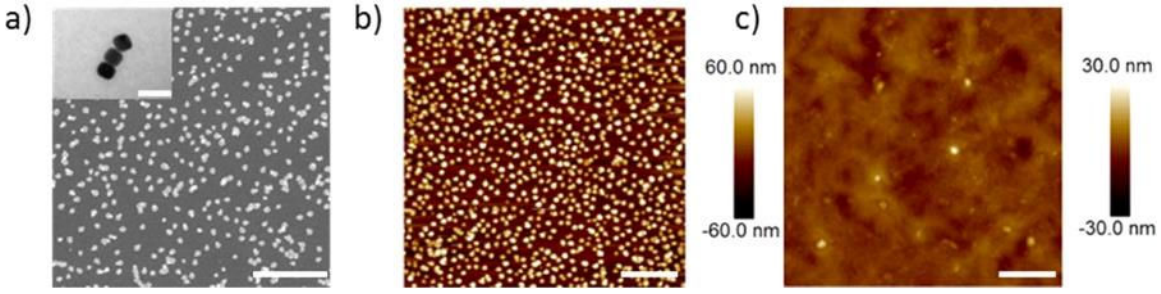

Figure 7.6: (a) SEM image of AgNCs on a silicon substrate prepared by LB deposition. The inset shows a TEM image of AgNCs (scale bar is 100 nm). AFM topographical images (5×5 μm^2) of (b) AgNCs on a quartz slide deposited by LB deposition and (c) composite material composed of a AgNC monolayer covered with compound 2. The scale bar is 1 μm for all images.

Next, a solution of compound **2** in toluene (2 wt %) was directly spin-cast on top of the LB monolayer at 3000 rpm. Using AFM cross-section analysis, we established that the total thickness of the composite was 80 nm (**Figure D.5**). The Rq value of the film was 2.7 nm, which is similar to that of the ultrathin film of Azo-POSS. Compound **2** covered all surfaces of the AgNCs completely for maximum exposure to active material (**Figure 7.6c**).

The extinction spectra of the AgNCs are presented in **Figure 7.7**. The LSPR position is located at 430 nm in water and shifts to 446 nm after the transfer to chloroform (see **Experimental Details**). This change is due to the higher refractive index of chloroform (n_{500} = 1.449) compared to water (n_{500} = 1.335) and possibly minor cube-edge rounding during the solvent exchange procedure. Upon the LB deposition of the AgNC monolayer onto the quartz substrate, the LSPR peak splits into antibonding (373 nm) and bonding (398 nm) modes because of the high refractive index of the quartz substrate (n = 1.46 at a wavelength of 400 nm).[262]

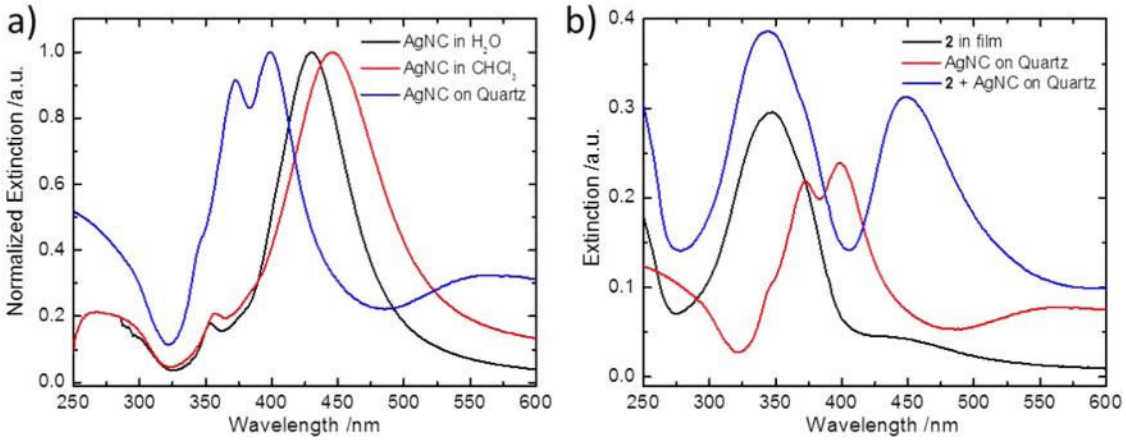

Figure 7.7: UV–Vis spectra of (a) AgNCs in H_2O and $CHCl_3$ and after deposition on quartz and (b) an AgNC monolayer on quartz coated with a thin layer of compound 2. In (b), the spectra of compound 2 and AgNCs on quartz are provided for reference.

After deposition of a high-index material (compound **2**) on top of and around the AgNC monolayer, the LSPR position red-shifted to 445 nm, and the peak splitting disappeared because of the similar refractive indices of the substrate and the active composite layer (**Figure 7.7b**). Despite the LSPR of the composite material being shifted from the wavelength of maximum refractive index variation (380 nm), the −0.06 refractive index unit (RIU) change at 445 nm should lead to a significant LSPR modulation, as discussed below.

7.3.5 *Photoinduced LSPR shifting*

AgNCs coated with compound **2** showed a 4-nm hypsochromic shift of the LSPR peak from 443 nm when the surrounding Azo-POSS was irradiated with 365-nm light (**Figure 7.8a**). Upon exposure to visible light (>450 nm), the LSPR peak returned to its initial position, demonstrating the reversibility of the photoinitiated process. To eliminate the overlap from the changing azobenzene absorption, the corresponding spectra of the film of compound **2** were subtracted from those of the coated nanocube monolayer, thus increasing the apparent shift to 6 nm (**Figure 7.8b**).

The LSPR shift can be explained based on exact measurements of the change in refractive index (Δn) upon photoisomerization of compound **2** and the refractive index sensitivity of AgNCs. The refractive index change of compound **2** at a particular wavelength can be found from **Figure 7.5a** and equals 0.06 RIU at 445 nm (LSPR wavelength). The refractive index sensitivity ($RIS = \Delta\lambda_{LSPR}/\Delta n$) is a measure of the change in plasmonic wavelength in response to the refractive index of the surrounding medium. The RIS depends on

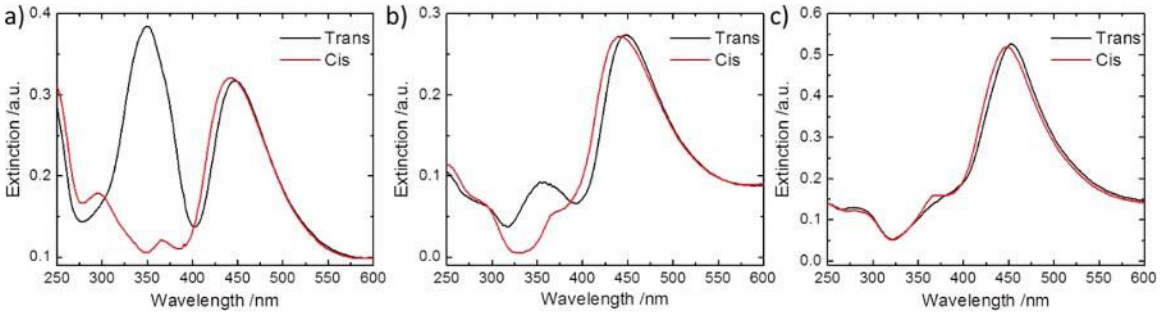

Figure 7.8: UV–Vis spectra of (a) AgNCs coated with compound 2 after UV irradiation (cis) and visible light irradiation (trans). (b) AgNCs coated with compound 2 after UV irradiation (cis) and visible light irradiation (trans) normalized to the corresponding spectra of the compound 2 film. (c) AgNCs coated with an AB-PMMA layer after UV irradiation (cis) and visible light irradiation (trans) normalized to the corresponding spectra of the AB-PMMA layer.

multiple factors such as the nanoparticle material and shape, nature of the substrate, size, edge rounding, and interparticle distance.[265, 368] Furthermore, the change in LSPR wavelength of AgNCs has a linear dependence on the refractive index: a decrease in the surrounding refractive index results in a reduction of the LSPR wavelength (blue shift).[369] The refractive index sensitivity of 65 nm AgNCs on a quartz substrate was previously found to be 113 nm/RIU.[88]

Considering the above results, a 6.8-nm hypsochromic LSPR shift can be expected for the combination of materials components, which is close to the experimentally observed LSPR peak shift of 6 nm. The same sequence of estimations can be repeated for an AgNC array coated with AB-PMMA layer as an alternative variable-refractive-index material. In this case, because of the smaller change in refractive index of the dye–polymer material (−0.05 RIU at 445 nm), a lower LSPR shift should be and was observed (5 nm) than for the composite layer based upon compound **2** (**Figure 7.8c**). Therefore, the higher photoinduced refractive index variation of branched compound **2** with a weight fraction of

grafted azobenzene arms and the ease of the robust ultrathin coating fabrication make such hybrid materials promising for applications in photoresponsive plasmonic coatings.

The experimental findings were further confirmed by FDTD simulations (**Figure 7.9a**). AgNCs were modeled with a 50 nm edge length and 25% edge rounding based on TEM analysis (see the **Experimental Details**). A blue shift of 6 nm was observed in the LSPR peak due to refractive index changes of the surrounding material as a result of trans–cis isomerization. It should be noted that the simulated nanocube extinction peak was red-shifted by 20 nm from the experimental findings, most likely because of the monodispersity and perfect periodicity of the FDTD model.

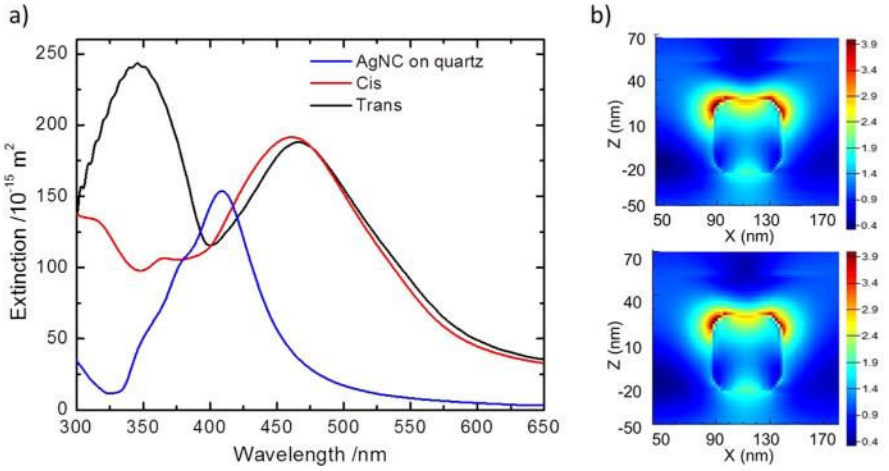

Figure 7.9: (a) Simulated spectra of AgNCs on quartz coated with compound 2 after UV irradiation (cis) and visible light irradiation (trans). (b) Simulated electric field intensity distribution for an individual AgNC embedded in compound 2 in trans (top) and cis (bottom) states. The scale bars are in units of E/E_0.

The electric field intensity distributions of the nanocubes embedded in compound **2** for the trans and cis states exhibit relatively minor differences (**Figure 7.9b**). Although the plasmonic modes are oriented away from the substrate and would typically be classified as

antibonding modes, it should be noted that the direction of light propagation (from the bottom through the quartz substrate) causes this effect and that the observed modes are, in fact, bonding modes.[275, 370]

Next, we investigated the control over the LSPR modulation and cycling stability of ultrathin AgNC–Azo-POSS films. A plot of LSPR wavelength versus irradiation time is presented in **Figure 7.10a**. These data show that fine control of the ratio of trans and cis isomers in the ultrathin film of compound **2** can be achieved by varying the irradiation time. The upper curve is the LSPR position of the AgNCs, and the bottom curve is the extinction at 350 nm of the Azo-POSS matrix (π–π* transition of *trans*-azobenzene). It can be seen that the LSPR modulation follows the change in the trans-isomer fraction in the film of compound **2**. Therefore, it is possible to control the exact LSPR shift by changing the UV exposure time.

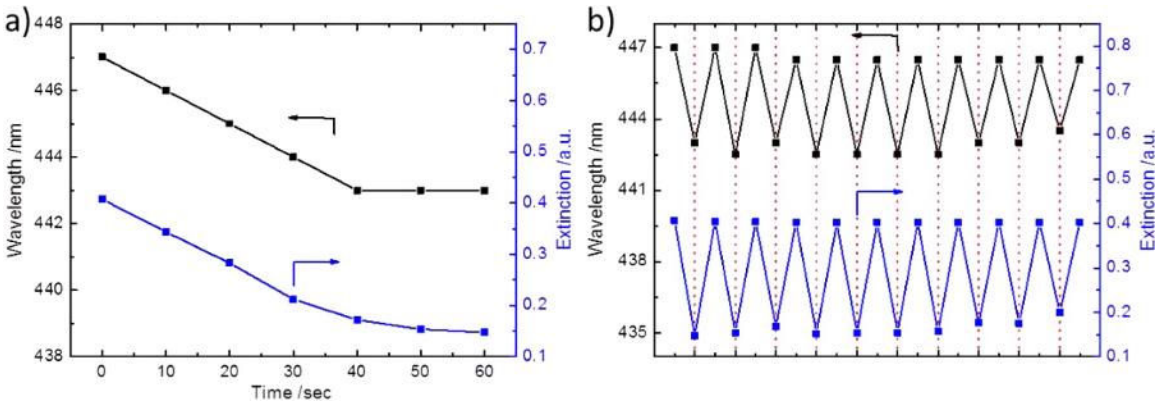

Figure 7.10: (a) Photoinitiated switching behavior of AgNCs coated with Azo-POSS compound 2. The upper curve is the LSPR position, whereas the bottom curve is the Azo-POSS absorbance at 350 nm. (b) LSPR peak position modulation upon exposure to 365-nm UV light over 10 UV/vis cycles. The dotted lines correspond to UV light exposure.

A stable switching of compound **2** is illustrated by the highly repeatable reduction and recovery of the *trans*-azobenzene absorption. Reproducible AgNC LSPR modulation was observed between 443 and 447 nm as the sample was alternately irradiated with UV and visible light (**Figure 7.10b**). The corresponding transmission spectra are provided in **Figure D.6**. The average plasmon resonance shift over 10 cycles was 3.8 ± 0.4 nm, with local deviations within 10%. Such stability arises from a strong adhesion of the LB monolayer of AgNCs to the quartz substrate and the photostability of ultrathin coatings of Azo-POSS compound **2**. Topographical images of the composite material obtained after multiple switching cycles show a relatively smooth morphology with an Rq value of 2.4 nm after UV irradiation and 2.5 nm after visible light irradiation (**Figure D.7**). Azobenzene-containing thin films can form surface relief gratings (SRGs) as a result of photoinduced molecular displacement when in close contact with metallic nanostructures.[370, 371] This aspect of the photoresponsive plasmonic system reported here will be investigated in due course.

7.3.6 *LSPR modulations in the TIR regime*

The placement of AgNCs as a monolayer at the surface of the quartz slide coated with a layer of compound **2** creates an anisotropic environment where the refractive index of the substrate (n_{450}=1.47) is lower than that of the active matrix (n_{450}=1.67). We considered that this index mismatch generates symmetry breaking and dipolar mode broadening similar to that observed for the quartz–air interphase (**Figure 7.7**). The modes oscillate parallel and perpendicular to the quartz–Azo-POSS interphase and can be distinguished under incident polarized light. Thus, we chose a TIR setup to probe the refractive index variation of AgNC–Azo-POSS ultrathin films by exciting the nanocube LSPR with evanescent waves.

As is known, the TIR regime occurs at an angle beyond the critical angle of the quartz–air interface (>43°), known from the following relation derived from Snell's law: [372]

$$\theta_c = \sin^{-1}(n_{air}/n_{quartz}) \quad \textbf{(15)}$$

Under TIR conditions, a pronounced difference in reflection spectra between s- and p-polarized incident light is observed (**Figure 7.11**). There is a noticeable blue shift and line-width narrowing of the LSPR from p-polarized light to s-polarized light. For the trans state, the LSPR is observed at 468 nm under p-polarized (parallel to the plane of incidence) light and at 427 nm under s-polarized (perpendicular to the plane of incidence) light. This difference can be explained by the fact that, at a 50° angle of incidence, p-polarized light excites oscillation both perpendicular and parallel to the interphase whereas s-polarized light excites only the component parallel to the interphase (**Figure 7.11b**).[100] The measurement under p-polarized light is therefore more sensitive to the refractive index variation, and the LSPR shifts during photoisomerization were measured at 4.4 ± 0.7 and 3.4 ± 1.3 nm for p- and s-polarized light, respectively, over four cycles (**Figure 7.11c**). As

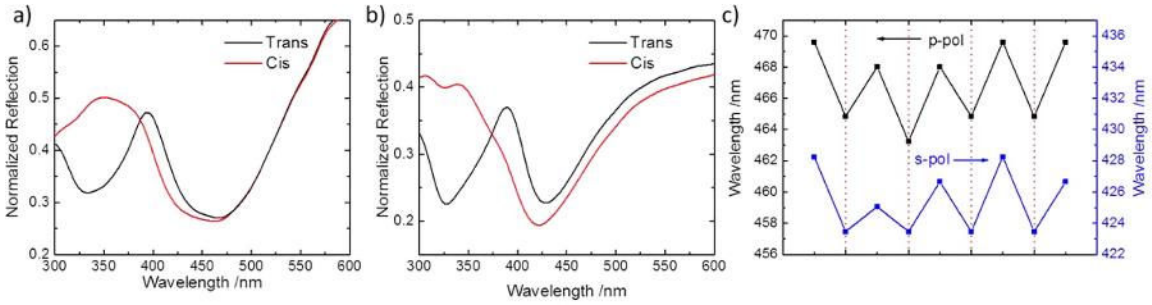

Figure 7.11: (a),(b) TIR measurements of different photoisomerized states with (a) p- and (b) s-polarized light. (c) Switching behavior of the reflectance minimum under alternating irradiation with UV and visible light. The dotted lines correspond to UV irradiation events.

with transmission extinction measurements, we observed a reversible cycling of reflection in the TIR regime when the sample was alternately irradiated with UV and visible light.

7.4 Conclusions

In conclusion, we have reported the fabrication of responsive AgNC arrays embedded in an active medium based on newly synthesized branched Azo-POSS compounds. The branched conjugate with a long spacer between the core and the azobenzene branches undergoes photoisomerization in solution but not in an ultrathin solid film. Azo-POSS conjugate **2**, with a shorter spacer between the core and the azobenzene moieties, exhibits a large refractive index variation when irradiated with UV light (−0.17 RIU change at a wavelength of 380 nm), higher than that of simple azobenzene embedded in a polymer matrix. We observed significant, reversible, and repeatable shifts in the AgNC LSPR peak position (from 4 to 6 nm) upon alternating irradiation of the composite Azo-POSS–nanocube ultrathin film with UV and visible light. Furthermore, a polarization-dependent variation in reflectance was observed in the TIR regime, supporting the ability to reversibly tune the LSPR by external stimuli such as light. Although the plasmonic response of the hybrid material based on mono azobenzene reported here is relatively slow (on the order of minutes), the use of push–pull azobenzenes with faster photoisomerization kinetics in a similar setup can shorten the response time and shift the operational wavelength into the visible wavelength range. Such robust photoswitchable plasmonic materials could find application in plasmonic devices with real-time and polarization-dependent responses, which have the potential for optical switching and filtering applications. In future research, the polarization-dependent behavior of azobenzene-containing materials can be combined with nanoparticle arrays to probe the photoinduced anisotropy of the photoactive materials.

Furthermore, oriented anisotropic nanostructures combined with such active layers could result in active polarizers and other devices.

CHAPTER 8. ELECTRICALLY CONTROLLED PLASMONIC BEHAVIOR OF GOLD NANOCUBE/POLYANILINE NANOSTRUCTURES: TRANSPARENT PLASMONIC AGGREGATES

8.1 Introduction

The establishment of a specific LSPR peak position is very important for preprogramming efficient responses for these materials. As is well known, the plasmonic properties of nanoparticles can be controlled during initial synthesis by varying the particle shape, size, and composition.[368, 373, 374] Over the past decade, significant progress has been made in the synthesis of well-defined plasmonic nanoparticles with a precise control of plasmonic properties for specific applications.[34, 243, 373, 375-379] However, for a given material and nanoparticle shape, the LSPR properties are fixed and it is difficult to change the LSPR peak position and cross-section intensity in a reversible and real-time manner.

One of the efficient ways to control the plasmonic properties in a reversible manner is to incorporate these nanostructures into surrounding active soft media, which can change their refractive properties depending on environmental conditions. In this case, a strong inverse dependence of plasmon resonance frequency on the dielectric constant of the surrounding makes it possible to control the plasmonic properties by utilizing active media.[19, 380] A wide range of stimuli-responsive organic and inorganic materials can be used as active media, including those responsive to pH, ionic strength, light, and temperature.[224, 301-303, 333, 335, 337, 339, 381-383] For example, the LSPR peak of gold nanoparticles in a weak polyelectrolyte gel

network has been reversibly tuned by changing the environmental pH, owing to the packing density change and hence the resulting refractive index change in the polyelectrolyte gel network induced by the swelling–deswelling mechanism.[301] In other examples, plasmonic resonances were successfully modulated using light-responsive materials under UV and visible light exposure as external stimuli.[302, 303] Recently, real-time tuning of plasmon lasers was demonstrated by introducing different liquid media around gold nanostructures through microfluidic channels in order to shift the emission peak from 859 to 890 nm depending on the liquids used.[384] However, it was necessary to incorporate several liquids having different refractive indices for modulating the laser emission into the microfluidic chip.

The electrical potential is one of the most attractive types of external control that allows incorporation of plasmonic materials in devices for real-time light modulation.[385] Electrical potential can be supplied and controlled in a precise and reproducible manner, and it can be readily adapted to device-oriented environments as well. This practical aspect gives electrically tunable optical systems an advantage over other external stimuli such as pH and temperature in prospective applications for adaptive light harvesting, colorimetric sensing, and light modulation.[120, 386-388]

There are a number of inorganic and organic electroactive materials including tungsten oxide, PANI, and polythiophene, poly(3,4-ethylenedioxythiophene) (PEDOT) that have been employed as active media to manipulate the plasmonic response of nanostructures.[269, 298, 299, 305, 311, 312, 389-394] The change in electronic structure, oxidation state, and conductivity of these electroactive materials results in a change in molecular polarizability and hence the effective dielectric constant. For instance, Baba et al. demonstrated that a large

variation in the real and imaginary dielectric constants occurs when thin films of conjugated polymers (such as PANI and PEDOT) are oxidized electrochemically.[391, 393, 394] Lacroix and co-workers further demonstrated several electrically tunable plasmonic systems based on electroactive PANI and PEDOT layers overlaid on gold nanostructures.[298, 299, 305, 392] In particular, gold nanoparticle arrays were fabricated on conductive ITO substrates via EBL, and a conjugated polymer was then deposited through electrochemical polymerization to modulate the gold nanoparticle LSPR. Although EBL allows for precise control of the size and shape of gold arrays at the nanoscale, it takes a significant amount of time and cost to create desired patterns, which hampers its large-scale applications.[395, 396] Recently, we presented an alternative bottom-up approach to assemble electrically tunable plasmonic hybrid nanomaterials with reversible LSPR shifts by controlling the applied electrochemical potential.[269] Specifically, a monolayer of AgNCs was deposited on an ITO substrate using the Langmuir–Blodgett technique and covered with a layer of water-soluble blue electrochromic polymer (ECP-Blue-WS).[269]

It is important to note that the densely packed assemblies of plasmonic nanoparticles in a solid state affect the electronic and optical properties, leading to significant LSPR peak broadening and the appearance of strong, broad extinction in the near-infrared (NIR) spectral region useful for solar panel applications.[61, 269, 397, 398] Because of the exponential decay of the electromagnetic field away from the surface of nanoparticles, for these applications it is critical to ensure intimate contact between the nanoparticles and the polymer matrix.[315, 399] However, well-defined narrow LSPR peaks with higher figures of merit and transparency in NIR region are required for other demanding applications including biosensing, plasmonic lasers, and metamaterials.[70, 120, 384, 400] On the other hand,

excessive light absorption and thermal dissipation in the near-infrared region might lead to premature thermal degradation of sensitive biological and soft matter environments and, thus, fundamental approaches to the suppression of the strong thermal absorption in solid plasmonic coatings by preventing plasmonic coupling should be considered. Furthermore, because the conjugated polymer matrices have high extinction coefficients in the visible and NIR spectral range, it is desirable to minimize the amount of polymer coating in order to avoid spectral overlap and excessive damping of the LSPR-driven light absorption. Considering these conditions, core/shell nanostructures can be promising candidates for obtaining larger LSPR peak shifts with a smaller amount of conjugated surrounding media while also avoiding uncontrollable coupling of plasmonic nanoparticles.

Therefore, in this study, we introduce novel electrically tunable plasmonic AuNC/PANI core/shell nanostructures that facilitate large LSPR shifts of individual nanostructures with precise control of the electrochromic PANI shell thickness (**Figure 8.1**). This PANI shell acts not only as an electroactive media but also as a controlled spacer that prevents strong plasmonic coupling and reduces the extinction in the near-infrared region. We selected AuNCs as a plasmonic core to avoid spectral overlap with the electroactive PANI shells in order to directly observe their tunable plasmonic behavior. These AuNC/PANI core/shell nanostructures can be synthesized by oxidative polymerization in the presence of colloidal AuNC dispersions and deposited onto conductive ITO substrates using a facile spray casting method. When an electric potential was applied to the AuNC/PANI core/shell nanostructure-coated conductive ITO electrode, a large, consistent, and reversible LSPR

shift of up to 24 nm with modest increase in NIR absorption was observed due to the oxidation state changes in electroactive PANI shells.

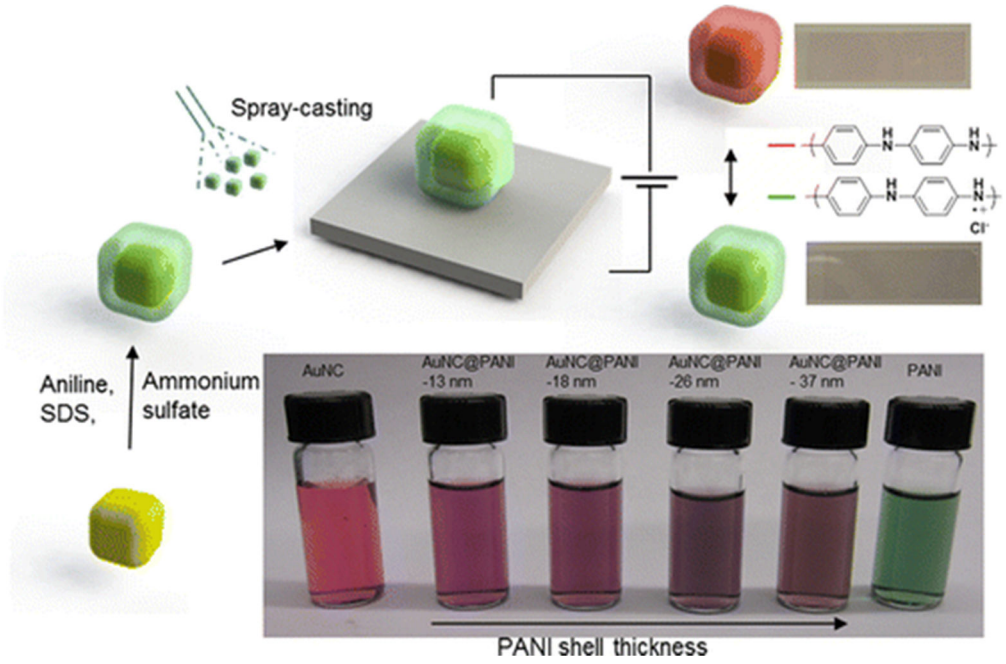

Figure 8.1: AuNC/PANI core/shell nanostructures for electrochemical LSPR modulation, and AuNC/PANI core/shell nanostructures with electrically tunable optical signatures (top), and AuNC/PANI solutions with different shell thicknesses (bottom).

Finally, FDTD simulations demonstrated that their plasmonic behavior can be related to the reversible changes in refractive index of PANI shells as induced by electrochemical oxidation. It has been suggested that the optimal PANI shell thickness for the most effective LSPR modulation should be comparable to the electromagnetic field decay length.[401] Finally, the AuNC/PANI core/shell nanostructures exhibited optical properties similar to individual AuNC/PANI core/shell properties due to the extensive PANI spacer, which effectively suppresses plasmonic coupling. This phenomenon leads to the reduced

extinction in the near-infrared region (700–1000 nm) with preservation of strong and narrow plasmonic absorption in the visible region.

8.2 Experimental Details

Synthesis of AuNCs:

The average size of the AuNCs was 39 ± 6 nm based on statistics from TEM images (**Figure E.1**). More than 200 nanoparticles were analyzed to obtain the average size of the AuNCs. Centrifugation was performed once to remove excessive CTAB on the AuNCs before synthesizing AuNC/PANI core/shell nanostructures. If centrifugation was repeated several times, irreversible aggregation was observed, most likely due to the dissociation of the CTAB surfactant bilayers from the AuNCs.[402]

Deposition of AuNC/PANI core/shell nanostructures on ITO: For substrate preparation, ITO slides were sonicated in dichloromethane, acetone, methanol, and water for 15 minutes each. To make the ITO positively charged, a (3-aminopropyl)-triethoxysilane (APTES) treatment was performed as follows.[403, 404] Washed ITO slides were dried and plasma-treated for 10 seconds with 100 mTorr air. The substrates were immersed in 2 vol % APTES in toluene at 75 °C for 30 minutes and washed with toluene, ethanol, and ultrapure water sequentially. The ITO substrates were blown with air and heated at 110 °C for 15 minutes. For PEI-coated ITO, plasma-treated ITO was immersed in 10 mg/mL PEI solution for at least 30 minutes and washed in ultrapure water for 10 minutes. The AuNC/PANI core/shell dispersion (3.5 mL) in 3.6 mM SDS was concentrated using centrifugation (6000 rpm for 15 min) and redispersed in ultrapure water (0.35 mL). The AuNC/PANI core/shell dispersion was sprayed using a spray gun (Iwata HP-CS) at 20 psi onto APTES-treated or

PEI-treated ITO slides (Delta Technologies, Ltd., 7 mm × 50 mm × 0.7 mm, sheet resistance = 15–25 Ω). For comparison, AuNCs were sprayed onto plasma-treated ITO (10 s with 100 mTorr air) in an area of 2.1 cm^2 of ITO (3 cm × 0.7 cm). After film deposition, all films were immersed in water to remove excessive SDS overnight. Then, films were immersed in 0.2 M HCl for 1 hour to attain the doped emeraldine salt form of PANI.

Characterization: The AuNC/PANI core/shell dispersion was drop-cast on a carbon-coated Cu grid (product no. 01800-F, Ted Pella) and dried under ambient conditions. The PANI shell thickness was obtained by measuring the AuNC/PANI core/shell nanostructures height from AFM images. To estimate the shell thickness, the average size of the AuNC was subtracted from the height and divided by two.

Zeta-potentials of the core/shell nanostructures in aqueous solution were measured on a Malvern Zetasizer Nano ZS instrument. The mean ζ potential values are provided in mV units and are results of three independent measurements that consist of 12 runs each. The measurements were conducted at 25 °C. For hyperspectral measurements, AuNC/PANI core/shell nanostructures deposited on an ITO substrate were exposed to hydrazine vapor for 10 min to reduce emeraldine salt PANI (PANI-ES) to leucoemeraldine base PANI (PANI-LB). The obtained spectra were normalized by a Lambertian >99% reflectance standard (Labsphere SRS-99–010). The scattering spectra were smoothed using adjacent-averaging with a 50-point window by OriginPro 8.5.

FDTD simulations: Individual AuNCs were approximated with a 39 nm edge length and a 40% edge rounding based on TEM image observations.[405] PANI-ES and PANI-LB shells with different thicknesses and the same edge rounding of 40% were then individually added

to the nanocubes. Refractive indices for PANI-ES and PANI-LB, and gold were obtained from literature while the refractive index for the ITO substrate was obtained experimentally using ellipsometry.[401]

8.3 Results and Discussion

8.3.1 *Synthesis of AuNC/PANI core/shell nanostructures*

AuNC/PANI core/shell nanostructures were prepared using surfactant-assisted oxidative polymerization of aniline in the presence of AuNCs.[224, 225] To obtain thicker PANI shells on the AuNCs, the same polymerization step was repeated up to four times in this study. For comparison, PANI homopolymer was also synthesized by the same polymerization process in the absence of AuNCs (see images of aqueous dispersions of different nanostructures in **Figure 8.1**). The PANI dispersion exhibited a green color characteristic of the conductive emeraldine salt (ES) form.[403] As the thickness of the PANI shell increased (the number of polymerization cycles increased), the AuNC/PANI core/shell nanostructure dispersion color changed from pink to dark-brown. All of the AuNC/PANI core/shell nanostructures synthesized were found to maintain colloidal stability even after six months due to a high negative surface potential. Indeed, the ζ potential of the AuNC/PANI core/shell nanostructures was highly negative (around −50 mV) due to the presence of SDS, whereas initial AuNCs possessed a lower positive charge (around +20 mV) because of the CTAB.[406]

The average PANI shell thickness formed on the AuNCs was 13 ± 3 nm after a one-step polymerization as estimated from transmission electron microscopy (TEM) images (**Figure 8.2a** and **Figure E.2a**). PANI shells with thicknesses of 18 ± 5, 26 ± 5, and 37 ±

5 nm were obtained by carrying out two, three, and four polymerization cycles respectively (**Figure 8.2b–e** and **Figure E.2b**, **c**). Overall, the PANI shell thickness increased consistently with the number of polymerization steps (**Figure 8.2f**).

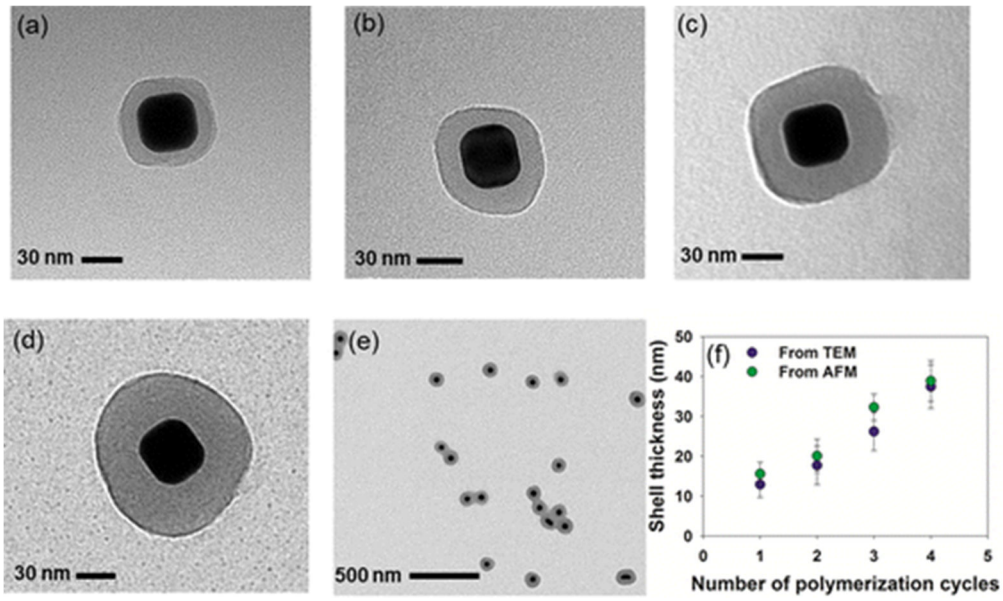

Figure 8.2: TEM images of AuNC/PANI core/shell nanostructures after (a) one, (b) two, (c) three, and (d), (e) four polymerization cycles. (f) PANI shell thickness vs number of polymerization cycles. The shell thickness is compared as obtained independently from TEM and AFM measurements.

The UV–vis spectra of the AuNCs, PANI, and the AuNC/PANI core/shell nanostructures with different thicknesses of the PANI shell in aqueous solution are displayed in **Figure 8.3a**. As known, PANI exhibits a strong absorption peak at 843 nm with a shoulder around 420 nm, which is a characteristic of the conductive ES form of PANI.[403, 407] The bare AuNCs in water had an extinction peak of 532 nm corresponding to the LSPR of the AuNCs.[408] In the case of the AuNC/PANI core/shell nanostructures, both the LSPR of the AuNCs and the absorption peak of the conductive ES form of PANI were observed as

expected. As the thickness of the PANI shell increased, the PANI peak at 830 nm became more pronounced and the ratio of the PANI peak to the AuNC peak increased from 0.36 to 1.4 (**Figure 8.3a, b**). The LSPR peak of the AuNC/PANI core/shell nanostructures continuously red-shifted with an increasing PANI shell thickness, most likely due to the refractive index of PANI shell being higher than that of the surrounding water.[409]

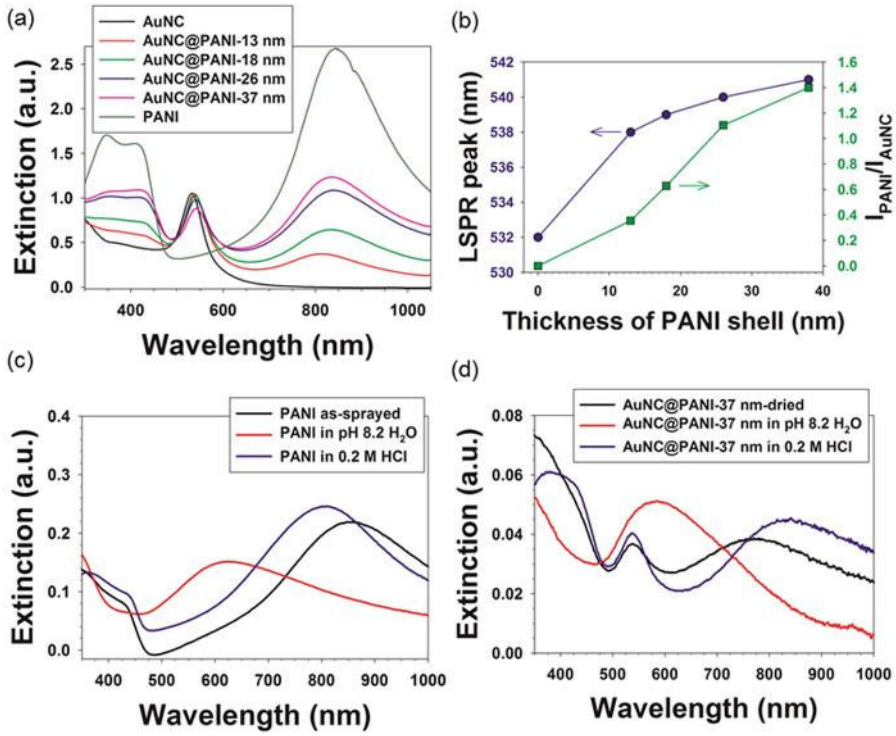

Figure 8.3: (a) UV–vis spectra of AuNCs and AuNC/PANI core/shell nanostructures in aqueous solutions and (b) their LSPR peak position and cross-section intensity ratio of PANI to AuNC as a function of the PANI shell thickness. AuNC and AuNC/PANI core/shell colloids are dispersed in water and 3.6 mM SDS, respectively. UV–vis spectra of (c) as-sprayed PANI on conductive PEI-ITO substrates and (d) AuNC/PANI-37 nm core/shell nanostructures deposited on PEI-ITO substrates exposed to air, 0.2 M HCl, and pH 8.2 water.

8.3.2 *AuNC/PANI core/shell nanostructures on conductive ITO substrates*

Having successfully synthesized stable AuNC/PANI core/shell colloids, we then deposited these nanomaterials on conductive ITO substrates to test their electrochemical behavior. Because AuNC/PANI core/shell nanostructures are negatively charged, the negatively charged ITO substrate was first modified with a cationic prelayer in order to promote nanocube stability after adsorption. In the present study, APTES and a PEI coating were used to modify the surface composition (see **Experimental Details**). A more uniform distribution of AuNC/PANI core/shell nanostructures was observed on PEI-ITO surfaces due to higher wettability, with a contact angle of 53.3 ± 4.6° for PEI-ITO versus 79.4 ± 6.5° for APTES-ITO (**Figure E.3**). Therefore, the PEI-ITO substrate was further used for the study of the electrochemical behavior of the AuNC/PANI core/shell nanostructures.

The LSPR peak of as-sprayed AuNC/PANI core/shell nanostructures on PEI-ITO substrates showed similar behavior compared to that for AuNC/PANI core/shell nanostructures in aqueous solution in respect to the LSPR peak position and the AuNC and PANI absorption peak intensity ratio (**Figure E.4a**). For comparison, UV–vis spectra of PANI films on ITO substrates were also measured in different environmental conditions (**Figure 8.3c**). The thickness of PANI films used for this comparison was varied between 50 and 300 nm. The PANI film had a peak located around 820 nm in air and acidic conditions (0.2 M HCl), which is attributed to the ES form of the polymer.[404] In weakly basic aqueous solution (pH 8.2), a peak around 630 nm appeared, which is a characteristic of the emeraldine base (EB) form.[404] As known, PANI can exist in either the ES or EB form as controlled by a doping–dedoping process at different pH conditions.[224]

Similarly, the PANI shell of AuNC/PANI core/shell nanostructures can also exist in different forms depending upon the solution pH, as confirmed by UV–vis spectra (**Figure 8.3d** and **Figure E.4b-d**). It is worth noting that the absorption peak position of the EB form is very close to the LSPR peak of AuNC, which makes it difficult to identify the LSPR peak shift in the extinction spectra.[224] AuNC/PANI core/shell nanostructures on PEI-ITO substrates were immersed sequentially in ultrapure water overnight and in acidic 0.2 M HCl for 1 h to ensure fully doped PANI shells. After additional doping with HCl, the PANI shell of all samples exhibited the well-developed emeraldine salt absorption peak around 810 nm (**Figure E.4e**).

The AFM images of AuNC/PANI core/shell nanostructures deposited on PEI-ITO substrates are shown in **Figure 8.4** and **Figure E.5**. It was observed that the AuNC/PANI core/shell nanostructures were randomly distributed on the substrates without particular orientations or configurations. A large amount of AuNC/PANI core/shell nanostructures are in physical contact with one another and formed aggregates or multimers. It should be noted that close contact between AuNC/PANI core/shell nanostructures did not affect the original optical signature of single core/shell particles, which is supported by UV–vis spectra in **Figure 8.3** and **Figure E.4** showing that the LSPR properties of AuNC/PANI core/shell multimers on ITO substrates were very similar to the monomer optical properties. This behavior is in contrast to most plasmonic aggregates and will be further discussed in the later single particle study section. In the case of the deposition of AuNCs, even if most of the as-sprayed AuNCs were found as individual nanostructures in AFM images (**Figure E.5a**), an aggregation peak around 670 nm was observed due to the partial coupling of AuNCs (**Figure E.4a**). Furthermore, it was also challenging to spray AuNCs

with the same degree of coupling in order to obtain the specific desired aggregation LSPR peak in a reproducible manner. On the other hand, no apparent aggregation peak or LSPR shift of AuNC/PANI core/shell nanostructures were observed after deposition. It is worth

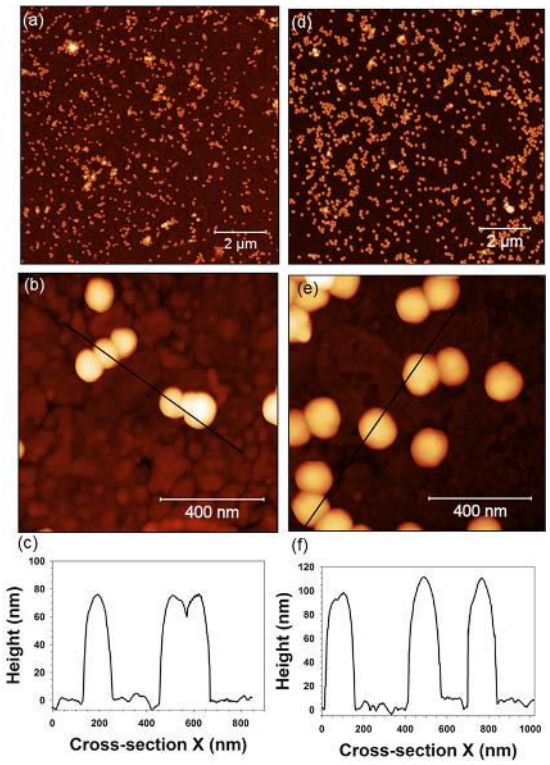

Figure 8.4: Topographical AFM images of (a,b) AuNC/PANI core/shell nanostructures with 13 nm PANI shells, and (c) their cross-sectional profiles. AFM images of (d,e) AuNC/PANI- core/shell nanostructures with 26 nm PANI shells, and (f) their cross-sectional profiles. The cross-section lines are marked with black lines in (b) and (e). AuNC/PANI core/shell nanostructures were deposited on PEI-modified ITO substrates.

noting that the PANI shell around the AuNCs effectively prevents undesirable and uncontrollable plasmon coupling between the AuNCs during spray casting.[104, 410-412]

The representative cross section height profiles of AuNC/PANI core/shell nanostructures with the 13 and 26 nm PANI shells are displayed in **Figure 8.4c, f**, respectively. As

expected, AuNC/PANI core/shell nanostructures with thicker PANI shells have higher average heights (**Figure E.5f**). For instance, AuNC/PANI core/shell nanostructures with 13 and 26 nm PANI shells have respective average heights of 70 and 101 nm. The PANI shell thicknesses obtained from AFM images were slightly higher than those from TEM images, most likely due to different conditions during the measurements (humid air vs high vacuum) (**Figure 8.2f**). The PANI shell is more likely to absorb some moisture and be hydrated during the ambient AFM measurements.

8.3.3 *Electrochemical switching of AuNC/PANI core/shell nanostructures*

An external electrical potential was applied to reversibly change the refractive index of the PANI shell with different oxidation states and in turn modulate the LSPR of the AuNC core. It was reported that the ES form of PANI can be reversibly switched to the leucoemeraldine base (LB) form by applying an electric potential both in aqueous and nonaqueous electrolytes.[403, 413] To find the optimal conditions, we explored both aqueous and nonaqueous electrolytes in the present study.

A slightly acidic aqueous electrolyte, 0.5 M NaCl in 0.01 M HCl electrolyte, was found to result in larger and more reversible LSPR shifts (**Figure 8.5a–c**). In the voltage range from −0.3 to 0 V (vs Ag/AgCl), there is no appreciable absorption in the near IR region (700 to 1200 nm), which is a typical characteristic of the reduced form of PANI (LB).[403] The absorbance in the near IR region appeared at 0 V and increased with an increasing voltage. These changes indicate that the LB form of the PANI shells started to transform to ES. Moreover, this change is accompanied by a blue-shift of the LSPR peak due to accompanying changes in the refractive index (**Figure 8.5b, c**). The LSPR position

changed from 555 to 533 nm when the voltage increased from −0.3 to 0.5 V. Indeed, the real part of the refractive index of the ES form (1.30 at 532 nm) is known to be significantly lower than that of the LB form (1.65 at 532 nm).[401] It is known that a decrease in the real part of the refractive index of surrounding media causes a blue-shift in the LSPR peak position due to the orthogonal relationship between the LSPR shift and a refractive index change.[269, 369] The cross-section intensity of the LSPR peak also decreased with increasing voltage because the ES form has a higher imaginary part of the refractive index than the LB form of PANI.[298, 401] It has previously been reported that the LSPR peak is damped with surrounding media which has a large imaginary refractive index.[298] To further investigate the stability and reversibility of these nanostructures, cyclic voltammetry (−0.3 to 0.5 V) was performed 100 times at a scan rate of 200 mV/s. The AuNC/PANI-26 nm core/shell nanostructures showed a great degree of reversibility without a noticeable decrease in electroactivity (**Figure 8.5e**). It is remarkable that even after 100 cycles, the LSPR could be reversibly tuned to a significant extent by applying electric potentials without a significant difference in the LSPR position and extinction (**Figure 8.5f**).

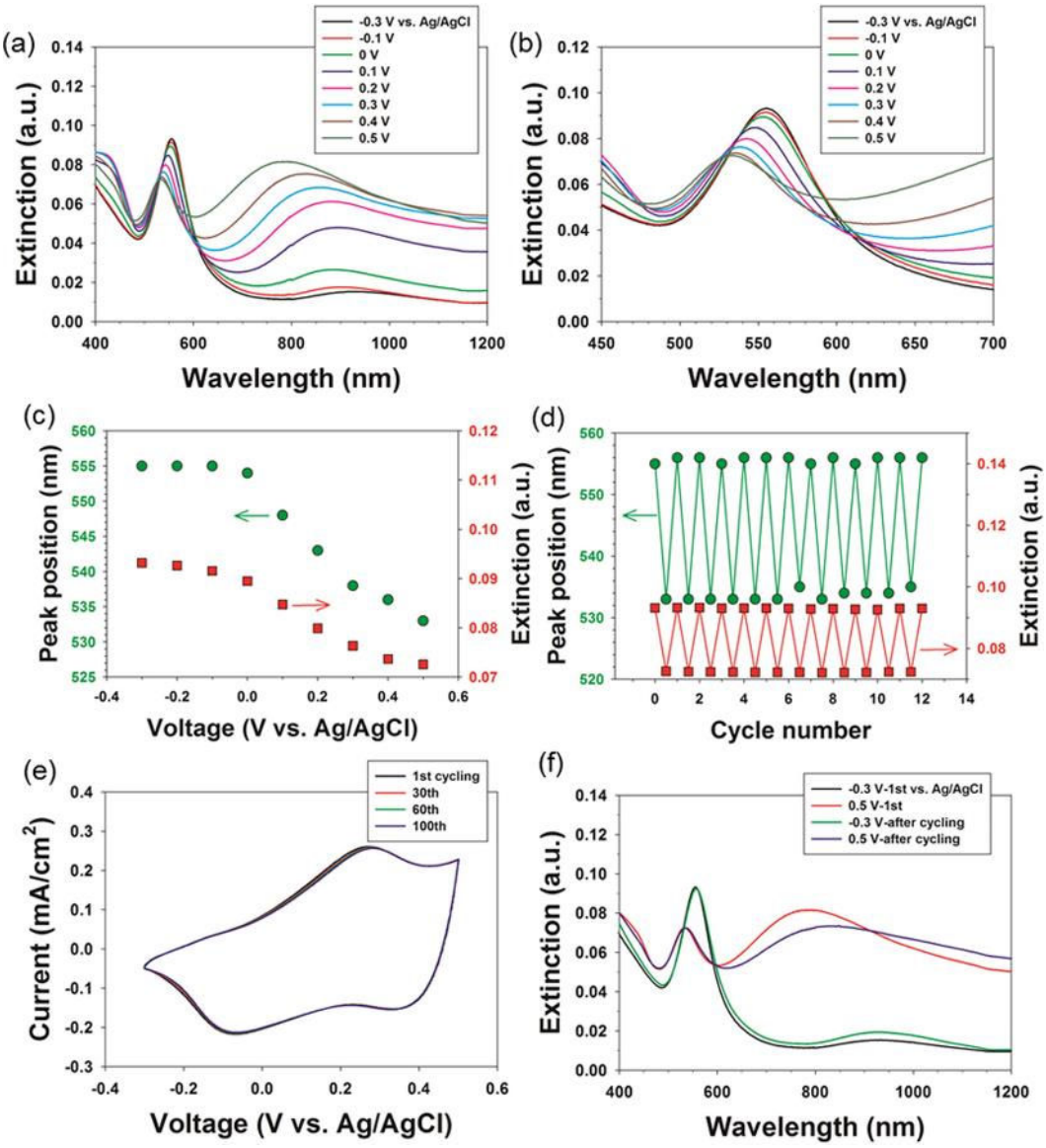

Figure 8.5: (a) UV–vis spectra of AuNC/PANI core/shell nanostructures with 26 nm PANI shells at different voltages with 0.5 M NaCl in 0.01 M HCl electrolyte, and (b) its magnified UV–vis spectra, (c) LSPR peak position and maximum peak extinction vs voltages (vs Ag/AgCl), (d) LSPR peak position and extinction during cycling, (e) cyclic voltammograms of AuNC/PANI core/shell nanostructures with 26 nm PANI shells at 200 mV/s from −0.3 to 0.5 V during cycling, and their UV–vis spectra at −0.3 and 0.5 V before and after 100 cycles.

When more acidic electrolytes were used, extinction over the full wavelength range increased with cycling (**Figure E.6c** and **Figure E.7a**) due to light scattering of small hydrogen bubbles generated by hydrogen evolution reactions (HER).[414, 415] Indeed, UV–vis spectra of AuNC/PANI core/shell nanostructures before and after cycling are nearly identical when baseline correction was used (**Figure E.6e** and **Figure E.7c**). We suggest that water can gradually penetrate the PANI shell, and the HER process takes place on the AuNC surface during cycling in the above case. However, by using a less acidic electrolyte (0.5 M NaCl in 0.01 M HCl) with a higher minimum cutoff voltage (−0.3 V vs Ag/AgCl), HER can be completely suppressed, which allows stable and reversible changes as confirmed by UV–vis spectra (**Figure 8.5d**).

In the case of a nonaqueous electrolyte, 0.5 M of lithium bis(trifluoromethyl)sulfonylimide (LiBTI) in propylene carbonate (PC), a smaller LSPR shift (up 17 nm) was obtained with 26 nm PANI shells. At high positive potentials above 0.2 V (vs Ag/Ag^{+}), the LSPR peak red-shifted when the applied voltage was increased from 0.2 to 0.4 V (**Figure E.8c**). Such a change indicates that the ES form of PANI changes to the pernigraniline form beyond 0.2 V. The fact that the real part of the refractive index of pernigraniline form is higher than that of the emeraldine form supports the observed red-shift of the LSPR of AuNC/PANI core/shell nanostructures beyond 0.3 V.[416] Indeed, a significantly different UV–vis spectrum of AuNC/PANI core/shell nanostructures at 0.4 V confirms the oxidation state change of PANI from the emeraldine to the pernigraniline form.[403] Cycling tests showed that the cross-section intensity of LSPR at 537 nm in the UV–vis spectra decreased

by 3.1% after five cycles, which might be due to partial dissolution of the AuNC/PANI core/shell nanostructures into the nonaqueous electrolyte.

With the optimized electrolyte and voltage range (0.5 M NaCl in 0.01 M HCl from −0.3 to 0.5 V (vs Ag/AgCl), electric potential stimuli were applied to all the AuNC/PANI core/shell nanostructures with different shell thicknesses in order to investigate the effect of the PANI shell thickness on the LPSR peak position. All AuNC/PANI core/shell nanostructures had a significantly higher LSPR shift than AuNCs alone regardless of the PANI shell thickness (**Figure 8.6a, b** and **Figure E.9**). The LSPR peak of bare AuNCs alone displayed a negligible change (within the standard deviation) of 0.9 ± 0.7 nm. Such a negligible response confirms that possible local variations of the buffer environment do not contribute significantly to the LSPR modulation discussed above. In general, the LSPR peak shift increased with thicker PANI shells (**Figure 8.6c**). For the AuNCs with thinner PANI shells, a small increase in shell thickness had a significant impact on the degree of the LSPR shift (from 14.8 ± 1.2 to 21.1 ± 0.7 nm for a shell thickness increase from 13 to 18 nm). For thicker shells, the role of shell thickness on the LSPR shift is less pronounced. For instance, the AuNC/PANI-37 nm core/shell nanostructures exhibited only a slightly higher LSPR shift (23.8 ± 1.3 nm) than the AuNC/PANI-26 nm core/shell nanostructures (22.2 ± 0.8 nm).

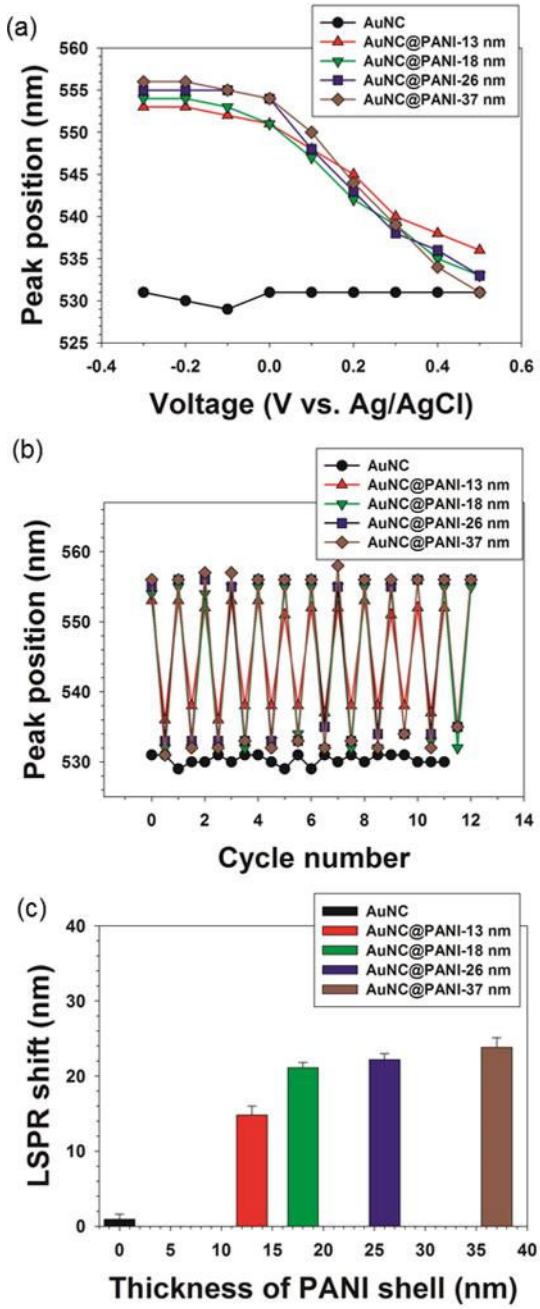

Figure 8.6: (a) LSPR peak position of AuNCs and AuNC/PANI core/shell nanostructures with a varying PANI shell thickness as a function of voltage applied (within 0.5 M NaCl in 0.01 M HCl electrolyte (vs Ag/AgCl), (b) their LSPR peak position during cycling with the voltage switched between −0.3 and 0.5 V, and (c) the average LSPR shift of AuNC/PANI core/shell nanostructures vs PANI shell thickness and in comparison with bare nanostructures.

8.3.4 *FDTD modeling of AuNC/PANI core/shell nanostructures*

FDTD simulations were conducted for AuNCs without shells in air and water and with PANI shells on an ITO substrate in order to verify experimental findings and interpret the mechanism behind the LSPR peak shifts (see **Experimental Details**). The simulated extinction spectra matched well with the experimental spectra obtained, and the same general trend was observed in both simulations and experiments (**Figure 8.7a** and **Table E.1**).

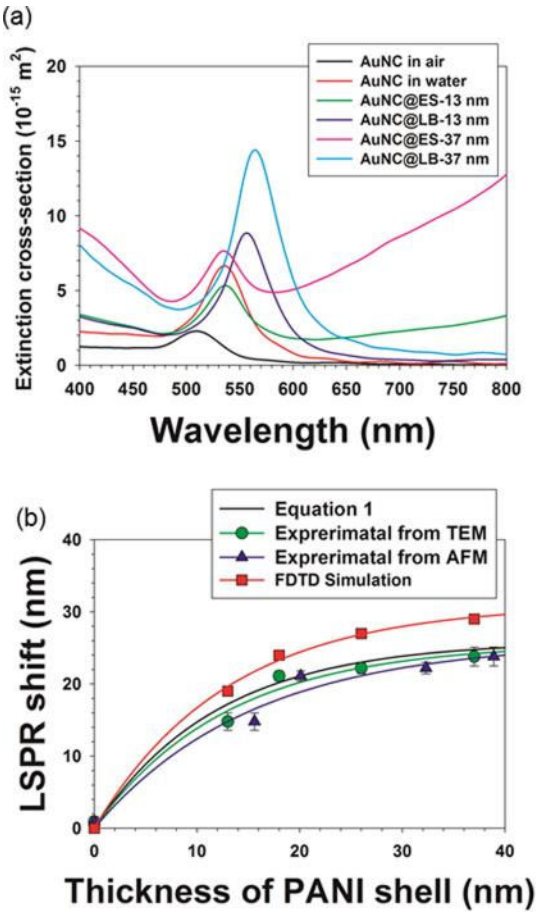

Figure 8.7: (a) Simulated extinction of AuNC in air and water and AuNC/PANI core/shell nanostructures with 13 and 37 nm thick PANI shells, and (b) LSPR peak shift as a function of PANI shell thickness based on Equation **4** with experimental and FDTD simulation results.

Simulations did however predict approximately 4 nm larger magnitude peak shifts for each of the shell thicknesses than were obtained experimentally. This observation might be attributed to the fact that the refractive indices of PANI in our study may be slightly different from the literature values used for the PANI refractive indices.[401] Another possibility is that additional surfactant such as CTAB and SDS exists beyond the approximated 2 nm shell even after the washing steps and consequently dilutes the LSPR shift or that the simulated nanocube differs slightly from the actual synthesized nanocubes. It is also possible that positively charged ES and neutral LB forms could interact with the AuNC differently and alter the surface charge of the AuNCs, thereby affecting the LSPR properties.[417, 418] It should be noted that simulations from single AuNC/PANI core/shell particle could reasonably predict the overall LSPR properties of AuNC/PANI core/shell nanostructures randomly deposited on ITO including monomers and multimers. This similarity confirms that the plasmonic coupling is intrinsically prohibited due to the PANI shells. The LSPR shift of plasmonic nanoparticles in various environments can be described using Equation **4**.[70, 315, 399, 419] Thus, we analyze how FDTD simulations of the more complex case of core/shell nanostructures follow this general prediction.

First, AuNCs were modeled without a shell or substrate in order to estimate m and l_d of the AuNCs for Equation **4**. The simulated LSPR of AuNC was 535 nm in water and 510 nm in air. An RIS of 75 nm/RIU for these nanocubes was calculated by observing the wavelength shift of the plasmon resonance between air and water media (**Figure 8.7a**). A near-field intensity plot was also constructed for the LSPR peak at 535 nm for an AuNC in water in order to find the electric field decay length (**Figure E.10a**). An electromagnetic

decay length of 24 nm for a bare AuNC was estimated from a horizontal cross-section through the center of the nanocube (**Figure E.10b**) using the following equation:[316]

$$E(z) = E_0 \exp\left(\frac{-z}{l_d}\right) \quad (16)$$

where E_0 is the maximum electromagnetic field, z is the horizontal position from the AuNC, l_d is the electromagnetic field decay length. The Δn at the LSPR peak of AuNC (535 nm) was taken from the literature refractive indices.[401]

Figure 8.7b shows the $\Delta\lambda_{max}$ obtained from FDTD simulation as a function of PANI shell thickness, which is in good agreement with the experimental results and the theoretical equation. Fitting with the experimental and FDTD simulation data also gave similar m and l_d values, which were obtained from a FDTD simulation on a bare AuNC (**Table E.2**). This further confirms the validity of our analysis.

From this analysis we can conclude that $\Delta\lambda_{max}$ greatly increases with a small increase of PANI shell thickness only when the shell thickness is relatively thin (below the electromagnetic decay length of 24 nm). An increase in the shell thickness above 24 nm results in a much smaller increase in $\Delta\lambda_{max}$ because strong electromagnetic fields are confined to distances within its characteristic decay length l_d. This result implies an important relationship between the thickness of the PANI shells and the LSPR shift when designing various core/shell nanostructures. Moreover, it confirms that sufficiently large LSPR shifts can be achieved with relatively thin PANI shells having an optimized thickness comparable to or below the electromagnetic decay length. This critical shell thickness can be independently determined from simulations and can be used to design core/shell parameters with the most efficient LSPR shifts in the plasmonic modes.

The electric field distribution of the AuNC/PANI core/shell nanostructures was also examined in order to further analyze the LSPR switching mechanism (**Figure 8.8a–d**). It is worth noting that the electric field is much more confined for the PANI-LB shells than for the PANI-ES shells due to the PANI-LB shell's higher refractive index. From electric field distributions at the peak plasmon wavelengths for nanocubes with 13 and 37 nm PANI

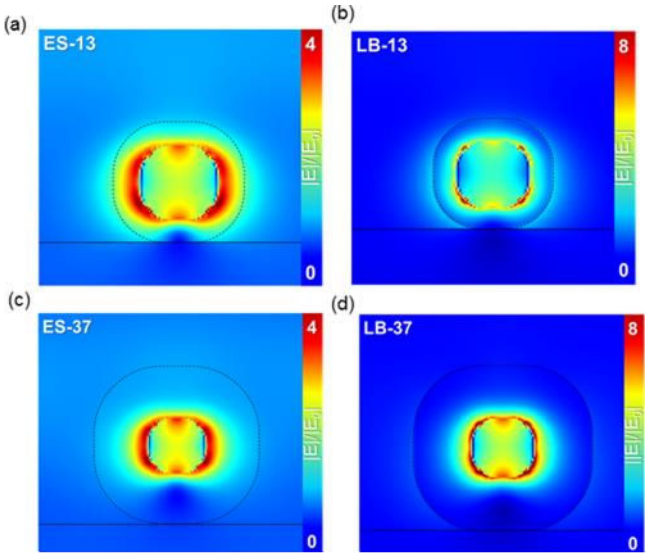

Figure 8.8: Electromagnetic field distribution, $|E|/|E|_0$, for core/shell nanostructures with different thickness of shells and their different oxidation states: (a) AuNC/PANI-ES-13 nm, (b) AuNC/PANI-LB-13 nm, (c) AuNC/PANI-ES-37 nm, and (d) AuNC/PANI-LB-37 nm core/shell nanostructures. Electromagnetic field distribution maximum values were set to 4 for the ES state and 8 for the LB state for clarity.

shells, it is readily seen that even though the nanocubes are resting on a substrate, no hybridized splitting occurs for the LSPR mode and that the dominant mode is a simple dipole compared to the split hybridized modes of other substrate-bound particles.[269] Thus, it can be concluded that the PANI shells provide enough of an insulating media so that the AuNCs do not interact with the substrate. This observation adds further support to the claim

that the nanoparticles cannot couple with one another due to the inherent interparticle distance imparted by the shells.

8.3.5 *Single nanoparticle study of AuNC/PANI core/shell nanostructures*

AuNC/PANI core/shell single particles were studied using a combination of hyperspectral imaging and AFM to further confirm that the PANI shells effectively prevent plasmonic coupling (**Figure 8.9**). A specific AuNC/PANI core/shell monomer and a dimer with 37 nm PANI shells were concurrently imaged using AFM (**Figure 8.9a–c**) and hyperspectral imaging (**Figure 8.9d**). AuNC/PANI monomer and dimer core/shell nanostructure scattering spectra (designated 1 and 2, respectively) were extracted for both PANI-ES and PANI-LB shells (**Figure 8.9e, f**). Both the monomer and the dimer showed very similar scattering spectra; the monomer had scattering peaks centered at 571 and 603 nm for ES and LB PANI shells, respectively, while the dimer possessed a scattering peak at 574 for the ES shell and 604 nm for the LB PANI shell. The scattering spectra were smoothed to identify the peak position (see **Chapter 8 Supporting Information**). The scattering intensity of the dimer was found to be higher than that of the monomer simply because the scattering cross-section of the dimer is larger than that of the monomer. These peaks were found to be red-shifted from extinction spectra peak positions, but it should be noted that the scattering peak position does not necessarily exactly correlate with the absorption or extinction peak position.[84] This is clear evidence that plasmonic coupling was intrinsically prevented by the existence of the PANI shells and that all the AuNC/PANI core/shell particles behave as single particle regardless of their physical contact. Indeed, as shown in **Figure E.11**, the UV–vis spectra of AuNC/PANI with 37 nm shell on ITO substrates were not affected by density of core/shell particles whereas AuNC coated on substrates were

coupled together and showed broad aggregation peak. This result is in good agreement with our single particle hyperspectral study and FDTD simulations.

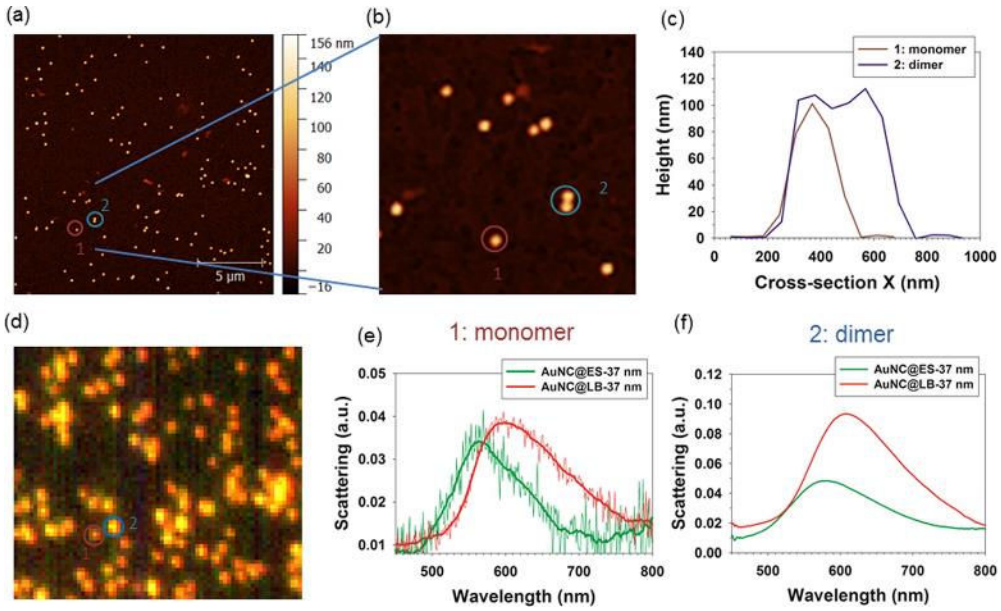

Figure 8.9: (a,b) Topographical AFM images of AuNC/PANI core/shell nanostructures with 37 nm PANI shells and (c) corresponding cross-sectional heights of a monomer and a dimer. (d) Hyperspectral image of the scattering from the nanoparticles corresponding to the same position of the AFM image shown in (a). The single particle scattering spectra of the marked (e) monomer (1) and (f) dimer (2) nanocubes in the AFM and hyperspectral images (see b and d).

8.4 Conclusions

The most significant conclusion is that the electroactive PANI shell could simultaneously act as an active media nanostructure as well as a physical spacer. The deposited AuNC/PANI core/shell nanostructures show extinction signature of a single particle due to the presence of the PANI shells which damp the LSPR coupling even for close packing. The closest distance between AuNCs with the thinnest PANI shells is 26 nm, which is larger than the electromagnetic field decay length (24 nm) of the AuNCs obtained from

FDTD simulations. Therefore, the AuNC/PANI core/shell nanostructures can be coated on diverse substrates with varying thickness in a reproducible manner without losing their original LSPR properties, even in the case of highly packed AuNC/PANI core/shell nanostructures on substrates. In contrast, bare AuNCs tend to form aggregates and couple with each other and lose their original characteristics due to peak shifts and strong coupling bands appearance, especially at a high density of nanoparticles.

Another feature is that the AuNC/PANI core/shell nanostructures synthesized here showed much larger LSPR shifts under electrical potential and significantly better stability than other electrically tunable plasmonic nanostructures. For example, only a 17 nm LSPR shift was demonstrated for a 50 nm-thick PANI planar film while our AuNC/PANI core/shell nanostructures showed an LSPR shift of 21.1 nm with 18 nm thick PANI shells.[298] Our AuNC/PANI core/shell nanostructure also exhibited a higher LSPR shift with a smaller amount of active media (PANI shells) than our previous electrically tunable AgNC monomer/ECP-Blue-WS hybrid system, which showed 3.1 nm LSPR shifts with a 55 nm thick ECP-Blue-WS layer.[269] On the other hand, the LSPR shift of AuNC/PANI core/shell nanostructures (22 nm shift with a 26 nm PANI shell thickness) are similar to that of a PANI/Au/PANI sandwiched structures, with an LSPR shift of 24 nm with a 50 nm total PANI thickness (25 nm for each PANI layer).[311] An AgNC dimer with a 55 nm thick ECP-Blue-WS layer also showed a similar LSPR shift of 23.7 nm.[269] Importantly, our AuNC/PANI core/shell nanostructures with optimized electrochemical conditions displayed much better stability as shown in **Figure 8.5e, f**. It was shown that the AgNC/ECP-Blue-WS layer composite exhibited LSPR peak drift during cycling

tests.[269] Furthermore, It was also reported that the LSPR signature can be lost during electrochemical switching.[311]

We suggest that the effective and reversible LSPR modulation of the AuNC/PANI core/shell nanostructures reported in this study is due to the PANI shell covering all facets of the AuNC core with intimate contact provided by polymerization at gold surface. Moreover, AuNC/PANI core/shell nanostructures possess other advantages for tuning the LSPR over other systems. First, the LSPR of AuNC core is easily modulated by applying an electric potential using the electroactive PANI shell, which can potentially be employed for electrical potential control in device-related environment.[384, 420] In addition, no data processing is required to analyze the LSPR shift of AuNC core because of the relatively thin PANI shells, which provide additional convenience for direct observation of the LSPR shift in real time if needed. It distinguishes them from conventional Au/PANI layered structures in which a careful subtraction of the PANI peak was necessary to evaluate the LSPR peak shift due to the strong extinction of the thicker PANI layer.[298, 311]

In conclusion, we have synthesized AuNC/PANI core/shell nanostructures with precise control of the electrochromic PANI shell thickness. AuNC/PANI core/shell nanostructures can be readily assembled on conductive ITO substrates using a simple and scalable spraying technique with the PANI shells preventing the common uncontrollable coupling of AuNCs. These AuNC/PANI core/shell nanostructures could deliver significantly reversible and easily detectable LSPR peak shifts with an optimized electrical potential window and an electrolyte. More importantly, the electroactive PANI shells act as active media to tune the LSPR shift as well as spacers to prevent coupling between AuNC cores. Single nanoparticle hyperspectral measurements and FDTD simulations show that the

thicker PANI nanoshell indeed effectively prevent plasmon coupling between the plasmons of individual AuNCs in close proximity.

Finally, FDTD simulations showed that increasing the shell thickness around the electromagnetic field decay length of plasmonic nanoparticles results in most significant LSPR shifts. The validated theoretical relationship can be widely applied for core/shell designs to optimize the active media thickness when designing responsive plasmonic nanostructures. We suggest that the water-dispersible AuNC/PANI core/shell nanostructures demonstrated in this study could easily be deposited onto a wide range of complex substrates required in practical device applications. Moreover, our method can readily be used for facile fabrication of core/shell electroactive systems such as multifunctional electrochromic devices, sensors, light modulators, and solar cell components by spraying over large surface areas of supporting electrodes without need for complex bottom-up microfabrication approaches.

CHAPTER 9. DESIGN OF HYBRID ELECTROCHROMIC MATERIALS WITH LARGE ELECTRICAL MODULATION OF PLASMONIC RESONANCES

9.1 Introduction

Active control of plasmonic signals can be achieved by implementing various stimuli-responsive materials (matrices) interfaced with metal nanoparticles that can exist in different electronic or conformational states as triggered by external means. Photochromic organic and polymeric materials are widely known for their reversible transformations under light illumination.[302, 355-357, 421] For instance, we have recently employed thermally stable azobenzene-modified oligomeric silsesquioxanes as photoresponsive matrices for real-time LSPR modulation.[303] An electric potential stimulus can be controlled in a highly reproducible and practical manner and is therefore considered to be advantageous for nanoscale light modulation at optical frequencies.[120, 385, 387, 388] An early example of a fully inorganic plasmonic electrochromic system based on silver nanoparticles (AgNP) and WO_3 was reported by Wang and Chumanov.[389] Since then, significant progress has been achieved in purely inorganic electrochromic materials.[422] A large variation in real and imaginary dielectric constants occurs when thin films of electropolymerized conjugated polymers, such as PANI and PEDOT, are oxidized electrochemically or chemically.[393, 394, 423]

This property of electrochromic polymers (ECPs) makes it possible to create functional media for electrochemical LSPR modulation.[298, 299, 305, 311, 312, 390-392] For instance, in recent

study, we employed a well-established ECP of PANI to create core/shell nanostructures with an electrically tunable LSPR.[292] Over the years, many conjugated electrochromic polymers with tunable light absorption in different ranges of the visible spectrum have been synthesized for applications in display technologies and smart windows.[424, 425] Furthermore, by variation of the side-chain functionalities, the solubility of these polymers in organic as well as aqueous solvents was improved, enabling solution processing. However, the full potential of hybrid systems that incorporate both organic and inorganic materials has yet to be realized. The major challenge is the preparation of these materials from presynthesized and well-characterized components by simple bottom-up methods.

We have recently employed a water-processable version of a switchable electrochromic polymer based on poly(3,4-propylenedioxythiophene-*co*-4,7-benzothiadiazole) with an absorption maximum centered at 620 nm to induce an LSPR shift in AgNCs.[269] However, due to the low oxidation potential of silver, the fully oxidized state of most ECPs cannot be accessed, which undermines the attainable LSPR modulation. The overall electrochemical stability can be improved by utilizing electron-rich ECPs with high HOMO (highest occupied molecular orbital) values and low oxidation potentials. Furthermore, tuning the HOMO–LUMO (lowest unoccupied molecular orbital) gap of the ECP allows shifting of the absorption maximum and the dielectric function variation to allow the modulation of LSPRs at any wavelength.[425]

In this study, we report robust electrically tunable plasmonic hybrid materials that showed reversible and stable LSPR modulation under external applied potential cycling. An electron-rich alkoxy-substituted poly(3,4-propylenedioxythiophene) [PProDOT($CH_2OEtHx)_2$], which switches from a magenta color to transmissive upon oxidation, was chosen as an electrochemically active layer (**Figure 9.1**). This polymer, termed ECP-M, was designed to have excellent solubility in organic solvents and a low oxidation potential. Chemical vapor-phase oxidative doping of ECP-M films allowed us to determine the refractive index of neutral and conductive states of the polymer by spectroscopic ellipsometry. We determined that ECP-M shows strong reversible refractive index variation of up to −0.28 in the visible and near-infrared (NIR) range and up to +0.15 at 370–540 nm when chemically oxidized. The polymer was then combined with AuNRs with extinction centered at 650 nm (in water) by using simple solution processing techniques such as spin-coating and spray coating.

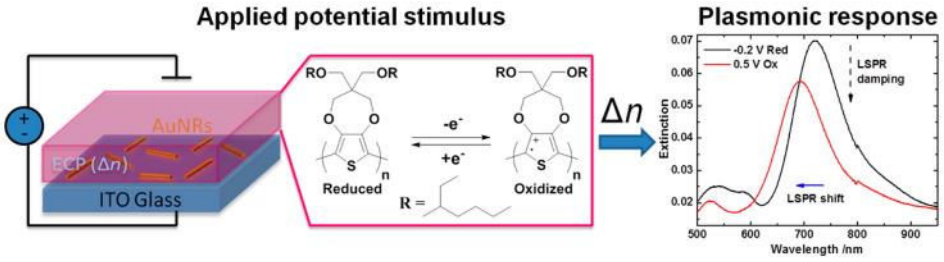

Figure 9.1: Experimental setup for electrooptical plasmon modulation with hybrid AuNR/ECP nanomaterials. A thin layer of electrochromic ECP-M material covers the gold AuNRs deposited on an ITO slide. Chemical or electrochemical oxidation results in a change in refractive index of ECP-M. The refractive index change results in modification of the AuNR LSPR band that can be observed by monitoring light absorption and scattering.

After optimizing the electrochemical conditions and polymer layer thickness, we observed a large and fully reversible 27 nm blue shift of the AuNR LSPR that can be detected in real time. This shift is an order of magnitude larger than that obtained by us previously when using a composite material prepared by a bottom-up approach from AgNCs and a blue electrochromic polymer.[269] Notably, in this report, the 40 nm ECP polymer film provided an effective and stable variable refractive index medium due to the short decay of the electric field in the vicinity of AuNRs, as further confirmed by FDTD simulations.

9.2 Experimental Details

Deposition of AuNRs on Transparent ITO Substrates: For substrate preparation, ITO slides (Delta Technologies, Ltd., 7 × 50 × 0.7 mm, sheet resistance =15–25 Ω) were sonicated in dichloromethane, acetone, methanol, and ultrapure water (Nanopure system, Barnstead, resistivity ≥18.2 MΩ·cm) for 15 min each. Washed ITO slides were dried and plasma-treated for 10 seconds with 100 mTorr air to impart a negative charge. The AuNR stock solution prepared as discussed above in water (10 mL, optical density at $\lambda_{max} \sim 1$) was concentrated via centrifugation (6,000 rpm for 15 minutes) and redispersed in ultrapure water (2 mL).

Preparation of Electrochromic Polymer Coatings: Bare ITO slides were cleaned by UV–ozone for 30 minutes prior to coating. The solution of ECP-M in toluene (1–2 wt %) was spin-cast onto silicon or ITO substrates at 1000–3000 rpm for 60 seconds. The solutions were filtered through a mesh size of 100 nm before spin-coating, and the films were dried in ambient conditions before measurements.

Polymer Oxidative Doping: Oxidation of ECP-M thin polymer films was achieved by exposure to iodine vapor for 30 seconds in a closed 20 mL vial. The films were briefly dried in air before UV–vis measurements and spectroscopic ellipsometry without intermediate washing steps. Deoxidation was performed by exposure of the oxidized thin film to hydrazine vapor (***caution:*** *hydrazine is highly toxic*). Several drops of aqueous solution of hydrazine hydrate were placed in a 20 mL test tube, which was heated to 70 °C on a hot plate. A slide with a polymer film was placed into the test tube until the recovery of magenta color (around 10 seconds of exposure time).

Finite-Difference Time-Domain Simulations: FDTD simulations were conducted with a mesh size of 0.25 nm. Individual AuNRs with a diameter of 15.2 nm and a length of 39.4 nm, based on an average of TEM measurements, were modeled on an ITO substrate. The nanorod end facets were approximated as ellipsoids with an ellipsoid radius of 15 nm. For calculation of the electromagnetic field decay length, a nanorod in water (n = 1.33) was modeled with a silica (n = 1.49) shell of varying thickness (1–40 nm).

9.3 Results and Discussion

9.3.1 *Polymeric thin films and refractive index measurements*

As a first step, we optimized the fabrication of thin films of the electrochromic magenta-colored polymer, which switches to a highly transmissive state upon electrochemical oxidation and can be converted between states by chemical redox processes (**Figure 9.2a**). The organic-soluble polymer was dissolved in toluene and spin-cast onto transparent ITO substrates as well as silicon wafers.

We observed that ECP-M formed smooth and uniform thin (60 nm) films with a root-mean-square roughness (R_q) of 1.5 nm (R_q was based on analysis of a 5 × 5 μm^2 topographical AFM image) that facilitates the fabrication of uniform materials with nanostructures and allows us to reliably determine the dielectric constants of the material (**Figure 9.2b**). Notably, the spray-coated films from the same polymer had an increased R_q of 14.7 nm (**Figure F.1**). The higher microroughness of spray-cast films makes it difficult to reliably establish the dielectric functions, and thus they have not been used here.

In situ spectroscopic ellipsometry of ECP films during electrochemical oxidation requires a complex electrochemical setup and extensive modeling due to the presence of the electrolyte solution and electrochemical cell walls.[426] On the other hand, chemical oxidative doping of thin films of electrochromic polymers can be achieved in vapor phase by use of strong oxidizing reagents such as iodine.[427] Polythiophene-based ECPs undergo oxidative p-doping with the formation of a polaron (cation radical) and, subsequently, bipolaron (dication) with an iodide anions providing charge neutrality.[428] Considering this, we suggested that chemical oxidative doping would provide a conductive form of ECP-M that will be amenable to spectroscopic ellipsometry measurements.

The high stability of the oxidized form of the polymer allows measurement of the complex refractive index of the smooth and uniform thin film. Furthermore, the polymer could be switched to its original reduced neutral state by treatment with hydrazine vapor. Indeed, exposure to iodine vapor for less than 1 min resulted in disappearance of polymer absorption in the visible range and appearance of the iodide absorption at around 400 nm,

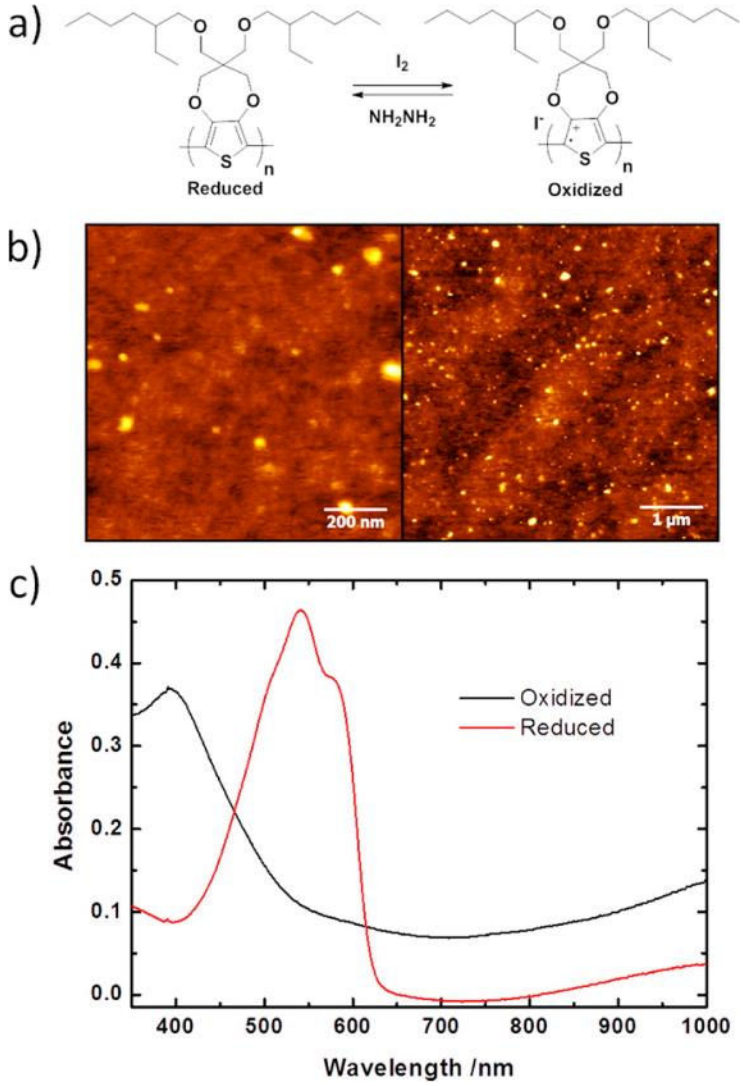

Figure 9.2: Chemical manipulation of the oxidation state of ECP-M films. (a) ECP-M repeat unit structure with oxidation by iodine and reduction by hydrazine. (b) Topographical AFM images of as-prepared ECP-M thin films. *Z*-scale is 10 nm. (c) Vis–NIR spectra of ECP-M polymer films as a result of oxidation by iodine and reduction by hydrazine.

thus confirming fast and reversible transformation (**Figure 9.2c**). In order to reliably establish the real part of the complex refractive index of the absorbing polymer in oxidized [$n(\lambda)_{ox}$] and reduced [$n(\lambda)_{red}$] states, we independently obtained the thickness of the polymer film from an AFM scratch test (158 ± 5 nm for this case). Good agreement between the extinction coefficients ($k(\lambda)$) obtained from ellipsometry and the data from transmission spectroscopy supports the validity of the data analysis (**Figure 9.2c** and **Figure 9.3a**).

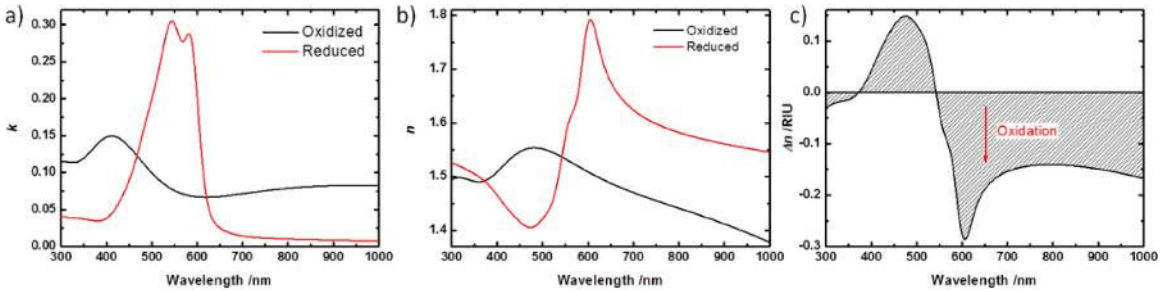

Figure 9.3: Spectroscopic ellipsometry measurements on ECP-M thin film in reduced and oxidized states. (a) Imaginary part of the complex refractive index for oxidized and reduced states of ECP-M. (b) Real part of the complex refractive index for oxidized and reduced states of ECP-M. (c) Change in real part of the complex refractive index [$\Delta n(\lambda)$] upon oxidation of ECP-M with iodine.

The difference in the real part of the refractive index between two oxidation states of ECP determines the magnitude of the LSPR shift of plasmonic nanostructures embedded in the polymer matrix.[324] Spectroscopic ellipsometry showed a pronounced change in the real part of the complex refractive index upon oxidation and reduction of the polymer (**Figure 9.3b**). The differential spectrum that shows the change in refractive index at a particular wavelength [$\Delta n(\lambda)$] was obtained by subtracting the refractive index in the neutral reduced state from that in the oxidized state [$\Delta n(\lambda) = n(\lambda)_{ox} - n(\lambda)_{red}$] (**Figure 9.3c**).

Δn changes dramatically for different wavelengths and increases from 375 to 545 nm, with a maximum increase reaching 0.15 at 475 nm (**Figure 9.3c**). The isosbestic point of the refractive index change is located at 545 nm. At higher wavelengths, the real part of the refractive index decreased after oxidation with the global maximum negative refractive index change of −0.28 observed at 605 nm (**Figure 9.3c**). These data indicate that the highest LSPR modulation could be obtained within the range of 600–700 nm that guided synthesis of AuNRs with proper aspect ratio (see below). Furthermore, oxidation of the ECP-M matrix will result in red shift of LSPRs located at 375–545 nm and blue shift of LSPRs located at higher than 545 nm wavelengths.

9.3.2 *Synthesis of gold nanorods and fabrication of nanocomposites*

In order to take full advantage of the large refractive index variation in ECP-M polymer upon oxidation and reduction, nanostructures with high refractive index sensitivity and the proper LSPR spectral position are required to maximize the refractive index sensitivity (RIS).[262] The RIS is defined as the spectral shift of the LSPR per refractive index unit change in the nanoparticle-surrounding medium. The figure of merit (FOM) is an important measure of the sensory performance of metal nanoparticles and is defined as FOM = RIS/FWHM, where FWHM is the full width at half-maximum of the plasmon peak.[17] AuNRs have strong extinction in the visible wavelength range due to excitation of the longitudinal plasmon mode. The extinction of AuNRs can be tuned by changing the aspect ratio. For AuNRs, experimental RIS values were reported to be in the range from 150 to 300 nm/RIU (refractive index unit), and the FOM value can be as high as 3 depending on the nanorod aspect ratio.[368] Although silver nanoparticles might have higher

RIS, the lack of oxidative stability makes AuNRs the nanostructures of choice for this electrochemical study.[429, 430]

We therefore synthesized AuNRs with an aspect ratio of 2.5 (median 42 nm length, 17 nm diameter) that display an extinction peak at 650 nm in water (**Figure 9.4a, c**). We employed a spray coating approach in which the aqueous solution of AuNRs was sprayed onto the ITO slides in order to form uniform films (see **Experimental Details**). AFM images show that the AuNRs were uniformly distributed with minimal aggregation (**Figure 9.4a**). UV–vis spectra of AuNR/ITO samples showed a small aggregation peak at 780–850 nm depending on the environment, but since the intensity of this peak is small compared to the monomer mode, we did not consider aggregation and nanoparticle coupling in our further analysis. It should be noted that AuNR aggregation could be induced by increasing the number of spray-coating cycles; however, such coupled systems are outside the scope of the current work. On the basis of comparison of the LSPR band position in water (677 nm) and air (626 nm), and with the refractive index difference between the two media (Δn = 0.33) taken into account, the RIS of the AuNR/ITO material was evaluated to be 154 nm/RIU, which is significantly higher than that of gold nanospheres and nanocubes (**Figure 9.4c**).[368]

Next, a thin layer of electrochromic polymer ECP-M was spin-cast on top of the AuNRs to create an electrically responsive polymer/nanorod material. In order to evaluate the plasmonic behavior and stability of these AuNR/ECP materials, we prepared them with different thicknesses (**Figure 9.5a**).

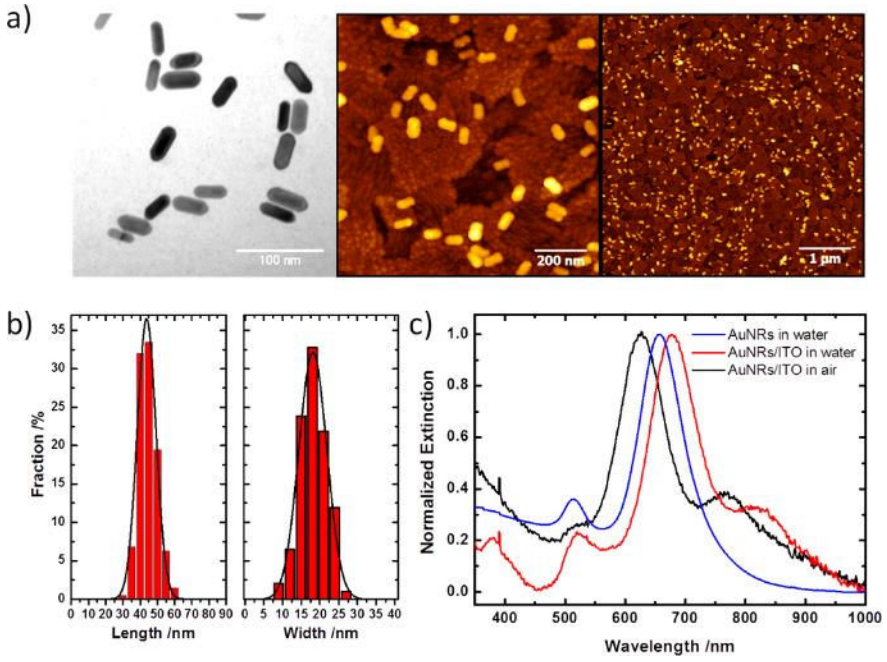

Figure 9.4: (a) (Left) TEM image of AuNRs synthesized in this study and (middle and right) topographical AFM images of AuNRs deposited on the conductive ITO substrate by spray coating. (b) Statistical distribution of nanorod length and width as determined from TEM. (c) Normalized UV–vis extinction spectra of AuNRs in water, on ITO substrate in air, and in water.

Importantly, the nanorod distribution remained intact during spin coating due to the inherent solubility difference between water-dispersible AuNR particles and organic-soluble ECP-M. We did not observe lower nanorod density after deposition of an EPC-M layer in topographic AFM images (**Figure 9.5a**). Furthermore, UV–vis spectra before and after deposition of the polymer showed neither significant LSPR broadening nor aggregation peaks (**Figure 9.5b**). Extinction spectra show that the LSPR resonance has red-shifted significantly in the AuNR/ECP film. The 96 nm red shift matches well with the difference in $n(\lambda)$ between air and the ECP-M layer (~0.62 at 710 nm) as estimated from the RIS of 154 nm/RIU (**Figure 9.3c** and **Figure 9.4c**). Importantly, since the AuNRs have

electromagnetic field enhancement mostly confined at their tips, the electric field decay length in the direction normal to the substrate is very short. Indeed, Tian et al. estimated the decay length to be 23 nm for 17 × 45 nm nanorods.[431] Therefore, a very thin polymer coating should be sufficient to have the maximum effect on LSPR resonance modulation.

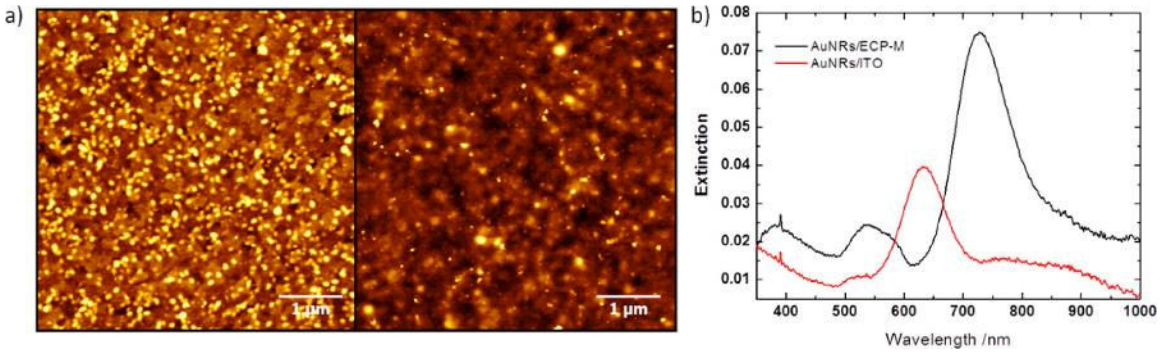

Figure 9.5: (a) AFM topographical images of AuNRs covered with 40 nm (left) and 60 nm (right) layers of ECP-M polymer. *Z*-scale is 15 nm. (b) Extinction spectrum of AuNR/ECP material (with absorbance of 40 nm polymer layer subtracted) in comparison to bare AuNRs on ITO.

9.3.3 *Electrochemical modulation of the localized surface plasmon resonance*

As was shown in **Figure 9.3**, chemical oxidation results in dramatic changes of the dielectric function in the visible and NIR parts of the electromagnetic spectrum. Due to the high sensitivity of AuNRs to the surrounding dielectric environment, a significant blue shift of the LSPR resonance can be expected as well during electrochemical oxidation of the conjugated polymer matrix. We therefore performed comparative electrochemical studies on AuNRs, ECP, and the AuNR/ECP-M material, using a three-electrode spectroelectrochemical setup for real-time monitoring of extinction spectra during application of an electric potential (**Figure 9.6**).

As a reference experiment, we first performed spectroelectrochemistry of the AuNRs adsorbed on the ITO substrate without an ECP layer. When AuNRs on ITO material were subjected to the applied potential, we observed a 3 nm red shift of the longitudinal mode as the potential was increased from −0.2 to 0.5 V (vs Ag/Ag^{+}), with a slight decrease of LSPR intensity (**Figure 9.6a, b**).

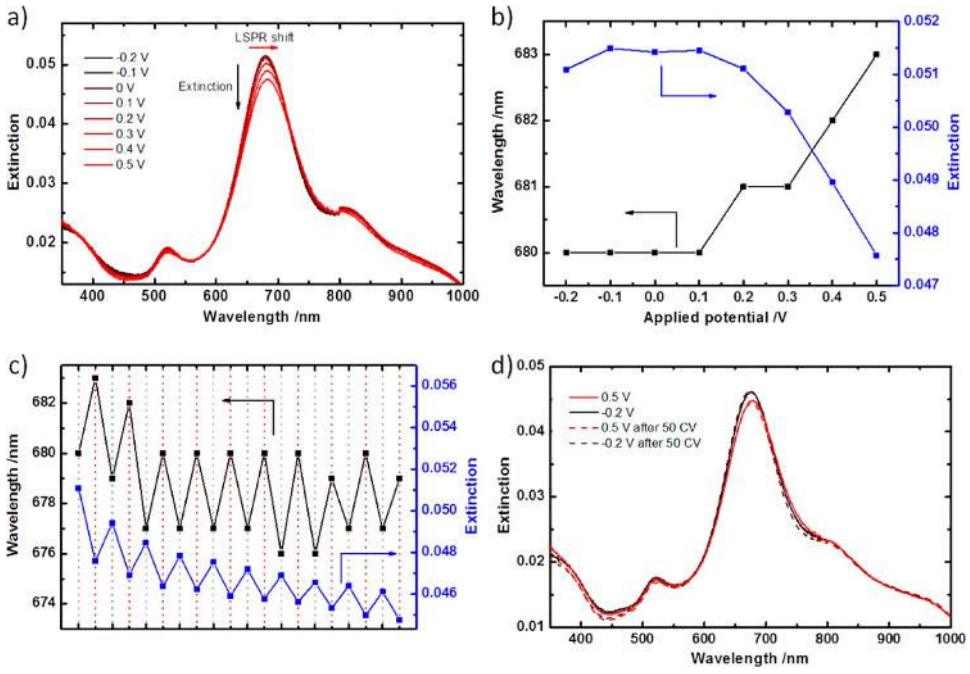

Figure 9.6: Spectroelectrochemistry experiments performed on AuNR/ITO in LiBTI/acetonitrile as an electrolyte. (a) Plasmonic response to the applied potential. (b) LSPR peak wavelength and magnitude. (c) Example of LSPR response during applied potential cycling between −0.2 and 0.5 V (vs Ag/Ag^{+}). Red dotted lines indicate electrochemical oxidation. (d) Extinction spectra of AuNR/ITO material before and after 50 cyclic voltammetry (CV) cycles that show electrochemical stability.

This very modest shift can be explained by electron transfer from the AuNR to ITO that decreases the electron density on the nanorods, as was discussed in earlier publications.[431-433] The effect is reversible and can be reproduced over more than 10 cycles. A slight

decrease in LSPR intensity was observed over 10 cycles, indicating possible nanorod desorption or partial oxidation (**Figure 9.6**c). Partial gold oxidation could also be concluded from the gradually blue-shifting LSPR wavelength, which could be a sign of nanoparticle truncation due to the presence of thermodynamically unstable high-order facets. After 50 cyclic voltammetry (CV) cycles there was virtually no difference in the extinction spectrum features, which indicates high oxidative stability (**Figure 9.6d**).

Furthermore, for benchmarking the electrochromic material, spectroelectrochemical measurements were first performed on 40 nm thin purely polymeric films that contained no AuNRs (**Figure 9.7**). In these measurements, we found that the optimal potential window for ECP-M oxidation and reduction is −0.2 to 0.5 V vs (Ag/Ag^+) when performed in 0.5 M bis(trifluoromethyl)sulfonylimide (LiBTI) in acetonitrile or in tetrabutylammonium hexafluorophosphate ($TBAPF_6$) in propylene carbonate (PC). We chose the former conditions to optimize stability as well as LSPR modulation during multiple electrochemical cycles. Upon electrochemical oxidation, the ECP-M absorption

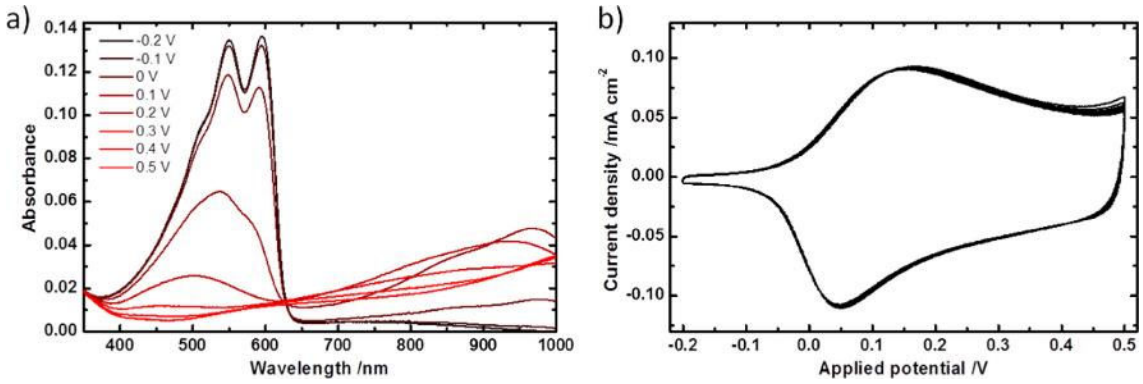

Figure 9.7: Electrochemical measurements of ECP-M on ITO. (a) Electrochromic behavior of ECP-M under applied electric potential between −0.2 and 0.5 V (vs Ag/Ag^+) in LiBTI/acetonitrile electrolyte. (b) Cyclic voltammogram of ECP-M (cycles 2–10) at 50 mV/s.

peak centered at 550 nm completely disappears when the applied potential reaches 0.5 V, and the absorbance recovers completely at −0.1 V (**Figure 9.7a**). Cyclic voltammetry (CV) was then used to characterize and evaluate the stability of the electroactive ECP-M layer (**Figure 9.7b**). The as-prepared ECP-M films show minimal current variation after 10 "break-in" cycles, which demonstrates negligible polymer dissolution.

Finally, the plasmonic behavior of AuNRs embedded within a 40 nm ECP-M layer was evaluated under the same electrochemical conditions (**Figure 9.8**). In order to extract the extinction spectrum of AuNRs, the absorbance spectra of an ECP-M layer with the same thickness was recorded under the same conditions and subtracted from the composite spectrum (**Figure 9.8b**). We found that as the ECP-M matrix was electrochemically oxidized, the LSPR peak of the AuNRs exhibited a pronounced blue shift of 27 nm.

The fully reduced hybrid material shows an LSPR peak at 722 nm at −0.2 V. When the applied potential was switched to 0.5 V in 0.1 V increments, we observed a gradual blue-shifting of the LSPR, as expected from the refractive index variation of ECP-M (**Figure 9.3** and **Figure 9.8**). Notably, this blue shift was opposite to the red shift that was observed for AuNRs without the ECP-M layer. A noticeable decrease in LSPR intensity (LSPR damping) was also observed under an applied positive potential (**Figure 9.8b, c**). The LSPR damping can be attributed to the increase in extinction of the ECP-M polaron band during electrochemical oxidation.[428] Importantly, the AuNR/ECP-M nanomaterial could be oxidized and reduced reversibly within seconds and maintained a strong LSPR response for many cycles.

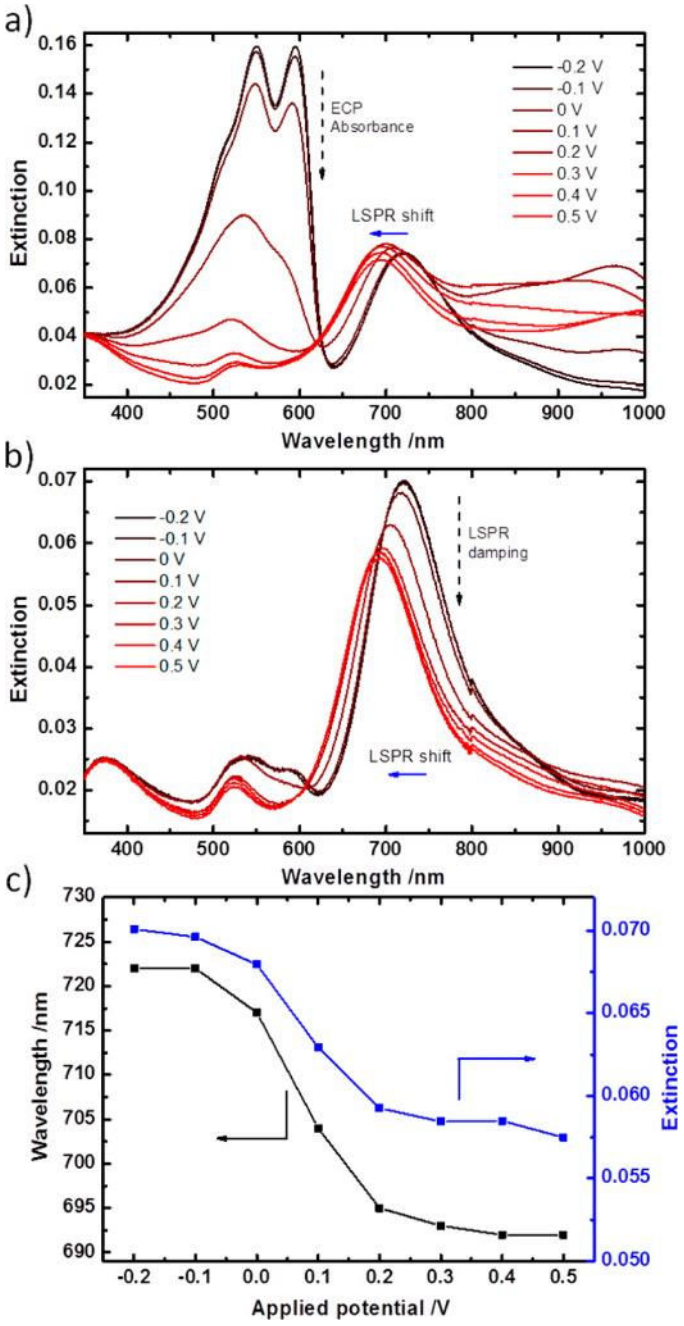

Figure 9.8: (a) Electrochromic behavior of AuNR/ECP-M films under applied potential in LiBTI/acetonitrile electrolyte. (b) Same spectra with absorbance of the polymer layer subtracted to make the LSPR contribution to the extinction more visible. (c) Extinction and LSPR wavelength changes under applied electrical potential.

The LSPR shift consistency was highest when the LiBTI/acetonitrile electrolyte was used and while the electric potential was maintained within −0.2 to 0.5 V. We achieved a stable reproducible LSPR modulation in the AuNR/ECP-M nanomaterial over 10 oxidation–reduction cycles (**Figure 9.9a**). Furthermore, the AuNR/ECP-M thin film showed full electrochemical bleaching of ECP-M visible light absorption (**Figure 9.9b**) and highly stable and reproducible CV response for over 50 cycles (**Figure 9.9c**).

Comparison of the results in **Figure 9.9a** with those in **Figure 9.6c** indicates significantly improved stability of the composite material when compared to bare AuNRs (**Figure 9.6**). We suggest that ECP-M acts as an electroresponsive material as well as a physical barrier to prevent AuNR desorption and significant gold dissolution during cycling. The polymer film thickness may have a significant impact on electrochemical behavior of the AuNR/ECP-M material. We therefore tested the electrical modulation of thicker ECP-M films (60 and 120 nm). We did not observe any difference in nanocomposite stability when thicker (60 and 120 nm) polymer films were used (**Figure F.2** and **Figure F.3**). Furthermore, the magnitude of the LSPR shift, contrary to our expectations, decreased with increasing polymer thickness (**Table 9.1**). This effect can at least be partially explained by the contribution of strong absorption of a polymer layer in the reduced (neutral) state.

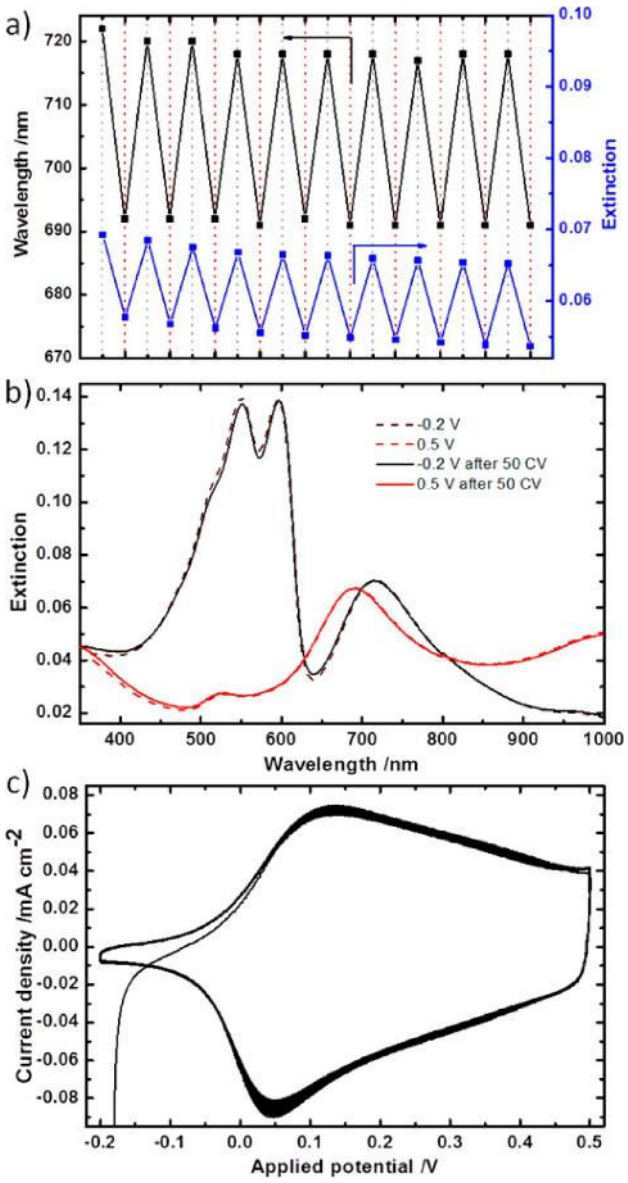

Figure 9.9: Cycling stability of AuNR/ITO material. (a) Electrochemical switching for 10 cycles in LiBTI/acetonitrile as an electrolyte. Red dotted lines indicate electrochemical oxidation. (b) Comparison of extinction spectra before and after 50 CV cycles. (c) Cyclic voltammogram of AuNR/ECP-M material (cycles 1–50) at 50 mV/s.

Table 9.1: Comparison of experimental and simulated LSPR band positions.

Sample	Reduced (nm)	Oxidized (nm)	LSPR Shift (nm)
AuNR only	677 ± 1	680 ± 1	3 ± 1
AuNR/ECP-M (40 nm)[b]	719 ± 1	691 ± 1	27 ± 1
AuNR/ECP-M (60 nm)[b]	715 ± 1	691 ± 1	24 ± 1
AuNR/ECP-M (120 nm)[b]	706 ± 1	687 ± 3	18 ± 2
Simulated extinction[a]	723	699	24
Simulated scattering[a]	723	695	28

[a] LSPR wavelength after subtraction of the polymer layer absorbance
[b] From FDTD simulations

9.3.4 *Finite-difference time-domain simulation of plasmonic phenomena*

In order to better understand the underlying mechanism for LSPR modulation, we performed FDTD simulations with dielectric constants of ECP-M obtained from spectroscopic ellipsometry during oxidative doping (**Figure 9.3**). Because the primary interest was the longitudinal LSPR band, simulations were run with only longitudinal polarization (polarization parallel to the length of the rod), resulting in the transverse peak not being visible on simulated curves (**Figure 9.10**).

Peak positions of a single AuNR on an ITO substrate in air and in water environments were found to be 622 and 677 nm, respectively, which agreed well with the experimentally obtained peaks of 627 and 672 nm (**Figure 9.4c** and **Figure F.4**). The slight red shift of the

simulated peaks can most likely be attributed to slight differences in the shape or size of the modeled nanorods. It should be noted that an aspect ratio difference of as little as 3% shifts the simulated LSPR peak by 8 nm.

For reduced and oxidized 60 nm thick ECP films overlaid on top of the AuNRs, the respective LSPR peaks were 723 and 700 nm compared to the experimentally observed 717 and 696 nm (**Figure 9.10a** and **Table 9.1**). Electromagnetic field monitors confirm that the main LSPR peak used in this study is indeed a longitudinal mode, with areas of high field enhancement located at the ends of the nanorod (**Figure 9.10c**). A 3D model based on electromagnetic field enhancement further illustrates the dipole shape of the nanorod longitudinal resonance (**Figure 9.10c**). Higher near-field enhancements were seen

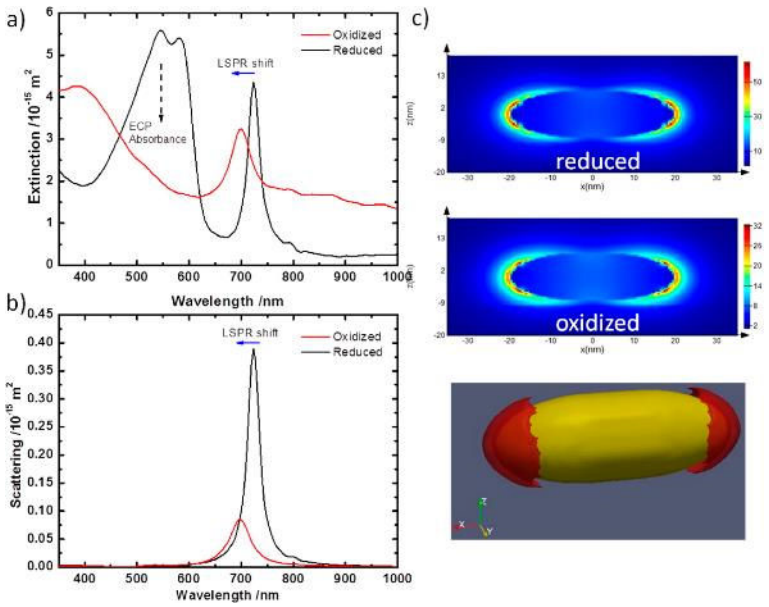

Figure 9.10: FDTD simulations of AuNR/ECP-M materials. (a) Simulated extinction spectra of ECP/AuNR material in oxidized and reduced ECP-M states. (b) Simulated scattering spectra of ECP/AuNR material in oxidized and reduced ECP-M states. (c) Effect of polymer oxidation on electric field enhancement (E/E_0) in the vicinity of AuNRs, and 3D distribution of the electric field with a value of $24E_0$ or higher for the reduced ECP-M state.

for the case of the AuNR surrounded by the reduced polymer compared to the case of the oxidized polymer, most likely due to the higher refractive index of this state that acts to more tightly confine the electromagnetic fields.

The magnitude of the LSPR shift in hybrid plasmonic systems is highest when the thickness of the dielectric layer is equal to or larger than the nanoparticle electromagnetic field decay length.[292, 316] Based on the results of spectroelectrochemical measurements, the increase in thickness of the ECP-M layer beyond 40 nm did not result in increase in the LSPR shift. Indeed, an electromagnetic field decay length of approximately 11 nm was estimated for the nanorods used in this study, based on a previous simulation method by Lu et al. (**Figure F.5**).[434] Furthermore, the electric field enhancement is closely confined to the tips of AuNRs oriented parallel to the substrate (**Figure 9.10c**). It can therefore be concluded that a very thin ECP-M coating is sufficient to induce a significant plasmon shift in AuNR/ECP-M material reported here with a total composite thickness as low as 25 nm.

9.4 Conclusions

By combining responsive electrochemical polymers with metal nanostructures that support surface plasmons, we generated a variety of electric field responses in which an electrical potential is converted to a change in light absorption and scattering. In the materials design suggested here, a refractive index variation of an electrochromic matrix caused by chemical oxidative doping is exploited to predict and study the plasmonic response of AuNRs. Spectrally matching AuNRs were synthesized that were tuned to sense the change in the oxidative state of the polymer matrix. For these hybrid materials, we achieved a significant, reversible, and reproducible LSPR shift of 27 nm thanks to a strong refractive index

variation of the electrochromic magenta-colored polymer matrix surrounding the AuNRs (Δn from +0.15 to −0.28). Notably, even the 40 nm ultrathin polymer film provided an effective refractive index medium due to the short decay of the electric field of the AuNRs.

Overall, the LSPR modulation depth and switching stability of the nanoparticle/ECP material suggested, synthesized, and fabricated in this study are much higher than those reported in other studies for responsive metal/polymer materials prepared by bottom-up approaches. We envisage that, by using this approach, a virtually unlimited number of polymer/nanoparticle combinations can be fabricated that provide tunability of LSPR bands across the visible and near-IR portions of the electromagnetic spectrum with large and readily detectable changes in light extinction. Such electrically tunable hybrid nanomaterials will be of interest as optical signal modulators and switches in plasmonic circuits, sensors, and photovoltaic devices.

CHAPTER 10. DEWETTING-INDUCED PHOTOLUMINESCENT ENHANCMENT OF POLY(LAURYL METHACRYLATE)/QUANTUM DOT THIN FILMS

10.1 Introduction

Several methods have been developed for the enhancement of PL films. Introducing photonic crystals with photonic bandgaps at the emission wavelength can lead to enhancement factors as high as 20 due to the negligible absorption or transmission that can occur at the crystal surfaces.[435-437] Purcell antennas can be formed using noble metal nanoparticles or shells that can enhance the PL of emitters as well, although this approach is very hard to control over large surface areas due to coupling interactions that may arise, and specific approaches must be tailored for different emission wavelengths.[438-442] Introducing scattering sites such as meshed surfaces,[443] microspheres,[444] and nanoparticles[445] has also proven to be an effective way of allowing more light outcoupling and higher PL by improving emission outcoupling to the far field and by reducing the amount of waveguided modes within the films. These approaches are more universal in nature and have been used with a wide variety of surfaces and architectures.

One method traditionally not considered for introducing scattering sites is the intentional dewetting of polymer thin films. Below approximately 100 nm, film interfaces with substrates are dominated by intermolecular interactions that are highly sensitive to perturbations in the environment.[446, 447] Depending on the polymer film/substrate and polymer film/air interface energy potential, films may be stable, unstable, or metastable.

[448, 449] For unstable films below a critical thickness, thermal annealing of a thin film polymer film can induce spinodal dewetting of films into patterns with a characteristic length scale. Besides directly raising the temperature above the glass transition, a polymer's chain mobility can be increased by immersing it in a poor solvent, thereby lowering its glass transition temperature.[447, 450] Solvent-assisted dewetting has also shown to enable stronger electrostatic interactions rather than weak van der Waals ones that promote faster dewetting and smaller characteristic lengths.[447, 451] While the mechanisms behind the dewetting process have been the subject of intensive research, few studies have investigated the optical properties of such dewetted films and the incorporation of other optical materials.

In this work, a facile, scalable, and fast method of enhancing QD PL on surfaces is presented. By intentionally dewetting a composite QD-containing poly(lauryl methacrylate) (PLMA) thin film with ethanol vapor, scattering sites are created and

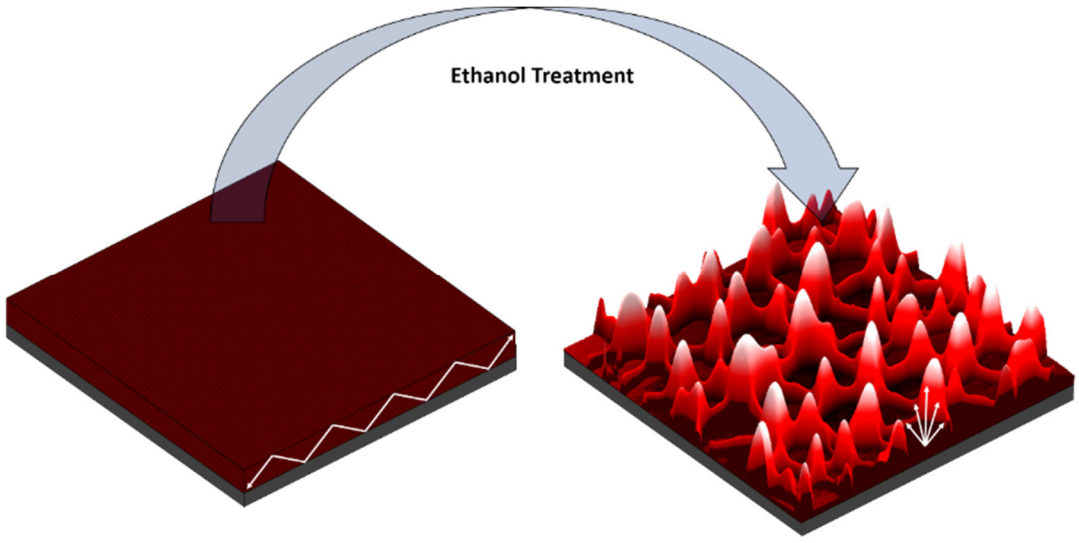

Figure 10.1: Schematic of the thin film morphology before and after ethanol treatment.

waveguided modes are broken up (**Figure 10.1**). PL enhancement factors of up to 5 over large areas (centimeter size) are realized using this method without the use of further cost- or time-intensive processes.

10.2 Experimental Details

PLMA/QD composite films: To prepare PLMA/QD composite films, 50 μL of QDs in toluene were first crashed out by adding acetone and centrifuging at 12,000 rpm for 10 min. After centrifugation, the supernatant was drained and 120 μL of PLMA of varying wt% (0.25-2%) in toluene was added. QDs were dispersed in solution by rotomixing for 30 s followed by sonication for 10 s. Longer sonication times were found to promote aggregation of the QDs. Films were then cast from solution onto silicon substrates by spin coating at 3k rpm for 30 s.

Dewetting procedure: PLMA/QD films were dewet immediately after being cast onto silicon substrates, as long dwell times promoted film adhesion to the substrate and resulted in no dewetting behavior. Films were then sprayed with ethanol using a spray gun (Iwata HP-CS) at 10 psi for 1 s in such a way that the substrate was only misted and so that the ethanol evaporated quickly. Longer evaporation times were found to lead to complete delamination of the film or irregular dewetting behavior. After treatment, films became visibly blue. For photopatterning beforehand, films were placed under a mask and exposed to a 120 W mercury arc lamp (Lumen Dynamics, X-cite series, 120Q) for half an hour.

10.3 Results and Discussion

10.3.1 *PLMA/QD film morphology*

PLMA/QD films were first characterized before dewetting to examine their thicknesses and morphologies prior to ethanol exposure. The films were found to scale roughly linearly in thickness with the PLMA concentration in solution as expected, with thicknesses of 9, 20, 26, 48, and 116 nm for respective PLMA solution concentrations of 0.25, 0.5, 0.75, 1, and 2 wt% (**Figure 10.2a**). The corresponding RMS surface roughness was found to decrease from 3.3 nm to 0.9 nm with an increase in film thickness from 0.25 wt% to 2 wt%, which is most likely due to QD aggregations being more fully encompassed within the films (**Figure 10.2b**). In a 0.5 wt% film for instance, PLMA/QD film surfaces appear mostly uniform but do display some aggregation and a 2.9 nm RMS roughness (**Figure 10.2c**). Corresponding AFM phase images also reveal slight phase separation within the film between the PLMA and QDs, although separation distances are below the diffraction limit and do not appear to alter the optical properties (**Figure 10.2d**).

Upon 1 s exposure to ethanol vapor and subsequent drying, PLMA/QD film morphologies were found to dewet in a manner dependent on the initial thicknesses of the films. In contrast, thermally annealed films dewet over much longer time periods of minutes or hours. It should also be noted that films aged >24 h in air became stable, most likely due to the evaporation of residual solvent, and did not display dewetting behavior. 0.25 wt% film features could not be resolved optically, although the dark field image appeared blue and composed of many scattering sites (**Figure 10.3a**). AFM images reveal a droplet morphology commonly associated with the dewetting behavior of very thin films (**Figure 10.3b**).[449] Micron-sized “coffee rings” are apparent as well that can be attributed to the

ethanol vapor droplet evaporation, although no differences in morphology or QD concentration were seen between ring centers and edges.

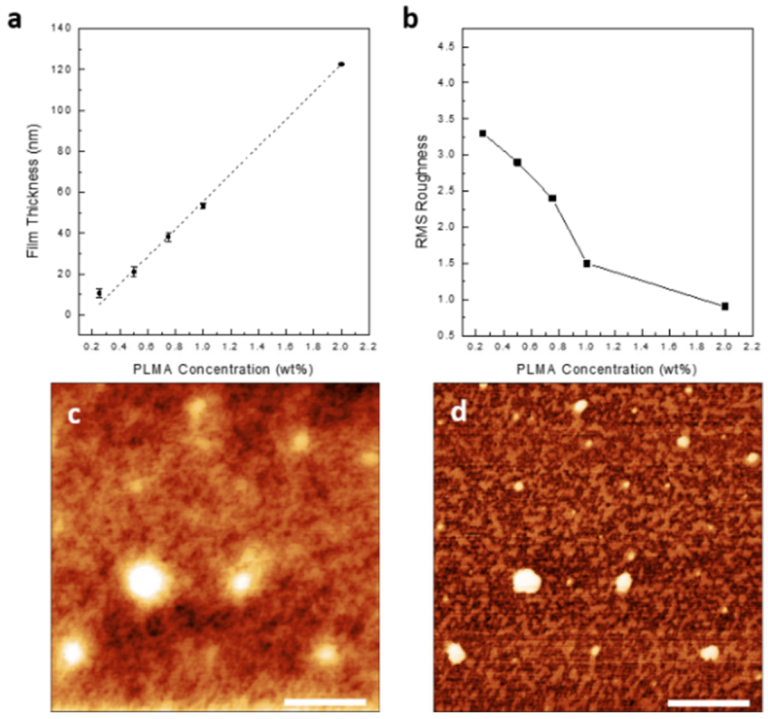

Figure 10.2: (a) PLMA/QD composite film thickness as a function of PLMA wt% in solution before spin coating. (b) AFM topography of a 0.25 wt% PLMA/QD film. The Z-scale is 14 nm. (c) Corresponding phase image. Scale bars are 500 nm.

The 0.5, 0.75, and 1 wt% PLMA/QD films all displayed network-like Voronoi patterns consistent with spinodal dewetting before droplet formation (**Figure 10.3c**,**d** and **Figure G.1**). Such patterns arise due to the interfacial energy between the film and the substrate and variations in local film density, which lead to variations in the Hamaker constants and areas of high conjoining pressure.[452] Due to the increased thickness of the films and therefore the weaker energies between the film/substrate and film/ethanol interfaces, films did not form into droplets as seen for the 0.25 wt% film. Maximum feature heights were

seen to drastically increase after dewetting and were found to scale linearly with the initial film thickness (**Figure G.2**). The dark field image of the 1 wt% film also depicts several areas of the film that did not completely dewet, as evidenced by their lack of scattering despite the same Voronoi pattern elsewhere (**Figure G.1**).

The 2 wt% film exhibited little dewetting, and ethanol vapor exposure only resulted in the random formation of holes with a uniform diameter, which can be attributed to the much

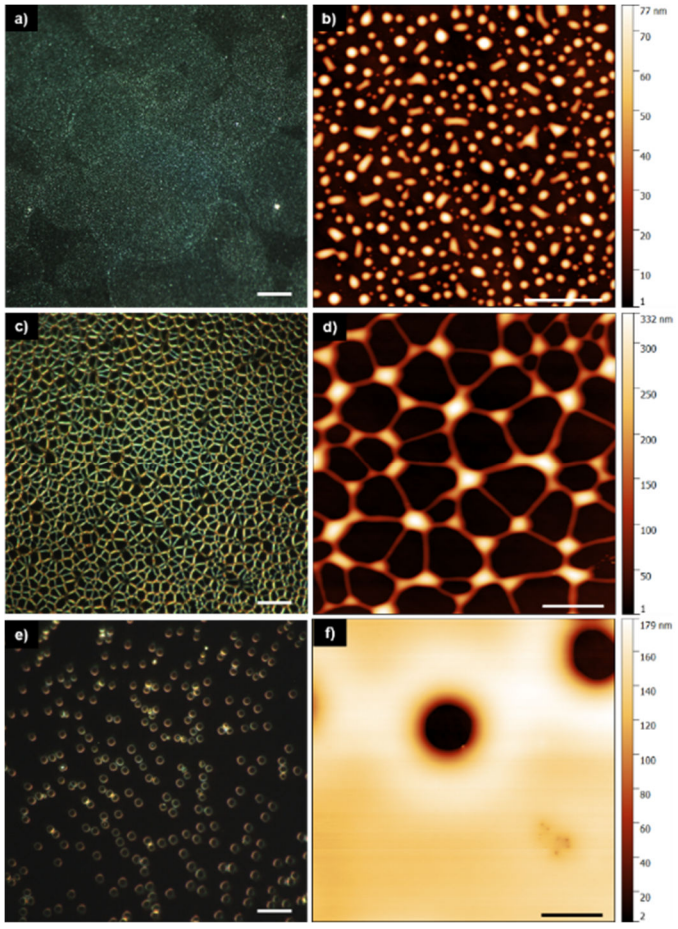

Figure 10.3: Dark field and corresponding AFM images of PLMA/QD films after dewetting with PLMA solution concentrations of (a), (b) 0.25 wt%, (c), (d) 0.75 wt%, and (e), (f) 2 wt%. Scale bars are 35 µm for the dark field images, 5 µm for (b), and 10 µm for (d) and (f).

larger thickness of the film and consequently its higher resistance to dewetting. Such dewetting behavior is independent of the global spinodal process and more indicative of local defect nucleation.[449] In this case, the excess composite material is not driven to areas of high conjoining pressure but instead deposits as rims around the holes (**Figure 10.3e, f**).

For all films, it should be noted that the volume of the films stayed approximately the same before and after the dewetting process (**Figure G.3**); volumes after dewetting are slightly larger than before, but this effect can be attributed to AFM tip convolution when measuring the dewetted samples. Importantly, this observation indicates that no portion of the PLMA/QD film completely dewets from the substrate during ethanol treatment. The dewetted 0.25, 0.5, and 0.75 wt% films also exhibited increasing respective characteristic length scales of 1.2, 4.8, and 8.29 μm as derived from the FFT transformation of the AFM images. Apart from confirming a feature size increase with a corresponding film thickness increase, the characteristic lengths are seen to scale linearly similarly to the maximum feature size. The 1 wt% film however featured a similar characteristic length to that of the 0.75 wt% film of 8.18. This observation may indicate a maximum feature size of the dewetting process, and further film thickness increases may result solely in dewetting inhibition, as seen with the 1 wt% film dark field image (**Figure G.1**).

10.3.2 *Dewetting-induced photoluminescent enhancement*

Upon exposure to ethanol vapor, the drastic film morphology changes seen in scattering affect the PL properties as well (**Figure 10.4a, b**). It is apparent that the regions that correspond to high amounts of scattering also correlate with high PL. While the increased brightness of the scattering sites can partially be attributed to higher volumes of material

in these areas, the PL remains higher than that before dewetting over averaged surface areas (**Figure 10.4c**). The mechanism behind this enhancement is proposed to be a reduction of internal waveguiding within the film and a corresponding increase in scattering that result in improved far-field outcoupling (**Figure 10.4d**). Indeed, previous studies have demonstrated the effectiveness of polymer/QD composites for waveguiding even under perpendicular excitation.[208, 209] The enhancement effect was also determined to be relatively unaffected by the excitation wavelength and solely a result of the polymer reconfiguration, as a pure film of QDs exposed to ethanol vapor did not display any PL enhancement (**Figure G.4** and **Figure G.5**). The scattering spectra of the dewet PLMA/QD films also do not overlap with the QD emission, as is required for photonic crystal

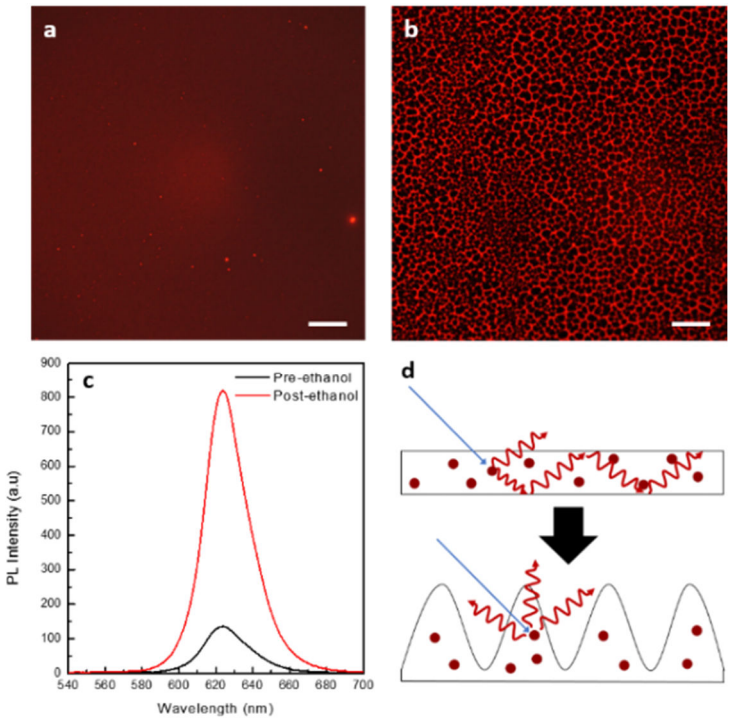

Figure 10.4: (a) 0.5 wt% PLMA/QD thin film before dewetting. (b) 0.5 wt% PLMA/QD film after dewetting. Scale bars are 35 µm. (c) PL intensity of films before and after ethanol treatment. (d) Proposed mechanism for PL enhancement.

enhancement, meaning this process can be facilely applied to many different systems and materials.

The effect of composite film thickness on the dewetting-induced photoluminescent enhancement can be seen in **Figure 10.5**. The 0.25, 0.5, 0.75, 1, and 2 wt% PLMA films display corresponding PL enhancement factors of approximately 3-, 4-, 5-, 2-, and 1-fold. Composite film thicknesses below 1 wt% PLMA (9, 20, and 26 nm-thick films) are seen to exhibit the largest PL enhancements upon dewetting, as thicker films do not dewet completely from the surface and consequently exhibit lower amounts of scattering (**Figure G.6**). This variation in the dewetting behavior also resulted in larger PL enhancement variability for the 1 and 2 wt% films, as seen by their corresponding intra-sample standard deviations (**Figure 10.5a**).

The loading of the QDs in a PLMA/QD film with a fixed PLMA wt% was also seen to affect the PL enhancement properties (**Figure 10.5b**). In a 0.5 wt% PLMA solution, QDs were loaded with concentrations of 1.56, 3.12, 4.69, 6.25, and 12.5 mg/mL. Composite films with higher loadings were found to benefit less from the dewetting process, with average enhancement factors being 3-5 for concentrations below 6.25 mg/mL and 2-2.5 for 6.25 and 12.5 mg/mL. Most likely, composite films with higher loadings exhibit naturally larger amounts of scattering due to an increased number of defects in the as-spun films and thus benefit less from the dewetting process, although the enhancement is still notable.

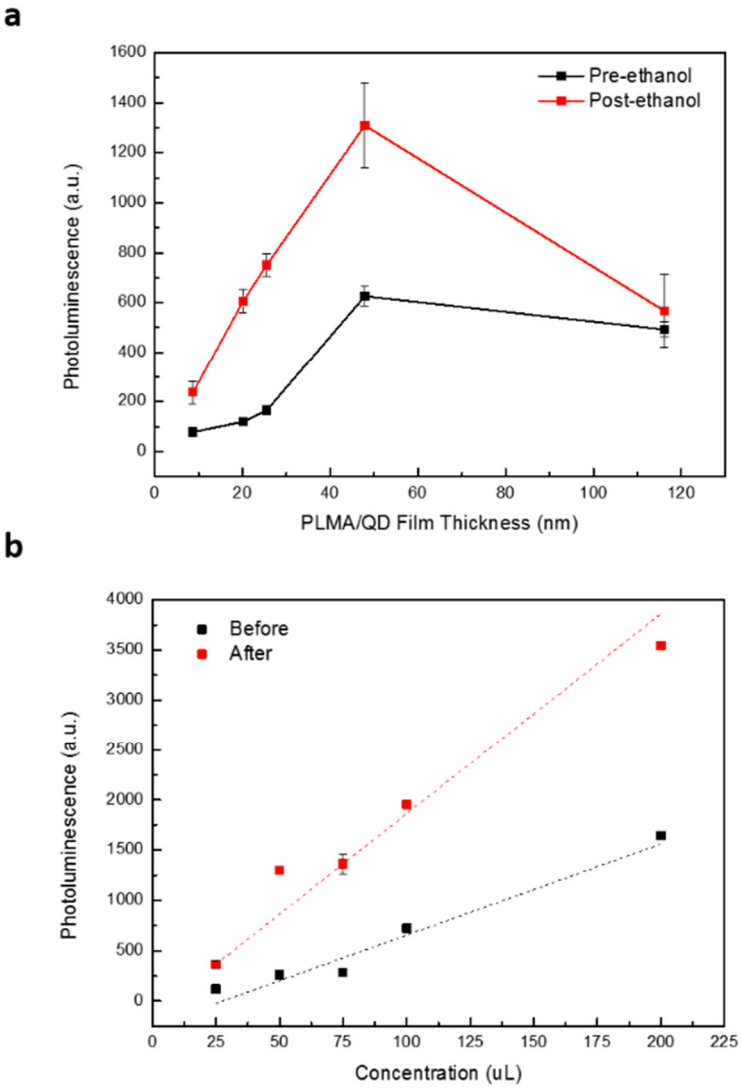

Figure 10.5: (a) PL as a function of initial PLMA/QD film thickness, with the concentration of QDs fixed. (b) PL as a function of the QD concentration, with the initial PLMA/QD film thickness fixed.

10.3.3 *Dewetting-based photopatterning:*

Because the PL enhancement is correlated with the dewetting behavior of the film, one can easily pattern areas of enhanced PL by modifying the film adhesion strength with the substrate. One possible route is by exposing films to light through a photopattern mask (**Figure 10.6a**). This process is able to selectively modify the polymer layer by light absorption in a manner analogous to baking by removing residual solvent and promoting surface adhesion. Baking processes were avoided due to the possibility of creating defects in the QDs at high temperatures and the limited spatial resolution achievable by heat transfer methods. Directly after light exposure, patterned areas of the film exhibited no PL enhancement or reduction, signifying that the QDs themselves are stable enough to remain unaffected by the exposure process. In contrast, less stable QDs such as CdSe/ZnS core/shell ones have exhibited PL enhancement after light exposure due to defect passivation mechanisms. It should however be noted that PL enhancement of QDs in this manner is short-lived and that continued exposure of QDs to light results in PL decay due to photooxidation of the shell and the formation of surface traps. After ethanol vapor exposure, the photopattern was successfully replicated in a negative manner, with exposed areas exhibiting lower amounts of PL (**Figure 10.6b**). The photopattern was also found to be replicated in dark field microscopy, further confirming that the patterning is not due to intrinsic modification of the QDs (**Figure 10.6c**). It should be noted that this patterning method is limited to micron-size features, as the dewetted polymer patterns themselves cannot be reduced in size. One significant benefit to this photopatterning process, in comparison to many photomasking techniques, is that no prior masking or templating needs

to be done with a sacrificial layer, thereby reducing the complexity of the patterning process.

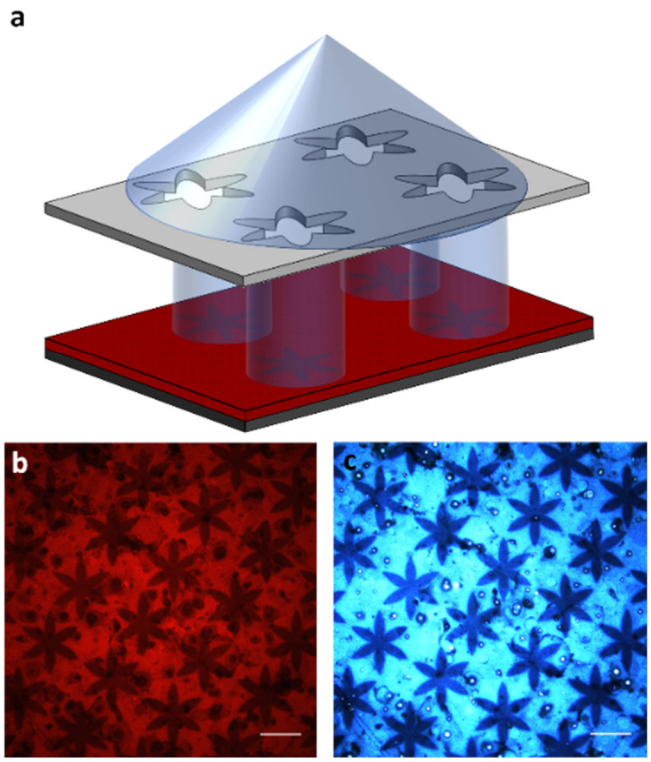

Figure 10.6: (a) Schematic of the PLMA/QD photopatterning process. (b) PL image of the PLMA/QD film after photopatterning. (c) Dark field microscopy of the same area. Scale bars are 200 μm.

10.4 Conclusions

Ultimately, we are able to demonstrate enhancement factors of up to 5 for PLMA/QD thin films, and showed that enhancement is possible for a wide range of film thicknesses and QD concentrations. Photopatterning was also demonstrated to be feasible in patterning

areas of film adhesion and dewetting, which consequently led to specifically selected areas of PL enhancement. Also, this process avoids the need for specific spectral overlaps, as in the case of photonic crystal or plasmonic systems, and it can be done easily in a quick and large-scale manner.

CHAPTER 11. GENERAL CONCLUSIONS AND BROADER IMPACT

11.1 General conclusions and discussion

Generally, this work focused on understanding and developing plasmonic and semiconductor nanostructure assemblies with novel, assembly-dependent emergent optical properties. In particular, the coupling behavior of metallic nanostructures as well as the combination of metallic or semiconducting nanostructures with polymeric components was stressed.

Important objected focused on were:

1. Understanding the nanostructure assembly fundamentals that can result in broadband absorbing plasmonic nanostructure assemblies through controlled coupling and assembly behavior;
2. Gaining insight into the various morphologies of conjugated polymer and plasmonic nanostructure composites and how their combination can be utilized for reversible and stimuli-responsive absorption and scattering spectra;
3. Examining the morphology of quantum dot/polymer composite films and how their interfacial properties can be altered for the enhancement of quantum dot fluorescence using polymer-mediated far-field coupling techniques.

This work also provides a general framework for the study of optical materials and assemblies. Major themes present throughout the work detailed here included:

1. Controlled coupling interactions between noble metal nanostructures through the use of polymeric materials and the governing of monolayer nanoparticle density;
2. Thorough characterization of material optical properties and the correlation of nanostructure optical properties with single particle and assembly morphology;
3. An expanded understanding of nanoparticle, polymeric, and composite film behavior under a variety of environmental conditions and stimuli;
4. The use of FDTD simulations to predict and confirm plasmonic phenomena as well as to elucidate the nanoscale fundamental interactions that these phenomena can be attributed to.

Specifically, the coupling of AgNCs with a nanogroove-containing gold film using a polymer spacer layer was demonstrated to provide **high broadband absorption in the visible-near-infrared range over a wide range of incident light angles**. These component nanostructures were shown to spectrally and spatially complement one another to result in a multiplicative absorption enhancement. Importantly, the absorption properties were demonstrated to be heavily influenced by the groove width, as grooves that were smaller than AgNCs had their resonances partially suppressed. The coupling of AgNCs to each other was also shown to be beneficial for broadband absorption by blueshifting the AgNC LSPR away from the nanogroove resonance. These findings were supported by FDTD simulations on the effects of nanocube coupling and nanogroove parameters on their resultant reflection properties.

The extension of broadband absorption to a TIR framework was accomplished using an AgNC aggregation gradient. AgNC aggregates were demonstrated to possess optical signatures covering a wide range of the visible spectrum under TIR conditions with low

surface coverages. Interestingly, such layers were found to possess a **highly polarization-selective and angle-dependent broadband absorption** over the visible wavelength range. The combination of plasmonic nanostructures with conjugated polymers to create stimuli-responsive nanostructures was thoroughly investigated and improved upon during the course of this work. Responsive assemblies were fabricated using a variety of nanoparticles and stimuli-responsive materials. Specifically, light- and electrically-responsive polymers and compounds were used with plasmonic nanoparticles to create tunable and reversible extinction signatures. An emphasis was placed on creating stable assemblies using nanoparticles with high refractive index sensitivities and polymers or compounds that demonstrated large reversible changes in their refractive properties.

P3HT-coated AgND assemblies were used to achieve ultrathin and electroactive assemblies for LSPR modulation. The role of AgND coupling within the assemblies was investigated for a wide range of nanoparticle monolayer densities to determine the **optimal coupling regime for electrochemical LSPR modulation of AgND monolayers**. It was discovered that moderate nanoparticle densities perform better than low densities due to an increase in hot spots within the layer. Importantly, it was also demonstrated that high densities result in a drastic decrease of the LSPR modulation capabilities due to LSPR delocalization across the monolayers.

Light-sensitive compounds were synthesized and combined with AgNCs to create **light-driven extinction modulating films**. The use of **novel light-responsive compounds** was reported along with their kinetics in films and solutions. When combined with AgNCs, the compounds resulted in higher LSPR modulation than the combination of AgNCs with simple azobenzene moieties.

Separately, AuNCs were combined with PANI shells to create composite **electrochemically responsive nanoparticles that were isolated from all resonance-shifting coupling interactions**. The polymerization of PANI around AuNCs was demonstrated to result in polymeric shells with a controllable thickness governed by the number of polymerization cycles conducted. Thicker shells were found to result in a higher degree of LSPR modulation with the tradeoff of an increased particle size. In a significant single particle study, the LSPR peaks of AuNC/PANI monomers and dimers were found to exhibit the same peak wavelengths and LSPR shifts upon an applied potential, thereby confirming the PANI shells simultaneously prevent coupling interactions between AuNC cores while also serving as a variable refractive index environment.

In a similar manner, AuNRs were combined with a novel ECP to form composite films that exhibited **high and reversible electrically-controllable LSPR modulation**. In this study, an ECP was specifically synthesized with a low oxidative potential and a large refractive index change at the AuNR LSPR peak wavelength. Due to the AuNR's high RIS along with the low potential necessary for the polymer to oxidize, stable and large LSPR modulations were achieved.

Finally, the **dewetting behavior of QD/polymer composite thin films** was utilized to increase PL outcoupling. In contrast to thermal annealing, poor solvent exposure provided a fast reconfiguration of the film over large centimeter-sized areas. The increase in scattering sites led to a proportional increase in the observed PL, and emissive patterns were generated by modifying film-substrate interfacial properties through light exposure. In particular, this method was able to generate **large area PL intensity enhancements in**

a facile, scalable, and universal manner in comparison to other PL enhancement methods.

11.2 Significance and broader impact

Light-matter interactions on the nanoscale are increasingly important due to the rapid miniaturization of photonic elements, and noble metal plasmonic nanostructures and semiconductor QDs can both be exploited at these length scales for the respective control of extinction and emission. Importantly, both possess tunable structure-dependent optical properties that can be used for the applications such as sensing, displays, and photonic and photovoltaic elements. The confinement of light at these scales can also lead to the generation of novel properties that are not present on the macro scale, such as the absorption of noble metal nanoparticles that on the macro scale would be reflective instead.

While single nanoparticle properties are largely understood and controlled for, their assembly behavior on substrates and their proximity to other nanostructures are less understood and can drastically influence their optical properties. The major emphasis of these studies was therefore on the **furthered understanding of nanostructure assembly morphology and their resultant optical properties, with the subsequent fabrication of nanoscale assemblies with emergent broadband absorption, reversible stimuli-responsive plasmon peaks, and enhanced photoluminescent intensity**. The relationships between interfacial properties, different coupling interactions, and the large scale arrangements of substrate-bound nanoparticles on their resultant optical properties were explored and significantly clarified during the course of this work. Novel compounds

and polymers were additionally extensively optically characterized to allow their use in electromagnetic models for the elucidation of optical modes and phenomena.

Realistic FDTD simulations that took factors such as nanoparticle edge rounding, nanoparticle coupling, and the presence of surfactants and substrates were instrumental in clarifying the mechanisms behind observed assembly phenomena. For instance, long-range interparticle coupling distances between Au film-coupled AgNCs were found to result in a blueshifted LSPR spectrum and increased reflection in contrast to most aggregation-induced redshifts. Generally, fine mesh sizes of half a nanometer or less were found to be necessary for modeling the corner rounding of nanocubes and the aspect ratios of nanorods in order to reproduce experimental LSPR peak locations. Importantly, the use of periodic arrays was found to give a reliable first-order approximation of LB monolayers and their interparticle coupling modes. FDTD simulation techniques can also be used for insights into nanoparticle electric field decay lengths, and therefore their minimum shell thicknesses required to prevent interparticle coupling.

Two different routes for the fabrication of broadband light absorbers were presented. While previous work in the field had focused on utilizing metamaterials or single plasmonic components to suppress reflection, the combination of AgNCs and Au nanogroove arrays proved the feasibility of engineering a broadband absorber by **selectively combining multiple plasmonic resonances** that spectrally and spatially complement one another. The chosen design was found to be relatively insensitive to the incident excitation angle in a marked difference from several previous absorber designs. At the time, this work also resulted in **one of the highest broadband absorptions over the visible-NIR wavelength**

regime for all studies in the field. Many studies to date have improved the fabrication of broadband absorbers by applying this same core concept with various other nanostructures.

In a different design, large AgNC aggregates, while normally highly scattering, could be used to achieve high broadband absorption in the visible wavelength range by acting as a total internal reflection interface. Importantly, while the formation of SPPs on a metal film-prism interface is well-known, this study investigated the **critical optical properties of AgNC aggregates and the relationship between aggregate orientation and light phase coupling at a prism interface**. In contrast to the first design, this setup demonstrated high incident light angle and phase sensitivity that could be useful for phase filtering or angle-controlled absorbance.

The design of several different types of nanoparticle assemblies with stimuli-responsive polymers largely progressed the fabrication and understanding of such composite behavior. The determination of refractive indices of novel polymers and the examination of plasmon modes and decay lengths was also critical to the entirety of this work and serve as an excellent framework for future studies. The fabrication of AuNC/PANI core/shell nanoparticles was shown to **intrinsically prevent coupling interactions between particles while offering an electrically controllable refractive index environment**. Such fabrication methods and resultant nanoparticles could be used for highly reproducible electrochromic devices, sensors, light modulators, and solar cell components due to the preservation of the original extinction spectrum of a single nanoparticle. This work was also served as a basis for the design of AuNR/PANI core/shell nanoparticles (not discussed previously) that exhibited >100 nm LSPR shifts and pH-responsiveness due to the AuNR's higher RIS and PANI's greater refractive index variation with a pH change.

In contrast and in the **first study of its kind**, electrically controllable P3HT-coated AgND LSPR shifts were examined as a function of nanoparticle density. Intermediate AgND densities were shown to exhibit higher refractive index sensitivities than low densities due to the increased number of formed hot spots within the layer. Small interparticle distances were shown to result in a drastic decrease of the LSPR shift due to plasmon delocalization over the nanoparticle film. Extending these design principals could lead to nanoparticle assemblies that exhibit drastically increased LSPR shifts if hot spot formation is favored and delocalization is avoided, such as through the creation of dimers or higher order aggregates.

Light-responsive arrays consisting of novel light-sensitive compounds and AgNCs were introduced for light-tunable LSPR switching. While a few studies previously examined the effects of light-responsive liquid crystalline matrices and self-assembled monolayers on Au nanoparticle LSPRs, this study was the first to incorporate Ag nanoparticles with a complementary environmental refractive index change for LSPR modulation below 500 nm. Importantly, the compounds synthesized during the course of this work also exhibited **higher refractive index changes when incorporated in a polymer film than simple light-sensitive azobenzene molecules**. Although switching kinetics were on the order of minutes, the use of push–pull azobenzenes with faster photoisomerization kinetics in a similar setup could shorten the response time and shift the operational wavelength into the visible wavelength range. This study was also used to extend the TIR reflectance of plasmonic nanoparticles, as previously demonstrated with AgNC aggregates, in a light-controllable manner that could enable further optical switching and filtering applications.

Finally, the induced dewetting of QD/PLMA composite films from substrates was used to enhance film emission through the reduction of internal waveguiding and a corresponding increase in scattering. Although many past studies have focused on the specific mechanisms behind thin film dewetting, this study was **the first to apply such principles for optical property enhancement**. Importantly, the dewetting of films could be accomplished fast (less than a second), simply, and over large areas without the addition of other materials or processing steps. This work could have potential applications for light-emitting displays or devices by increasing the apparent brightness or by reducing the amount of costly nanoparticles necessary for a desired brightness level.

Overall, the integration of multiple components in nanoscale assemblies and the subsequent characterization processes presented in this work can be used to address several existing challenges in present photonic and sensor applications. For instance, current LEDs often incorporate brightness enhancing layers that promote the outcoupling of light. The dewetting of QD/polymer composite films discussed in this work may be a convenient way to natively incorporate such a layer, thereby eliminating further processing time and costs. The tunable LSPR modulation presented during the course of this work can largely serve as potential optical filters, switches, or future photonic circuit elements. Lastly, broadband absorbers can serve thermophotovoltaic or photovoltaic elements that boost their efficiency. In a recent example, a plasmonic broadband absorber was also used to generate steam under solar irradiation.[146]

Additionally, the controlled combination and assembly of noble metal and semiconductor nanostructures realized during the course of this work can serve as future frameworks for further control of light-matter interactions at the nanoscale. In particular, the use of

polymeric materials to govern assembly and coupling interactions is of import for future commercial applications for which lithography is impractical. One future direction to be explored that builds on the work presented here is the creation of ECP/QD composites for electrical control over the PL behavior. Such structures could result in reversible PL quenching depending on the absorption and emission peak overlaps and the bandgaps of the respective materials and could prove useful for optical lighting applications and responsive optical tags. Similarly, responsive emissive behavior could also be realized through the coupling of plasmonic nanostructures and QDs with stimuli-responsive polymers that shrink or swell. The switching between FRET-induced quenching and Purcell-induced enhancement depending on the nanoparticle-QD interparticle distance could result in large PL modulation.

ACKNOWLEDGEMENTS

Financial support this work was provided by a number of sources and is gratefully appreciated. Primary financial support was provided by the U.S. Department of Energy, Office of Basic Energy Sciences, Division of Materials Sciences and Engineering under Award #DE-FG02-09ER46604. Quantum dot synthesis was conducted by Prof. Lin's group with financial support from the Air Force Office of Scientific Research FA9550-14-1-0037 (Synthetic Photonics Multidisciplinary University Research Initiative: synthesis, fabrication, and development). Electrochromic polymer synthesis was conducted by Prof. Reynolds' group with financial support from the National Science Foundation CHE-1506046.

DISSEMINATION OF WORK

This work has been conveyed to the scientific community through the following publications and presentations:

Publications

1. **Geldmeier, J.**; Rile, L.; Yoon, Y. J.; Jung, J.; Lin, Z.; Tsukruk, V. V. Dewetting-Induced Photoluminescent Enhancement of Poly(lauryl methacrylate)/Quantum Dot Thin Films. *In preparation*.

2. Ledin, P. A.; Jeon, J.-W.; **Geldmeier, J. A.**; Ponder, J. F.; Mahmoud, M. A.; El-Sayed, M.; Reynolds, J. R.; Tsukruk, V. V. Design of Hybrid Electrochromic Materials with Large Electrical Modulation of Plasmonic Resonances. *ACS Appl. Mater. Interfaces* **2016**, *8*, 13064-13075.

3. Jeon, J.-W.; Ledin, P. A.; **Geldmeier, J. A.**; Ponder, J. F.; Mahmoud, M. A.; El-Sayed, M.; Reynolds, J. R.; Tsukruk, V. V. Electrically Controlled Plasmonic Behavior of Gold Nanocube@Polyaniline Nanostructures: Transparent Plasmonic Aggregates. *Chem. Mater.* **2016**, *28*, 2868-2881.

4. **Geldmeier, J. A.**; Mahmoud, M. A.; Jeon, J.-W.; El-Sayed, M.; Tsukruk, V. V. The effect of plasmon resonance coupling in P3HT-coated silver nanodisk monolayers on their optical sensitivity. *Journal of Materials Chemistry C* **2016**, *4*, 9813-9822.

5. Ledin, P. A.; Russell, M.; **Geldmeier, J. A.**; Tkachenko, I. M.; Mahmoud, M. A.; Shevchenko, V.; El-Sayed, M. A.; Tsukruk, V. V. Light-Responsive Plasmonic Arrays Consisting of Silver Nanocubes and a Photoisomerizable Matrix. *ACS Appl. Mater. Interfaces* **2015**, *7*, 4902-4912.

6. Konig, T. A. F.; Ledin, P. A.; Russell, M.; **Geldmeier, J. A.**; Mahmoud, M. A.; El-Sayed, M. A.; Tsukruk, V. V. Silver nanocube aggregation gradient materials in search for total internal reflection with high phase sensitivity. *Nanoscale* **2015**, *7*, 5230-5239.

7. **Geldmeier, J.**; König, T.; Mahmoud, M. A.; El-Sayed, M. A.; Tsukruk, V. V. Tailoring the Plasmonic Modes of a Grating-Nanocube Assembly to Achieve Broadband Absorption in the Visible Spectrum. *Adv. Funct. Mater.* **2014**, *24*, 6797-6805.

Presentations

1. **Geldmeier, J.**; Mahmoud, M.; Jeon, J.-W.; El-Sayed, M.; Tsukruk, V. V. The effect of plasmon resonance coupling in P3HT-coated silver nanodisks monolayers on their optical sensitivity. 2016 MRS Fall Meeting, Boston, MA (Poster).

2. Jeon, J.-W.; **Geldmeier, J.**; Ledin, P.; Ponder, J.; Mahmoud, M.; El-Sayed, M.; Reynolds, J.; Tsukruk, V. V. Responsive plasmonic behavior of gold nanocrystal@polyaniline core/shell nanostructures . 2016 MRS Fall Meeting, Boston, MA (Poster).

3. **Geldmeier, J.**; Mahmoud, M.; Jeon, J.-W.; El-Sayed, M.; Tsukruk, V. V. The effect of plasmon resonance coupling in P3HT-coated silver nanodisks monolayers on their optical sensitivity. 2016 Georgia Tech MSE Meeting, Atlanta, GA (Poster).

4. **Geldmeier, J.**; Koenig, T.; Mahmoud, M.; El-Sayed, M.; Tsukruk, V. V. Tailoring plasmonic modes to create a broadband absorber in the visible spectrum. 2014 Georgia Tech MSE Meeting, Atlanta, GA (Poster, **3rd place** in Nanomaterials).

5. **Geldmeier, J.**; Koenig, T.; Mahmoud, M.; El-Sayed, M.; Tsukruk, V. V. Tailoring plasmonic modes to create a broadband absorber in the visible spectrum. 2013 MRS Fall Meeting, Boston, MA (Poster).

6. Koenig, T.; **Geldmeier, J.**; Santer, S.; Tsukruk, V. V. Controlled topographic change of subdiffraction structures based on photosensitive polymer films induced by surface plasmon polaritons. 2013 MRS Fall Meeting, Boston, MA (Poster).

7. Koenig, T.; **Geldmeier, J.**; Geryak, R.; Tsukruk, V. V. Theoretical and computational modeling of complex aggregated nanoparticles in soft matrices. 2013 MRS Fall Meeting, Boston, MA (Poster).

APPENDICES

Appendix A: Chapter 4 Supporting Information

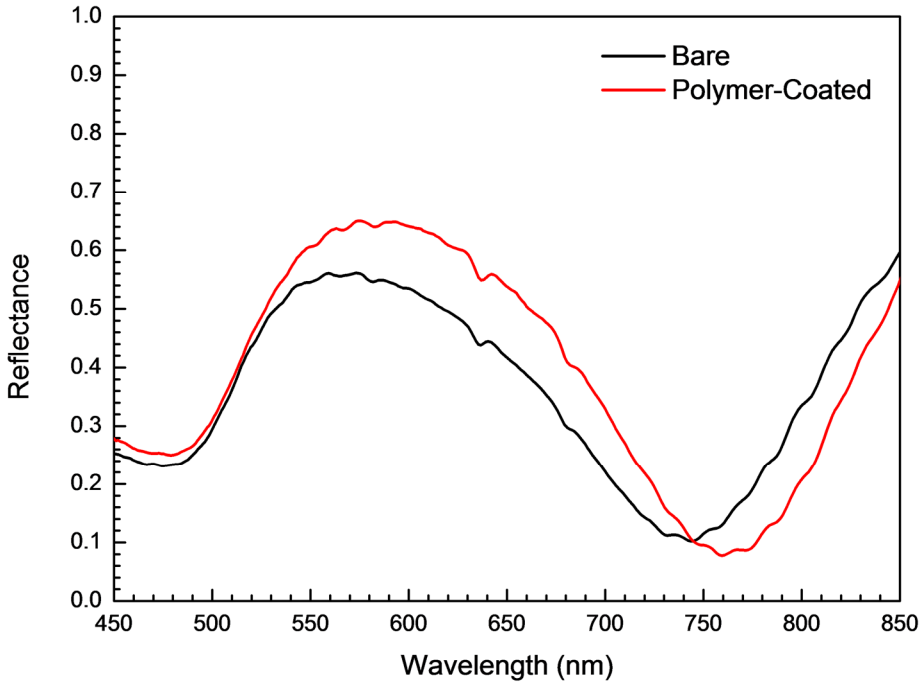

Figure A.1: Experimental spectra for a nano-grating before and after deposition of the polymer dielectric bilayers.

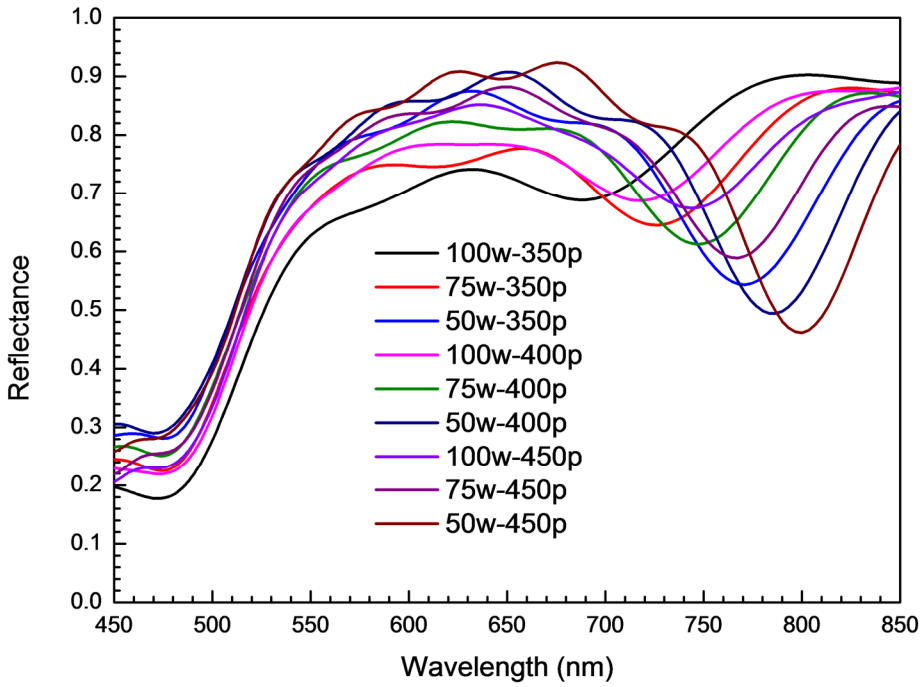

Figure A.2: Simulated spectra for all groove widths and periodicities of the nano-gratings. Peak positions closely match experimental values but display higher reflectance values overall due to the effects of imperfect periodicities and the finite size of the arrays.

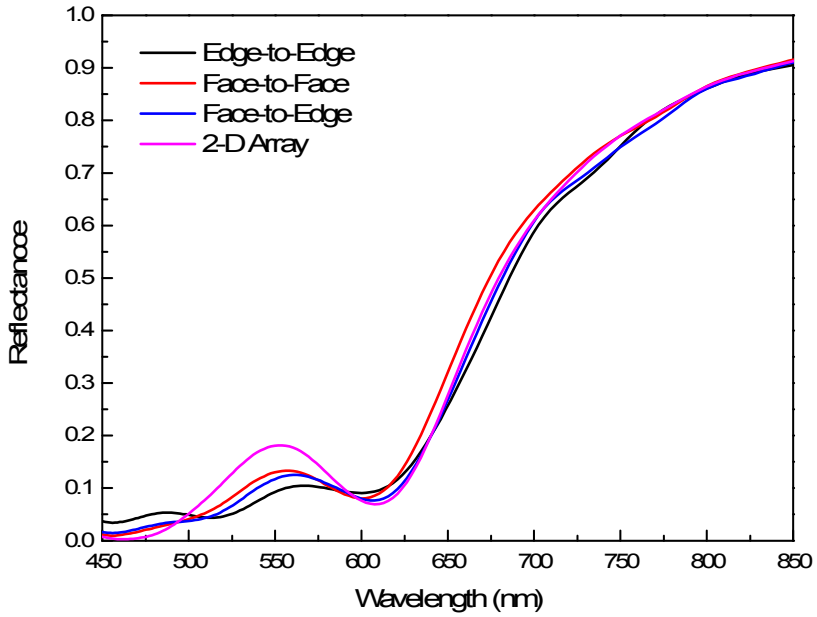

Figure A.3: Simulated spectra for 1-D nanocube arrays with face-to-face, face-to-edge, and edge-to-edge orientations for an interparticle spacing of 125 nm and a 2-D nanocube array with an interparticle spacing of 150 nm.

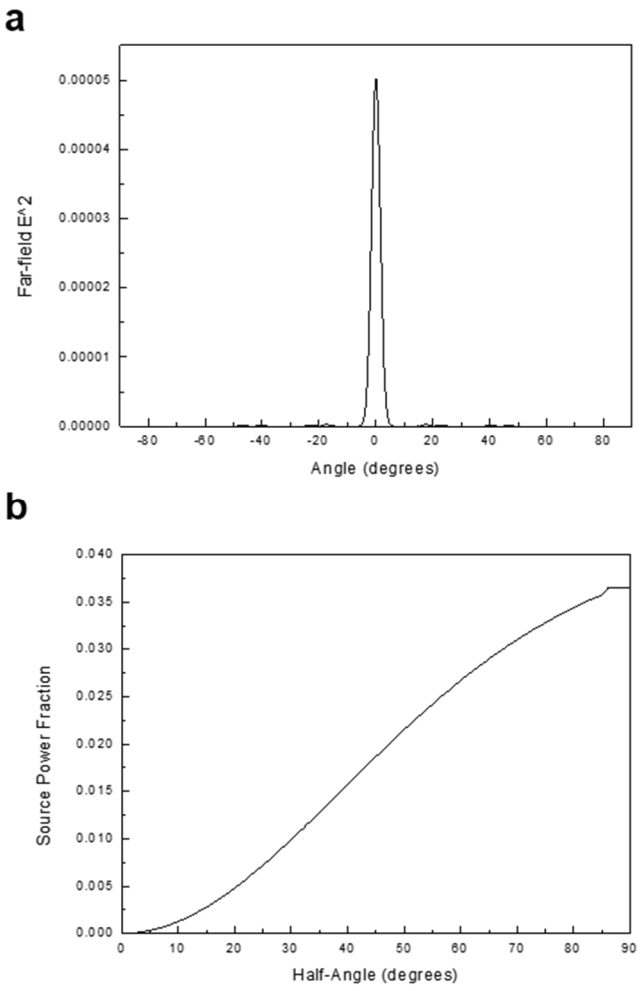

Figure A.4: a) The far-field electric field intensity of the 2D nano-grating peak resonance as a function of angle. b) The far-field source power fraction of coupled nanocubes on a substrate as a function of half-angle for an integrating cone. Both simulations result in less than a 5% loss of power between the near-field monitor and the far-field collection region with a numerical aperture of 0.3 (~17°).

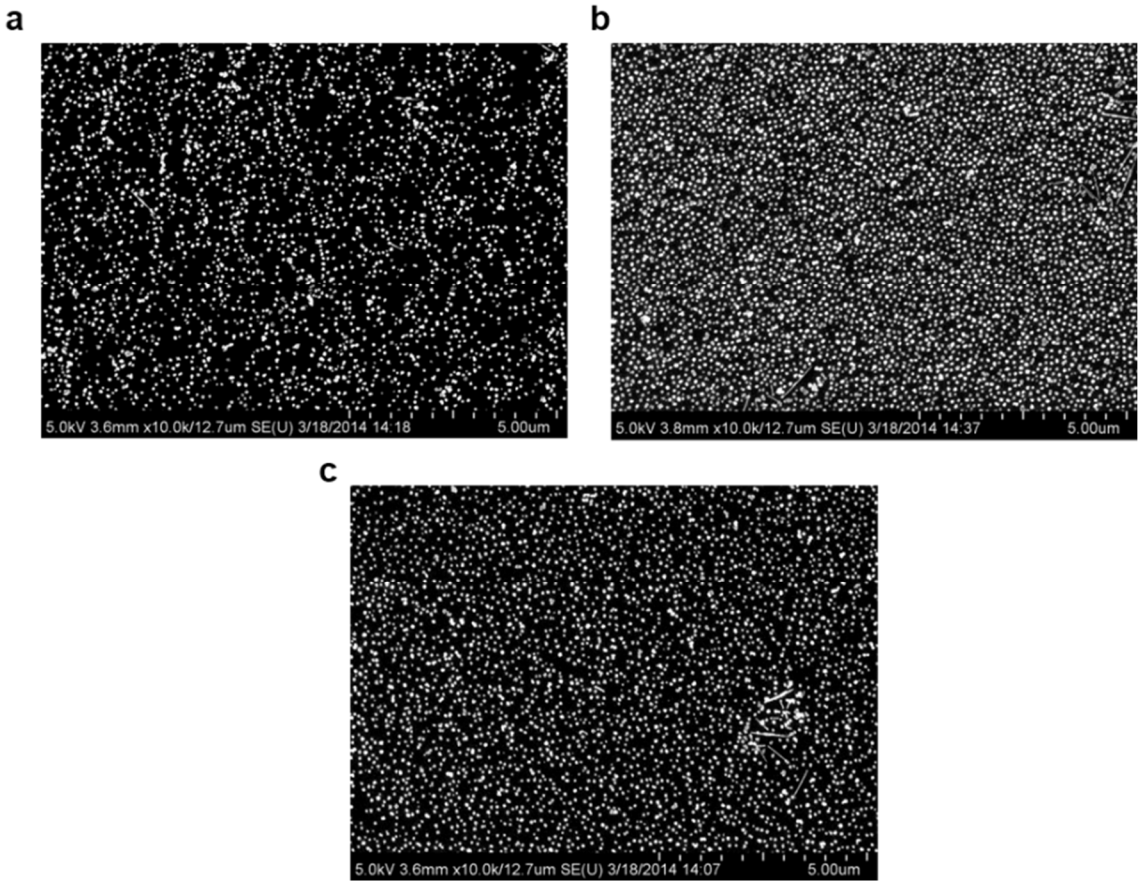

Figure A.5: High-contrast SEM images of a) 12%, b) 15%, and c) 22% nanocube surface densities. Images were used to calculate both surface coverage and interparticle distances after being binary thresholded.

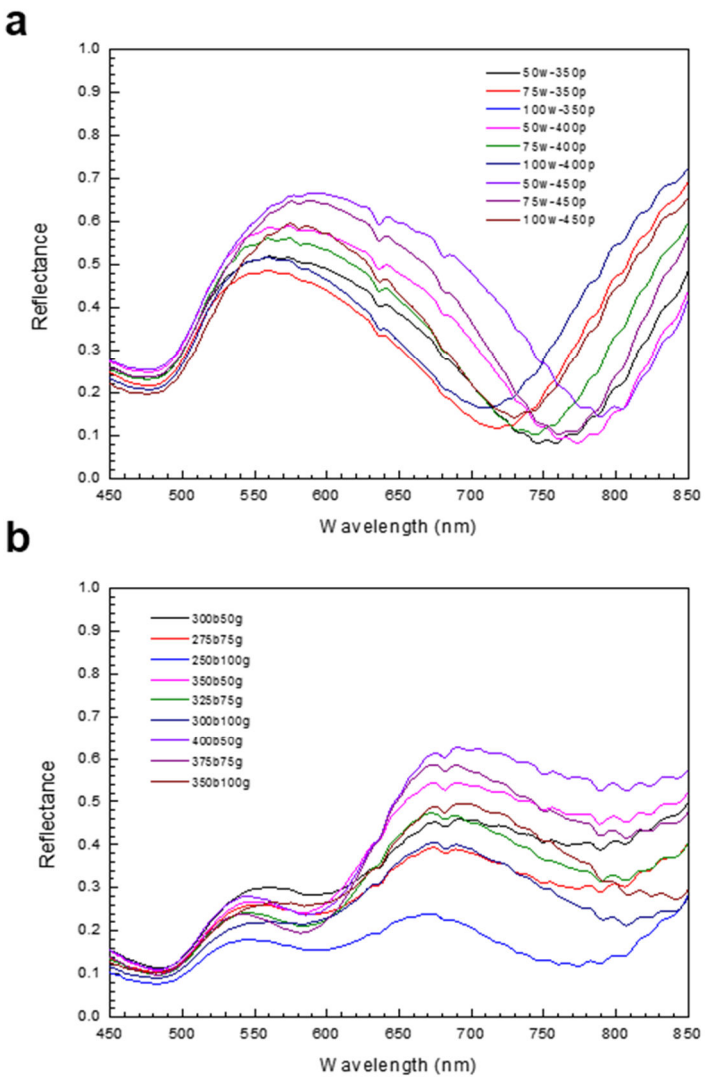

Figure A.6: Experimental spectra for all groove widths and periodicities of a) the nano-gratings and b) the grating-nanocube assemblies.

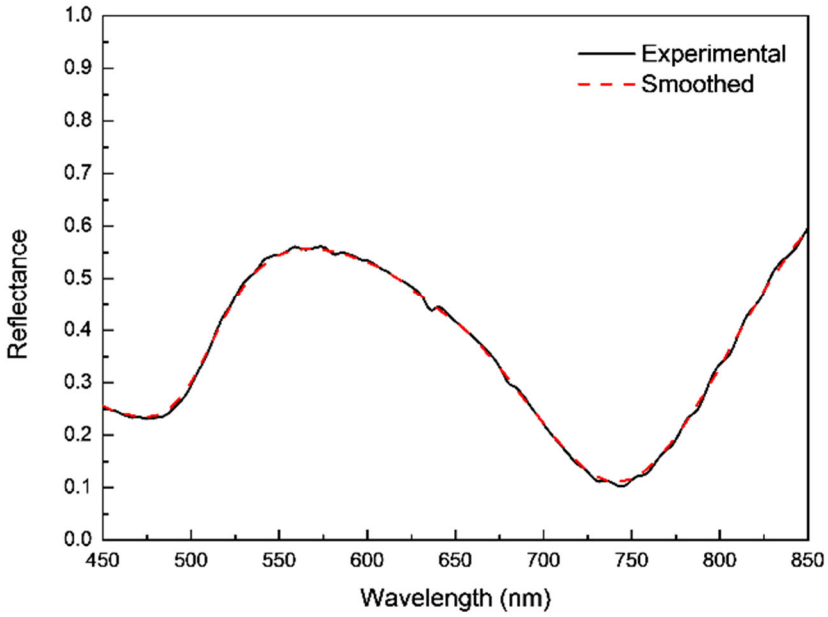

Figure A.7: Example of smoothing performed on an individual nano-grating spectrum (75w-400p). Spectra were smoothed using adjacent averaging over a 20 nm to eliminate instrumentation and normalization effects while still preserving all spectra features.

Appendix B: Chapter 5 Supporting Information

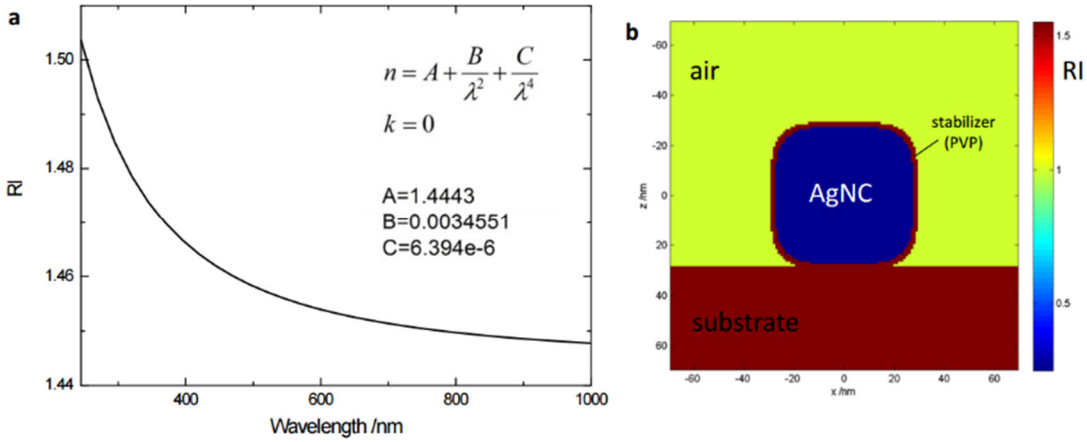

Figure B.1: (a) Refractive index (n) of quartz glass (purchased from ChemGlass) as determined from ellipsometry data by Cauchy model (units for λ in μm). (b) Measured substrate refractive index inside the simulation setup shown with an AgNC coated with 2 nm stabilizers and 25% edge/corner rounding. Refractive index cross-section image at 400 nm wavelength and 1 nm mesh size (image resolution).

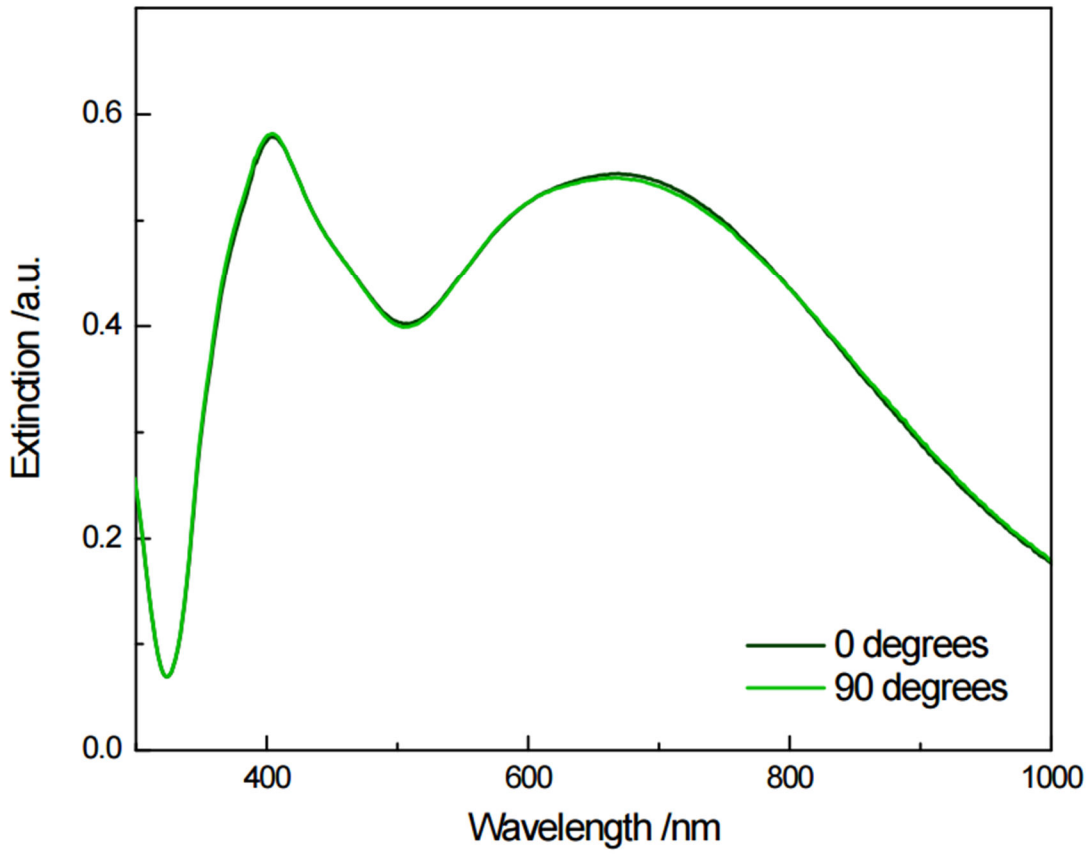

Figure B.2: UV-Vis measurement of the 12 mN/m sample in two different mounting condition relative to the incoming light (rotation axis).

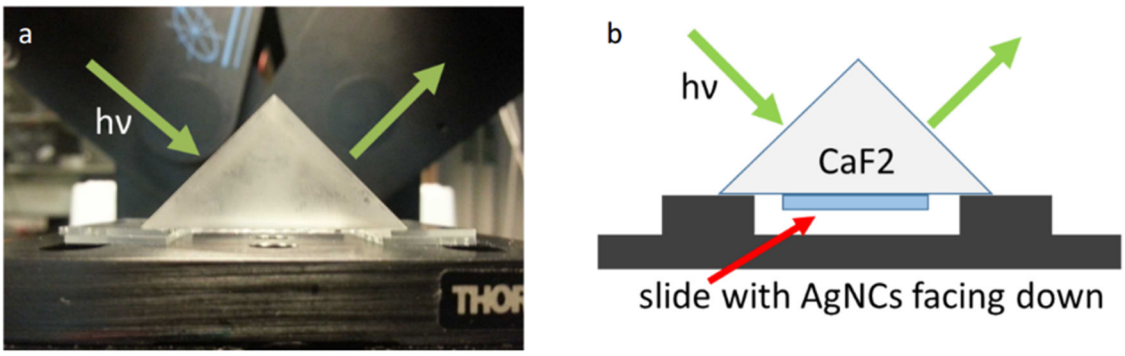

Figure B.3: (a) Photograph of TIR setup on spectral ellipsometer and (b) schematic of the experimental apparatus.

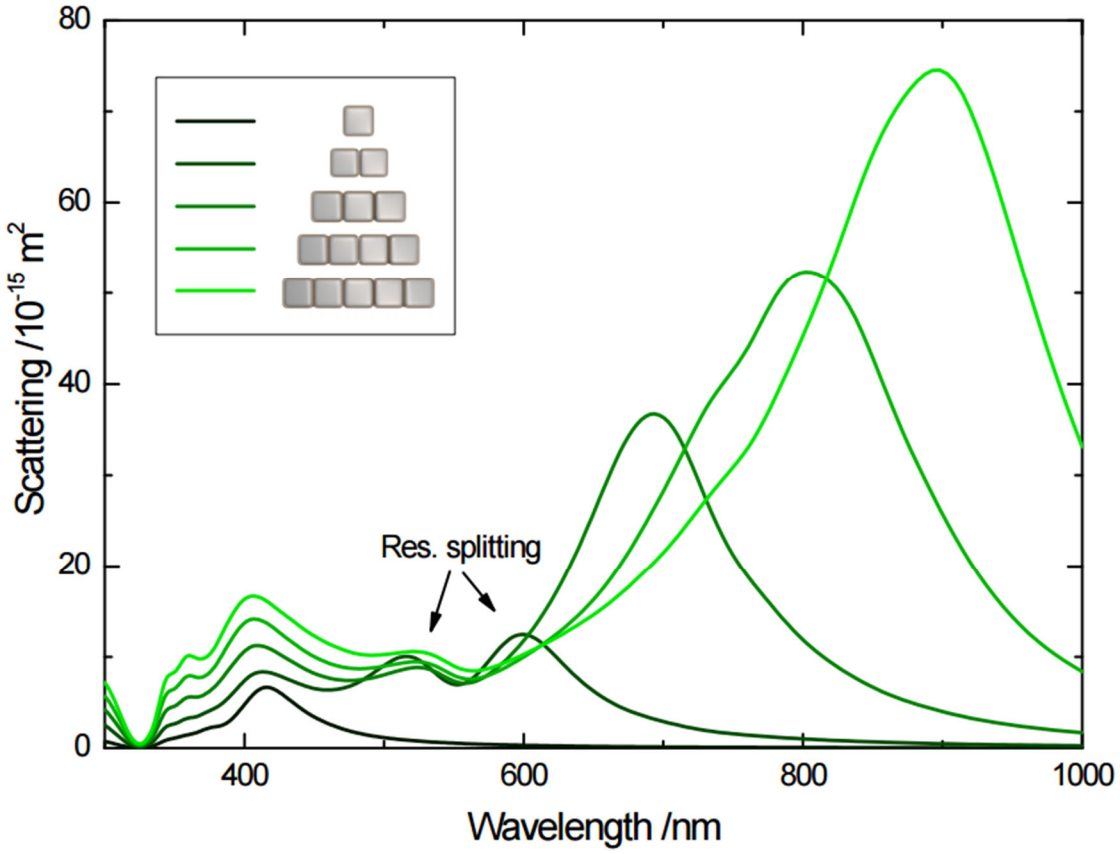

Figure B.4: Simulated scattering cross-sections of different aggregation types with an inter-particle spacing of 2 nm.

Appendix C: Chapter 6 Supporting Information

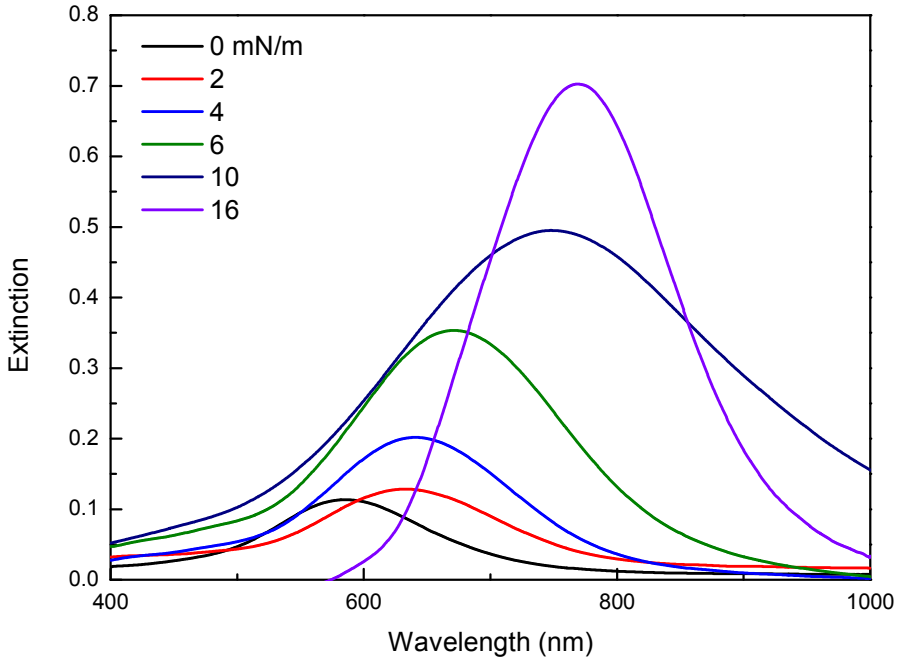

Figure C.1: UV-Vis spectra of AgND monolayers deposited in an LB-compressed manner on ITO substrates.

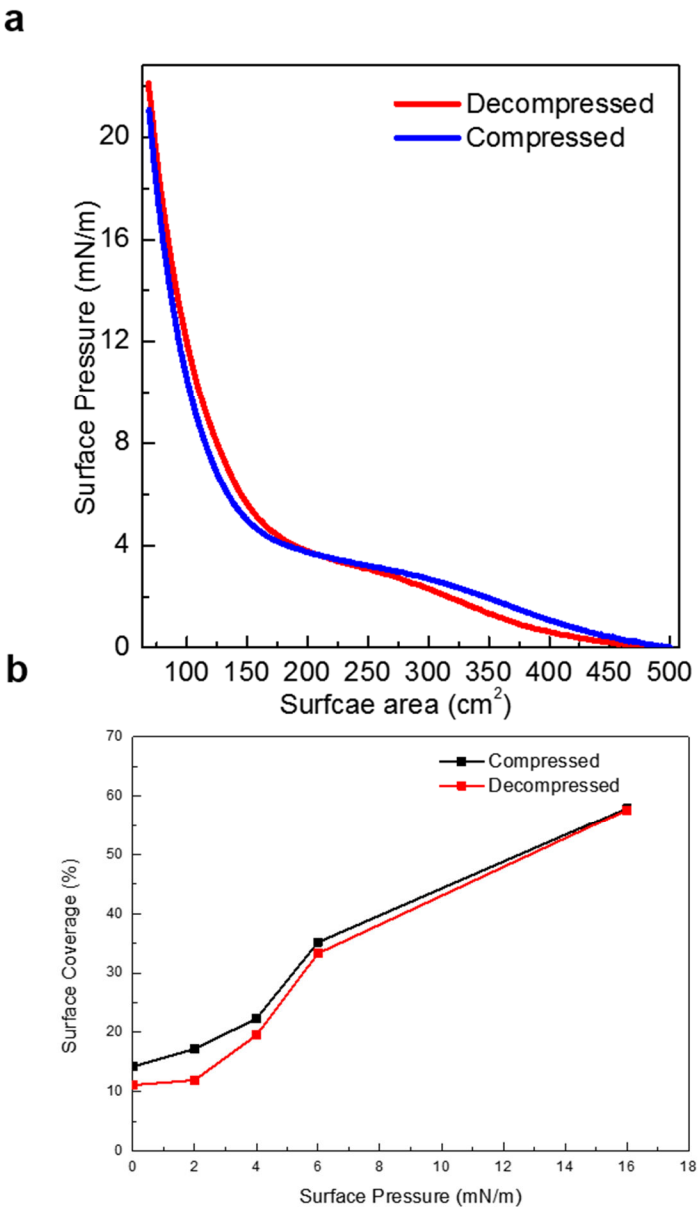

Figure C.2: (a) The LB isotherms for AgND monolayers deposited using compressed and decompressed deposition methods. The variation between the two curves indicates a slight hysteresis effect. (b) The surface coverage of the AgND monolayers as a function of LB surface pressure deposition for both compressed and decompressed deposition.

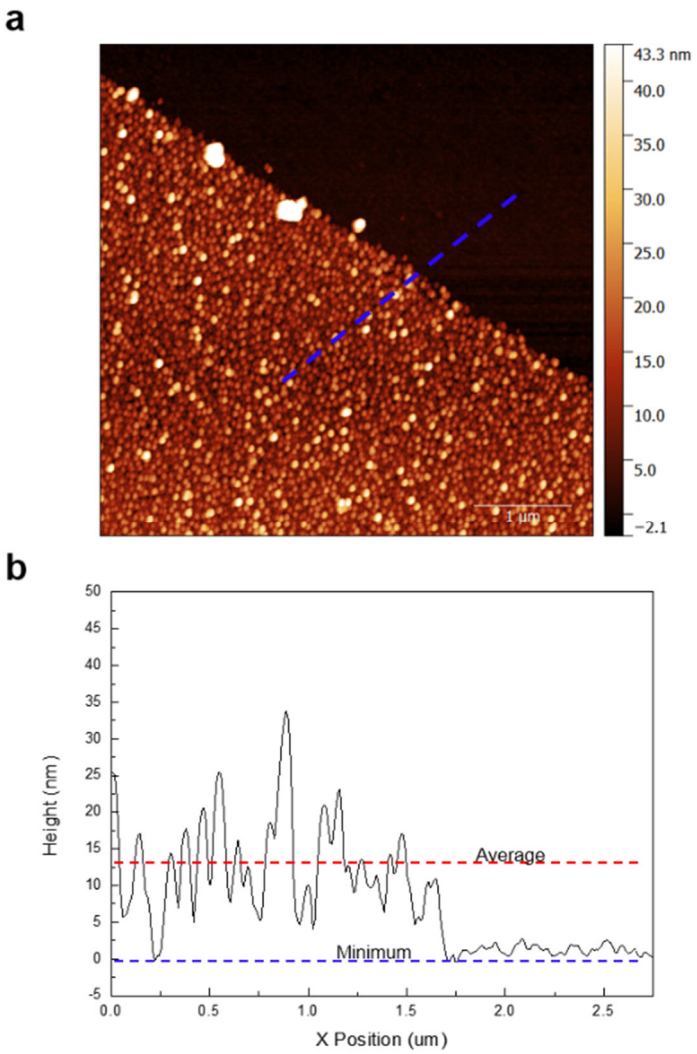

Figure C.3: (a) A scratched AgND monolayer for thickness measurements. (b) Cross-section showing the same minimum height in the monolayer and in the scratch, confirming that there is no underlying polymer layer present in the monolayer.

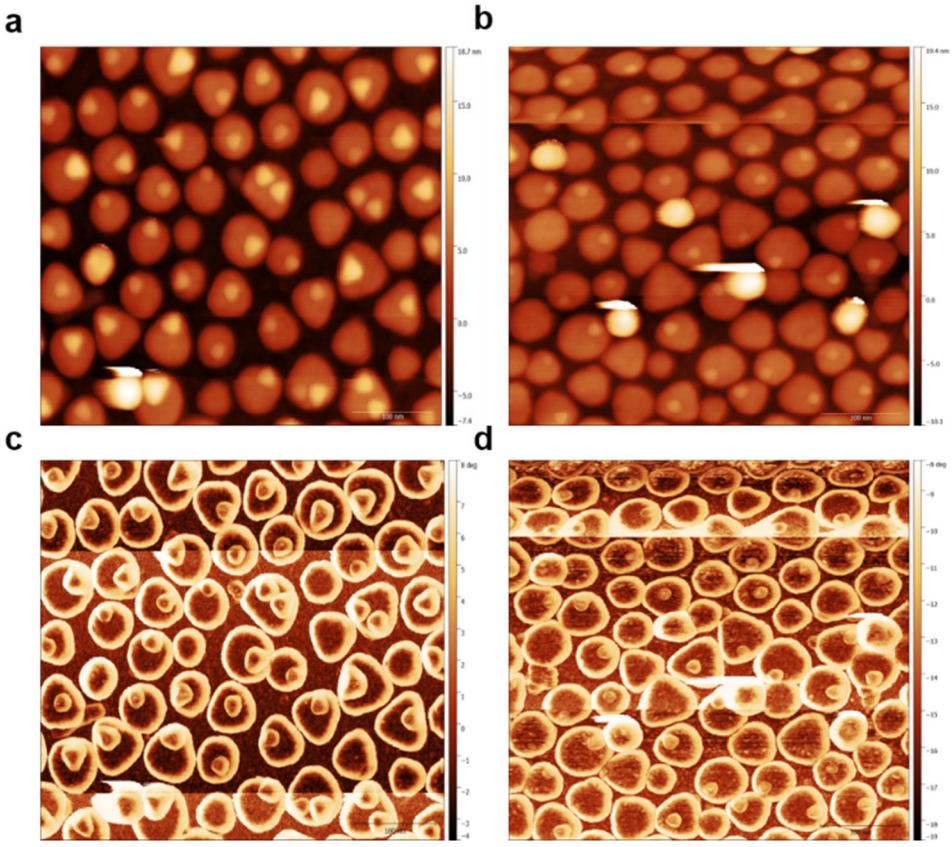

Figure C.4: AFM topographical images of (a) compressed and (b) decompressed AgND monolayers deposited at 6 mN/m. Very few micelles, visible as the elevated spots, are present for both samples. (c) Corresponding phase image for (a). (d) Corresponding phase image for (b).

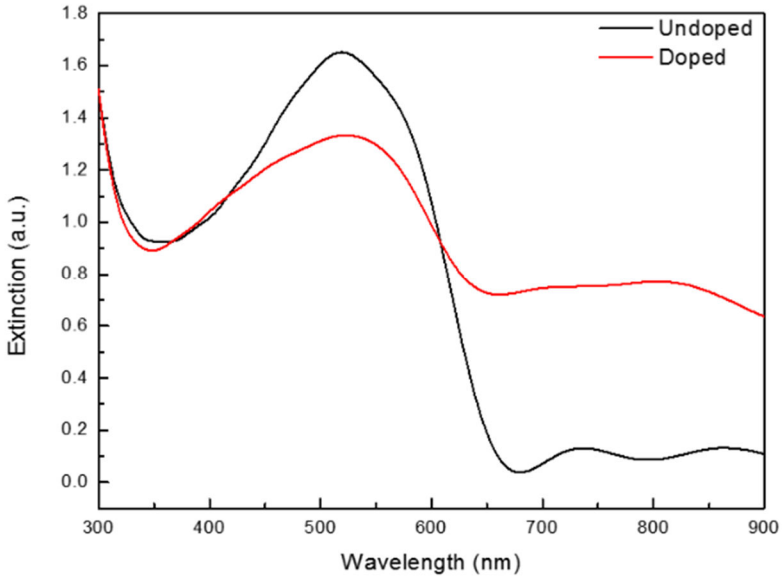

Figure C.5: FDTD-simulated spectra of undoped and iodine-doped P3HT films based on refractive indices obtained from literature.

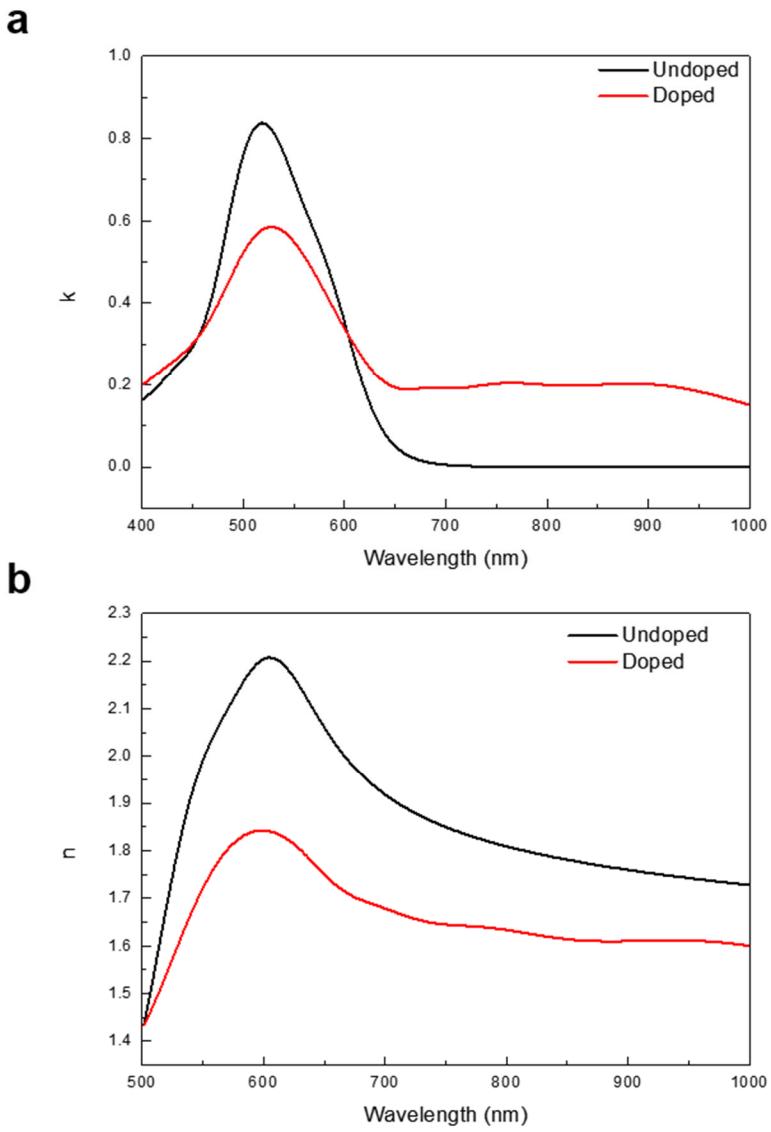

Figure C.6: (a) Ellipsometry-derived *k* values for undoped and partially doped P3HT films. The ellipsometry-derived absorption is a closer match to the experimental results (**Figure 6.8**a) than the absorption values obtained from literature refractive indices (**Figure C.5**). (b) The real refractive index, *n*, for undoped and partially doped P3HT films used to calculate Δn (**Figure 6.8**b).

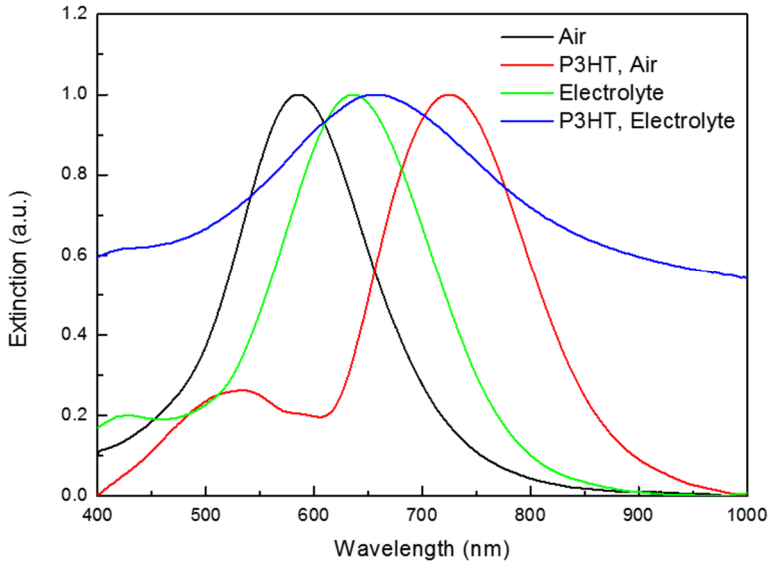

Figure C.7: UV-Vis spectra of an AgND monolayer deposited at 0 mN/m with and without a P3HT coating in air and electrolyte environments. Broadening of the P3HT, electrolyte spectrum is attributed to a lower signal and higher background from the electrochemical cell setup.

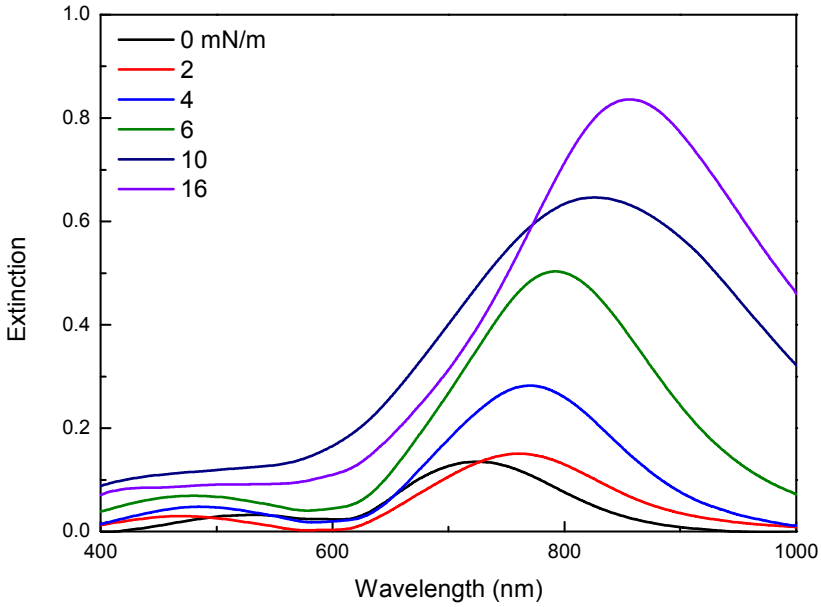

Figure C.8: UV-Vis spectra of P3HT-coated AgND monolayers deposited using LB compression.

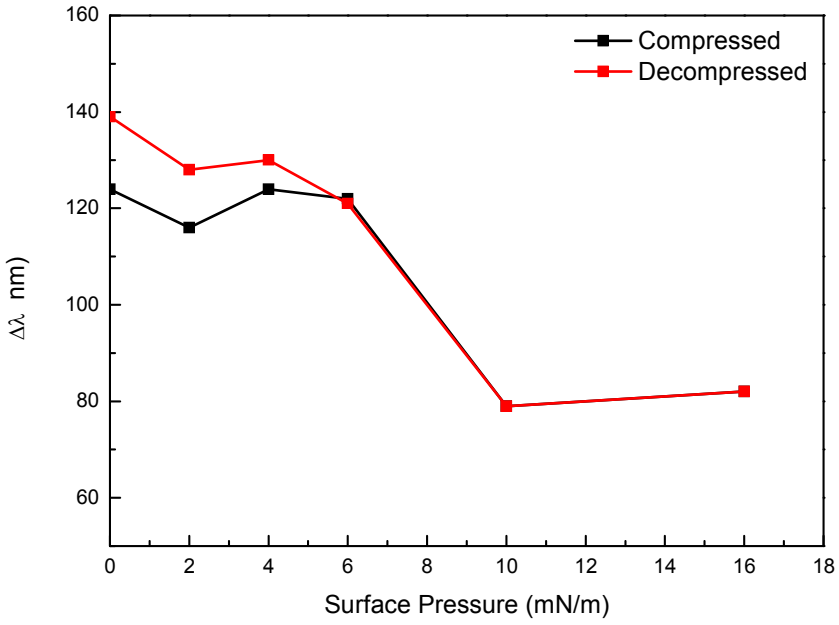

Figure C.9: Red shift of the AgND monolayer LSPR peak after P3HT deposition for both compression (black) and decompression (red) methods.

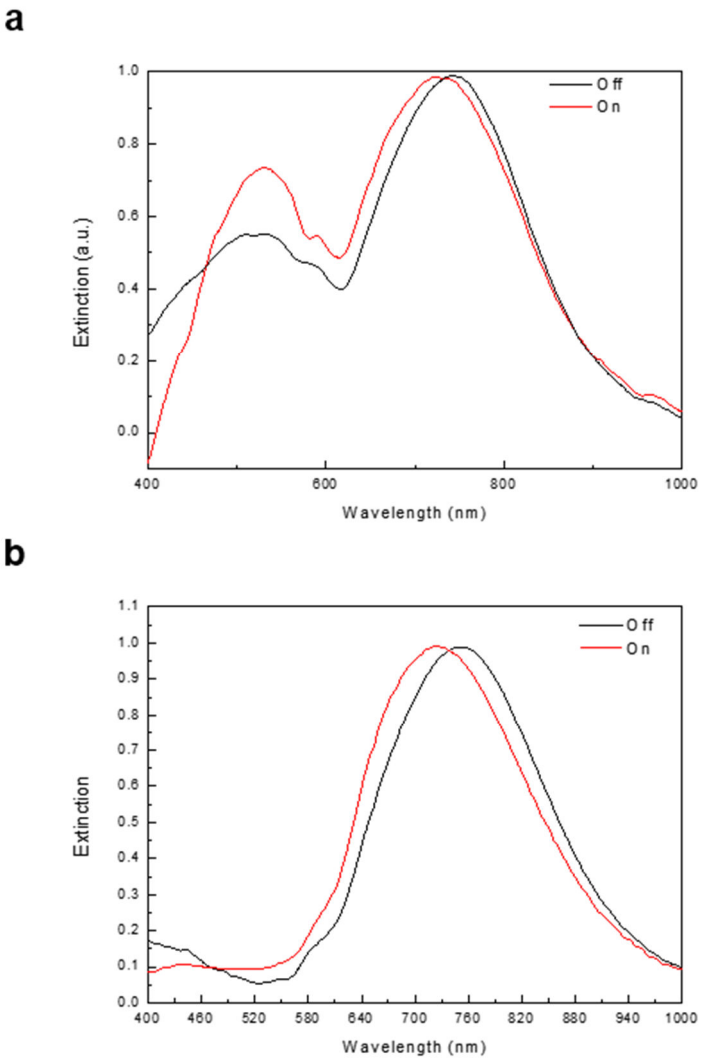

Figure C.10: a) One switching cycle for a compressed 4 mN/m P3HT-coated AgND monolayer showing a 13 nm LSPR shift. The peak at 500 nm is due to P3HT absorption. b) One switching cycle for a decompressed 4 mN/m P3HT-coated AgND monolayer showing a 26 nm LSPR shift.

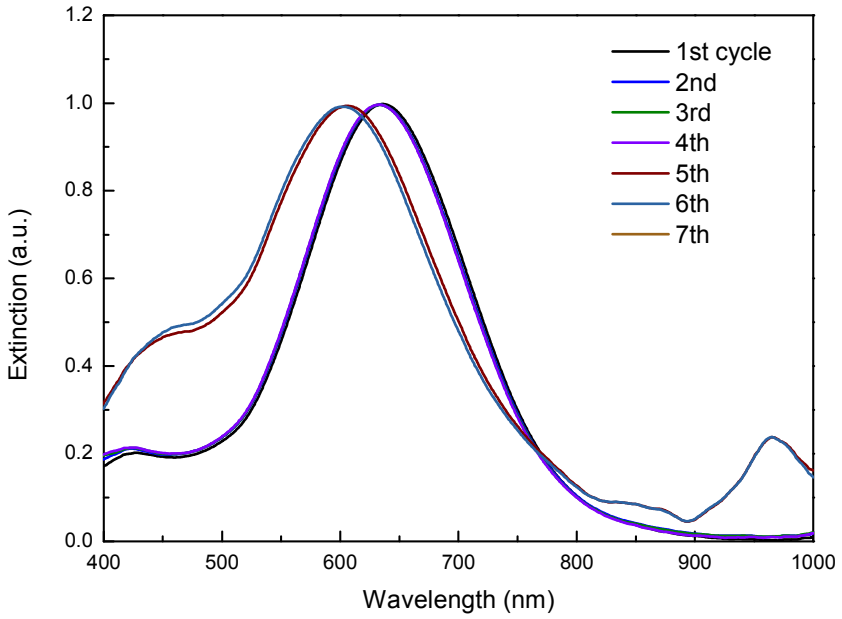

Figure C.11: Electropotential cycles of a bare AgND monolayer without a P3HT coating.

Appendix D: Chapter 7 Supporting Information

Synthetic Procedures

All chemicals were purchased from Sigma-Aldrich unless stated otherwise. 4-Phenylazophenol (S1), octakis(dimethylsilyloxy)silsesquioxane (**POSS-H**), platinum(0)-1,3-divinyl-1,1,3,3- tetramethyldisiloxane complex solution (Karsted's Catalyst) in xylene (Pt ~ 2%), 2- allyloxyethanol (98 %), and NaH (60 % dispersion in mineral oil) were used as received. THF was distilled from sodium/benzophenone, and toluene was distilled over calcium hydride. All other reagents and solvents were used as received from standard vendors. Reactions were performed at room temperature (20-22 °C), unless stated otherwise. AgNCs with a 50 nm edge length were synthesized using the polyol method as described earlier.[1] The compound **2** was synthesized as described previously.2 Reactions were monitored by Thin Layer Chromatography (TLC) using aluminum backed silica gel plates, visualized using 254 nm UV light. Flash chromatography was carried out using silica gel as the stationary phase. Compound (E)-1-(4-(6-bromohexyloxy)phenyl)-2-phenyldiazene (**S2**) was prepared according to the literature procedure.[3] ^{1}H NMR spectra were recorded on a Bruker Avance DRX 500 MHz spectrometer at room temperature in deuterated chloroform ($CDCl_3$). Chemical shifts are reported relative to chloroform (δ = 7.25 ppm). The ^{13}C NMR spectra were recorded on Bruker DMX 400 spectrometers at 25°C in $CDCl_3$. Coupling constants (J) are measured in Hertz (Hz). FTIR spectra were obtained on a Bruker Vertex 70 spectrometer in KBr pellets. Freshly cut silicon substrates with dimensions of 1 cm x 2 cm and the [100] orientation (Semiconductor Processing) and a native silicon oxide layer were cleaned with piranha solution (3:1 concentrated sulfuric acid and hydrogen peroxide mixture) in accordance with the usual procedure.[4]

Subsequently, they were rinsed with Nanopure water and dried with a dry air stream. Assembly of AgNCs on quartz substrates was done via the Langmuir-Blodgett (LB) technique S2 using a KSV2000 LB minitrough filled with Nanopure water (18.2 MΩ cm). The surface pressure was measured with a platinum Wilhelmy plate. The quartz slides (CGQ-0640-01, 75×25 mm) were purchased from Chemglass Life Sciences. The quartz slide (cleaned with acetone and by O_2 plasma etching for 1 min at 100 μTorr (0.13 mbar)) was submerged into a water phase prior to the formation of a monolayer. The stock solution of PVP-coated AgNCs in water (1 mL) was diluted to 10 mL using Nanopure water in a conical-bottom glass centrifuge tube. The AgNCs were separated by centrifugation for 30 min at 4000 rpm and subsequently washed in a similar manner with EtOH/H20 (10 ml, 1/1, v/v) and EtOH (10 mL). Finally, the residue was suspended in CHCl3 (2 mL) and used within 1 h for LB deposition. The solution of AgNCs in $CHCl_3$ (1 mL) was carefully spread over the water surface and the monolayer was left for 30 min to allow for evaporation of the organic solvent and equilibration. The Langmuir monolayer of AgNCs was then compressed at a rate of 5 mm/min to reach a surface pressure of 2 mN/m. The monolayer was transferred onto quartz slide at the air-water interface by pulling the substrate up vertically at a rate of 1 mm/min. Since both sides of the quartz slide were coated with a monolayer, one side and the edges were carefully cleaned with acetone to remove the AgNCs on that side. All samples were stored in a vacuum desiccator before characterization.

Compounds **1** and **2** were prepared using a hydrosilylation approach utilizing **POSS-H** as a scaffold for attachment of azo dyes bearing reactive allyloxy groups (see **Figure D.1**).[2] Commercially available 4-phenylazophenol (**S1**) served as a precursor for synthesis of

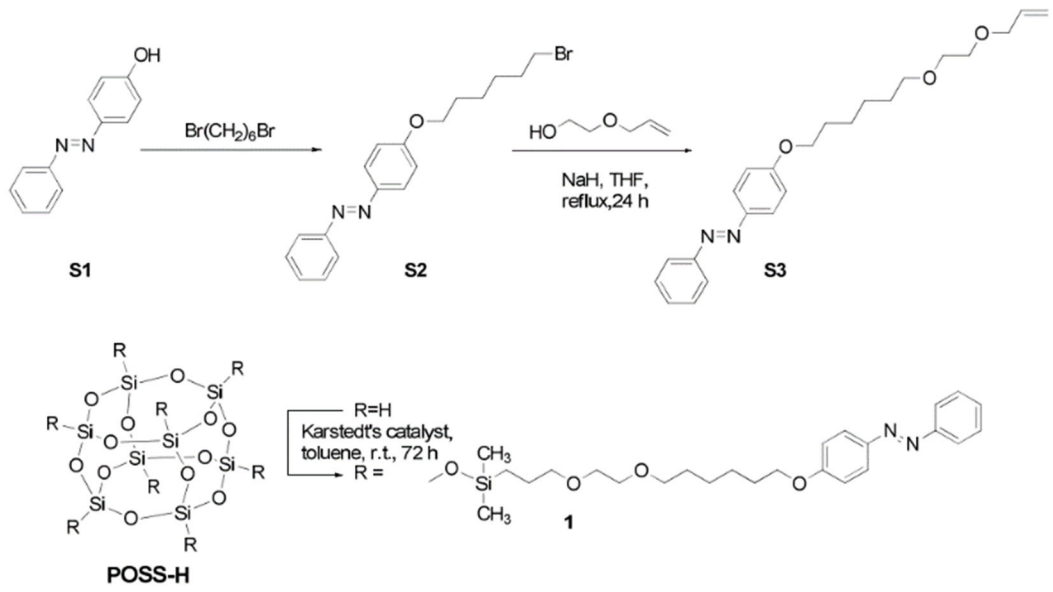

Figure D.1: Synthesis of compound 1.

compounds **AB** and **S3**. The allyl handle for subsequent hydrosilylation reaction was introduced by etherification of compound **S1** with an allyl bromide or compound **S2** with 2-allyloxyethanol in the presence of a base. The hydrosilylation was conducted by stirring S3 octakis(dimethylsilyloxy)silsesquioxane with eight equivalents of respective allyloxy derivative (**AB** or **S3**) in dry toluene at 40 ºC in the presence of 2 mol% of platinum(0)-1,3-divinyl-1,1,3,3- tetramethyldisiloxane (Karsted's catalyst). The reactions were terminated after 72 h and the products were isolated by evaporation of the solvent followed by silica-gel chromatography. The purification gave compounds **1** and **2** in yields of 65% and 53% respectively. The successful grafting of dyes onto POSS-H was indicated by IR spectra of Azo-POSS compounds, in particular by a disappearance of a Si-H stretching band at 2140 cm^{-1} (Figure S2). Furthermore, both sets of signals from the POSS core (Si-C at 1250 cm^{-1}, Si-O-Si at 1090 cm^{-1}) and the aromatic dyes (C-H at 3050 cm^{-1}, C=C at

1600 and 1500 cm^{-1}) were present in conjugate spectra. ^1H NMR spectroscopy indicated nearly complete modification of octavalent POSS core with azo dyes. From comparison of integral areas of CH3 proton signals of the POSS cage and the total integral area of attached dye molecules, the degree of functionalization was 90% for both **1** and **2**.

*Synthesis of (E)-phenyl[4-(6-[2-(prop-2-en-1-yloxy)ethoxy]hexyloxy)phenyl]diazene (**S3**):* A solution of 2-allyloxyethanol (0.25 g, 0.0024 mol) in dry THF (8 mL) was added to a suspension of sodium hydride (0.058 g (0.097 g – 60%), 0.0024 mol) in dry THF (2 mL) under inert atmosphere. The resulting mixture was stirred at room temperature for 1 h. Then dye **S2** (0.8 g, 0.0022 mol) was added and the mixture was heated at reflux for 24 h. Suspension was cooled to room temperature and poured into dilute HCl (5%, 20 mL). The product was extracted with dichloromethane, and then an organic layer was isolated with a separating funnel and washed with aqueous Na_2CO_3, then H_2O. After drying over Na_2SO_4, the solvent was evaporated in vacuo. The obtained product was column chromatographed on silica gel with a mixture of hexane and ethyl acetate (5/1) as the eluent. Yield: 60 %. ^1H NMR ($CDCl_3$, δ, ppm): 1.42-1.55 (m, 4H, Ph-$O(CH_2)_2CH_2CH_2(CH_2)_2O$-), 1.65 (p, 2H, J_1=6.6 Hz, J_2=7.7 Hz, $PhO(CH_2)_4CH_2CH_2O$-), 1.84 (p, 2H, J_1=6.6 Hz, J_2=7.7 Hz, Ph-$OCH_2CH_2(CH_2)_4O$-), 3.5 (t, 2H, J=6.6 Hz, Ph-$O(CH_2)_5CH_2O$-), 3.61 (s, 4H, -OCH_2CH_2O-), 4.03 (br.s, 4H, [Ph-$OCH_2(CH_2)_5O$-] + [-$CH_2CH=CH_2$]), 5.19 (d, 1H, J_{cis}=10.4 Hz, $=CH_2^a$), 5.29 (d, 1H, J_{trans}=17.0 Hz, $=CH_2^b$), 5.90- 5.97 (m, 1H, =CH-), 7.05 (d, 2H, J=8.8 Hz, Ph), 7.44 (t, 1H, J=7.1 Hz, Ph), 7.51 (t, 2H, J_1=7.1 Hz, J_2=7.7 Hz, Ph), 7.85 (d, 2H, J=7.7 Hz, Ph), 7.92 (d, 2H, J=8.8 Hz, Ph). FTIR (KBr, cm^{-1}): 3120-2990 (w), 2960–2640 (s), 1607 (s, C=C, arom.), 1504 (s, C=C, arom.),

1262 (s, C-O), 1123 (s), 1016 (m), 915 (m), 843 (m), 804 (m), 768 (s), 682 (m). UV-vis, CHCl3: λ_{max} = 348 nm.

*Synthesis of Azo-POSS derivative **1**:* A total of 0.3 g (0.7859 mmol) of **S1** and 0.1 g (0.0982 mmol) of **POSS-H** was dissolved in 3 mL of toluene, and 30 μL of Karsted's Catalyst was added to the reaction solution. The reaction mixture was stirred at r.t. for 72 h and then cooled to room temperature. After removing all the solvents at reduced pressure, the residue was dissolved in CH_2Cl_2 and passed through a silica gel. The solvent was concentrated and the obtained solid was purified by double precipitation from chloroform solution into hexane. The final product was dried in a vacuum oven overnight at 40 ºC. Yield: 65%. ^{1}H NMR ($CDCl_3$, δ, ppm): 0.14 (s, 6H, - $SiCH_3$), 0.59 (br.s, -$SiCH_2CH_2CH_2O$-), 1.42 (br.s, 2H, Ph-O$(CH_2)_2CH_2(CH_2)_3O$-), 1.50 (br.s, 2H, Ph-O$(CH_2)_3CH_2(CH_2)_2O$-), 1.60-1.66 (m, 4H, [Ph-O $(CH_2)_4CH_2CH_2O$-] + [- $SiCH_2CH_2CH_2O$-]), 1.84 (br.s, 2H, Ph-$OCH_2CH_2(CH_2)_4O$-), 3.42 (t, 2H, J=7.7 Hz, $PhO(CH_2)_5CH_2O$-), 3.47 (t, 2H, J=7.1 Hz, -$SiCH_2CH_2CH_2O$-), 3.57 (s, 4H, -OCH_2CH_2O-), 4.02 (t, 2H, J=6.6 Hz, Ph-$OCH_2(CH_2)_5O$-), 6.98 (d, 2H, J=8.2 Hz, Ph), 7.43 (t, 1H, J=7.7 Hz, Ph), 7.49 (t, 2H, J1=7.7 Hz, J2=7.7 Hz, Ph), 7.87 (d, 2H, J=8.2 Hz, Ph), 7.90 (d, 2H, J=8.2 Hz, Ph). FTIR (KBr, cm^{-1}): 3120-3017 (m), 3000–2764 (s), 1606 (m, C=C, arom.), 1505 (s, C=C, arom.), 1471- 1300 (m), 1259 (s, C-O), 1108 (s, Si-O), 901 (m), 844 (s), 687 (m). UV-vis, $CHCl_3$: λ_{max} = 349 nm.

^{1}H NMR of **S3**

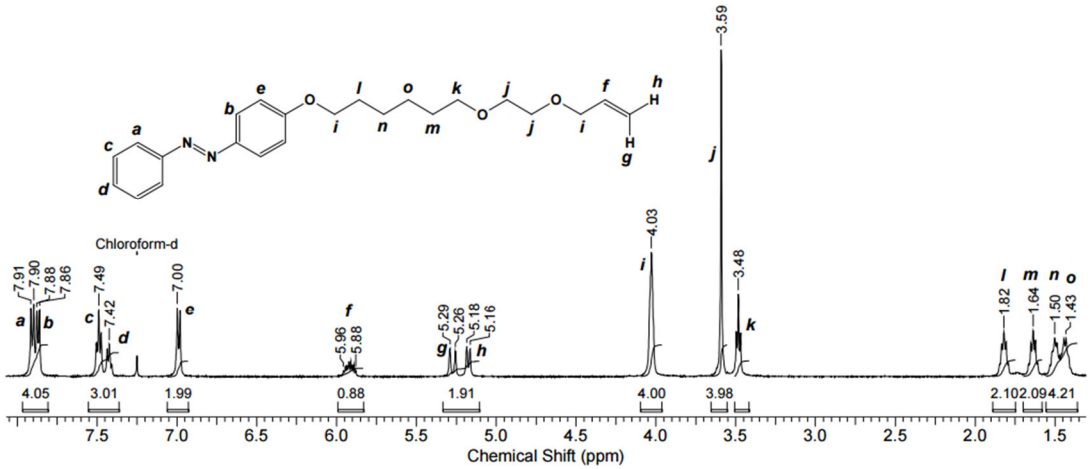

^{13}C NMR of **S3**

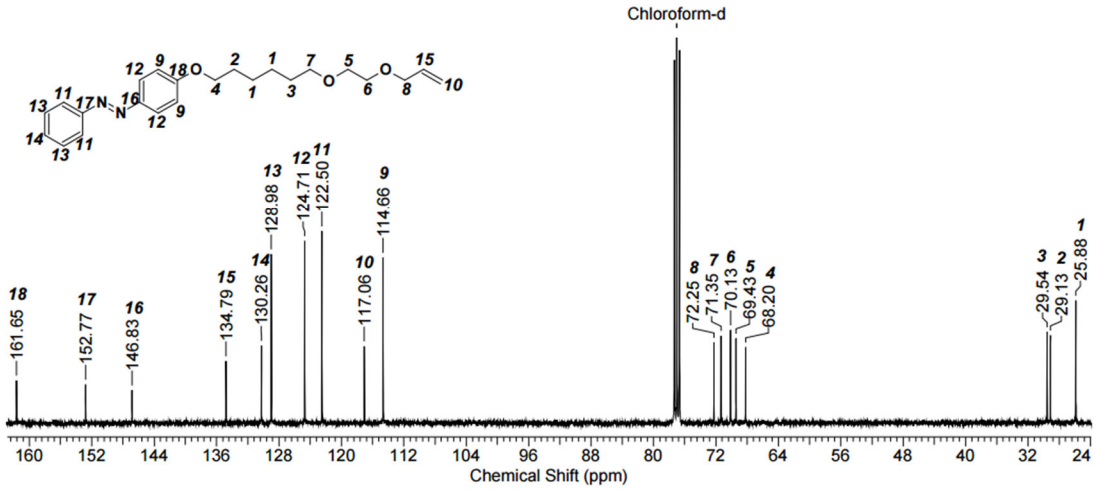

^{1}H NMR of **1**

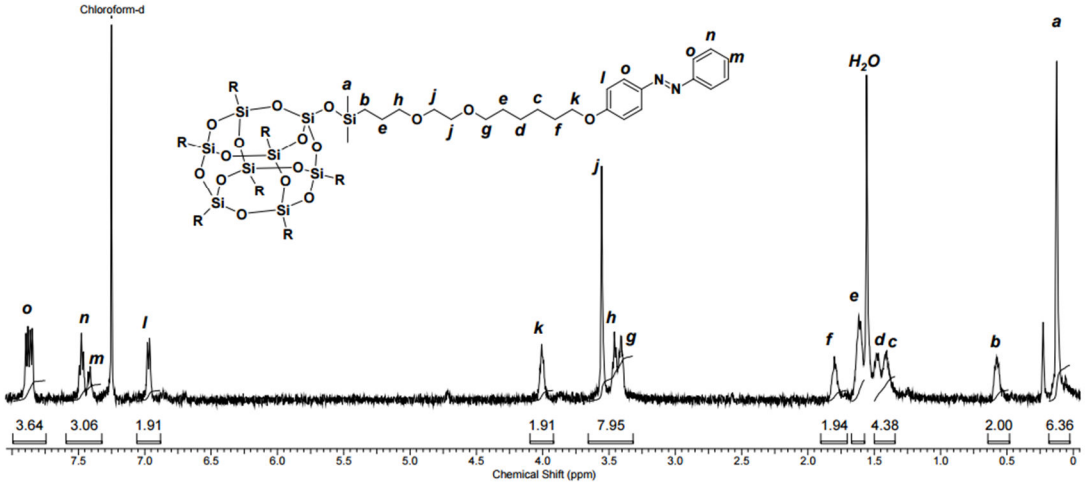

^{13}C NMR of **1**

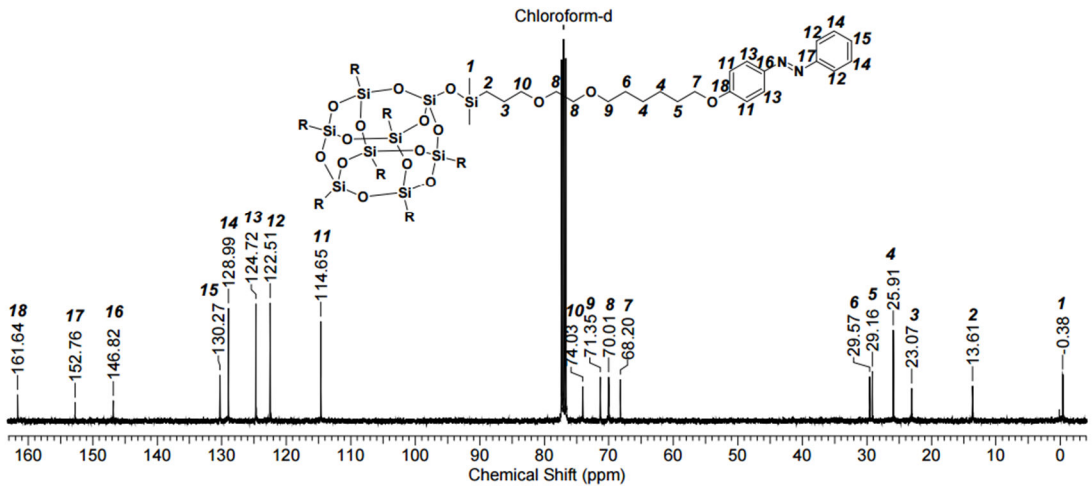

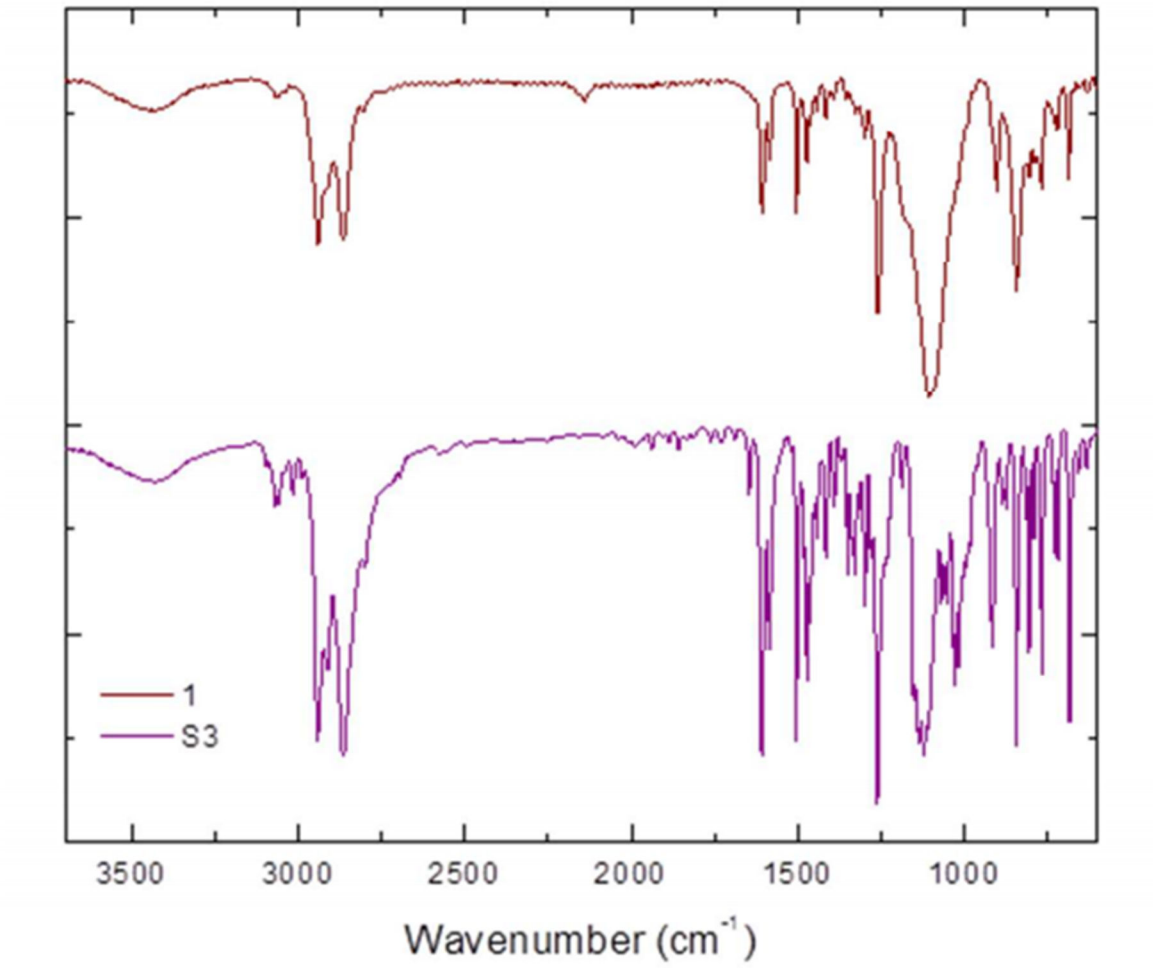

FTIR spectra of S3 and 1. KBr

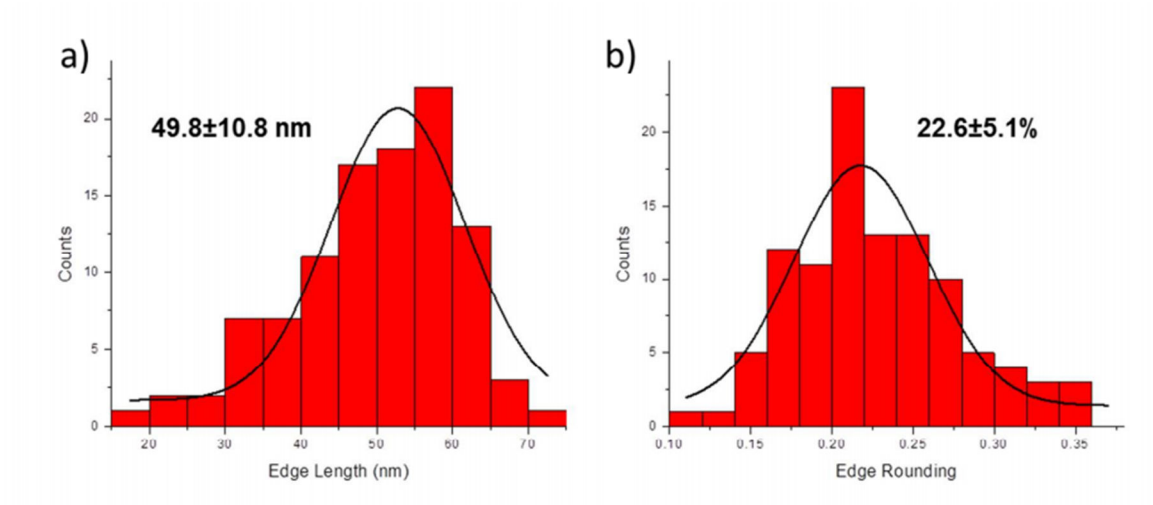

Figure D.2: Statistical analysis of AgNC (a) edge length and (b) edge rounding based on TEM images.

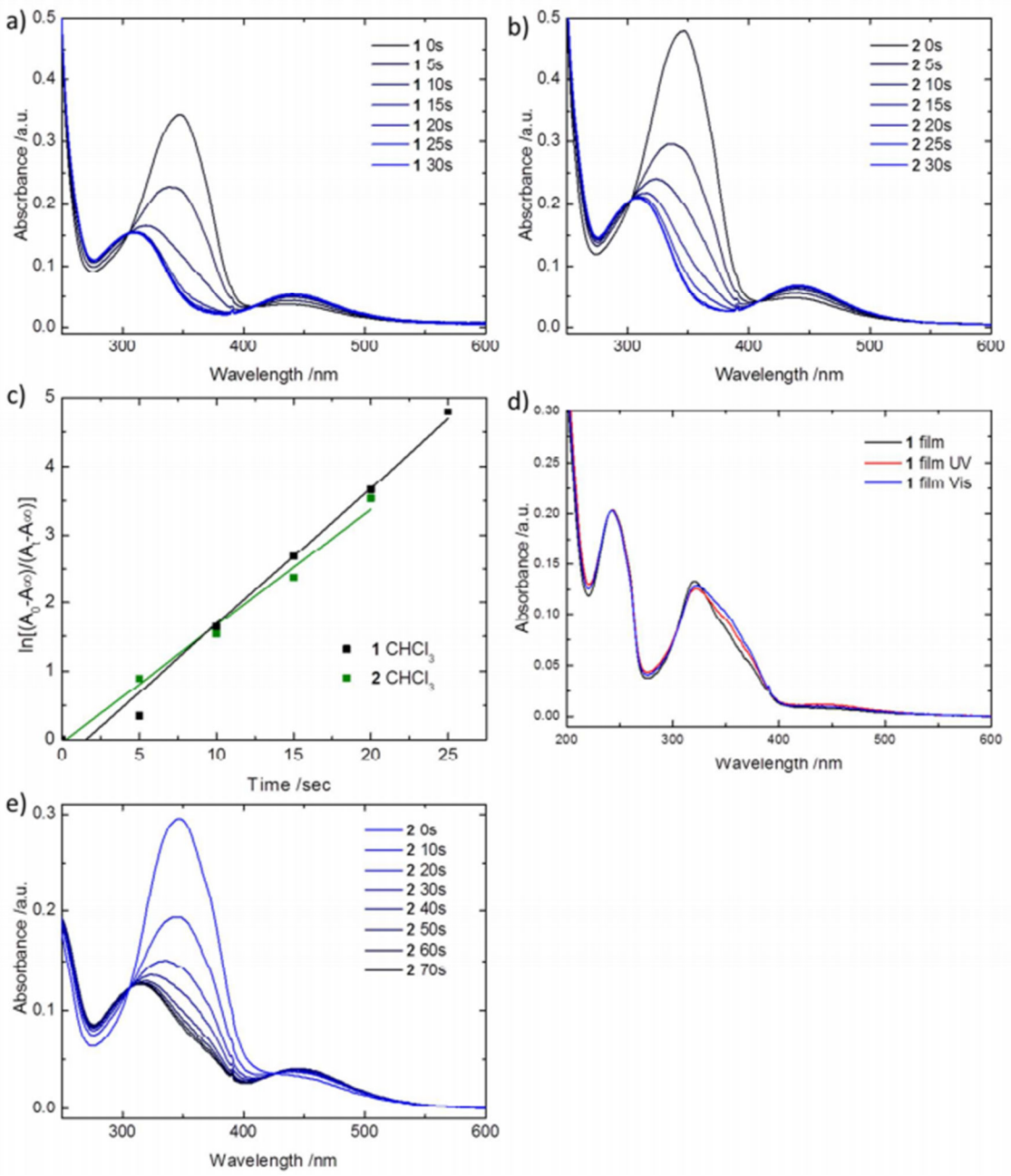

Figure D.3: Photoisomerization of 1 and 2. a) 1 in $CHCl_3$ solution, b) 2 in $CHCl_3$ solution, c) Kinetics of trans-cis photoisomerization of 1 and 2 in $CHCl_3$ solution. d) UV-Vis absorbance spectra of 1 spincast on a quartz slide before and after irradiation with UV light (365 nm, 15 sec) and white light (>450 nm, 15 sec). e) Photoisomerization of 2 in a thin film.

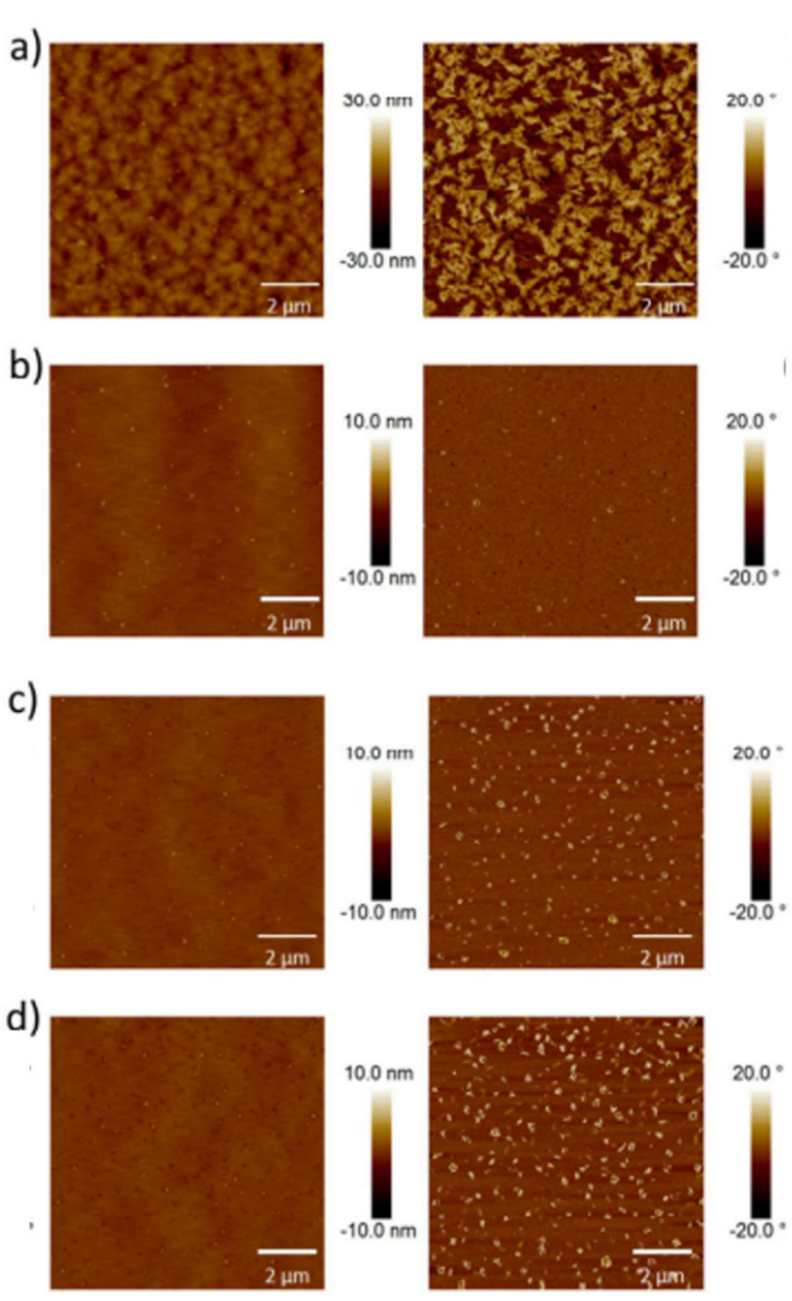

Figure D.4: 10×10 µm^2 AFM topographical images of a thin film of 2 on silicon substrate; height is on the left, and phase is on the right. (a) As spun film. (b) Film after UV irradiation. (c) After Vis irradiation. (d) 10 min after Vis irradiation.

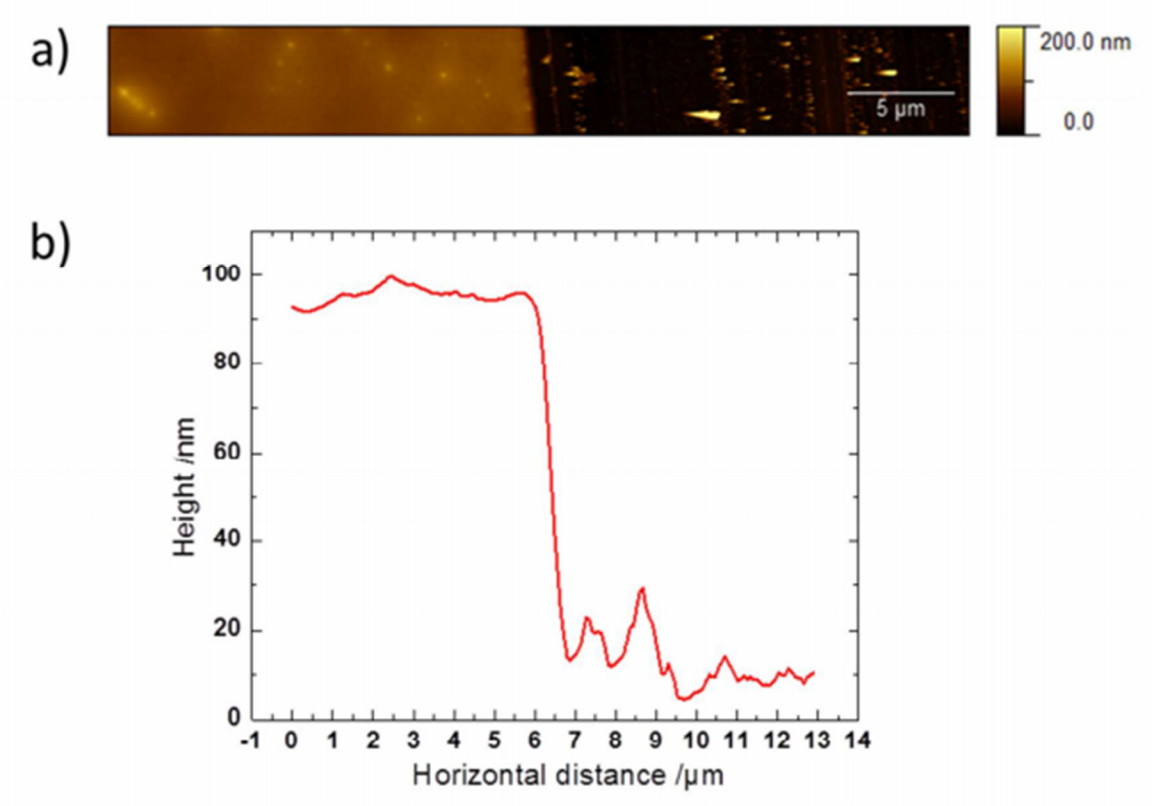

Figure D.5: Determination of the thickness of an AgNC monolayer coated with 2 using AFM profilometry. (a) 40×5 μm^2 AFM topographical scan of the scratch in the film. (b) The y-averaged height profile obtained from an AFM image.

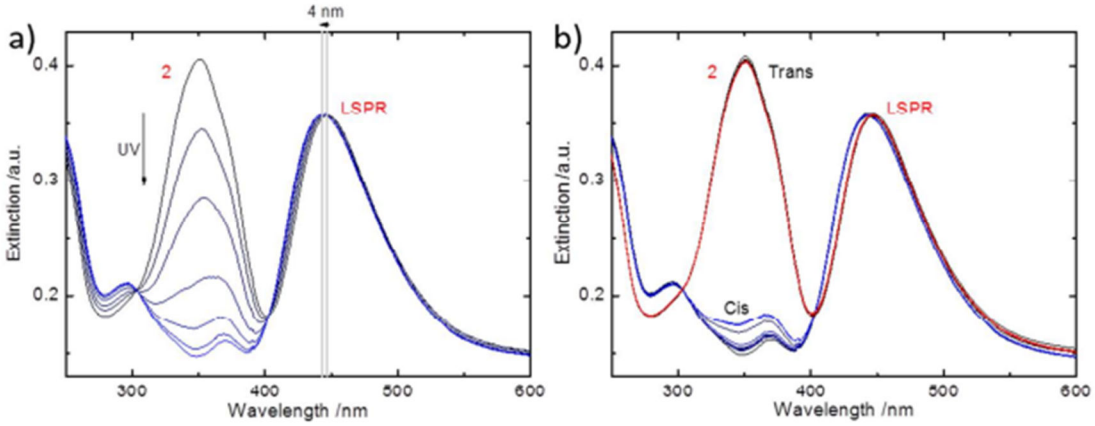

Figure D.6: (a) Photoinitiated switching behavior of AgNCs coated with Azo-POSS compound 2 irradiated for 1 min. (b) LSPR peak position modulation upon exposure to 365 nm UV light over 10 UV/Vis cycles.

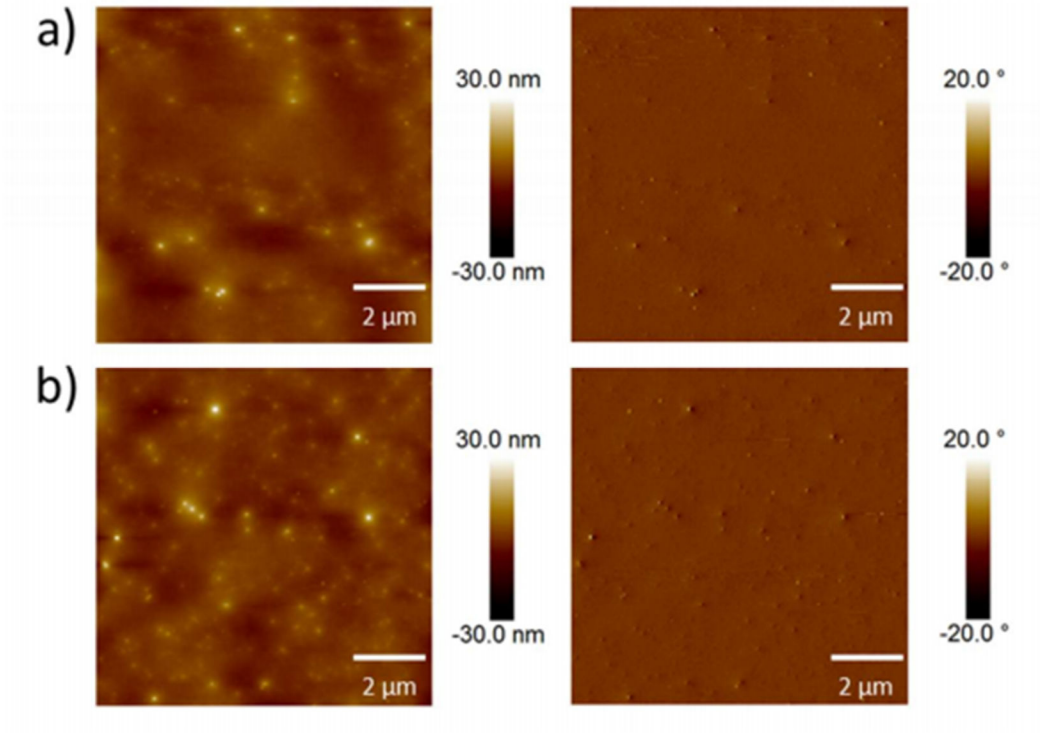

Figure D.7: 10×10 µm^2 AFM topographical images of a thin film of 2 top of the AgNC monolayer (not the same area) after performing multiple switching studies. (a) After UV irradiation. (b) After Vis irradiation.

Appendix E: Chapter 8 Supporting Information

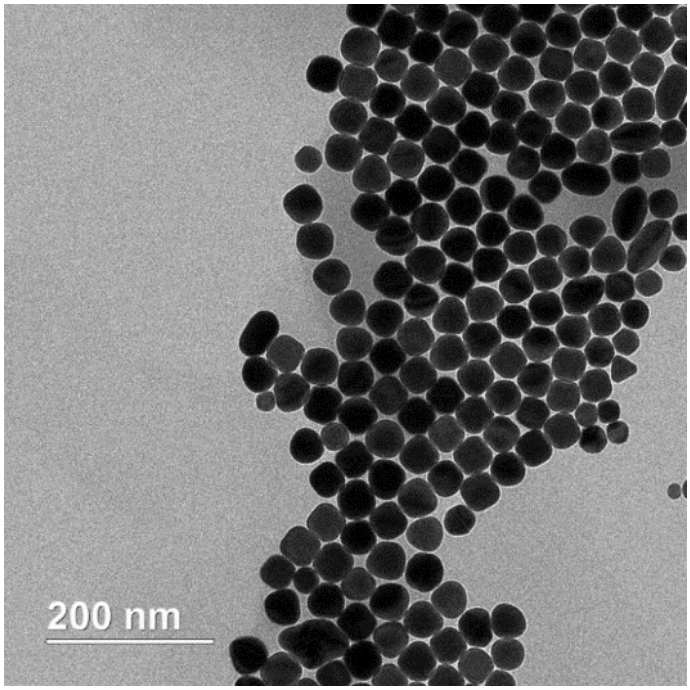

Figure E.1: TEM image of as-synthesized AuNCs dropcast on a TEM grid.

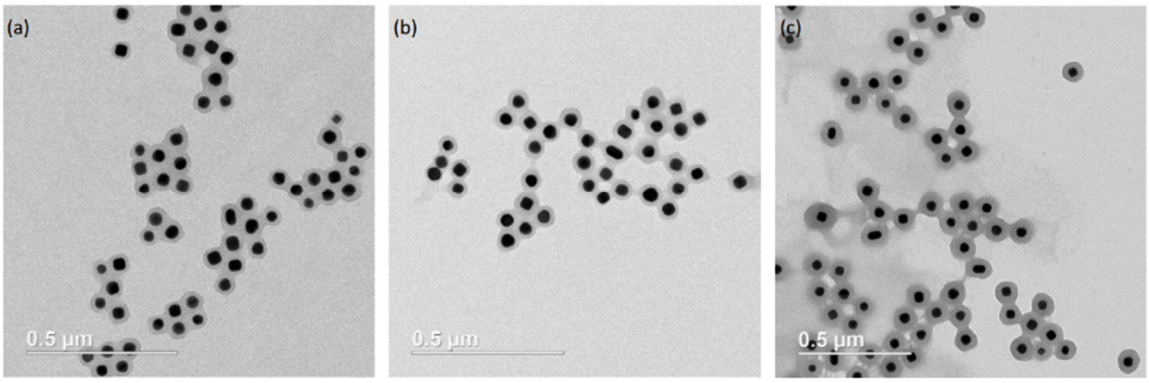

Figure E.2: TEM images of (a) AuNC/PANI-13 nm, (b) AuNC/PANI-18 nm, and (c) AuNC/PANI-26 nm.

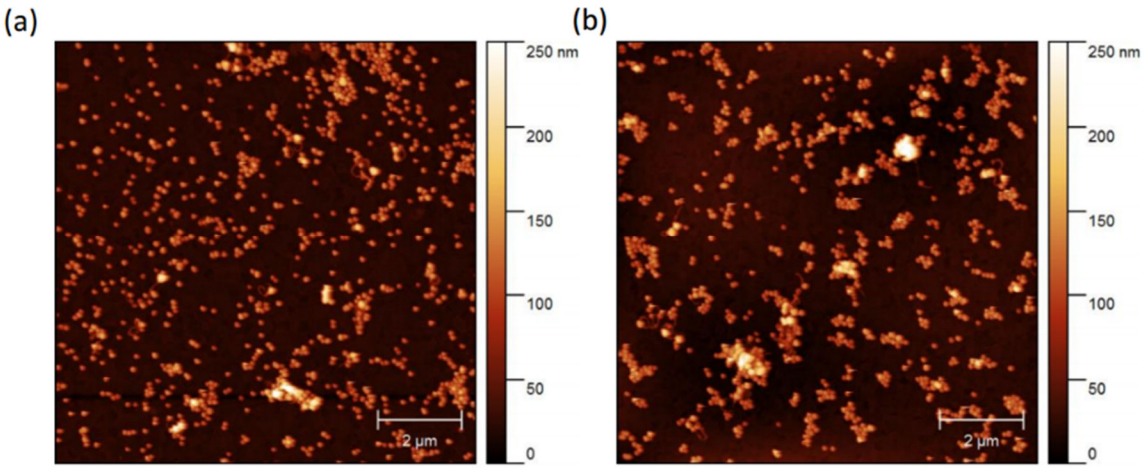

Figure E.3: AFM images of as-sprayed AuNC/PANI-18 nm on (a) PEI-ITO and (b) APTES-ITO.

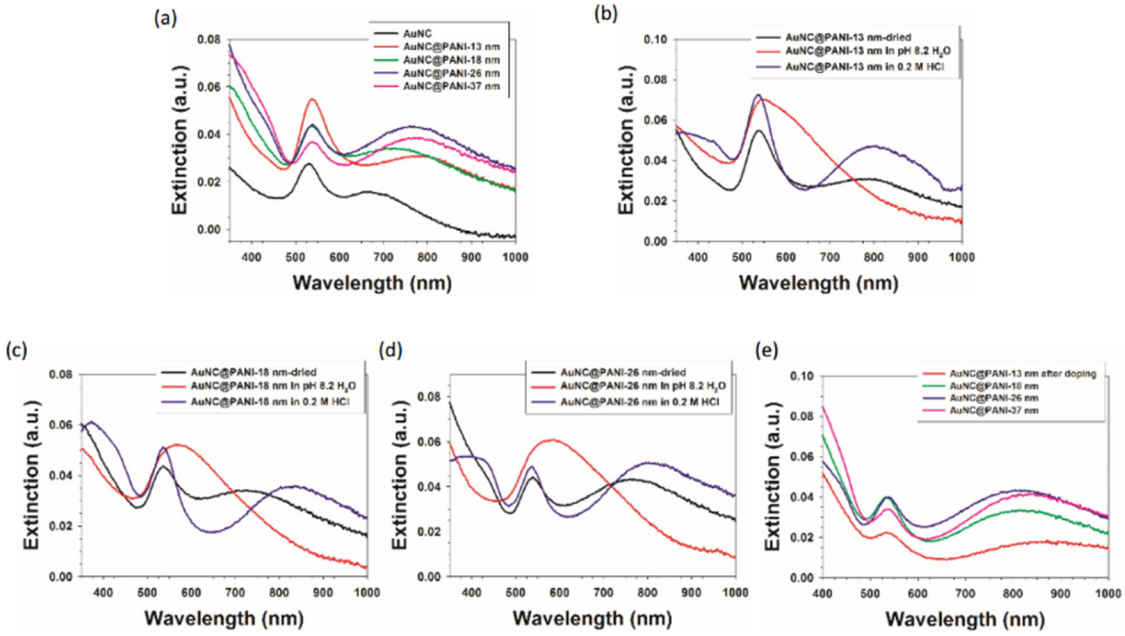

Figure E.4: UV-vis spectra of (a) as-sprayed AuNCs and AuNC/PANI, (b) AuNC/PANI-13 nm, (c) AuNC/PANI-18 nm, and (d) AuNC/PANI-26 nm in air, pH 8.2 water, and 0.2 M HCl aqueous solution. (e) UV-vis spectra of AuNC/PANI with different PANI shell thicknesses after sequential washing and doping processes.

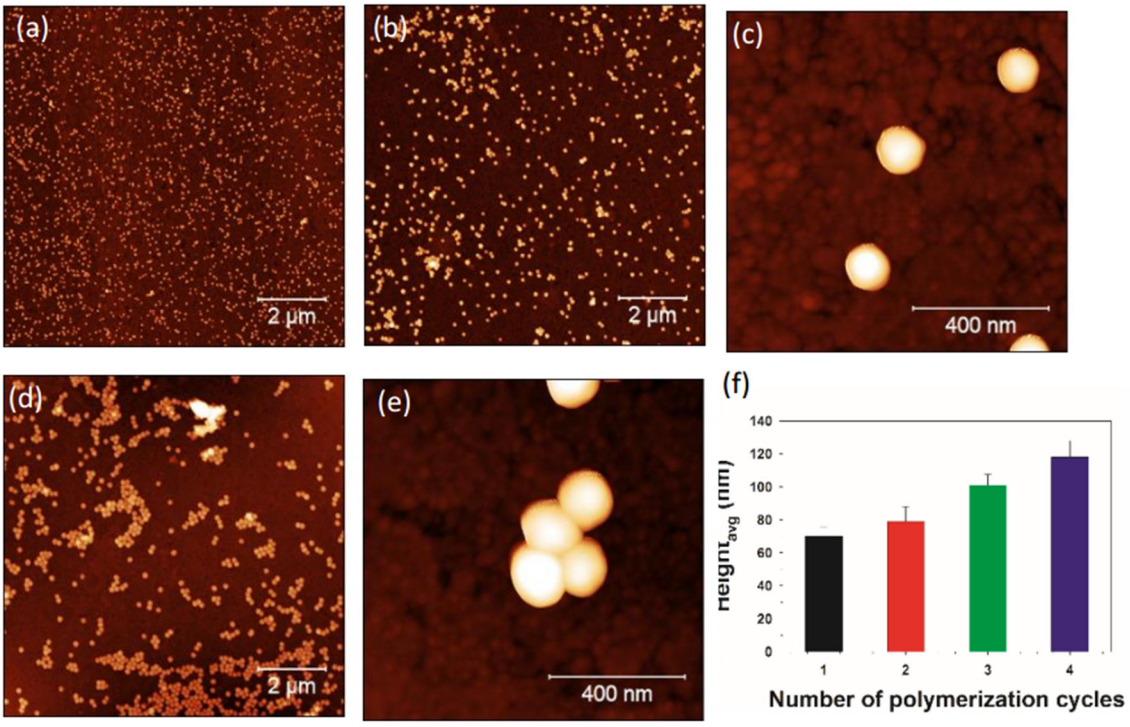

Figure E.5: AFM images of (a) AuNC on plasma-treated ITO, (b), (c) AuNC/PANI-18 nm on PEI-ITO, (d), (e) AuNC/PANI-37 nm on PEI-ITO, and (f) average height of AuNC/PANI particles on PEI-ITO correlated with the number of polymerization cycles.

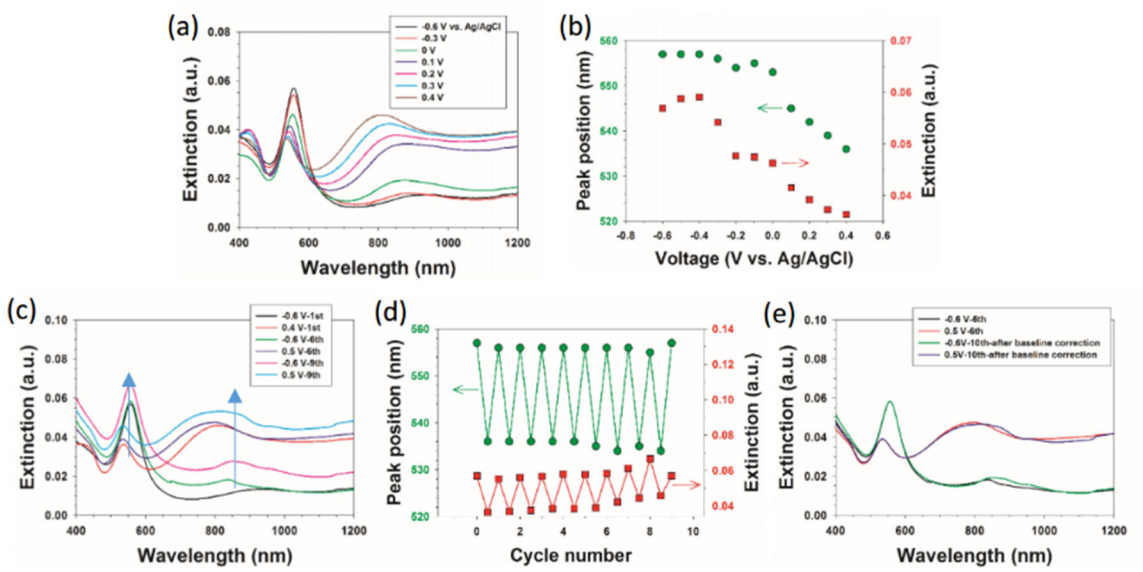

Figure E.6: (a) UV-vis spectra of AuNC/PANI-37 nm in a 0.5 M HCl electrolyte, and (b) its LSPR peak position and extinction vs. voltage (vs. Ag/AgCl). (c) UV-vis spectra of AuNC/PANI-37 nm during cycling from -0.6 to 0.4 V, and (d) its LSPR peak position and extinction. (e) UV-vis spectra of AuNC/PANI-37 nm before cycling and after cycling with baseline correction.

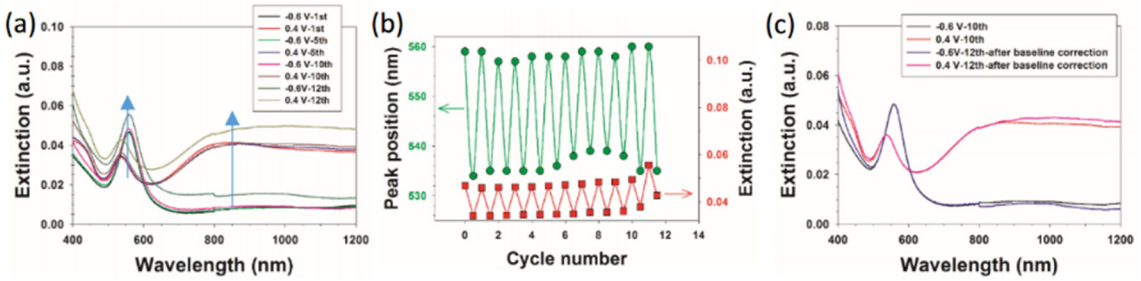

Figure E.7: (a) UV-vis spectra of AuNC/PANI-37 nm with a 0.5 M NaCl in 0.1 M HCl electrolyte during cycling (vs. Ag/AgCl) and (b) its LSPR peak position and extinction. (c) UV-vis spectra of AuNC/PANI-37 nm before cycling and after cycling with baseline correction.

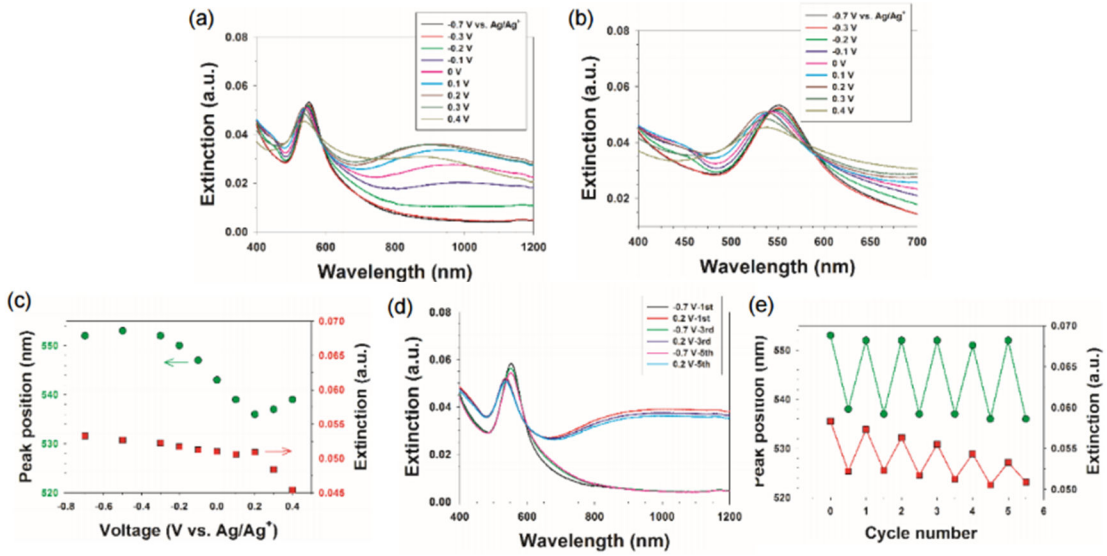

Figure E.8: (a), (b) UV-vis spectra of AuNC/PANI-26 nm at different voltages (vs. Ag/Ag+) with 0.5 M LiBTI in PC electrolyte, (c) LSPR peak position and maximum peak extinction vs. voltages, (d) UV-vis spectra of AuNC/PANI-26 nm during cycling, and (e) LSPR peak position and maximum peak extinction during cycling from -0.7 to 0.2 V.

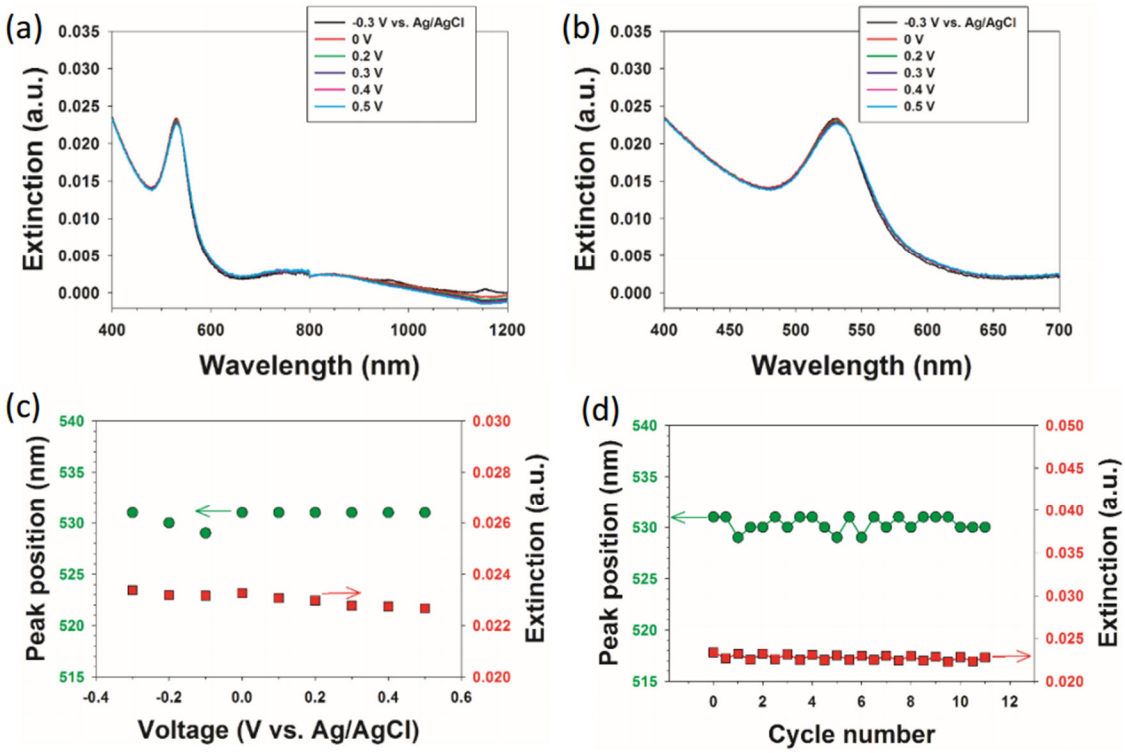

Figure E.9: (a), (b) UV-vis spectra of AuNCs at different voltage (vs. Ag/AgCl) and, its peak LSPR peak position and extinction with a 0.5 M NaCl in 0.01 M HCl electrolyte (c) vs. voltage and (d) during cycling from -0.3 to 0.5 V.

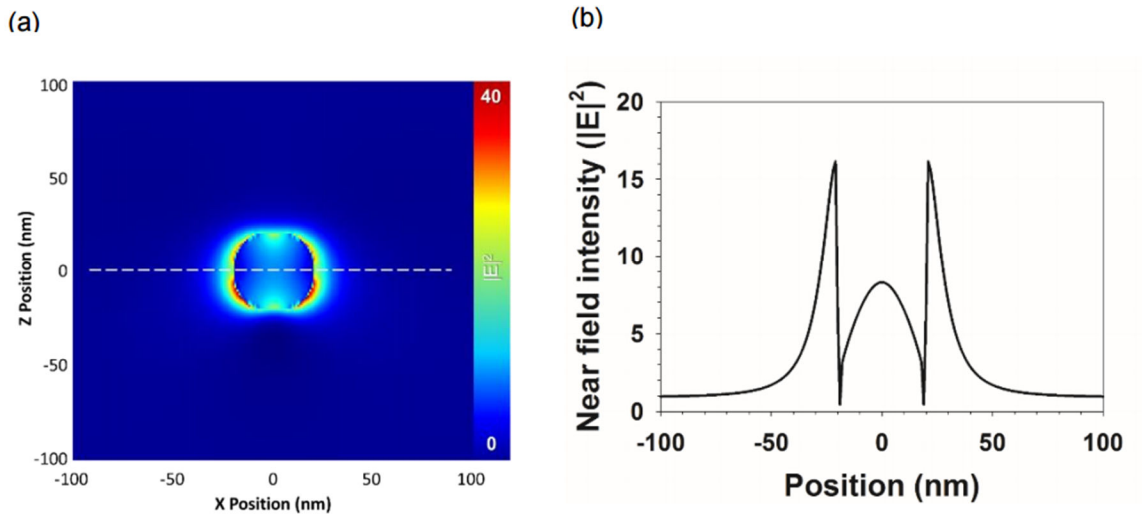

Figure E.10: (a) Near field intensity for an AuNC in water, and (b) the cross-sectional near field intensity vs. position for obtaining the electromagnetic decay length. The zero position indicates the center of the cube.

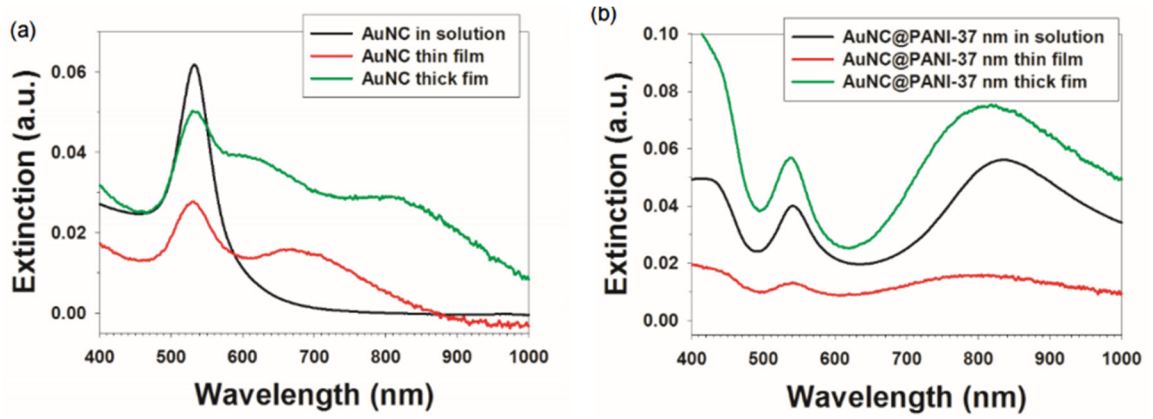

Figure E.11: (a) UV-vis spectra of AuNC solution and AuNC nanoparticles deposited on ITO substrates with different densities. (b) UV-vis spectra of AuNC/PANI-37 nm core/shell nanostructures in solution and AuNC/PANI core/shell nanostructures deposited on ITO substrates.

Table E.1: LSPR peak position and LSPR shift from experiments and simulations.

	LB – experiments (nm)	ES – experiments (nm)	LSPR shift – experiment (nm)	LB – simulation (nm)	ES – simulation (nm)	LSPR shift – simulation (nm)
AuNC@PANI-13 nm	552.3 ± 0.8	537.5 ± 0.8	14.8 ± 1.2	556	537	19
AuNC@PANI-18 nm	554.6 ± 0.5	533.6 ± 0.7	21.1 ± 0.7	560	536	24
AuNC@PANI-26 nm	555.7 ± 0.5	533.5 ± 0.7	22.2 ± 0.8	562	535	27
AuNC@PANI-37 nm	556.3 ± 0.6	532.6 ± 1.1	23.8 ± 1.3	564	535	29

Table E.2: Refractive index sensitivity (m), electromagnetic field decay length (l_d), and R 2 for fitting.

	m	l_d	R^2
FDTD without the PANI shell	75 nm/RIU	23.9 nm	None
Using the shell thickness from TEM	74.2	25.8	0.976
Using the shell thickness from AFM	74.9	30.7	0.966
FDTD with the PANI shell	89.7	25.9	0.998

Appendix F: Chapter 9 Supporting Information

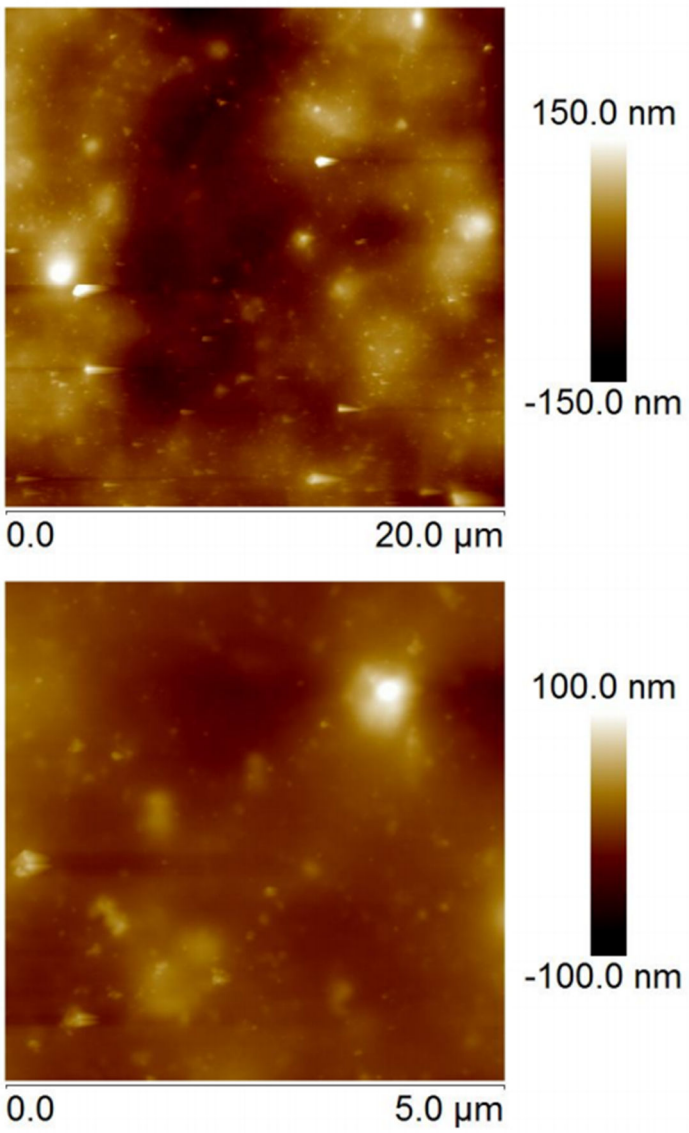

Figure F.1: Topographical AFM images of spraycoated ECP-Magenta films.

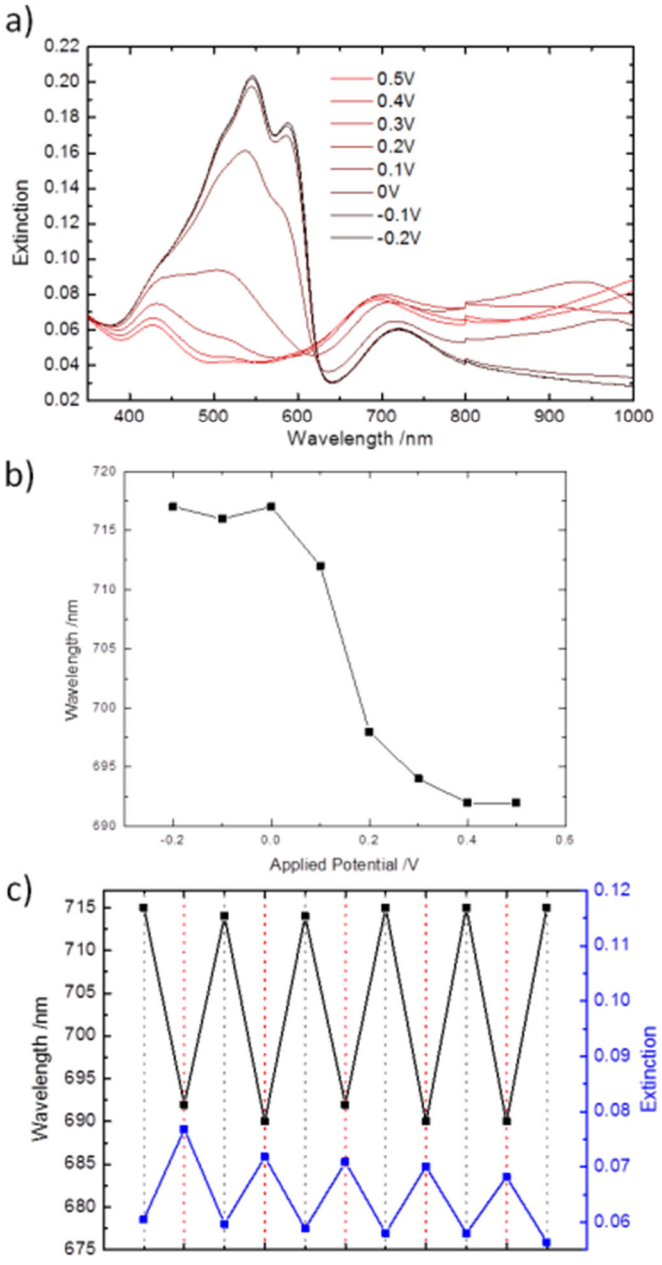

Figure F.2: Electrochromic behavior of AuNR/ECP-Mg composite material with 60 nm polymer thickness under applied potential. (a) Change in extinction over one cycle. (b) LSPR peak wavelength plotted versus applied potential. (c) Electrochemical cycling for 5 cycles. Red dotted lines indicate electrochemical oxidation.

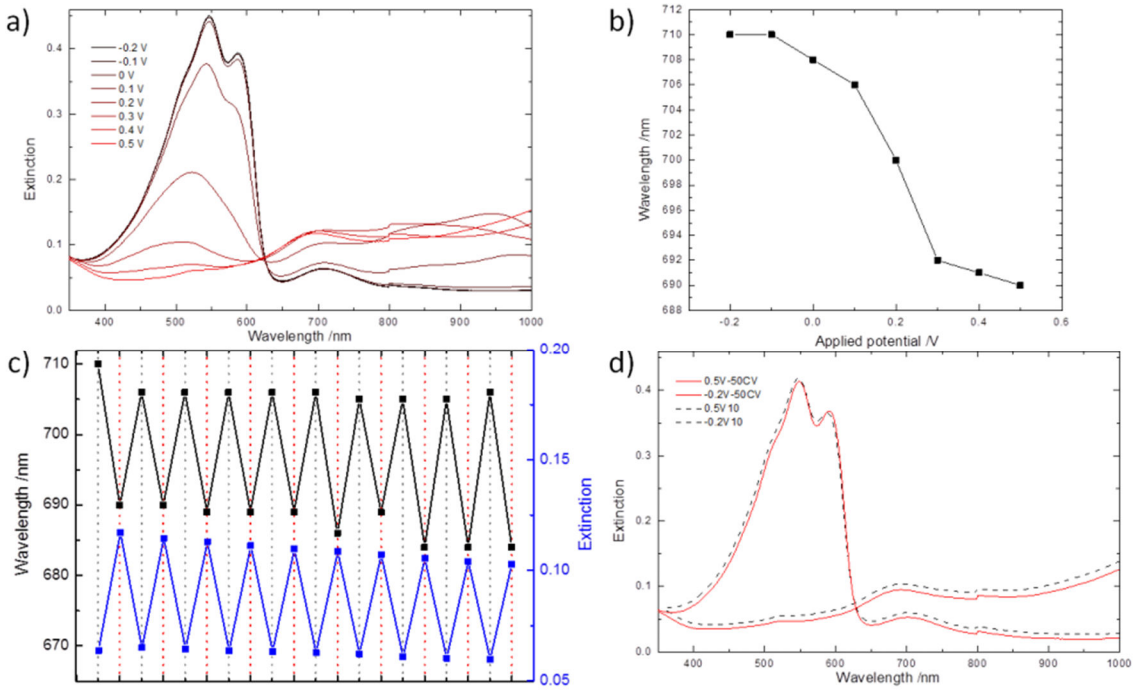

Figure F.3: Electrochromic behavior of AuNR/ECP-Mg composite material with 120 nm polymer thickness under applied potential. (a) Change in extinction over one cycle. (b) LSPR peak wavelength plotted versus applied potential. (c) Electrochemical cycling for 10 cycles. Red dotted lines indicate electrochemical oxidation. (d) Stability before and after 50 CV cycles.

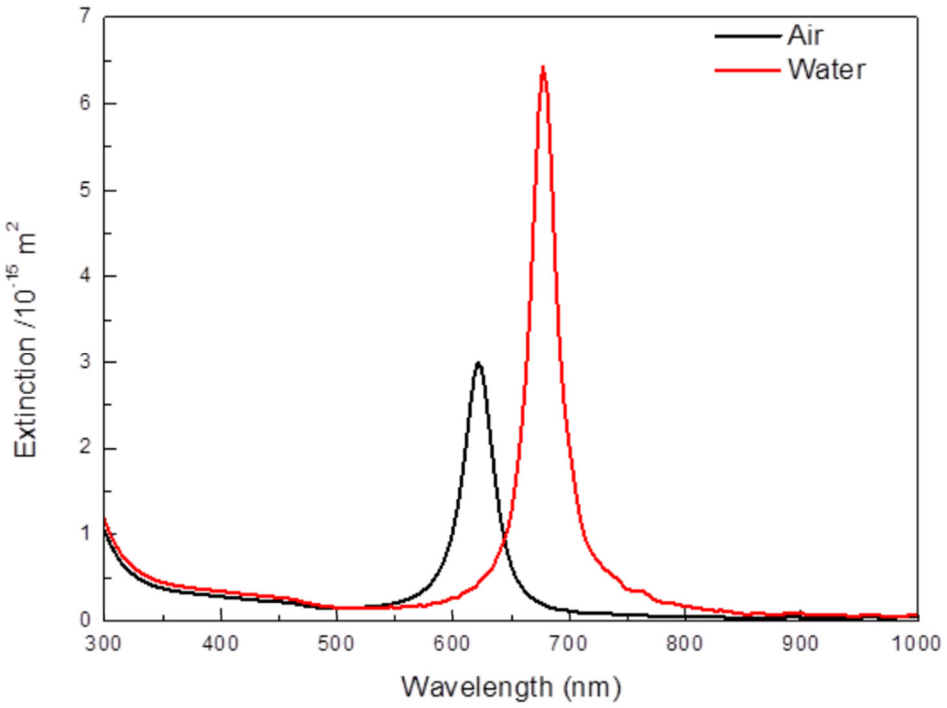

Figure F.4: Simulated extinction spectra of AuNRs on ITO substrate in air and water.

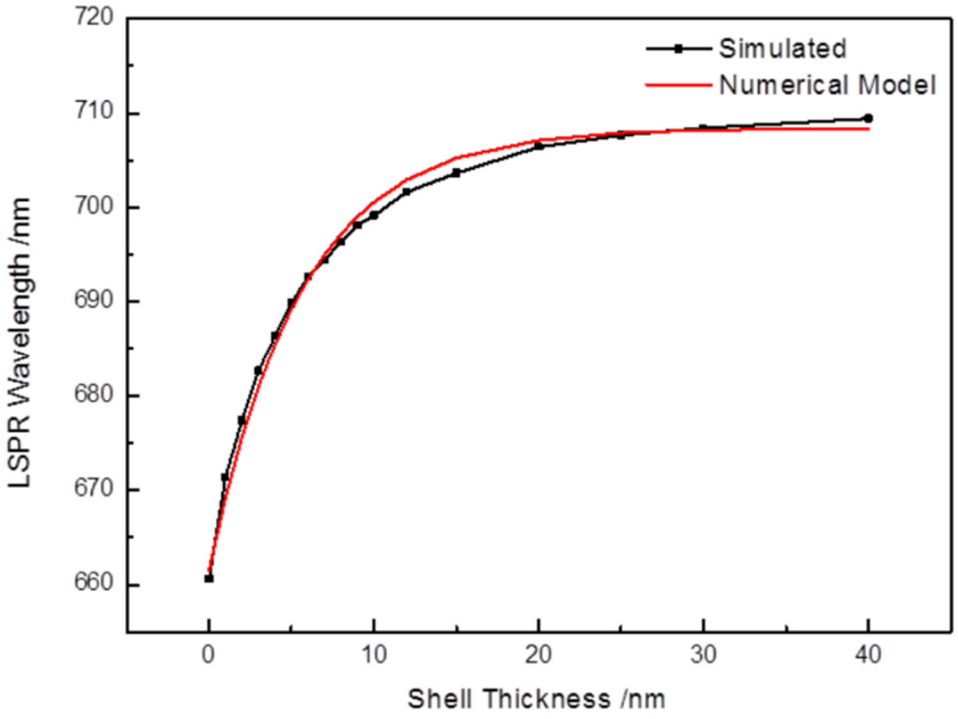

Figure F.5: Simulated LSPR wavelength of AuNRs with various silica shell thicknesses (black line). Exponential fit to Equation 4 to determine the electromagnetic field decay length (l_d) (red line).

Appendix G: Chapter 10 Supporting Information

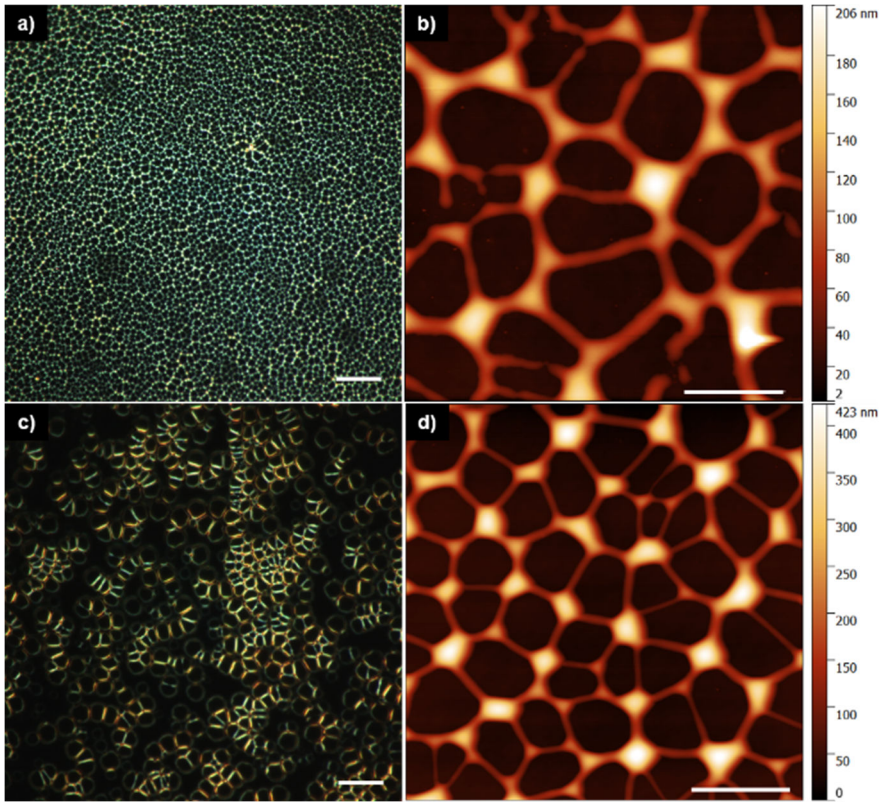

Figure G.1: (a),(b) 0.5 wt% and (c), (d) 1 wt% PLMA/QD composite film morphologies. Scale bars are 35 μm for (a) and (c), 5 μm for (b), and 10 μm for (d).

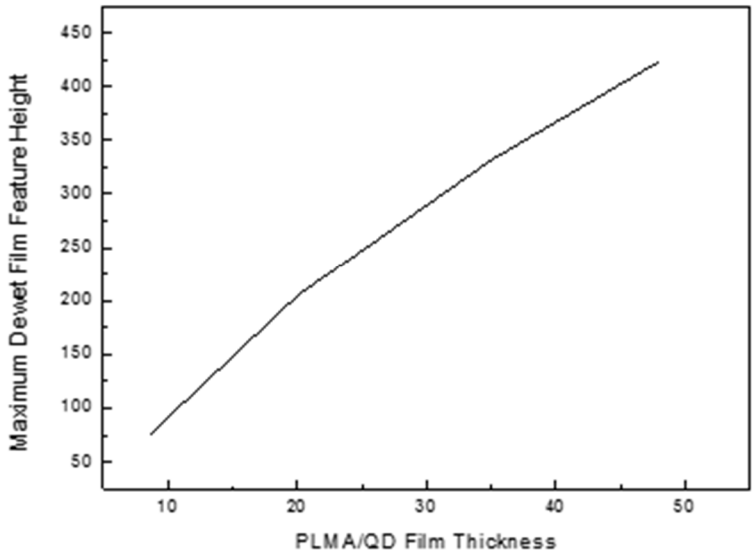

Figure G.2: Maximum feature height of dewet QD/PLMA films as a function of film thickness before dewetting.

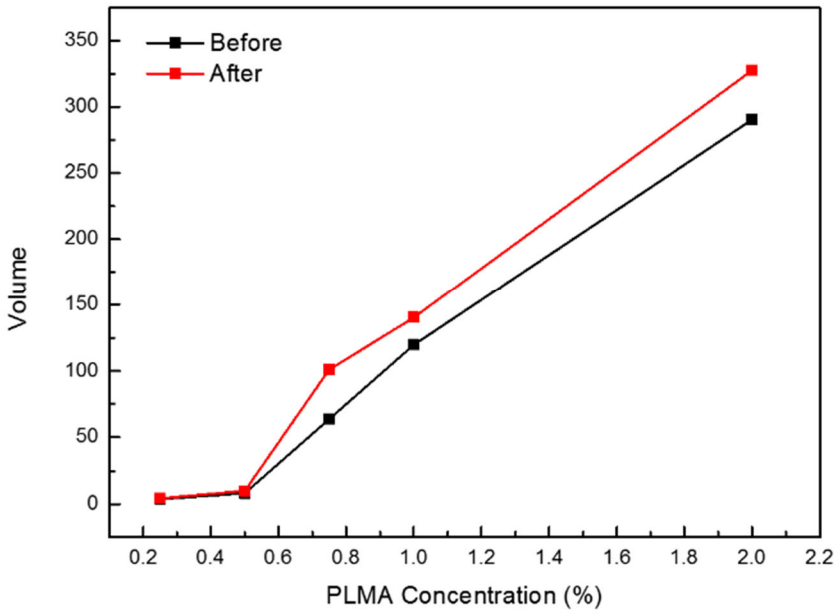

Figure G.3: The volume of QD/PLMA films before and after dewetting as measured by AFM.

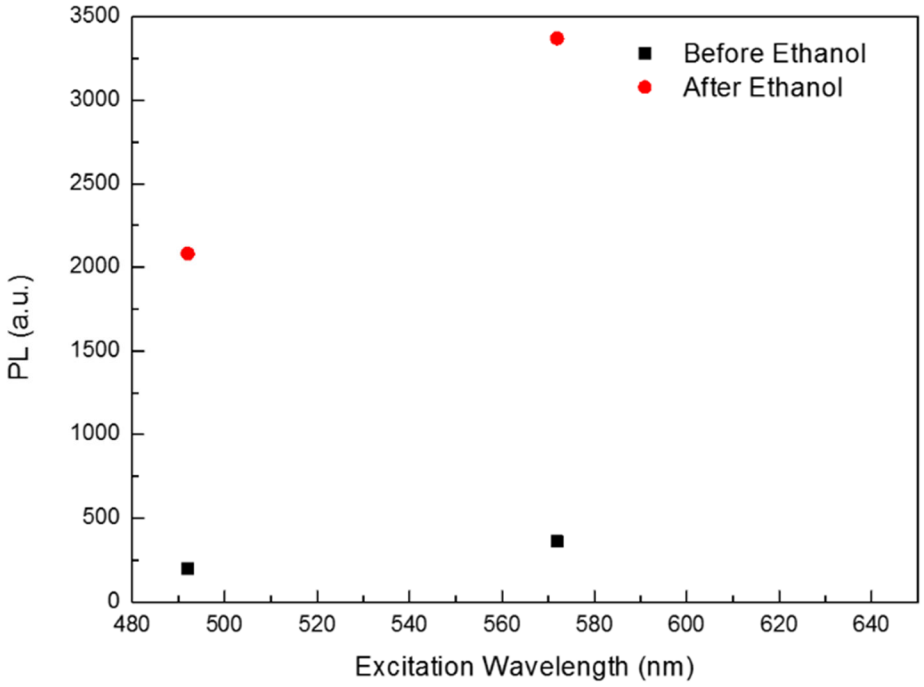

Figure G.4: The PL of a QD/PLMA film excited with 492 nm and 572 nm light before and after dewetting.

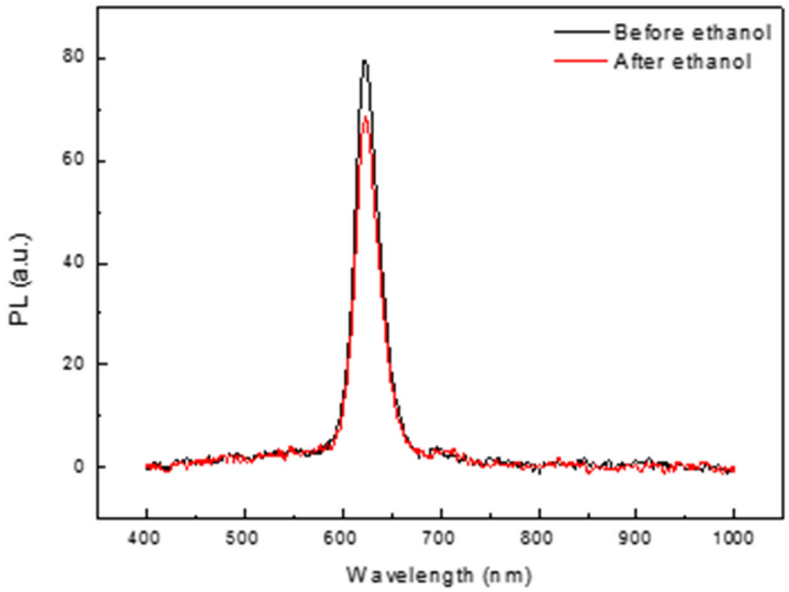

Figure G.5: The PL of a pure QD film before and after exposure to ethanol.

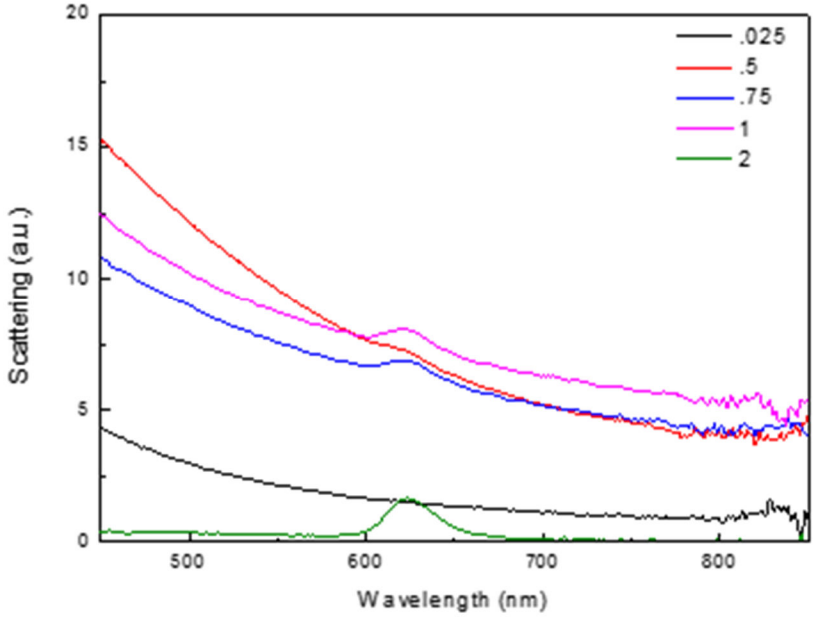

Figure G.6: The scattering spectra of 0.25, 0.5, 0.75, 1, and 2 wt% PLMA/QD composite films.

REFERENCES

1. Paris, A.; Vaccari, A.; Calà Lesina, A.; Serra, E.; Calliari, L. *Plasmonics* **2012,** 7, (3), 525-534.

2. Li, J.; Cushing, S. K.; Zheng, P.; Meng, F.; Chu, D.; Wu, N. *Nat Commun* **2013,** 4.

3. Maier, S. A.; Kik, P. G.; Atwater, H. A.; Meltzer, S.; Harel, E.; Koel, B. E.; Requicha, A. A. G. *Nat. Mater.* **2003,** 2, (4), 229-232.

4. Haes, A. J.; Haynes, C. L.; McFarland, A. D.; Schatz, G. C.; Van Duyne, R. P.; Zou, S. *MRS Bull.* **2005,** 30, (05), 368-375.

5. Stewart, M. E.; Anderton, C. R.; Thompson, L. B.; Maria, J.; Gray, S. K.; Rogers, J. A.; Nuzzo, R. G. *Chem. Rev.* **2008,** 108, (2), 494-521.

6. Sorger, V. J.; Oulton, R. F.; Ma, R.-M.; Zhang, X. *MRS Bull.* **2012,** 37, (08), 728-738.

7. Ozbay, E. *Science* **2006,** 311, (5758), 189-193.

8. Hess, O.; Pendry, J. B.; Maier, S. A.; Oulton, R. F.; Hamm, J. M.; Tsakmakidis, K. L. *Nat. Mater.* **2012,** 11, (7), 573-584.

9. Zhang, S.; Genov, D. A.; Wang, Y.; Liu, M.; Zhang, X. *Phys. Rev. Lett.* **2008,** 101, (4), 047401.

10. Pan, L.; Park, Y.; Xiong, Y.; Ulin-Avila, E.; Wang, Y.; Zeng, L.; Xiong, S.; Rho, J.; Sun, C.; Bogy, D. B.; Zhang, X. *Sci. Rep.* **2011,** 1.

11. Srituravanich, W.; Fang, N.; Sun, C.; Luo, Q.; Zhang, X. *Nano Lett.* **2004,** 4, (6), 1085-1088.

12. Rycenga, M.; Cobley, C. M.; Zeng, J.; Li, W.; Moran, C. H.; Zhang, Q.; Qin, D.; Xia, Y. *Chem. Rev.* **2011,** 111, (6), 3669-3712.

13. Genet, C.; Ebbesen, T. W. *Nature* **2007,** 445, (7123), 39-46.

14. Lee, H.-S.; Yoon, Y.-T.; Lee, S.-s.; Kim, S.-H.; Lee, K.-D. *Opt. Express* **2007,** 15, (23), 15457-15463.

15. Diest, K.; Dionne, J. A.; Spain, M.; Atwater, H. A. *Nano Lett.* **2009,** 9, (7), 2579-2583.

16. Laux, E.; Genet, C.; Skauli, T.; Ebbesen, T. W. *Nat Photon* **2008,** 2, (3), 161-164.

17. Anker, J. N.; Hall, W. P.; Lyandres, O.; Shah, N. C.; Zhao, J.; Van Duyne, R. P. *Nat. Mater.* **2008,** 7, (6), 442-453.

18. Chang, S.; Combs, Z. A.; Gupta, M. K.; Davis, R.; Tsukruk, V. V. *ACS Appl. Mater. Interfaces* **2010,** 2, (11), 3333-3339.

19. Jain, P. K.; Huang, X.; El-Sayed, I. H.; El-Sayed, M. A. *Acc. Chem. Res.* **2008,** 41, (12), 1578-1586.

20. Qian, X.; Peng, X.-H.; Ansari, D. O.; Yin-Goen, Q.; Chen, G. Z.; Shin, D. M.; Yang, L.; Young, A. N.; Wang, M. D.; Nie, S. *Nat Biotech* **2008,** 26, (1), 83-90.

21. Fang, N.; Lee, H.; Sun, C.; Zhang, X. *Science* **2005,** 308, (5721), 534-537.

22. Guo, X.; Qiu, M.; Bao, J.; Wiley, B. J.; Yang, Q.; Zhang, X.; Ma, Y.; Yu, H.; Tong, L. *Nano Lett.* **2009,** 9, (12), 4515-4519.

23. Atwater, H. A.; Polman, A. *Nat. Mater.* **2010,** 9, (3), 205-213.

24. *Nat Photon* **2012,** 6, (11), 714-715.

25. Rycenga, M.; McLellan, J. M.; Xia, Y. *Adv. Mater.* **2008,** 20, (12), 2416-2420.

26. Jana, N. R.; Gearheart, L.; Murphy, C. J. *Langmuir* **2001,** 17, (22), 6782-6786.

27. Wu, H.-L.; Kuo, C.-H.; Huang, M. H. *Langmuir* **2010,** 26, (14), 12307-12313.

28. Turkevich, J.; Stevenson, P. C.; Hillier, J. *Discussions of the Faraday Society* **1951,** 11, (0), 55-75.

29. Frens, G. *Nature: Phys. Sci.* **1973,** 241, 20.

30. Zhao, P.; Li, N.; Astruc, D. *Coord. Chem. Rev.* **2013,** 257, (3–4), 638-665.

31. Li, C.; Li, D.; Wan, G.; Xu, J.; Hou, W. *Nanoscale Res. Lett.* **2011,** 6, (1), 440.

32. Fievet, F.; Lagier, J. P.; Blin, B.; Beaudoin, B.; Figlarz, M. *Solid State Ionics* **1989,** 32, 198-205.

33. Sun, Y.; Xia, Y. *Adv. Mater.* **2002,** 14, (11), 833-837.

34. Sun, Y.; Xia, Y. *Science* **2002,** 298, (5601), 2176.

35. Mahmoud, M. A. *Crystal Growth & Design* **2015,** 15, (9), 4279-4286.

36. Jana, N. R.; Gearheart, L.; Murphy, C. J. *J. Phys. Chem. B* **2001,** 105, (19), 4065-4067.

37. Johnson, C. J.; Dujardin, E.; Davis, S. A.; Murphy, C. J.; Mann, S. *J. Mater. Chem.* **2002,** 12, (6), 1765-1770.

38. Gole, A.; Murphy, C. J. *Chem. Mater.* **2004,** 16, (19), 3633-3640.

39. Lu, X.; Rycenga, M.; Skrabalak, S. E.; Wiley, B.; Xia, Y. *Annu. Rev. Phys. Chem.* **2009,** 60, 167-192.

40. Murphy, C. J.; Thompson, L. B.; Chernak, D. J.; Yang, J. A.; Sivapalan, S. T.; Boulos, S. P.; Huang, J.; Alkilany, A. M.; Sisco, P. N. *Current Opinion in Colloid & Interface Science* **2011,** 16, (2), 128-134.

41. Sau, T. K.; Murphy, C. J. *Langmuir* **2004,** 20, (15), 6414-6420.

42. Nikoobakht, B.; El-Sayed, M. A. *Chem. Mater.* **2003,** 15, (10), 1957-1962.

43. Sau, T. K.; Murphy, C. J. *J. Am. Chem. Soc.* **2004,** 126, (28), 8648-8649.

44. Rommel, M.; Nilsson, B.; Jedrasik, P.; Bonanni, V.; Dmitriev, A.; Weis, J. *Microelectron. Eng.* **2013,** 110, 123-125.

45. Grigorescu, A.; Hagen, C. *Nanotechnology* **2009,** 20, (29), 292001.

46. Duan, H.; Hu, H.; Kumar, K.; Shen, Z.; Yang, J. K. W. *ACS Nano* **2011,** 5, (9), 7593-7600.

47. Kollmann, H.; Piao, X.; Esmann, M.; Becker, S. F.; Hou, D.; Huynh, C.; Kautschor, L.-O.; Bösker, G.; Vieker, H.; Beyer, A.; Gölzhäuser, A.; Park, N.; Vogelgesang, R.; Silies, M.; Lienau, C. *Nano Lett.* **2014,** 14, (8), 4778-4784.

48. Sivis, M.; Duwe, M.; Abel, B.; Ropers, C. *Nat Phys* **2013,** 9, (5), 304-309.

49. Huang, J.-S.; Kern, J.; Geisler, P.; Weinmann, P.; Kamp, M.; Forchel, A.; Biagioni, P.; Hecht, B. *Nano Lett.* **2010,** 10, (6), 2105-2110.

50. Chen, Y.; Xiang, Q.; Li, Z.; Wang, Y.; Meng, Y.; Duan, H. *Nano Lett.* **2016,** 16, (5), 3253-3259.

51. Min, Y.; Akbulut, M.; Kristiansen, K.; Golan, Y.; Israelachvili, J. *Nat. Mater.* **2008,** 7, (7), 527-538.

52. Velev, O. D.; Gupta, S. *Adv. Mater.* **2009,** 21, (19), 1897-1905.

53. Grzelczak, M.; Vermant, J.; Furst, E. M.; Liz-Marzán, L. M. *ACS nano* **2010,** 4, (7), 3591-3605.

54. Gao, B.; Arya, G.; Tao, A. R. *Nat Nano* **2012,** 7, (7), 433-437.

55. Elghanian, R.; Storhoff, J. J.; Mucic, R. C.; Letsinger, R. L.; Mirkin, C. A. *Science* **1997,** 277, (5329), 1078-1081.

56. Thacker, V. V.; Herrmann, L. O.; Sigle, D. O.; Zhang, T.; Liedl, T.; Baumberg, J. J.; Keyser, U. F. *Nat. Commun.* **2014,** 5, 3448.

57. Ding, B.; Deng, Z.; Yan, H.; Cabrini, S.; Zuckermann, R. N.; Bokor, J. *J. Am. Chem. Soc.* **2010,** 132, (10), 3248-3249.

58. Hung, A. M.; Micheel, C. M.; Bozano, L. D.; Osterbur, L. W.; Wallraff, G. M.; Cha, J. N. *Nat. Nanotechnol.* **2010,** 5, (2), 121-126.

59. Shen, X.; Song, C.; Wang, J.; Shi, D.; Wang, Z.; Liu, N.; Ding, B. *J. Am. Chem. Soc.* **2011,** 134, (1), 146-149.

60. Schreiber, R.; Do, J.; Roller, E.-M.; Zhang, T.; Schuller, V. J.; Nickels, P. C.; Feldmann, J.; Liedl, T. *Nat Nano* **2014,** 9, (1), 74-78.

61. Gandra, N.; Abbas, A.; Tian, L.; Singamaneni, S. *Nano Lett.* **2012,** 12, (5), 2645-2651.

62. Maenosono, S.; Okubo, T.; Yamaguchi, Y. *J. Nanopart. Res.* **2003,** 5, (1), 5-15.

63. Tao, A. R.; Huang, J.; Yang, P. *Acc. Chem. Res.* **2008,** 41, (12), 1662-1673.

64. Mahmoud, M. A. *The Journal of Chemical Physics* **2015,** 143, (7), 074703.

65. Kraus, T.; Malaquin, L.; Schmid, H.; Riess, W.; Spencer, N. D.; Wolf, H. *Nat Nano* **2007,** 2, (9), 570-576.

66. Lee, S. Y.; Hung, L.; Lang, G. S.; Cornett, J. E.; Mayergoyz, I. D.; Rabin, O. *ACS Nano* **2010,** 4, (10), 5763-5772.

67. Henzie, J.; Andrews, S. C.; Ling, X. Y.; Li, Z.; Yang, P. *Proceedings of the National Academy of Sciences* **2013,** 110, (17), 6640-6645.

68. Hanske, C.; Tebbe, M.; Kuttner, C.; Bieber, V.; Tsukruk, V. V.; Chanana, M.; König, T. A. F.; Fery, A. *Nano Lett.* **2014,** 14, (12), 6863-6871.

69. Pérez-Juste, J.; Pastoriza-Santos, I.; Liz-Marzán, L. M.; Mulvaney, P. *Coord. Chem. Rev.* **2005,** 249, (17-18 SPEC. ISS.), 1870-1901.

70. Petryayeva, E.; Krull, U. J. *Anal. Chim. Acta* **2011,** 706, (1), 8-24.

71. van Dijk, M. A.; Tchebotareva, A. L.; Orrit, M.; Lippitz, M.; Berciaud, S.; Lasne, D.; Cognet, L.; Lounis, B. *PCCP* **2006,** 8, (30), 3486-3495.

72. Jain, P. K.; Lee, K. S.; El-Sayed, I. H.; El-Sayed, M. A. *J. Phys. Chem. B* **2006,** 110, (14), 7238-7248.

73. Ru, E. L.; Etchegoin, P., *Principles of Surface-Enhanced Raman Spectroscopy: and related plasmonic effects*. Elsevier Science: 2008.

74. Murray, W. A.; Barnes, W. L. *Adv. Mater.* **2007,** 19, (22), 3771-3782.

75. West, P. R.; Ishii, S.; Naik, G. V.; Emani, N. K.; Shalaev, V. M.; Boltasseva, A. *Laser Photon. Rev.* **2010,** 4, (6), 795-808.

76. Chan, G. H.; Zhao, J.; Hicks, E. M.; Schatz, G. C.; Van Duyne, R. P. *Nano Lett.* **2007,** 7, (7), 1947-1952.

77. Kelly, K. L.; Coronado, E.; Zhao, L. L.; Schatz, G. C. *J. Phys. Chem. B* **2002,** 107, (3), 668-677.

78. Noguez, C. *J. Phys. Chem. C* **2007,** 111, (10), 3806-3819.

79. Jain, P. K.; El-Sayed, M. A. *Nano Lett.* **2008,** 8, (12), 4347-4352.

80. Lee, K.-S.; El-Sayed, M. A. *J. Phys. Chem. B* **2006,** 110, (39), 19220-19225.

81. Lee, K.-S.; El-Sayed, M. A. *J. Phys. Chem. B* **2005,** 109, (43), 20331-20338.

82. Jain, P. K.; El-Sayed, M. A. *Chem. Phys. Lett.* **2010,** 487, (4), 153-164.

83. Haynes, C. L.; McFarland, A. D.; Zhao, L.; Van Duyne, R. P.; Schatz, G. C.; Gunnarsson, L.; Prikulis, J.; Kasemo, B.; Käll, M. *J. Phys. Chem. B* **2003,** 107, (30), 7337-7342.

84. Jain, P. K.; Lee, K. S.; El-Sayed, I. H.; El-Sayed, M. A. *J. Phys. Chem. B* **2006,** 110, (14), 7238-7248.

85. Liz-Marzán, L. M. *Langmuir* **2006,** 22, (1), 32-41.

86. Kreibig, U.; Vollmer, M., *Optical properties of metal clusters*. Springer: 1995.

87. Zhou, F.; Li, Z.-Y.; Liu, Y.; Xia, Y. *J. Phys. Chem. C* **2008,** 112, (51), 20233-20240.

88. Mahmoud, M. A.; Chamanzar, M.; Adibi, A.; El-Sayed, M. A. *J. Am. Chem. Soc.* **2012,** 134, (14), 6434-6442.

89. Zhang, Q.; Li, W.; Moran, C.; Zeng, J.; Chen, J.; Wen, L.-P.; Xia, Y. *J. Am. Chem. Soc.* **2010,** 132, (32), 11372-11378.

90. Rivera, V. A. G.; Ferri, F. A.; Jr, E. M., Localized Surface Plasmon Resonances: Noble Metal Nanoparticle Interaction with Rare-Earth Ions. In *Plasmonics - Principles and Applications*, Kim, K. Y., Ed. InTech: Rijeka, 2012; p Ch. 11.

91. Mock, J. J.; Barbic, M.; Smith, D. R.; Schultz, D. A.; Schultz, S. *The Journal of Chemical Physics* **2002,** 116, (15), 6755-6759.

92. Grillet, N.; Manchon, D.; Bertorelle, F.; Bonnet, C.; Broyer, M.; Cottancin, E.; Lermé, J.; Hillenkamp, M.; Pellarin, M. *ACS Nano* **2011,** 5, (12), 9450-9462.

93. Jin, R.; Cao, Y.; Mirkin, C. A.; Kelly, K. L.; Schatz, G. C.; Zheng, J. G. *Science* **2001,** 294, (5548), 1901.

94. Alvarez, M. M.; Khoury, J. T.; Schaaff, T. G.; Shafigullin, M. N.; Vezmar, I.; Whetten, R. L. *J. Phys. Chem. B* **1997,** 101, (19), 3706-3712.

95. Link, S.; El-Sayed, M. A. *J. Phys. Chem. B* **1999,** 103, (40), 8410-8426.

96. Shen, Y.; Zhou, J.; Liu, T.; Tao, Y.; Jiang, R.; Liu, M.; Xiao, G.; Zhu, J.; Zhou, Z.-K.; Wang, X.; Jin, C.; Wang, J. *Nat. Commun.* **2013,** 4, 2381.

97. Ringe, E.; McMahon, J. M.; Sohn, K.; Cobley, C.; Xia, Y.; Huang, J.; Schatz, G. C.; Marks, L. D.; Van Duyne, R. P. *J. Phys. Chem. C* **2010,** 114, (29), 12511-12516.

98. Zhang, S.; Bao, K.; Halas, N. J.; Xu, H.; Nordlander, P. *Nano Lett.* **2011,** 11, (4), 1657-1663.

99. Halas, N. J.; Lal, S.; Chang, W.-S.; Link, S.; Nordlander, P. *Chem. Rev.* **2011,** 111, (6), 3913-3961.

100. Knight, M. W.; Wu, Y.; Lassiter, J. B.; Nordlander, P.; Halas, N. J. *Nano Lett.* **2009,** 9, (5), 2188-2192.

101. Nordlander, P.; Prodan, E. *Nano Lett.* **2004,** 4, (11), 2209-2213.

102. Hu, M.; Ghoshal, A.; Marquez, M.; Kik, P. G. *J. Phys. Chem. C* **2010,** 114, (16), 7509-7514.

103. Pelton, M.; Aizpurua, J.; Bryant, G. *Laser Photon. Rev.* **2008,** 2, (3), 136-159.

104. Jain, P. K.; Huang, W.; El-Sayed, M. A. *Nano Lett.* **2007,** 7, (7), 2080-2088.

105. Su, K. H.; Wei, Q. H.; Zhang, X.; Mock, J. J.; Smith, D. R.; Schultz, S. *Nano Lett.* **2003,** 3, (8), 1087-1090.

106. Fang, Y.; Seong, N.-H.; Dlott, D. D. *Science* **2008,** 321, (5887), 388-392.

107. Xu, H.; Bjerneld, E. J.; Käll, M.; Börjesson, L. *Phys. Rev. Lett.* **1999,** 83, (21), 4357-4360.

108. Nordlander, P.; Oubre, C.; Prodan, E.; Li, K.; Stockman, M. I. *Nano Lett.* **2004,** 4, (5), 899-903.

109. Etchegoin, P. G.; Le Ru, E. C. *PCCP* **2008,** 10, (40), 6079-6089.

110. Ritchie, R. H. *Physical Review* **1957,** 106, (5), 874-881.

111. Sambles, J. R.; Bradbery, G. W.; Yang, F. *Contemp. Phys.* **1991,** 32, (3), 173-183.

112. Kretschmann, E.; Raether, H. *Z. Naturforsch. A.* **1968,** 23, 2135-2136.

113. Otto, A. *Z. Angew. Phys.* **1968,** 216, (4), 398-410.

114. Ruffato, G.; Zacco, G.; Romanato, F., Innovative Exploitation of Grating-Coupled Surface Plasmon Resonance for Sensing. In *Plasmonics - Principles and Applications*, Kim, K. Y., Ed. 2012.

115. Hecht, B.; Bielefeldt, H.; Novotny, L.; Inouye, Y.; Pohl, D. W. *Phys. Rev. Lett.* **1996,** 77, (9), 1889-1892.

116. Ebbesen, T. W.; Lezec, H. J.; Ghaemi, H. F.; Thio, T.; Wolff, P. A. *Nature* **1998,** 391, (6668), 667-669.

117. Raether, H., *Surface Plasmons on Smooth and Rough Surfaces and on Gratings*. Springer: Berlin, 1988.

118. Ghaemi, H. F.; Thio, T.; Grupp, D. E.; Ebbesen, T. W.; Lezec, H. J. *Phys. Rev. B* **1998,** 58, (11), 6779-6782.

119. Montgomery, J. M.; Imre, A.; Welp, U.; Vlasko-Vlasov, V.; Gray, S. K. *Opt. Express* **2009,** 17, (10), 8669-8675.

120. Barnes, W. L.; Dereux, A.; Ebbesen, T. W. *Nature* **2003,** 424, (6950), 824-830.

121. Taflove, A., *Advances in Computational Electrodynamics: The Finite-Difference Time-Domain Method*. Artech House: 1998.

122. Kunz, K. S.; Luebbers, R. J., *The Finite Difference Time Domain Method for Electromagnetics*. Taylor & Francis: 1993.

123. Kodiyath, R.; Malak, S. T.; Combs, Z. A.; Koenig, T.; Mahmoud, M. A.; El-Sayed, M. A.; Tsukruk, V. V. *J. Mater. Chem. A* **2013,** 1, (8), 2777-2788.

124. Lumerical Solutions, I. Overcoming the Multi-wavelength FDTD Challenge. http://www.lumerical.com/solutions/innovation/fdtd_multicoefficient_material_modeling.html

125. Kane, Y. *Antennas and Propagation, IEEE Transactions on* **1966,** 14, (3), 302-307.

126. LLC, T. The Yee Cell. http://fdtd.wikispaces.com

127. Alsunaidi, M. A.; Al-Jabr, A. A. *IEEE Photonics Technol. Lett.* **2009,** 21, (12), 817-819.

128. Nagra, A. S.; York, R. A. *Antennas and Propagation, IEEE Transactions on* **1998,** 46, (3), 334-340.

129. Toland, B.; Houshmand, B.; Itoh, T. *Microwave and Guided Wave Letters, IEEE* **1993,** 3, (9), 333-335.

130. Luebbers, R.; Hunsberger, F. P.; Kunz, K. S.; Standler, R. B.; Schneider, M. *Electromagnetic Compatibility, IEEE Transactions on* **1990,** 32, (3), 222-227.

131. Berenger, J.-P. *J. Comput. Phys.* **1996,** 127, (2), 363-379.

132. Hoa, X. D.; Kirk, A. G.; Tabrizian, M. *Biosens. Bioelectron.* **2007,** 23, (2), 151-160.

133. Nguyen, H. H.; Park, J.; Kang, S.; Kim, M. *Sensors* **2015,** 15, (5).

134. Homola, J.; Yee, S. S.; Gauglitz, G. *"Sens. Actuators, B "* **1999,** 54, (1–2), 3-15.

135. Haes, A. J.; Van Duyne, R. P. *Anal. Bioanal.Chem.* **2004,** 379, (7), 920-930.

136. McVey, C.; Huang, F.; Elliott, C.; Cao, C. *Biosens. Bioelectron.* **2017,** 92, 502-508.

137. Haes, A. J.; Van Duyne, R. P. *J. Am. Chem. Soc.* **2002,** 124, (35), 10596-10604.

138. Stiles, P. L.; Dieringer, J. A.; Shah, N. C.; Van Duyne, R. P. *Annual Review of Analytical Chemistry* **2008,** 1, (1), 601-626.

139. Fleischmann, M.; Hendra, P. J.; McQuillan, A. J. *Chem. Phys. Lett.* **1974,** 26, (2), 163-166.

140. Sharma, B.; Frontiera, R. R.; Henry, A.-I.; Ringe, E.; Van Duyne, R. P. *Mater. Today* **2012,** 15, (1–2), 16-25.

141. Yang, S.; Dai, X.; Stogin, B. B.; Wong, T.-S. *Proceedings of the National Academy of Sciences* **2016,** 113, (2), 268-273.

142. Pala, R. A.; White, J.; Barnard, E.; Liu, J.; Brongersma, M. L. *Adv. Mater.* **2009,** 21, (34), 3504-3509.

143. Lu, Y.; Dong, W.; Chen, Z.; Pors, A.; Wang, Z.; Bozhevolnyi, S. I. *Scientific Reports* **2016,** 6, 30650.

144. Tsai, M.-W.; Chuang, T.-H.; Meng, C.-Y.; Chang, Y.-T.; Lee, S.-C. *Appl. Phys. Lett.* **2006,** 89, (17), 173116.

145. Wu, C.; Neuner III, B.; John, J.; Milder, A.; Zollars, B.; Savoy, S.; Shvets, G. *J. Opt.* **2012,** 14, (2), 024005.

146. Zhou, L.; Tan, Y.; Ji, D.; Zhu, B.; Zhang, P.; Xu, J.; Gan, Q.; Yu, Z.; Zhu, J. *Science Advances* **2016,** 2, (4).

147. Alivisatos, A. P. *Science* **1996,** 271, (5251), 933.

148. Dabbousi, B. O.; Rodriguez-Viejo, J.; Mikulec, F. V.; Heine, J. R.; Mattoussi, H.; Ober, R.; Jensen, K. F.; Bawendi, M. G. *J. Phys. Chem. B* **1997,** 101, (46), 9463-9475.

149. Bimberg, D.; Grundmann, M.; Ledentsov, N. N., *Quantum dot heterostructures*. John Wiley & Sons: 1999.

150. Kim, S.; Bawendi, M. G. *J. Am. Chem. Soc.* **2003,** 125, (48), 14652-14653.

151. Murphy, C. J. *Anal. Chem.* **2002,** 74, (19), 520 A-526 A.

152. Algar, W. R.; Susumu, K.; Delehanty, J. B.; Medintz, I. L. *Anal. Chem.* **2011,** 83, (23), 8826-8837.

153. Bruchez, M.; Moronne, M.; Gin, P.; Weiss, S.; Alivisatos, A. P. *science* **1998,** 281, (5385), 2013-2016.

154. Caruge, J.; Halpert, J.; Wood, V.; Bulović, V.; Bawendi, M. *Nat. Photonics* **2008,** 2, (4), 247-250.

155. Anikeeva, P. O.; Halpert, J. E.; Bawendi, M. G.; Bulovic, V. *Nano Lett.* **2009,** 9, (7), 2532-2536.

156. Nozik, A. *Physica E* **2002,** 14, (1), 115-120.

157. Hines, M. A.; Guyot-Sionnest, P. *The Journal of Physical Chemistry* **1996,** 100, (2), 468-471.

158. Hammer, N. I.; Emrick, T.; Barnes, M. D. *Nanoscale Res. Lett.* **2007,** 2, (6), 282-290.

159. Bailey, R. E.; Smith, A. M.; Nie, S. *Physica E* **2004,** 25, (1), 1-12.

160. Walling, M. A.; Novak, J. A.; Shepard, J. R. E. *Int. J. Mol. Sci.* **2009,** 10, (2), 441-491.

161. Michalet, X.; Pinaud, F. F.; Bentolila, L. A.; Tsay, J. M.; Doose, S.; Li, J. J.; Sundaresan, G.; Wu, A. M.; Gambhir, S. S.; Weiss, S. *Science* **2005,** 307, (5709), 538.

162. Lin, K.-F.; Cheng, H.-M.; Hsu, H.-C.; Lin, L.-J.; Hsieh, W.-F. *Chem. Phys. Lett.* **2005,** 409, (4–6), 208-211.

163. Morello, G.; De Giorgi, M.; Kudera, S.; Manna, L.; Cingolani, R.; Anni, M. *J. Phys. Chem. C* **2007,** 111, (16), 5846-5849.

164. Guzelian, A. A.; Banin, U.; Kadavanich, A. V.; Peng, X.; Alivisatos, A. P. *Appl. Phys. Lett.* **1996,** 69, (10), 1432-1434.

165. Guzelian, A. A.; Katari, J. E. B.; Kadavanich, A. V.; Banin, U.; Hamad, K.; Juban, E.; Alivisatos, A. P.; Wolters, R. H.; Arnold, C. C.; Heath, J. R. *The Journal of Physical Chemistry* **1996,** 100, (17), 7212-7219.

166. Tsay, J. M.; Pflughoefft, M.; Bentolila, L. A.; Weiss, S. *J. Am. Chem. Soc.* **2004,** 126, (7), 1926-1927.

167. Murray, C. B.; Norris, D. J.; Bawendi, M. G. *J. Am. Chem. Soc.* **1993,** 115, (19), 8706-8715.

168. Peng, X.; Schlamp, M. C.; Kadavanich, A. V.; Alivisatos, A. P. *J. Am. Chem. Soc.* **1997,** 119, (30), 7019-7029.

169. Xie, R.; Kolb, U.; Li, J.; Basché, T.; Mews, A. *J. Am. Chem. Soc.* **2005,** 127, (20), 7480-7488.

170. García-Santamaría, F.; Chen, Y.; Vela, J.; Schaller, R. D.; Hollingsworth, J. A.; Klimov, V. I. *Nano Lett.* **2009,** 9, (10), 3482-3488.

171. Chen, Y.; Vela, J.; Htoon, H.; Casson, J. L.; Werder, D. J.; Bussian, D. A.; Klimov, V. I.; Hollingsworth, J. A. *J. Am. Chem. Soc.* **2008,** 130, (15), 5026-5027.

172. Jung, J.; Lin, C. H.; Yoon, Y. J.; Malak, S. T.; Zhai, Y.; Thomas, E. L.; Vardeny, V.; Tsukruk, V. V.; Lin, Z. *Angew. Chem. Int. Ed.* **2016,** 55, (16), 5071-5075.

173. Bailey, R. E.; Nie, S. *J. Am. Chem. Soc.* **2003,** 125, (23), 7100-7106.

174. Malak, S. T.; Lafalce, E.; Jung, J.; Lin, C. H.; Smith, M. J.; Yoon, Y. J.; Lin, Z.; Vardeny, Z. V.; Tsukruk, V. V. *Journal of Materials Chemistry C* **2016,** 4, (42), 10069-10081.

175. Templeton, A. C.; Wuelfing, W. P.; Murray, R. W. *Acc. Chem. Res.* **2000,** 33, (1), 27-36.

176. Potapova, I.; Mruk, R.; Prehl, S.; Zentel, R.; Basché, T.; Mews, A. *J. Am. Chem. Soc.* **2003,** 125, (2), 320-321.

177. Bruchez, M.; Moronne, M.; Gin, P.; Weiss, S.; Alivisatos, A. P. *Science* **1998,** 281, (5385), 2013.

178. Gerion, D.; Pinaud, F.; Williams, S. C.; Parak, W. J.; Zanchet, D.; Weiss, S.; Alivisatos, A. P. *J. Phys. Chem. B* **2001,** 105, (37), 8861-8871.

179. Wang, X.-S.; Dykstra, T. E.; Salvador, M. R.; Manners, I.; Scholes, G. D.; Winnik, M. A. *J. Am. Chem. Soc.* **2004,** 126, (25), 7784-7785.

180. Tan, Z.; Zhang, Y.; Xie, C.; Su, H.; Liu, J.; Zhang, C.; Dellas, N.; Mohney, S. E.; Wang, Y.; Wang, J.; Xu, J. *Adv. Mater.* **2011,** 23, (31), 3553-3558.

181. Zhang, Y.; Xie, C.; Su, H.; Liu, J.; Pickering, S.; Wang, Y.; Yu, W. W.; Wang, J.; Wang, Y.; Hahm, J.-i.; Dellas, N.; Mohney, S. E.; Xu, J. *Nano Lett.* **2011,** 11, (2), 329-332.

182. Pons, T.; Pic, E.; Lequeux, N.; Cassette, E.; Bezdetnaya, L.; Guillemin, F.; Marchal, F.; Dubertret, B. *ACS Nano* **2010,** 4, (5), 2531-2538.

183. Peng, X.; Manna, L.; Yang, W.; Wickham, J.; Scher, E.; Kadavanich, A.; Alivisatos, A. P. *Nature* **2000,** 404, (6773), 59-61.

184. Cox, J. *Chem. Br.* **2003,** 39, (9), 21-25.

185. Fox, M., Optical properties of solids. AAPT: 2002.

186. Grahn, H. T., *Introduction to semiconductor physics*. World Scientific Publishing Co Inc: 1999.

187. Zhu, H.; Lian, T. *Energy Environ. Sci.* **2012,** 5, (11), 9406-9418.

188. Kim, S.; Fisher, B.; Eisler, H.-J.; Bawendi, M. *J. Am. Chem. Soc.* **2003,** 125, (38), 11466-11467.

189. Zhu, H.; Song, N.; Rodríguez-Córdoba, W.; Lian, T. *J. Am. Chem. Soc.* **2012,** 134, (9), 4250-4257.

190. Kurzmann, A.; Ludwig, A.; Wieck, A. D.; Lorke, A.; Geller, M. *Nano Lett.* **2016,** 16, (5), 3367-3372.

191. Klimov, V. I.; Mikhailovsky, A. A.; McBranch, D. W.; Leatherdale, C. A.; Bawendi, M. G. *Science* **2000,** 287, (5455), 1011.

192. Park, Y.-S.; Bae, W. K.; Padilha, L. A.; Pietryga, J. M.; Klimov, V. I. *Nano Lett.* **2014,** 14, (2), 396-402.

193. Dennis, A. M.; Mangum, B. D.; Piryatinski, A.; Park, Y.-S.; Hannah, D. C.; Casson, J. L.; Williams, D. J.; Schaller, R. D.; Htoon, H.; Hollingsworth, J. A. *Nano Lett.* **2012,** 12, (11), 5545-5551.

194. Nazzal, A. Y.; Wang, X.; Qu, L.; Yu, W.; Wang, Y.; Peng, X.; Xiao, M. *J. Phys. Chem. B* **2004,** 108, (18), 5507-5515.

195. Van Sark, W. G.; Frederix, P. L.; Van den Heuvel, D. J.; Gerritsen, H. C.; Bol, A. A.; Van Lingen, J. N.; de Mello Donega, C.; Meijerink, A. *J. Phys. Chem. B* **2001,** 105, (35), 8281-8284.

196. Medintz, I. L.; Clapp, A. R.; Mattoussi, H.; Goldman, E. R.; Fisher, B.; Mauro, J. M. *Nat. Mater.* **2003,** 2, (9), 630-638.

197. Sapsford, E. K.; Pons, T.; Medintz, L. I.; Mattoussi, H. *Sensors* **2006,** 6, (8).

198. Li, M.; Cushing, S. K.; Wu, N. *Analyst* **2015,** 140, (2), 386-406.

199. Lessard-Viger, M.; Rioux, M.; Rainville, L.; Boudreau, D. *Nano Lett.* **2009,** 9, (8), 3066-3071.

200. Mertens, H.; Koenderink, A.; Polman, A. *Phys. Rev. B* **2007,** 76, (11), 115123.

201. Dulkeith, E.; Morteani, A.; Niedereichholz, T.; Klar, T.; Feldmann, J.; Levi, S.; Van Veggel, F.; Reinhoudt, D.; Möller, M.; Gittins, D. *Phys. Rev. Lett.* **2002,** 89, (20), 203002.

202. Jennings, T.; Singh, M.; Strouse, G. *J. Am. Chem. Soc.* **2006,** 128, (16), 5462-5467.

203. Tang, Z.; Wang, Y.; Kotov, N. A. *Langmuir* **2002,** 18, (18), 7035-7040.

204. Hongjoo, S.; Seonghoon, L. *Nanotechnology* **2007,** 18, (5), 055402.

205. Zimnitsky, D.; Jiang, C.; Xu, J.; Lin, Z.; Tsukruk, V. V. *Langmuir* **2007,** 23, (8), 4509-4515.

206. Kharlampieva, E.; Kozlovskaya, V.; Zavgorodnya, O.; Lilly, G. D.; Kotov, N. A.; Tsukruk, V. V. *Soft Matter* **2010,** 6, (4), 800-807.

207. Lee, J.; Sundar, V. C.; Heine, J. R.; Bawendi, M. G.; Jensen, K. F. *Adv. Mater.* **2000,** 12, (15), 1102-1105.

208. Liu, H.; Edel, J. B.; Bellan, L. M.; Craighead, H. G. *Small* **2006,** 2, (4), 495-499.

209. Suárez, I.; Gordillo, H.; Abargues, R.; Albert, S.; Martínez-Pastor, J. *Nanotechnology* **2011,** 22, (43), 435202.

210. Oh, E.; Hong, M.-Y.; Lee, D.; Nam, S.-H.; Yoon, H. C.; Kim, H.-S. *J. Am. Chem. Soc.* **2005,** 127, (10), 3270-3271.

211. Dong, H.; Gao, W.; Yan, F.; Ji, H.; Ju, H. *Anal. Chem.* **2010,** 82, (13), 5511-5517.

212. Algar, W. R.; Krull, U. J. *Anal. Chim. Acta* **2007,** 581, (2), 193-201.

213. Samsung QLED TV. http://www.samsung.com/global/tv/qled/quantum-dot/

214. Coe, S.; Woo, W.-K.; Bawendi, M.; Bulovic, V. *Nature* **2002,** 420, (6917), 800-803.

215. Sun, Q.; Wang, Y. A.; Li, L. S.; Wang, D.; Zhu, T.; Xu, J.; Yang, C.; Li, Y. *Nat Photon* **2007,** 1, (12), 717-722.

216. Colvin, V. L.; Schlamp, M. C.; Alivisatos, A. P. *Nature* **1994,** 370, (6488), 354-357.

217. Sun, L.; Choi, J. J.; Stachnik, D.; Bartnik, A. C.; Hyun, B.-R.; Malliaras, G. G.; Hanrath, T.; Wise, F. W. *Nat Nano* **2012,** 7, (6), 369-373.

218. Mahmoud, M. A.; El-Sayed, M. A. *J. Phys. Chem. C* **2008,** 112, (37), 14618-14625.

219. Mahmoud, M. A.; Tabor, C. E.; El-Sayed, M. A. *J. Phys. Chem. C* **2009,** 113, (14), 5493-5501.

220. Sisco, P. N.; Murphy, C. J. *The Journal of Physical Chemistry A* **2009,** 113, (16), 3973-3978.

221. Jung, J.; Lin, C. H.; Yoon, Y. J.; Malak, S. T.; Zhai, Y.; Thomas, E. L.; Vardeny, V.; Tsukruk, V. V.; Lin, Z. *Angewandte Chemie* **2016,** 128, (16), 5155-5159.

222. Ledin, P. A.; Tkachenko, I. M.; Xu, W.; Choi, I.; Shevchenko, V. V.; Tsukruk, V. V. *Langmuir* **2014,** 30, (29), 8856-8865.

223. Padilla, J.; Österholm, A. M.; Dyer, A. L.; Reynolds, J. R. *Sol. Energy Mater. Sol. Cells* **2015,** 140, 54-60.

224. Jiang, N.; Shao, L.; Wang, J. *Adv. Mater.* **2014,** 26, (20), 3282-3289.

225. Xing, S.; Tan, L. H.; Yang, M.; Pan, M.; Lv, Y.; Tang, Q.; Yang, Y.; Chen, H. *J. Mater. Chem.* **2009,** 19, (20), 3286-3291.

226. Nečas, D.; Klapetek, P. *Cent. Eur. J. Phys.* **2011,** 10, (1), 181-188.

227. Lumerical Solutions, I. FDTD Solutions 8.7. http://www.lumerical.com/tcad-products/fdtd/

228. Palik, E. D., *Handbook of Optical Constants of Solids*. Academic Press: 1998.

229. Hagemann, H. J.; Gudat, W.; Kunz, C. *J. Opt. Soc. Am.* **1975,** 65, (6), 742-744.

230. Maier, S. A.; Brongersma, M. L.; Kik, P. G.; Meltzer, S.; Requicha, A. A. G.; Atwater, H. A. *Adv. Mater.* **2001,** 13, (19), 1501-1505.

231. Hicks, E. M.; Zou, S.; Schatz, G. C.; Spears, K. G.; Van Duyne, R. P.; Gunnarsson, L.; Rindzevicius, T.; Kasemo, B.; Käll, M. *Nano Lett.* **2005,** 5, (6), 1065-1070.

232. Bigioni, T. P.; Lin, X.-M.; Nguyen, T. T.; Corwin, E. I.; Witten, T. A.; Jaeger, H. M. *Nat. Mater.* **2006,** 5, (4), 265-270.

233. Zeng, H.; Li, J.; Liu, J. P.; Wang, Z. L.; Sun, S. *Nature* **2002,** 420, (6914), 395-398.

234. Aydin, K.; Ferry, V. E.; Briggs, R. M.; Atwater, H. A. *Nat. Commun.* **2011,** 2, 517.

235. Moreau, A.; Ciraci, C.; Mock, J. J.; Hill, R. T.; Wang, Q.; Wiley, B. J.; Chilkoti, A.; Smith, D. R. *Nature* **2012,** 492, (7427), 86-89.

236. Zhu, P.; Jay Guo, L. *Appl. Phys. Lett.* **2012,** 101, (24), 241116.

237. Hao, J.; Wang, J.; Liu, X.; Padilla, W. J.; Zhou, L.; Qiu, M. *Appl. Phys. Lett.* **2010,** 96, (25), 251104.

238. Liu, N.; Mesch, M.; Weiss, T.; Hentschel, M.; Giessen, H. *Nano Lett.* **2010,** 10, (7), 2342-2348.

239. Wu, C.; Neuner, B.; Shvets, G.; John, J.; Milder, A.; Zollars, B.; Savoy, S. *Phys. Rev. B* **2011,** 84, (7), 075102.

240. Chen, A.; Miller, R. L.; DePrince, A. E.; Joshi-Imre, A.; Shevchenko, E.; Ocola, L. E.; Gray, S. K.; Welp, U.; Vlasko-Vlasov, V. K. *Small* **2013,** 9, (11), 1939-1946.

241. Ko, H.; Singamaneni, S.; Tsukruk, V. V. *Small* **2008,** 4, (10), 1576-1599.

242. Chang, S.; Ko, H.; Gunawidjaja, R.; Tsukruk, V. V. *J. Phys. Chem. C* **2011,** 115, (11), 4387-4394.

243. Gunawidjaja, R.; Peleshanko, S.; Ko, H.; Tsukruk, V. V. *Adv. Mater.* **2008,** 20, (8), 1544-1549.

244. Laroche, M.; Carminati, R.; Greffet, J.-J. *J. Appl. Phys.* **2006,** 100, (6), 063704.

245. Ma, W.; Wen, Y.; Yu, X. *Opt. Express* **2013,** 21, (25), 30724-30730.

246. Feng, R.; Ding, W.; Liu, L.; Chen, L.; Qiu, J.; Chen, G. *Opt. Express* **2014,** 22, (S2), A335-A343.

247. Feng, Q.; Pu, M.; Hu, C.; Luo, X. *Opt. Lett.* **2012,** 37, (11), 2133-2135.

248. Park, J. W.; Van Tuong, P.; Rhee, J. Y.; Kim, K. W.; Jang, W. H.; Choi, E. H.; Chen, L. Y.; Lee, Y. *Opt. Express* **2013,** 21, (8), 9691-9702.

249. Cao, T.; Wei, C.-w.; Simpson, R. E.; Zhang, L.; Cryan, M. J. *Sci. Rep.* **2014,** 4, 3955.

250. Yan, M.; Dai, J.; Qiu, M. *J. Opt.* **2014,** 16, (2), 025002.

251. Dhawan, A.; Canva, M.; Vo-Dinh, T. *Opt. Express* **2011,** 19, (2), 787-813.

252. García-Vidal, F. J.; Martín-Moreno, L. *Phys. Rev. B* **2002,** 66, (15), 155412.

253. Lee, K.-L.; Wu, S.-H.; Wei, P.-K. *Opt. Express* **2009,** 17, (25), 23104-23113.

254. Sobnack, M. B.; Tan, W. C.; Wanstall, N. P.; Preist, T. W.; Sambles, J. R. *Phys. Rev. Lett.* **1998,** 80, (25), 5667-5670.

255. Rechberger, W. *Opt. Commun.* **2003,** 220, (1-3), 137-141.

256. Sherry, L. J.; Chang, S.-H.; Schatz, G. C.; Van Duyne, R. P.; Wiley, B. J.; Xia, Y. *Nano Lett.* **2005,** 5, (10), 2034-2038.

257. Jian, Y.; Pol Van, D.; Liesbet, L.; Guido, M.; Gustaaf, B. *Nanotechnology* **2009,** 20, (46), 465203.

258. Alaee, R.; Menzel, C.; Huebner, U.; Pshenay-Severin, E.; Bin Hasan, S.; Pertsch, T.; Rockstuhl, C.; Lederer, F. *Nano Lett.* **2013,** 13, (8), 3482-3486.

259. Gordon, R. *Phys. Rev. B* **2006,** 73, (15), 153405.

260. Pile, D. F. P.; Gramotnev, D. K. *Appl. Phys. Lett.* **2006,** 89, (4), 041111.

261. Søndergaard, T.; Novikov, S. M.; Holmgaard, T.; Eriksen, R. L.; Beermann, J.; Han, Z.; Pedersen, K.; Bozhevolnyi, S. I. *Nat. Commun.* **2012,** 3, 969.

262. König, T.; Kodiyath, R.; Combs, Z. A.; Mahmoud, M. A.; El-Sayed, M. A.; Tsukruk, V. V. *Part. Part. Syst. Charact.* **2014,** 31, (2), 274-283.

263. Toma, M.; Toma, K.; Michioka, K.; Ikezoe, Y.; Obara, D.; Okamoto, K.; Tamada, K. *PCCP* **2011,** 13, (16), 7459-7466.

264. Ingle, J. D.; Crouch, S. R., *Spectrochemical Analysis*. Pearson Education: 1988.

265. Ahamad, N.; Bottomley, A.; Ianoul, A. *J. Phys. Chem. C* **2012,** 116, (1), 185-192.

266. Rose, A.; Hoang, T. B.; McGuire, F.; Mock, J. J.; Ciracì, C.; Smith, D. R.; Mikkelsen, M. H. *Nano Lett.* **2014,** 14, (8), 4797-4802.

267. Lisunova, M.; Mahmoud, M.; Holland, N.; Combs, Z. A.; El-Sayed, M. A.; Tsukruk, V. V. *J. Mater. Chem.* **2012,** 22, (33), 16745-16753.

268. Lassiter, J. B.; McGuire, F.; Mock, J. J.; Ciracì, C.; Hill, R. T.; Wiley, B. J.; Chilkoti, A.; Smith, D. R. *Nano Lett.* **2013,** 13, (12), 5866-5872.

269. König, T. A. F.; Ledin, P. A.; Kerszulis, J.; Mahmoud, M. A.; El-Sayed, M. A.; Reynolds, J. R.; Tsukruk, V. V. *ACS Nano* **2014,** 8, (6), 6182-6192.

270. Mock, J. J.; Hill, R. T.; Degiron, A.; Zauscher, S.; Chilkoti, A.; Smith, D. R. *Nano Lett.* **2008,** 8, (8), 2245-2252.

271. Geldmeier, J.; König, T.; Mahmoud, M. A.; El-Sayed, M. A.; Tsukruk, V. V. *Adv. Funct. Mater.* **2014,** 24, (43), 6797-6805.

272. Kravets, V. G.; Schedin, F.; Jalil, R.; Britnell, L.; Gorbachev, R. V.; Ansell, D.; Thackray, B.; Novoselov, K. S.; Geim, A. K.; Kabashin, A. V.; Grigorenko, A. N. *Nat. Mater.* **2013,** 12, (4), 304-309.

273. Malassis, L.; Massé, P.; Tréguer-Delapierre, M.; Mornet, S.; Weisbecker, P.; Barois, P.; Simovski, C. R.; Kravets, V. G.; Grigorenko, A. N. *Adv. Mater.* **2014,** 26, (2), 324-330.

274. Thongrattanasiri, S.; Koppens, F. H. L.; García de Abajo, F. J. *Phys. Rev. Lett.* **2012,** 108, (4), 047401.

275. Müller, M. B.; Kuttner, C.; König, T. A. F.; Tsukruk, V. V.; Förster, S.; Karg, M.; Fery, A. *ACS Nano* **2014,** 8, (9), 9410-9421.

276. Svedendahl, M.; Johansson, P.; Käll, M. *Nano Lett.* **2013,** 13, (7), 3053-3058.

277. Johnson, P. B.; Christy, R. W. *Phys. Rev. B* **1972,** 6, (12), 4370-4379.

278. Drachev, V. P.; Chettiar, U. K.; Kildishev, A. V.; Yuan, H.-K.; Cai, W.; Shalaev, V. M. *Opt. Express* **2008,** 16, (2), 1186-1195.

279. Klinkova, A.; Thérien-Aubin, H.; Ahmed, A.; Nykypanchuk, D.; Choueiri, R. M.; Gagnon, B.; Muntyanu, A.; Gang, O.; Walker, G. C.; Kumacheva, E. *Nano Lett.* **2014,** 14, (11), 6314-6321.

280. König, T.; Weidemüller, M.; Hemmerich, A. *Appl. Phys. B* **2008,** 93, (2), 545.

281. Christensen, N. E. *physica status solidi (b)* **1972,** 54, (2), 551-563.

282. Aubry, A.; Lei, D. Y.; Maier, S. A.; Pendry, J. B. *Phys. Rev. Lett.* **2010,** 105, (23), 233901.

283. Slaughter, L. S.; Willingham, B. A.; Chang, W.-S.; Chester, M. H.; Ogden, N.; Link, S. *Nano Lett.* **2012,** 12, (8), 3967-3972.

284. Barrow, S. J.; Rossouw, D.; Funston, A. M.; Botton, G. A.; Mulvaney, P. *Nano Lett.* **2014,** 14, (7), 3799-3808.

285. Citrin, D. S. *Nano Lett.* **2005,** 5, (5), 985-989.

286. Willingham, B.; Link, S. *Opt. Express* **2011,** 19, (7), 6450-6461.

287. Raether, H., *Surface plasmons on smooth and rough surfaces and on gratings*. Springer-Verlag: Berlin ;, 1988.

288. Homola, J. *Chem. Rev.* **2008,** 108, (2), 462-493.

289. Kraus, T.; Brodoceanu, D.; Pazos-Perez, N.; Fery, A. *Adv. Funct. Mater.* **2013,** 23, (36), 4529-4541.

290. Karg, M.; König, T. A. F.; Retsch, M.; Stelling, C.; Reichstein, P. M.; Honold, T.; Thelakkat, M.; Fery, A. *Mater. Today* **2015,** 18, (4), 185-205.

291. Hira, T.; Uchiyama, T.; Kuwamura, K.; Kihara, Y.; Yawatari, T.; Saiki, T. *Advances in Optical Technologies* **2015,** 2015.

292. Jeon, J.-W.; Ledin, P. A.; Geldmeier, J. A.; Ponder, J. F.; Mahmoud, M. A.; El-Sayed, M.; Reynolds, J. R.; Tsukruk, V. V. *Chem. Mater.* **2016,** 28, (8), 2868-2881.

293. Stockhausen, V.; Martin, P.; Ghilane, J.; Leroux, Y.; Randriamahazaka, H.; Grand, J.; Felidj, N.; Lacroix, J. C. *J. Am. Chem. Soc.* **2010,** 132, (30), 10224-10226.

294. Wu, C.; Xu, Q.-H. *Langmuir* **2009,** 25, (16), 9441-9446.

295. Zheng, Y. B.; Yang, Y.-W.; Jensen, L.; Fang, L.; Juluri, B. K.; Flood, A. H.; Weiss, P. S.; Stoddart, J. F.; Huang, T. J. *Nano Lett.* **2009,** 9, (2), 819-825.

296. Enoch, S.; Quidant, R.; Badenes, G. *Opt. Express* **2004,** 12, (15), 3422-3427.

297. Haynes, C. L.; McFarland, A. D.; Zhao, L.; Van Duyne, R. P.; Schatz, G. C.; Gunnarsson, L.; Prikulis, J.; Kasemo, B.; Käll, M. *J. Phys. Chem. B* **2003,** 107, (30), 7337-7342.

298. Leroux, Y.; Lacroix, J. C.; Fave, C.; Trippe, G.; Félidj, N.; Aubard, J.; Hohenau, A.; Krenn, J. R. *ACS Nano* **2008,** 2, (4), 728-732.

299. Leroux, Y. R.; Lacroix, J. C.; Chane-Ching, K. I.; Fave, C.; Félidj, N.; Lévi, G.; Aubard, J.; Krenn, J. R.; Hohenau, A. *J. Am. Chem. Soc.* **2005,** 127, (46), 16022-16023.

300. Huang, J.; Kim, F.; Tao, A. R.; Connor, S.; Yang, P. *Nat. Mater.* **2005,** 4, (12), 896-900.

301. Tokarev, I.; Tokareva, I.; Minko, S. *Adv. Mater.* **2008,** 20, (14), 2730-2734.

302. Hsiao, V. K. S.; Zheng, Y. B.; Juluri, B. K.; Huang, T. J. *Adv. Mater.* **2008,** 20, (18), 3528-3532.

303. Ledin, P. A.; Russell, M.; Geldmeier, J. A.; Tkachenko, I. M.; Mahmoud, M. A.; Shevchenko, V.; El-Sayed, M. A.; Tsukruk, V. V. *ACS Appl. Mater. Interfaces* **2015,** 7, (8), 4902-4912.

304. Gehan, H.; Mangeney, C.; Aubard, J.; Lévi, G.; Hohenau, A.; Krenn, J. R.; Lacaze, E.; Félidj, N. *The Journal of Physical Chemistry Letters* **2011,** 2, (8), 926-931.

305. Stockhausen, V.; Martin, P.; Ghilane, J.; Leroux, Y.; Randriamahazaka, H.; Grand, J.; Felidj, N.; Lacroix, J. C. *J. Am. Chem. Soc.* **2010,** 132, (30), 10224-10226.

306. Kozlovskaya, V.; Kharlampieva, E.; Khanal, B. P.; Manna, P.; Zubarev, E. R.; Tsukruk, V. V. *Chem. Mater.* **2008,** 20, (24), 7474-7485.

307. Bandara, H. M. D.; Burdette, S. C. *Chem. Soc. Rev.* **2012,** 41, (5), 1809-1825.

308. Mühlstein, L. A.; Sauer, J.; Bein, T. *Adv. Funct. Mater.* **2009,** 19, (13), 2027-2037.

309. Beverina, L.; Pagani, G. A.; Sassi, M. *Chem. Commun.* **2014,** 50, (41), 5413-5430.

310. Beaujuge, P. M.; Reynolds, J. R. *Chem. Rev.* **2010,** 110, (1), 268-320.

311. Leroux, Y.; Eang, E.; Fave, C.; Trippe, G.; Lacroix, J. C. *Electrochem. Commun.* **2007,** 9, (6), 1258-1262.

312. Yavuz, M. S.; Jensen, G. C.; Penaloza, D. P.; Seery, T. A. P.; Pendergraph, S. A.; Rusling, J. F.; Sotzing, G. A. *Langmuir* **2009,** 25, (22), 13120-13124.

313. Sugawa, K.; Akiyama, T.; Yamada, S. *Molecular Crystals and Liquid Crystals* **2011,** 539, (1), 1/[341]-4/[344].

314. Mortimer, R. J. *Electrochim. Acta* **1999,** 44, (18), 2971-2981.

315. Whitney, A. V.; Elam, J. W.; Zou, S.; Zinovev, A. V.; Stair, P. C.; Schatz, G. C.; Van Duyne, R. P. *J. Phys. Chem. B* **2005,** 109, (43), 20522-20528.

316. Jung, L. S.; Campbell, C. T.; Chinowsky, T. M.; Mar, M. N.; Yee, S. S. *Langmuir* **1998,** 14, (19), 5636-5648.

317. Tan, T.; Tian, C.; Ren, Z.; Yang, J.; Chen, Y.; Sun, L.; Li, Z.; Wu, A.; Yin, J.; Fu, H. *PCCP* **2013,** 15, (48), 21034-21042.

318. O'Brien, M. N.; Jones, M. R.; Kohlstedt, K. L.; Schatz, G. C.; Mirkin, C. A. *Nano Lett.* **2015,** 15, (2), 1012-1017.

319. Zheng, Y. B.; Juluri, B. K.; Mao, X.; Walker, T. R.; Huang, T. J. *J. Appl. Phys.* **2008,** 103, (1), 014308.

320. Kaganer, V. M.; Möhwald, H.; Dutta, P. *Rev. Mod. Phys.* **1999,** 71, (3), 779-819.

321. Tao, A.; Sinsermsuksakul, P.; Yang, P. *Nat Nano* **2007,** 2, (7), 435-440.

322. Israelachvili, J. *Langmuir* **1994,** 10, (10), 3774-3781.

323. Yin, B.; Ma, H.; Wang, S.; Chen, S. *J. Phys. Chem. B* **2003,** 107, (34), 8898-8904.

324. Mock, J. J.; Smith, D. R.; Schultz, S. *Nano Lett.* **2003,** 3, (4), 485-491.

325. Chiang, C. K.; Fincher, C. R.; Park, Y. W.; Heeger, A. J.; Shirakawa, H.; Louis, E. J.; Gau, S. C.; MacDiarmid, A. G. *Phys. Rev. Lett.* **1977,** 39, (17), 1098-1101.

326. Gasiorowski, J.; Kollender, J. P.; Hingerl, K.; Sariciftci, N. S.; Mardare, A. I.; Hassel, A. W. *PCCP* **2014,** 16, (8), 3739-3748.

327. Lok, C.-N.; Ho, C.-M.; Chen, R.; He, Q.-Y.; Yu, W.-Y.; Sun, H.; Tam, P. K.-H.; Chiu, J.-F.; Che, C.-M. *JBIC Journal of Biological Inorganic Chemistry* **2007,** 12, (4), 527-534.

328. Kuzma, A.; Weis, M.; Flickyngerova, S.; Jakabovic, J.; Satka, A.; Dobrocka, E.; Chlpik, J.; Cirak, J.; Donoval, M.; Telek, P.; Uherek, F.; Donoval, D. *J. Appl. Phys.* **2012,** 112, (10), 103531.

329. Lee, B.-H.; Hsu, M.-S.; Hsu, Y.-C.; Lo, C.-W.; Huang, C.-L. *J. Phys. Chem. C* **2010,** 114, (14), 6222-6227.

330. Seal, K.; Genov, D. A.; Sarychev, A. K.; Noh, H.; Shalaev, V. M.; Ying, Z. C.; Zhang, X.; Cao, H. *Phys. Rev. Lett.* **2006,** 97, (20), 206103.

331. Borys, N. J.; Shafran, E.; Lupton, J. M. *Scientific Reports* **2013,** 3, 2090.

332. Combs, Z. A.; Malak, S. T.; König, T.; Mahmoud, M. A.; Chávez, J. L.; El-Sayed, M. A.; Kelley-Loughnane, N.; Tsukruk, V. V. *Part. Part. Syst. Charact.* **2013,** 30, (12), 1071-1078.

333. Stuart, M. A. C.; Huck, W. T. S.; Genzer, J.; Muller, M.; Ober, C.; Stamm, M.; Sukhorukov, G. B.; Szleifer, I.; Tsukruk, V. V.; Urban, M.; Winnik, F.; Zauscher, S.; Luzinov, I.; Minko, S. *Nat. Mater.* **2010,** 9, (2), 101-113.

334. Karg, M.; Lu, Y.; Carbó-Argibay, E.; Pastoriza-Santos, I.; Pérez-Juste, J.; Liz-Marzán, L. M.; Hellweg, T. *Langmuir* **2009,** 25, (5), 3163-3167.

335. Karg, M.; Pastoriza-Santos, I.; Pérez-Juste, J.; Hellweg, T.; Liz-Marzán, L. M. *Small* **2007,** 3, (7), 1222-1229.

336. Sánchez-Iglesias, A.; Grzelczak, M.; Rodríguez-González, B.; Guardia-Girós, P.; Pastoriza-Santos, I.; Pérez-Juste, J.; Prato, M.; Liz-Marzán, L. M. *ACS Nano* **2009,** 3, (10), 3184-3190.

337. Gupta, S.; Agrawal, M.; Uhlmann, P.; Simon, F.; Stamm, M. *Chem. Mater.* **2010,** 22, (2), 504-509.

338. Lu, Y.; Mei, Y.; Drechsler, M.; Ballauff, M. *Angew. Chem. Int. Ed.* **2006,** 45, (5), 813-816.

339. Tokareva, I.; Minko, S.; Fendler, J. H.; Hutter, E. *J. Am. Chem. Soc.* **2004,** 126, (49), 15950-15951.

340. Gupta, M. K.; Chang, S.; Singamaneni, S.; Drummy, L. F.; Gunawidjaja, R.; Naik, R. R.; Tsukruk, V. V. *Small* **2011,** 7, (9), 1192-1198.

341. Rivas, J. G.; Kuttge, M.; Kurz, H.; Bolivar, P. H.; Sánchez-Gil, J. A. *Appl. Phys. Lett.* **2006,** 88, (8), 082106.

342. Krasavin, A. V.; Zheludev, N. I. *Appl. Phys. Lett.* **2004,** 84, (8), 1416-1418.

343. Andrew, P.; Barnes, W. L. *Science* **2004,** 306, (5698), 1002.

344. Bozhevolnyi, S. I.; Volkov, V. S.; Devaux, E.; Laluet, J.-Y.; Ebbesen, T. W. *Nature* **2006,** 440, (7083), 508-511.

345. Dintinger, J.; Klein, S.; Ebbesen, T. W. *Adv. Mater.* **2006,** 18, (10), 1267-1270.

346. Wang, H.; Vial, A. *J. Phys. Chem. C* **2013,** 117, (46), 24537-24542.

347. Xu, S.; Shan, J.; Shi, W.; Liu, L.; Xu, L. *Opt. Express* **2011,** 19, (13), 12336-12341.

348. Tsukruk, V. V.; Luzinov, I.; Larson, K.; Li, S.; McGrath, D. V. *J. Mater. Sci. Lett.* **2001,** 20, (9), 873-876.

349. Sidorenko, A.; Houphouet-Boigny, C.; Villavicencio, O.; Hashemzadeh, M.; McGrath, D. V.; Tsukruk, V. V. *Langmuir* **2000,** 16, (26), 10569-10572.

350. Manna, A.; Chen, P.-L.; Akiyama, H.; Wei, T.-X.; Tamada, K.; Knoll, W. *Chem. Mater.* **2003,** 15, (1), 20-28.

351. Ahonen, P.; Schiffrin, D. J.; Paprotny, J.; Kontturi, K. *PCCP* **2007,** 9, (5), 651-658.

352. Müller, M.; Jung, U.; Gusak, V.; Ulrich, S.; Holz, M.; Herges, R.; Langhammer, C.; Magnussen, O. *Langmuir* **2013,** 29, (34), 10693-10699.

353. Joshi, G. K.; Blodgett, K. N.; Muhoberac, B. B.; Johnson, M. A.; Smith, K. A.; Sardar, R. *Nano Lett.* **2014,** 14, (2), 532-540.

354. Evans, S. D.; Johnson, S. R.; Ringsdorf, H.; Williams, L. M.; Wolf, H. *Langmuir* **1998,** 14, (22), 6436-6440.

355. Delaire, J. A.; Nakatani, K. *Chem. Rev.* **2000,** 100, (5), 1817-1846.

356. Nishi, H.; Asahi, T.; Kobatake, S. *J. Phys. Chem. C* **2009,** 113, (40), 17359-17366.

357. Baudrion, A.-L.; Perron, A.; Veltri, A.; Bouhelier, A.; Adam, P.-M.; Bachelot, R. *Nano Lett.* **2013,** 13, (1), 282-286.

358. Schomburg, C.; Wark, M.; Rohlfing, Y.; Schulz-Ekloff, G.; Wohrle, D. *J. Mater. Chem.* **2001,** 11, (8), 2014-2021.

359. Ventura, C.; Thornton, P.; Giordani, S.; Heise, A. *Polym. Chem.* **2014,** 5, (21), 6318-6324.

360. Zhou, J.; Zhao, Y.; Yu, K.; Zhou, X.; Xie, X. *New J. Chem.* **2011,** 35, (12), 2781-2792.

361. Chi, H.; Mya, K. Y.; Lin, T.; He, C.; Wang, F.; Chin, W. S. *New J. Chem.* **2013,** 37, (3), 735-742.

362. Miniewicz, A.; Girones, J.; Karpinski, P.; Mossety-Leszczak, B.; Galina, H.; Dutkiewicz, M. *Journal of Materials Chemistry C* **2014,** 2, (3), 432-440.

363. Su, X.; Guang, S.; Xu, H.; Liu, X.; Li, S.; Wang, X.; Deng, Y.; Wang, P. *Macromolecules* **2009,** 42, (22), 8969-8976.

364. Kawai, T.; Umemura, J.; Takenaka, T. *Langmuir* **1989,** 5, (6), 1378-1383.

365. Sasaki, T.; Ikeda, T.; Ichimura, K. *Macromolecules* **1993,** 26, (1), 151-154.

366. Tanchak, O. M.; Barrett, C. J. *Macromolecules* **2005,** 38, (25), 10566-10570.

367. Toccafondi, C.; Occhi, L.; Cavalleri, O.; Penco, A.; Castagna, R.; Bianco, A.; Bertarelli, C.; Comoretto, D.; Canepa, M. *Journal of Materials Chemistry C* **2014,** 2, (23), 4692-4698.

368. Chen, H.; Kou, X.; Yang, Z.; Ni, W.; Wang, J. *Langmuir* **2008,** 24, (10), 5233-5237.

369. Mayer, K. M.; Hafner, J. H. *Chem. Rev.* **2011,** 111, (6), 3828-3857.

370. König, T.; Tsukruk, V. V.; Santer, S. *ACS Appl. Mater. Interfaces* **2013,** 5, (13), 6009-6016.

371. Haggui, M.; Dridi, M.; Plain, J.; Marguet, S.; Perez, H.; Schatz, G. C.; Wiederrecht, G. P.; Gray, S. K.; Bachelot, R. *ACS Nano* **2012,** 6, (2), 1299-1307.

372. Fornel, F. d. r. d., *Evanescent waves from Newtonian optics to atomic optics*. Springer: Berlin ;, 2011.

373. Huang, X.; El-Sayed, I. H.; Qian, W.; El-Sayed, M. A. *J. Am. Chem. Soc.* **2006,** 128, (6), 2115-2120.

374. Shahjamali, M. M.; Bosman, M.; Cao, S.; Huang, X.; Saadat, S.; Martinsson, E.; Aili, D.; Tay, Y. Y.; Liedberg, B.; Loo, S. C. J.; Zhang, H.; Boey, F.; Xue, C. *Adv. Funct. Mater.* **2012,** 22, (4), 849-854.

375. Mackey, M. A.; Ali, M. R. K.; Austin, L. A.; Near, R. D.; El-Sayed, M. A. *J. Phys. Chem. B* **2014,** 118, (5), 1319-1326.

376. Lohse, S. E.; Burrows, N. D.; Scarabelli, L.; Liz-Marzán, L. M.; Murphy, C. J. *Chem. Mater.* **2014,** 26, (1), 34-43.

377. Vigderman, L.; Khanal, B. P.; Zubarev, E. R. *Adv. Mater.* **2012,** 24, (36), 4811-4841.

378. Mayer, M.; Scarabelli, L.; March, K.; Altantzis, T.; Tebbe, M.; Kociak, M.; Bals, S.; García de Abajo, F. J.; Fery, A.; Liz-Marzán, L. M. *Nano Lett.* **2015,** 15, (8), 5427-5437.

379. Barrow, S. J.; Wei, X.; Baldauf, J. S.; Funston, A. M.; Mulvaney, P. *Nat. Commun.* **2012,** 3, 1275.

380. Huang, X.; Neretina, S.; El-Sayed, M. A. *Adv. Mater.* **2009,** 21, (48), 4880-4910.

381. Joshi, G. K.; Johnson, M. A.; Sardar, R. *RSC Advances* **2014,** 4, (30), 15807-15815.

382. Li, D.; Jang, Y. J.; Lee, J.; Lee, J.-E.; Kochuveedu, S. T.; Kim, D. H. *J. Mater. Chem.* **2011,** 21, (41), 16453-16460.

383. Kim, S.; Cheng, N.; Jeong, J.-R.; Jang, S.-G.; Yang, S.-M.; Huck, W. T. S. *Chem. Commun.* **2008**, (31), 3666-3668.

384. Yang, A.; Hoang, T. B.; Dridi, M.; Deeb, C.; Mikkelsen, M. H.; Schatz, G. C.; Odom, T. W. *Nat. Commun.* **2015,** 6, 6939.

385. Sun, Y.; Jiang, L.; Zhong, L.; Jiang, Y.; Chen, X. *Nano Res.* **2015,** 8, (2), 406-417.

386. Gramotnev, D. K.; Bozhevolnyi, S. I. *Nat Photon* **2010,** 4, (2), 83-91.

387. Kim, J.; Son, H.; Cho, D. J.; Geng, B.; Regan, W.; Shi, S.; Kim, K.; Zettl, A.; Shen, Y.-R.; Wang, F. *Nano Lett.* **2012,** 12, (11), 5598-5602.

388. Yao, Y.; Kats, M. A.; Genevet, P.; Yu, N.; Song, Y.; Kong, J.; Capasso, F. *Nano Lett.* **2013,** 13, (3), 1257-1264.

389. Wang, Z.; Chumanov, G. *Adv. Mater.* **2003,** 15, (15), 1285-1289.

390. Leroux, Y.; Lacroix, J. C.; Fave, C.; Stockhausen, V.; Félidj, N.; Grand, J.; Hohenau, A.; Krenn, J. R. *Nano Lett.* **2009,** 9, (5), 2144-2148.

391. Baba, A.; Tada, K.; Janmanee, R.; Sriwichai, S.; Shinbo, K.; Kato, K.; Kaneko, F.; Phanichphant, S. *Adv. Funct. Mater.* **2012,** 22, (20), 4383-4388.

392. Schaming, D.; Nguyen, V.-Q.; Martin, P.; Lacroix, J.-C. *J. Phys. Chem. C* **2014,** 118, (43), 25158-25166.

393. Baba, A.; Lübben, J.; Tamada, K.; Knoll, W. *Langmuir* **2003,** 19, (21), 9058-9064.

394. Baba, A.; Tian, S.; Stefani, F.; Xia, C.; Wang, Z.; Advincula, R. C.; Johannsmann, D.; Knoll, W. *J. Electroanal. Chem.* **2004,** 562, (1), 95-103.

395. Kolodziej, C. M.; Maynard, H. D. *Chem. Mater.* **2012,** 24, (5), 774-780.

396. Grigorescu, A. E.; Hagen, C. W. *Nanotechnology* **2009,** 20, (29), 292001.

397. Choueiri, R. M.; Klinkova, A.; Thérien-Aubin, H. s.; Rubinstein, M.; Kumacheva, E. *J. Am. Chem. Soc.* **2013,** 135, (28), 10262-10265.

398. Seo, E.; Ko, S.-J.; Min, S. H.; Kim, J. Y.; Kim, B.-S. *Chem. Mater.* **2015,** 27, (13), 4789-4798.

399. Willets, K. A.; Duyne, R. P. V. *Annu. Rev. Phys. Chem.* **2007,** 58, (1), 267-297.

400. Kravets, V. G.; Schedin, F.; Grigorenko, A. N. *Phys. Rev. Lett.* **2008,** 101, (8), 087403.

401. Barbero, C.; Kötz, R. *J. Electrochem. Soc.* **1994,** 141, (4), 859-865.

402. Schmidt, A. J.; Alper, J. D.; Chiesa, M.; Chen, G.; Das, S. K.; Hamad-Schifferli, K. *J. Phys. Chem. C* **2008,** 112, (35), 13320-13323.

403. Jeon, J.-W.; Ma, Y.; Mike, J. F.; Shao, L.; Balbuena, P. B.; Lutkenhaus, J. L. *PCCP* **2013,** 15, (24), 9654-9662.

404. Shao, L.; Jeon, J.-W.; Lutkenhaus, J. L. *Chem. Mater.* **2012,** 24, (1), 181-189.

405. Konig, T. A. F.; Ledin, P. A.; Russell, M.; Geldmeier, J. A.; Mahmoud, M. A.; El-Sayed, M. A.; Tsukruk, V. V. *Nanoscale* **2015,** 7, (12), 5230-5239.

406. Kim, S. K.; Cho, H.; Jeong, J.; Kwon, J. N.; Jung, Y.; Chung, B. H. *Chem. Commun.* **2010,** 46, (19), 3315-3317.

407. Jeon, J.-W.; O'Neal, J.; Shao, L.; Lutkenhaus, J. L. *ACS Appl. Mater. Interfaces* **2013,** 5, (20), 10127-10136.

408. Link, S.; El-Sayed, M. A. *J. Phys. Chem. B* **1999,** 103, (21), 4212-4217.

409. Menegazzo, N.; Herbert, B.; Banerji, S.; Booksh, K. S. *Talanta* **2011,** 85, (3), 1369-1375.

410. Cha, H.; Yoon, J. H.; Yoon, S. *ACS Nano* **2014,** 8, (8), 8554-8563.

411. Reinhard, B. M.; Siu, M.; Agarwal, H.; Alivisatos, A. P.; Liphardt, J. *Nano Lett.* **2005,** 5, (11), 2246-2252.

412. Hill, R. T.; Mock, J. J.; Hucknall, A.; Wolter, S. D.; Jokerst, N. M.; Smith, D. R.; Chilkoti, A. *ACS Nano* **2012,** 6, (10), 9237-9246.

413. Tarver, J.; Yoo, J. E.; Dennes, T. J.; Schwartz, J.; Loo, Y.-L. *Chem. Mater.* **2009,** 21, (2), 280-286.

414. Brust, M.; Gordillo, G. J. *J. Am. Chem. Soc.* **2012,** 134, (7), 3318-3321.

415. Jerkiewicz, G.; Zolfaghari, A. *J. Electrochem. Soc.* **1996,** 143, (4), 1240-1248.

416. Massari, A. M.; Stevenson, K. J.; Hupp, J. T. *J. Electroanal. Chem.* **2001,** 500, (1–2), 185-191.

417. Nguyen, M.; Sun, X.; Lacaze, E.; Winkler, P. M.; Hohenau, A.; Krenn, J. R.; Bourdillon, C.; Lamouri, A.; Grand, J.; Lévi, G.; Boubekeur-Lecaque, L.; Mangeney, C.; Félidj, N. *ACS Photonics* **2015,** 2, (8), 1199-1208.

418. Byers, C. P.; Hoener, B. S.; Chang, W.-S.; Yorulmaz, M.; Link, S.; Landes, C. F. *J. Phys. Chem. B* **2014,** 118, (49), 14047-14055.

419. Riboh, J. C.; Haes, A. J.; McFarland, A. D.; Ranjit Yonzon, C.; Van Duyne, R. P. *J. Phys. Chem. B* **2003,** 107, (8), 1772-1780.

420. Mahmoud, M. A. *J. Phys. Chem. C* **2015,** 119, (33), 19359-19366.

421. Shibaev, V.; Bobrovsky, A.; Boiko, N. *Prog. Polym. Sci.* **2003,** 28, (5), 729-836.

422. Runnerstrom, E. L.; Llordes, A.; Lounis, S. D.; Milliron, D. J. *Chem. Commun.* **2014,** 50, (73), 10555-10572.

423. Al-Attar, H. A.; Al-Alawina, Q. H.; Monkman, A. P. *Thin Solid Films* **2003,** 429, (1–2), 286-294.

424. Dyer, A. L.; Thompson, E. J.; Reynolds, J. R. *ACS Appl. Mater. Interfaces* **2011,** 3, (6), 1787-1795.

425. Amb, C. M.; Dyer, A. L.; Reynolds, J. R. *Chem. Mater.* **2011,** 23, (3), 397-415.

426. Fujiwara, H., Data Analysis. In *Spectroscopic Ellipsometry*, John Wiley & Sons, Ltd: 2007; pp 147-207.

427. Hattori, T.; Hayes, W.; Wong, K.; Kaneto, K.; Yoshino, K. *J. Phys. C: Solid State Phys.* **1984,** 17, (29), L803.

428. Bubnova, O.; Crispin, X. *Energy Environ. Sci.* **2012,** 5, (11), 9345-9362.

429. Lee, K.-S.; El-Sayed, M. A. *J. Phys. Chem. B* **2006,** 110, (39), 19220-19225.

430. Jones, M. R.; Osberg, K. D.; Macfarlane, R. J.; Langille, M. R.; Mirkin, C. A. *Chem. Rev.* **2011,** 111, (6), 3736-3827.

431. Tian, L.; Chen, E.; Gandra, N.; Abbas, A.; Singamaneni, S. *Langmuir* **2012,** 28, (50), 17435-17442.

432. Scanlon, M. D.; Peljo, P.; Mendez, M. A.; Smirnov, E.; Girault, H. H. *Chem. Sci.* **2015,** 6, (5), 2705-2720.

433. Byers, C. P.; Zhang, H.; Swearer, D. F.; Yorulmaz, M.; Hoener, B. S.; Huang, D.; Hoggard, A.; Chang, W.-S.; Mulvaney, P.; Ringe, E.; Halas, N. J.; Nordlander, P.; Link, S.; Landes, C. F. *Science Advances* **2015,** 1, (11).

434. Lu, G.; Hou, L.; Zhang, T.; Li, W.; Liu, J.; Perriat, P.; Gong, Q. *J. Phys. Chem. C* **2011,** 115, (46), 22877-22885.

435. Ganesh, N.; Zhang, W.; Mathias, P. C.; Chow, E.; Soares, J. A. N. T.; Malyarchuk, V.; Smith, A. D.; Cunningham, B. T. *Nat Nano* **2007,** 2, (8), 515-520.

436. Tan, Y.; Sutanto, E.; Alleyne, A. G.; Cunningham, B. T. *J. Biophotonics* **2014,** 7, (3-4), 266-275.

437. See, G. G.; Naughton, M. S.; Xu, L.; Nuzzo, R. G.; Kenis, P. J. A.; Cunningham, B. T. *Appl. Phys. Lett.* **2016,** 108, (17), 171108.

438. Pompa, P.; Martiradonna, L.; Della Torre, A.; Della Sala, F.; Manna, L.; De Vittorio, M.; Calabi, F.; Cingolani, R.; Rinaldi, R. *Nat. Nanotechnol.* **2006,** 1, (2), 126-130.

439. Aslan, K.; Wu, M.; Lakowicz, J. R.; Geddes, C. D. *J. Am. Chem. Soc.* **2007,** 129, (6), 1524-1525.

440. Akselrod, G. M.; Argyropoulos, C.; Hoang, T. B.; Ciracì, C.; Fang, C.; Huang, J.; Smith, D. R.; Mikkelsen, M. H. *Nat. Photonics* **2014,** 8, (11), 835-840.

441. Hoang, T. B.; Akselrod, G. M.; Argyropoulos, C.; Huang, J.; Smith, D. R.; Mikkelsen, M. H. *Nat. Commun.* **2015,** 6, 7788.

442. Nepal, D.; Drummy, L. F.; Biswas, S.; Park, K.; Vaia, R. A. *ACS nano* **2013,** 7, (10), 9064-9074.

443. Karvinen, P.; Nuutinen, T.; Rahomäki, J.; Hyvärinen, O.; Vahimaa, P. *Opt. Lett.* **2009,** 34, (20), 3208-3210.

444. Pan, Y.-L.; Hill, S. C.; Wolf, J.-P.; Holler, S.; Chang, R. K.; Bottiger, J. R. *Appl. Opt.* **2002,** 41, (15), 2994-2999.

445. Derkacs, D.; Chen, W.; Matheu, P.; Lim, S.; Yu, P.; Yu, E. *Appl. Phys. Lett.* **2008,** 93, (9), 091107.

446. Reiter, G.; Sharma, A.; Casoli, A.; David, M.-O.; Khanna, R.; Auroy, P. *Langmuir* **1999,** 15, (7), 2551-2558.

447. Xu, L.; Sharma, A.; Joo, S. W. *Macromolecules* **2012,** 45, (16), 6628-6633.

448. Reiter, G. *Phys. Rev. Lett.* **1992,** 68, (1), 75-78.

449. Seemann, R.; Herminghaus, S.; Jacobs, K. *Phys. Rev. Lett.* **2001,** 86, (24), 5534-5537.

450. Xue, L.; Han, Y. *Langmuir* **2009,** 25, (9), 5135-5140.

451. Verma, A.; Sekhar, S.; Sachan, P.; Reddy, P. D. S.; Sharma, A. *Macromolecules* **2015,** 48, (10), 3318-3326.

452. Xue, L.; Han, Y. *Prog. Mater Sci.* **2012,** 57, (6), 947-979.

VITA

Jeffrey A. Geldmeier was born in Statesville, North Carolina on November 13th, 1989 to Richard and Susan Geldmeier. He later moved with his family to Boone, North Carolina, where he attended Watauga High School and graduated as valedictorian in 2008. In 2012, he earned his BS in Materials Science and Engineering (*summa cum laude*) with minors in Green Engineering and Psychology from Virginia Tech. He pursued his Ph.D. in Materials Science and Engineering at the Georgia Institute of Technology under the guidance of Professor Vladimir V. Tsukruk. After graduation in 2017, he plans to pursue a career in industry or government pertaining to research and development.